Drying Shrinkage Performance of Slabs-on-Grade Reinforced with Recycled Tyre Steel Fibres

A thesis presented for the degree of

Doctor of Philosophy in Civil and Structural Engineering

at The University of Sheffield

By

Shanker Lal Meghwar

The Department of Civil and Structural Engineering

January 2023

To my parents for their never-ending support and encouragement.

To my late grandfather for opening a primary school in my home town and dreaming of higher education for his grandchildren and the next generation!

To my partner Shahneela for your continued support during my PhD.

To my daughter Bhumi Meghwar. Thanks for coming into our lives; and pouring love and happiness during tough times.

To all those who supported me during my entire life.

To those who believe in hard work, kindness, empathy, collective well-being and welfare of all the living beings in the universe.

Abstract

Fibre reinforced concrete (FRC) is extensively used in slabs-on-grade (SoG) for ease and speed of construction. Manufactured steel fibres (MSF) are typically used in conventional concrete mixes to eliminate the use of discrete reinforcement and control shrinkage and structural cracks. Owing to their excellent environmental credentials and mechanical properties, recycled steel fibres from tyres (RTSF) can be blended with MSF to increase the performance and sustainability of floor construction. However, there is a lack of research on the actual performance of RTSF in SoG and their effectiveness in controlling shrinkage cracks.

This research investigates the structural properties of concrete made with RTSF. It uses a complementary set of numerical modelling and extensive laboratory testing to examine moisture distribution and differential shrinkage over time. Moisture, temperature and strain in prismatic elements were monitored in the lab for almost a year.

Shrinkage results from moisture loss, so accurate modelling of moisture diffusion is essential, as it dominates the drying process in concrete and governs the development of shrinkage strains that affect structural elements' short- and long-term deformation and cracking behaviour. To address this, this study uses readily available quantities (namely w/c ratio and concrete maturity) as primary material modelling parameters to investigate the effects of pore relative humidity and ambient temperature on the diffusivity properties of concrete using inverse numerical analysis. As a result, a diffusion modelling approach that can be used in practical applications is proposed and verified through finite element analyses. The results show that numerical predictions are in good agreement with experimental data. Specifically, the model can capture the effects of the w/c ratio, concrete maturity and thermal conditions on the evolution of the moisture profile within drying reinforced and unreinforced concrete elements.

The proposed model is used to quantify the drying shrinkage strains and curvature in the laboratory specimens. Finally, a full-scale SoG is numerically modelled to assess its behaviour in terms of curling stresses, lifting up of free edges, cracking strains and differential shrinkage. The model can be used to determine drying shrinkage strains with a high degree of accuracy, thereby allowing for a more realistic assessment of crack evolution in drying concrete elements and its effects on overall structural performance.

This work will lead to the development of improved design models for shrinkage in SoG in a format that can be easily implemented in current design recommendations (e.g. TR 34, Model Code, Eurocode).

Acknowledgement

Table of Contents

List of Figures

List of Tables

List of Symbols and Abbreviations

Abbreviations

1D	One Dimensional
2D	Two Dimensional
3D	Three Dimensional
ACI	American Concrete Institute
Amb.	Ambient
ASE	All Surface Exposed
ASE_W	All Surface Exposed all Time in Water
ASE-WRHS	All Surface Exposed with RH Sensors
Avg.	Average
B	Bottom
CDP	Concrete Damage Plasticity
CMOD	Crack Mouth Opening Displacement
CS	Completely Sealed
CTE	Coefficient of Thermal Expansion
DEMEC	Demountable Mechanical Strain Gauge
EC-2	Eurocode 2
EN	European Standard
ETG	Equivalent Thermal Gradient
EU	European Union
FA	Fly Ash
FE	Finite Element
FEA	Finite Element Analysis
FEM	Finite Element Methods
fib	International Federation for Structural Concrete
FRC	Fibre Reinforced Concrete
G	Giga
GC	Gauge constant

GGBS	Ground Granulated Blast Slag
HCC	Hygral Contraction Coefficient
IE	Inelastic Strain
IV	Invar rod measurement
JSCE	Japanese Society of Civil Engineers
MC-10	Model Code 2010
MPa	Mega Pascal
MV	Measured value
NIST	National Institute of Standards and Technology
NPL	National Physical Laboratory
OSE	One Surface Exposed
OSE-WRHS	One Surface Exposed with RH Sensors
RH	Pore Relative Humidity
RILEM	International Union of Laboratories and Experts in Construction Materials, Systems and Structures
RTSF	Recycled Tyre Steel Fibres
RTSFRC	Recycled Tyre Steel Fibre Reinforced Concrete
SoGs	Slabs on Grade
T	Top
TR 34	Concrete Society's Technical Report 34
UK	United Kingdom
UTM	Universal Testing Machine
w/c	Water to Cement Ratio

Symbols

H_e	Ambient environmental humidity
H_s	Humidity at the surface or near the surface in the interior of the concrete
D	Diffusion or diffusion coefficient or diffusivity
f	Convection coefficient
d	Depth of prism

b	Width of prism
h	Height of prism
t	time
t_0	Initial time when the first measurement was observed
H	Internal relative humidity
D_1	Maximum diffusivity at $H = 1$,
α_o	Ratio of minimum to maximum diffusivity
T	Temperature
Q	Activation energy for migration of water along with the adsorption layer
R	Universal gas constant
$\emptyset_{te,28}$	Porosity at equivalent age of 28 days
$\emptyset_{te}$	Porosity at an equivalent time t_e
F	Heat flux
k	Thermal conductivity
c	Specific heat capacity
ρ	Material density
J	Diffusion flux
$\varepsilon_{ms}(y,t)$	Total mechanical strain
$\varepsilon_{fs}(y,t)$	Free drying shrinkage strain
$\varepsilon_{cs}(y,t)$	Creep strain
$\varepsilon_{as}(y,t)$	Autogenous shrinkage strain
$\varepsilon_{ts}(y,t)$	Temperature strain
T_t	Temperature at time t
T_r	Reference temperature when the first experimental value is observed
k_{sh}	Hygral contraction coefficient
β and γ	Fitting parameters
H_0	Relative humidity at the start of drying
δ	Central deflection
P	Load
L	Clear span length
I	Second moment of area
E	Young's modulus of elasticity

E_{fm}	Flexural modulus of elasticity
σ	Stress
ε	Strain
k	Curvature
$k_{cs}(t)$	Theoretical curvature
$\varepsilon_{cs}(t)$	Free drying shrinkage
A_c	Total area of concrete
e	Eccentricity
G_c	Geometric centroid
$G_{c,ef}$	Effective centroid of concrete stiffness
C	Amount of coarse aggregates
B	Amount of binder
S	Amount of slump
F	Amount of fine aggregate

Chapter 1: Introduction

This chapter discusses the motivation, background and need of this research. The main aim and objectives are also presented, along with a summary of each chapter of the thesis.

1.1 Motivation

Climate change is a worldwide challenge, causing various adverse impacts on the natural and built environment, economy, and society. The ever-increasing risk of extreme weather, floods and acid rain is creating the need to develop solutions for more sustainable, robust, resilient and adaptable infrastructure. In addition, the construction industry is one of the primary users of natural resources and produces a large amount of waste. It is responsible for 12 % of the European Union's (EU) total greenhouse gas emissions (equivalent to around 450 mega tonnes per annum or around one tonne per person, excluding imported materials). Therefore, there is a need for drastic changes, particularly when considering material use and recycling.

More than 25 billion tonnes of concrete, or 3.8 tonnes per person yearly, are used worldwide (Klee, 2009). Ground slabs and pavements account for 20 % to 50 % of concrete usage, depending on the country. Industrial ground floors are either supported by the ground (slabs-on-grade, SoG) or supported on piles (suspended slabs). These floors are spread over large areas (up to 100,000 m^2) and can be either *jointed* or *jointless*. The current trend for SoG construction is the use of jointless slabs with formed free movement joints at the perimeter of each bay up to 35 m intervals (TR-34, 2013). This type of construction can only be achieved when steel reinforcing bars are used or when short discrete fibres are added directly to the concrete mix (fibre reinforced concrete, FRC). FRC-SoGs are becoming more common due to simplicity in construction, toughness, reasonable shrinkage crack control and cost-effectiveness.

Manufactured steel fibres (MSF) are commonly used in FRC-SoG, with around 1.6 million tonnes of MSF used globally every year and about 400 k tonnes in the EU alone (Hu, 2018). The production of MSF is extremely energy intensive and generates greenhouse gases that contribute to global warming. On average, one tonne of steel production emits 1.9 tonnes of CO_2, which accounts for 4 %-5 % of total global greenhouse emissions (Kundak et al., 2009). It is estimated that steel manufacturing for concrete reinforcement emits 2.8 kilograms of CO_2 and requires 35 Mega Joules of energy per kg of steel production (Hammond and Jones, 2008; Purnell, 2013). In addition to the steel production industry, the cement manufacturing industry emitted around 1.45 G tonnes of CO_2 in 2016, equivalent to 8 % of overall global CO_2 emission (Andrew, 2018). Thus, there is a need to develop sustainable alternative solutions to address the global challenge of climate change and sustainability.

Possible solutions to meet global construction sustainability targets include using fly ash (FA), ground granulated blast slag (GGBS) and other pozzolanic materials as a partial replacement of cement, recycled concrete aggregates, recycled fibres from post-consumers vehicle tyres etc. For structural concrete, the basic mechanical properties and long-term durability should be assessed, particularly the shrinkage properties, as they change vastly with material characteristics.

1.1.1 Recycled Tyre Steel Fibres (RTSF)

In the European Union (EU), post-consumer tyre production is one tyre per person per year and is expected to exceed 3.4 million tons per annum (ETRA, 2010). In a steel market-based survey study published by Smithers Rapra (2019), it is reported that the global vehicle tyre production is around 20 million tonnes. According to Tlemat (2004), post-consumers car tyres contains 10 % steel wires, 86 % rubber and 4 % textile; while truck tyre consists of 15 % and 85 % of steel wires and rubber, respectively. Hence, conservatively, around 1 million tonnes

of high quality steel wire is disposed with waste tyres each year. At the same time around 100 k tonnes of steel fibres (MSF) are manufactured each year.

A large amount of waste tyres is broken down mechanically into its constituent components (see Fig. 1.1, after Abdulaziz Alsaif, 2019).

| Whole tyre | Shredded tyre 50 – 300 mm | RTSF | Polymer fibres |
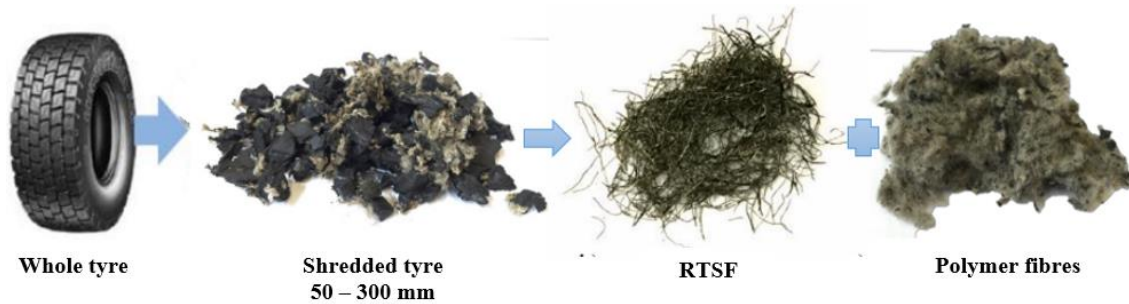
Figure 1.1 Processed RTSF.

The steel fibres extracted from post-consumers vehicle tyres are a promising alternative to MSF. Their sorting, processing and use in concrete has been studied extensively at the University of Sheffield. Till now, several research studies have already been carried out to investigate the cost-benefit ratio, basic properties and performance of RTSF-reinforced concrete (RTSFRC) in terms of mechanical properties and long-term durability under harsh environmental conditions (Tlemat, 2004; Graeff, 2011; Jafarifar, 2012; Al-Kamyani, 2018; Hu, 2018; Younis, 2014; Abdulaziz Alsaif, 2019; Isa, 2021). However, the performance of RTSF and their ability to control shrinkage in SoG still needs to be investigated in depth, specifically in terms of crack control and drying shrinkage stresses due to non-linear moisture distribution.

The deleterious effects (i.e., cracking) due to drying shrinkage can be controlled by including fibres to constrain cracks due to shrinkage contraction (Destrée et al., 2016; Gribniak et al., 2013). Randomly distributed fibres can also provide an increased flexural, shear and punching performance (Al-Kamyani et al., 2018a). As a result, RTSFs has emerged as a promising low-carbon alternative to manufactured steel fibres. The fibres effectively control both micro- and

meso-cracks, owing to the variability of their lengths (Younis, 2014), as well as provide better toughness and post-cracking performance (Jafarifar et al., 2016; Hu et al., 2019; Isa, 2021).

1.2 Problem Statement

Over time, concrete contracts as it matures and dries due to the hydration of the cement paste and water evaporation (Donald J. Janssen, 1986; Suprenant, 2002). As a result of the unique boundary conditions, non-linear moisture distribution generally develops in SoG. It causes a shrinkage gradient along the depth (higher strain at the top), resulting in differential shrinkage stresses (Younis, 2014). Non-uniform shrinkage induces detrimental intrinsic stresses in the concrete (Losberg, 1978), such as curling or warping, that should be considered during the design of the SoG.

Industrial ground floors are designed in the United Kingdom (UK) based on the Concrete Society's technical report 34 (TR 34, 2013). These structural design guidelines are based on yield line theory and empirical equations on elastic subgrade soil proposed by (Westergaard, 1925; Westergaard, 1926; Meyerhof, 1960). However, these guidelines do not directly consider the effect of drying shrinkage stresses due to non-uniform moisture distribution in the SoGs. To avoid any restrained shrinkage stresses, the guidelines suggest using impermeable membranes underneath the SoG to reduce ground friction. However, this still causes a higher moisture gradient with a complete saturation at the bottom of the SoGs.

Furthermore, the guidelines assume that the ground completely supports SoGs; however, due to differential shrinkage stresses, SoGs tend to curl, and the outer edges lift up, which induces additional stresses and, ultimately, cracking in critical regions (Ytterberg, 1987a; Destrée et al., 2016). Various researchers have proposed empirical equations for quantitatively assessing these stresses, as shown in Chapter 5. However, these empirical relations do not account for: 1) how moisture varies with time due to temperature, humidity and pore structure development;

2) how differential shrinkage develops with time due to the nonlinearity of moisture variations. It is essential that differential shrinkage stresses are considered during the analysis and design of SoGs. In addition, full-scale physical and numerical modelling can accurately predict the non-linear moisture distribution with time.

1.3 Background

1.3.1   Shrinkage

Shrinkage is the result of time-dependent changes in the volume of concrete. Concrete changes in volume due to the evaporation of bleeding water (plastic shrinkage) from fresh concrete, hydration of cement (autogenous shrinkage) and loss of water trapped in the pores of hardened concrete (drying shrinkage).

Plastic shrinkage occurs very early as water evaporates from the fresh concrete surface. Higher water-to-cement ratio mixes contain a large amount of free water, some of which rises to the surface of the concrete (i.e. bleeding of concrete) due to its lower density. Water evaporation occurs due to wind blowing over the top surface, high concrete temperature and dry environmental conditions. Plastic shrinkage is mitigated in current SoG construction practice by spreading a *dry shake* (i.e. dry mix of cement and sand) and polishing the surface (i.e. creating a thin dense layer) after a few hours of casting to eliminate plastic shrinkage cracks. However, although surface polishing may mitigate or eliminate surface cracks caused by plastic shrinkage, any deeper plastic shrinkage cracks may still remain and impair the development of tensile strength, thus resulting in overall larger crack width due to stress and drying shrinkage. The impact of plastic shrinkage is assessed separately by other researchers in the group (e.g. Alshammari et al., 2023) and it is not discussed further in this thesis.

Drying shrinkage of concrete usually occurs simultaneously with autogenous shrinkage but depends on humidity levels. The hydration of cement (i.e. chemical reaction of the cement

paste) generates heat, which causes an initial rise in temperature and consumes water leading to the development of pores (Zhang et al., 2013b; Destrée et al., 2016) and volume loss through a contraction. During drying, concrete shrinks mainly due to the loss of moisture (adsorbed water) from the finer capillary pores (2.5 to 50 nm size) of hydrated cement paste rather than the loss of free water from the larger capillary pores (Mehta, 1986). Due to the loss of moisture, an internal negative pressure (compressive force) is developed at the curved menisci of the capillary pores, which pulls the walls closer due to surface tension (Neville, 2011), leading to further contraction.

1.3.2 Restrained Shrinkage

The aggregates can resist shrinkage of the cement paste internally, resulting in numerous micro-cracks in the concrete. In large concrete elements, such as SoG, the overall movement of the slab is also restrained by the ground, which can create tensile strains in the slab, forcing the micro cracks to open up and, when many micro-cracks join together, meso and macro cracks develop. Meso cracks can be detrimental to the durability of concrete as they allow the flow of water and chemicals to attack the concrete and reinforcement.

1.3.3 Differential Shrinkage

Differential shrinkage results from differential drying, leading to differential strains and curling in SoGs. The main causes of shrinkage-induced strain gradient in hardened concrete are: early age temperature gradient; differential moisture distribution (lower at the top than the bottom of the SoG); non-uniform distribution of aggregates (higher density at the bottom than the top layer), and restraint to free shrinkage movement. Indoor slabs are dominated by differential drying, which results in the upward curling of end edges. Differential temperature gradients also affect outdoor slabs, leading to the downward curling of end edges.

1.3.4 Shrinkage Mitigation

Shrinkage cracking can be mitigated by providing skin reinforcement, adopting a higher concrete strength, and providing movement joints at regular intervals. All of these measures, however, can lead to higher costs and complicate construction. The use of relatively high amounts of reinforcement in large structures can lead to bar congestion. In SoGs, mesh reinforcement is a trip hazard and slows down construction. Skin reinforcement needs considerable cover for protection from the environment, as inadequate concrete cover may eventually cause concrete cracking and corrosion. High-strength concrete can also be used because of its higher tensile strength. However, it also has higher stiffness, which may cause higher shrinkage as shrinkage stresses are directly proportional to the stiffness of concrete. Concrete shrinkage can also be mitigated by reducing the paste/aggregate ratio, minimising C_3S content in cement, reducing the use of secondary cementitious materials (SCM), using expansive additives, shrinkage-reducing chemical admixtures and internal curing materials (Gardner and Weiss, 2005). However, these solutions are not environmentally and cost-effective (Al-Kamyani, 2018). Therefore, alternative solutions are needed, and the use of fibres in concrete has the potential to offer one of the most sustainable approaches for controlling concrete shrinkage. Fibres in concrete tend to control the cracks and enable the design of jointless SoGs up to 70 m in length.

1.4 Aims and Objectives

This research aims to investigate the behaviour of industrial ground floors with recycled tyre steel fibres (RTSF) through experimental and numerical modelling so as to understand the performance of recycled fibres in controlling cracks due to a combination of drying shrinkage and structural loading. This work will help design safer and more sustainable industrial ground floors.

1.4.1 Objectives

1. To perform a pilot study on a selected concrete mix to assess the ability of commercially available sensors to detect variations in humidity and temperature with sufficient accuracy and devise a methodology to install them in controlled test specimens.

2. To identify the critical parameters that affect the moisture distribution in conventional and FRC and model them using FEM analysis (ABAQUS CAE).

3. To calibrate the numerical moisture model using data from the literature and from original experimental work.

4. To cast control and RTSF mixes and determine the moisture and drying shrinkage distribution in laboratory specimens.

5. To determine the mechanical properties (compressive, tensile and flexural strength) required for numerical shrinkage modelling and design.

6. To perform hygro-mechanical analysis (by coupling moisture field with mechanical model) for modelling the drying shrinkage.

7. To review the state-of-the-art on SoG and perform a finite element analysis on an equivalent physical full-scale SoG to examine the effect of critical parameters on shrinkage-induced phenomena (i.e. curling).

1.5 Thesis Layout

This thesis consists of six chapters. Two chapters (Chapters 3 and 4) are standalone research journal papers (Chapter 3 has already been published, while Chapter 4 is ready to be submitted to peer-reviewed research journals). The remaining four chapters (Chapters 1, 2, 5 and 6) are presented following a conventional thesis format. Chapter 1 is the introduction of this study; Chapter 2 provides detail of the instrumentation, their calibration and the methodology implemented for the pilot study and all relevant results; Chapter 5 provides a state-of-the-art review of curling stresses in SoGs, and presents the implementation and results of a full-scale

numerical model; overall conclusion and recommendations are summarised in Chapter 6. Additional information about the results of the experimental work and numerical modelling is provided in the appendixes.

Chapter 2: '*Instrumentation and Pilot Study*' is based on **Objective 1**. This chapter summarizes how a sensor survey was conducted to select a suitable sensor for humidity, temperature and shrinkage measurements. The WAGNER METERS' humidity sensors were selected. This company produces both single-use and reusable humidity sensors for concrete, and their accuracy is traceable and acceptable according to current design guidelines (see **Appendix A**). The selected sensors are installed in concrete specimens using different techniques, and a methodology is devised for their installation in the test specimens used in the experimental programme. A new calibration rig was also prepared to calibrate the DEMEC gauges.

Chapter 3: '*Numerical Determination of Moisture Diffusivity in Concrete*' is based on (Meghwar et al., 2022), a peer-reviewed research article published in *KSCE Civil Engineering Journal*. This chapter addresses **Objectives 2 and 3**. It discusses when non-linear moisture distribution is considered in concrete, and which parameter (i.e., water content or pore relative humidity) is most suitable for the experimental measurement and modelling. Existing diffusion models in the literature are critically assessed, and as a result, moisture distribution in terms of humidity is adopted. Based on literature data, moisture analysis (hygral analysis) is performed in Abaqus by exploiting the analogy between heat transfer and moisture. Finally, a modified diffusion coefficient is proposed and validated, which considers readily available quantities (water-to-cement ratio and concrete maturity) as governing parameters. The effects of pore relative humidity and ambient temperature on the diffusivity properties of concrete are investigated using inverse numerical analysis.

Chapter 4: *'Hygro-mechanical Analysis of Drying Shrinkage of Recycled Tyre Steel Fibre Reinforced Concrete'* is to be submitted to a peer-reviewed research journal. This chapter addresses **Objectives 3, 4, 5 and 6**. In total, 25 prisms (500 × 150 × 150 mm) and 49 cubes (100 × 100 × 100 mm) were cast for humidity, shrinkage (see **Appendix D**) and compressive strength measurements. A standard concrete mix for SoG construction is used, and the performance of both a reference plain mix (Plain) as well as RTSF reinforced (see **Appendix B**) mixes with 30 kg/m^3 (F30) and 40 kg/m^3 (F40) is assessed. Specimens with different sealing conditions (i.e., completely sealed, once surface sealed, and all surface exposed) are examined to investigate the effect of self-desiccation, 1D and 3D moisture diffusion.

Additional specimens from each mix are also water cured to investigate the effect of curing conditions on their mechanical performance (see **Appendix E**). At the end of the measurements, all the prisms (shrinkage and humidity prisms, and all the time water cured prisms) are notched and tested in three-point bending (see **Appendix F**) to assess the effect of shrinkage, environmental exposure and curing regime on their flexural performance (see **Appendix C**). Finally, numerical modelling (hygro-mechanical modelling) is performed to validate the modified diffusion coefficient proposed in Chapter 3 and predict the drying shrinkage of the tested prisms. The effect of differential shrinkage and non-uniform aggregate distribution on concrete curvature and cracking is also examined both analytically and numerically.

Chapter 5: *'State-of-the-Art Review of Slabs-on-Grade and Numerical Modelling'* critically reviews curling stresses and current UK design guidelines for SoG. This chapter addresses **Objective 7** and discusses why non-uniform moisture distribution differs in SoG construction from a differential temperature gradient. It also discusses the analytical formulae used to quantify curling, including the recommendations of the Concrete Society's Technical Report

TR-34. Finally, as a case study, a 3D numerical analysis is performed on a full-scale SoG ($10000 \times 10000 \times 150$ mm) adopting the parameters derived from Chapter 4.

Chapter 6: *'Conclusions and Recommendations for Future Research'* summarizes the main findings of this thesis and proposes recommendations for the design of SoG. Recommendations for future work are also proposed and discussed.

Chapter 2: Instrumentation and Pilot Study

This chapter discusses the methodology devised for the preparation and instrumentation of a pilot specimen. The aim is to check the quality of used sensors and gauges and arrive at a reliable methodology to install them in the following phases of this research study.

First, steel cube moulds were designed to create holes at different depths to enable measurement of internal pore relative humidity (RH) at given locations. After casting and curing, the RH sensors were installed to measure the variation in humidity level with time. In addition, four demountable mechanical (DEMEC) strain gauges were used to measure the shrinkage in a concrete prism. For quality control, the gauges were calibrated against a standard Vernier calliper.

2.1 Water Content vs Relative Humidity

Moisture distribution in concrete is strongly non-linear and can be expressed in terms of either moisture content or relative humidity. However, moisture content or relative humidity are not equivalent quantities as the former measures the ratio of liquid in voids, whilst the latter is the ratio of vapour in voids to the maximum amount the air can hold at that temperature. Whilst relative humidity can be measured at a specific location/depth, the water content can only be measured over a volume, generally through concrete slices (Jafarifar et al., 2014).

If the water content is measured to determine the moisture distribution in the presence of hydration, it should be kept in mind that for concrete exposed to a drying environment, and specifically in early-age concrete, Fick's law (in terms of water content) does not hold valid (Bažant and Najjar, 1972; Mensi et al., 1988) as the distribution of pores (available for water evaporation) becomes non-uniform as hydration proceeds. In addition, the measured water content at a particular time results from evaporation and hydration and totally evaporated water

must be separated from the water consumed by hydration to model diffusivity. Hence, determining the exact water content at a particular point is practically impossible.

For diffusion in concrete, the RH is a more suitable parameter than moisture content for several reasons. Humidity is easier to determine at a specific location/depth using commercially available humidity probes. Moreover, the change in humidity due to self-desiccation is negligible (i.e. approximately ≥ 97% for normal water-to-cement ratios) and can be neglected ((Copeland and Bragg, 1955) cited in (Bažant and Najjar, 1972)). Finally, for the boundary conditions (Robin boundary condition) as given in Eq. (2.1) (usually expressed in terms of ambient humidity and RH), the rate of moisture exchange between the environment and the surface is directly related to the gradient of Gibbs' free energy per unit evaporable water, which is the actual driving force of diffusion:

$$D \left(\frac{\partial H}{\partial x} \right)_s = f(H_e - H_s) \qquad (2.1)$$

Where f is the surface film factor or convective moisture transfer coefficient that considers wind velocity, surface temperature and surface roughness; H_e is the environmental humidity; H_s is the humidity at the surface or near the surface in the interior of the concrete; D is the concrete diffusivity; and $\left(\frac{\partial H}{\partial x} \right)_s$ is the humidity gradient.

2.2 Instrumentation

The initial aim was to find the all-in-one type of sensor (i.e., that can measure shrinkage strain, temperature and RH of concrete). After contacting several companies and conducting a literature survey, it was concluded that no such sensor could measure all the parameters together in space and time. Thus, two separate instruments were needed in this study to monitor the concrete parameters: a) humidity sensors that can measure RH and temperature and b) DEMEC gauges for shrinkage measurements.

2.2.1 Humidity Sensors

Selecting an appropriate humidity sensor for concrete is challenging for various reasons:

i.   *Specification* of the sensor, whether it can measure the humidity in early-age concrete and how reliable it is (accuracy).

ii. *Size* of the sensor, if big, it can be challenging to measure the humidity near the top surface.

iii. *Calibration*, how often the device needs to be calibrated, and how complex the calibration process is.

iv. *Reusing* whether it is possible to reuse the device.

v.   *Cost-to-benefit* ratio is vital due to limited funds.

Based on these challenges, a market survey was conducted to select a suitable sensor. Different companies were contacted and invited to demonstrate how their devices work and inquired whether the devices were suited for this research study. After this process, the WAGNER METERS' humidity sensors were selected. This company produces both single-use and reusable humidity sensors for concrete. Two of their sensors, *Rapid RH L6-single use* (Wagnermeters, 2019b) and *Rapid RH 5.0-reusable* (Wagnermeters, 2019a), were selected, as shown in Fig. 2.1. The sensors' working principle is the same; the only difference is the reusability. The reusable sensor has a calibration kit and can easily be calibrated after every use. On the other hand, the single-use sensor is already calibrated, so it is ready to use in concrete. The sensors measure both humidity and temperature at the desired location.

Figure 2.1 Humidity Sensors; (a) Rapid RH L6, (b) Rapid RH 5.0.

The sensors are calibrated according to ISO/IEC 17025 and their calibration is traceable to the National Institute of Standards and Technology (NIST) and National Physical Laboratory (NPL), see **Appendix A**. Over the 0-90 % humidity range, accuracy is 1.5 % typical with a 2 % maximum, and over the 90-100 % humidity range, 1.8 % typical with 3 % maximum accuracy.

The humidity test kit also includes a *Smart Logger^{TM}* (Wagnermeters, 2018), which measures the ambient relative humidity and temperature. This sensor is kept close to the specimens, and stored in a temperature-controlled room after curing, to measure the change in ambient conditions.

2.2.2 Strain Gauges

Four DEMEC strain gauges, 50 mm, 100 mm, 200 mm and 300 mm, were available in the Lab. The gauge accessories contain a mechanical dial or digital gauge, invar or reference rod and setting rod, as shown in Fig. 2.2. Every gauge has its unique gauge constant, which needs to be multiplied by the observed difference in measured values to obtain the shrinkage strain in microstrain (see Eq. (2.2)).
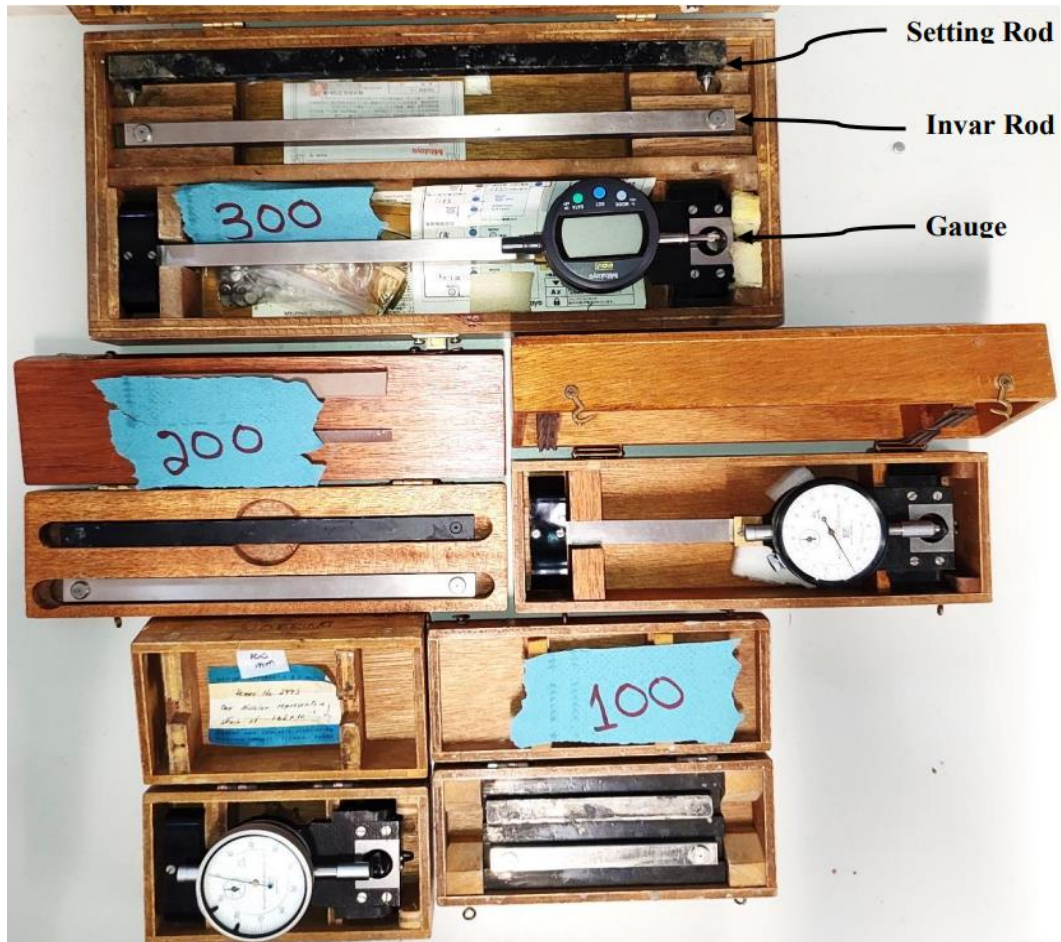
Figure 2.2 DEMEC gauges and accessories.

All the gauges were checked, and time history shrinkage results were examined to assess the accuracy of the instruments. Three measurements were taken between DEMEC points each time with each gauge, and the average of all the results is reported as a measured value.

$$Shrinkage\ strain\ (\mu) = [(IV - MV) \times GC]_t - [(IV - MV) \times GC]_{t_0} \qquad (2.2)$$

Where

IV = Invar rod measurement

MV = Measured value

t = any time t in days

t_0 = Initial time when the first measurement was observed

GC = Gauge constant

2.3 Materials and Method

The humidity sensors are designed for concrete floors and follow the installation procedure of ASTM F2170 (ASTM, 2019). Drilling a hole in large concrete floors might not damage the concrete, but it may damage small laboratory specimens. Therefore, a methodology was devised to prepare new moulds and install steel rods at desired depths to avoid drilling.

2.3.1 Sample Preparation and Humidity Sensor Installation

Measurements of RH at two depths, 60 mm and 100 mm, were required. Two cubes (S1 and S2) for RH measurements were cast in specially designed moulds ($150 \times 150 \times 150$ mm) with preinstalled steel rods having a diameter of 21mm (1 mm larger than the diameter of the RH sensors), as shown in Fig. 2.3.

Figure 2.3 Steel mould with preinstalled steel rods.

A plain concrete mix, details of the mix design are given in Chapter 4, adopted from industrial partner TWINTEC LDT. The mix is based on C28/35 concrete target strength, which is widely used for the construction of SoGs in the United Kingdom. Alshammari et al. (2023) and Hu (2018) also used this mix to investigate the plastic shrinkage and mechanical performance of

concrete. Thus the same mix is used in this study to further investigate the drying shrinkage performance of the concrete.

Four additional cubes, $100 \times 100 \times 100$ mm for compressive strength and density were cast. The cubes were demoulded after 24 hours; the steel rods were removed, and the specimens were cured for seven days. On the 8th day after casting, the cubes were sealed (with aluminium foil) from all sides except the top, where the RH sensors (Rapid L6) were installed, to mimic the drying process of slabs-on-grade (SoGs), which dry from the top surface only (Fig. 2.4).
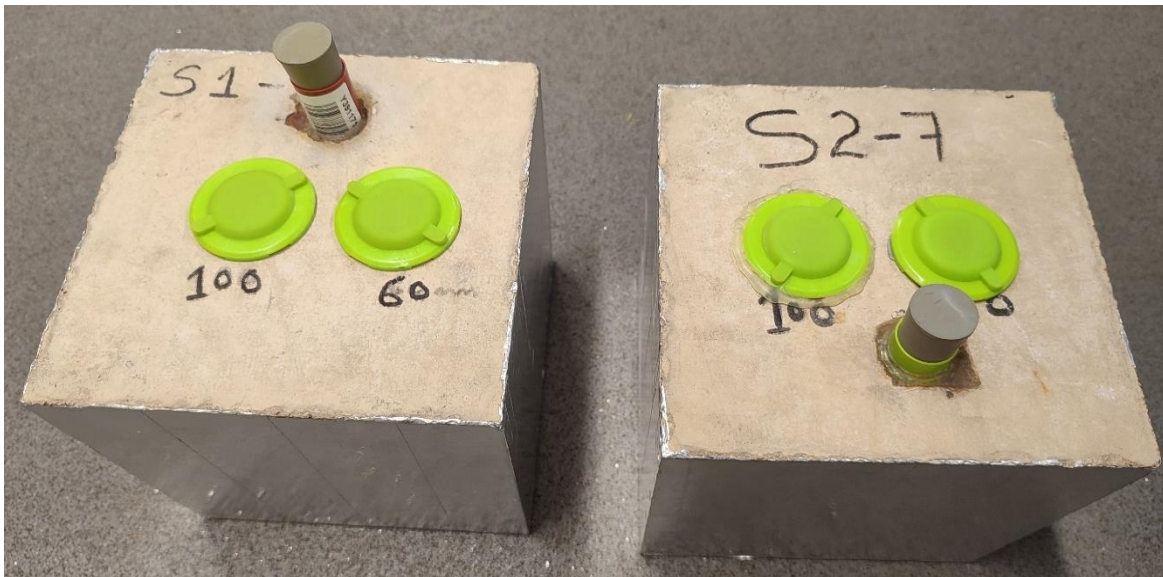
Figure 2.4 RH sensors in S1 and S2 cubes.

2.3.2 DEMEC Point Installation

An already cast prism ($100 \times 100 \times 400$ mm) was selected for shrinkage measurements. The DEMEC points were installed at three depths (i.e., 10, 30, and 70 mm) from the top surface, as shown in Fig. 2.5. Epoxy resin was used to bond the DEMEC points onto the surface of the prism. The prism was supported on round steel rods to minimise the contact area of the

boundaries, as for the RH specimens. The first reading was recorded after 24 hours, and readings continued for 57 days.
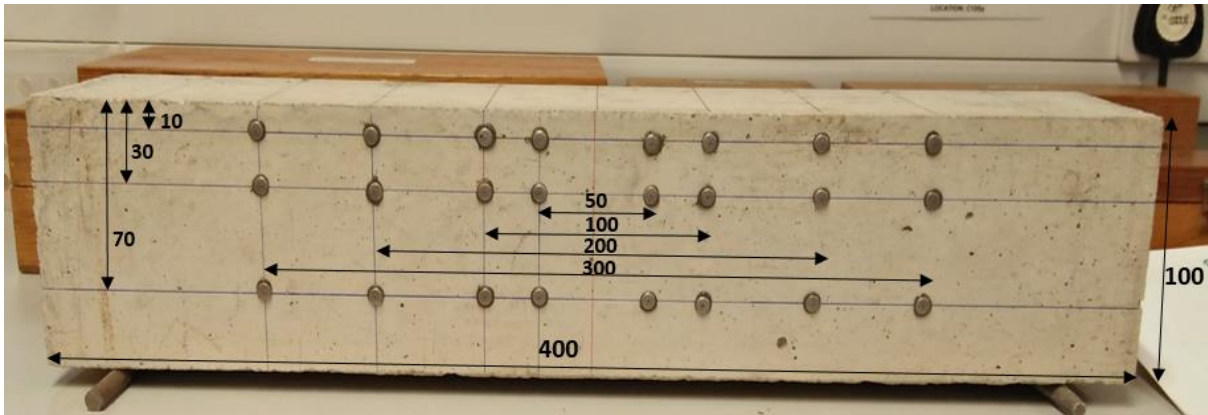
Figure 2.5 Prism geometry (all dimensions are in mm) with DEMEC discs.

2.4 Experimental Results and Discussions

2.4.1 Compressive Strength

The cubes were cured in a water tank for up to 7 and 28 days and tested in a universal testing machine (UTM) following the procedure recommended in BS EN 12390-3:2009 (EN 12390, 2009). The results are given in Table 2.1.

Table 2.1 Compressive strength.

	7 Days	28 Days
Strength (MPa)	25.6	33.1
Density (kg/m^3)		2326

2.4.2 RH Measurements

The cubes were stored in a temperature-controlled room. The first reading was recorded after 24 hours (as recommended by the sensor manufacturer), and readings continued for 74 days. There was no change in the RH (i.e., humidity stayed at 99 %) at both depths, as shown in Fig. 2.6. The temperature at both depths was the same and proportional to the ambient temperature, as shown in Fig. 2.7.

19
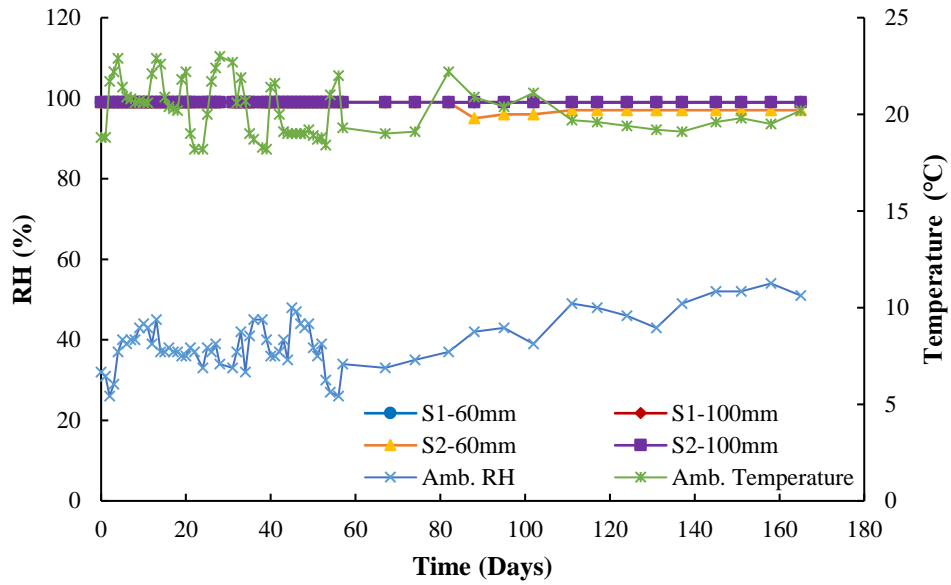
Figure 2.6 Internal RH evaluation in S1 and S2 cubes at 60 mm and 100 mm depths with ambient Humidity and temperature.
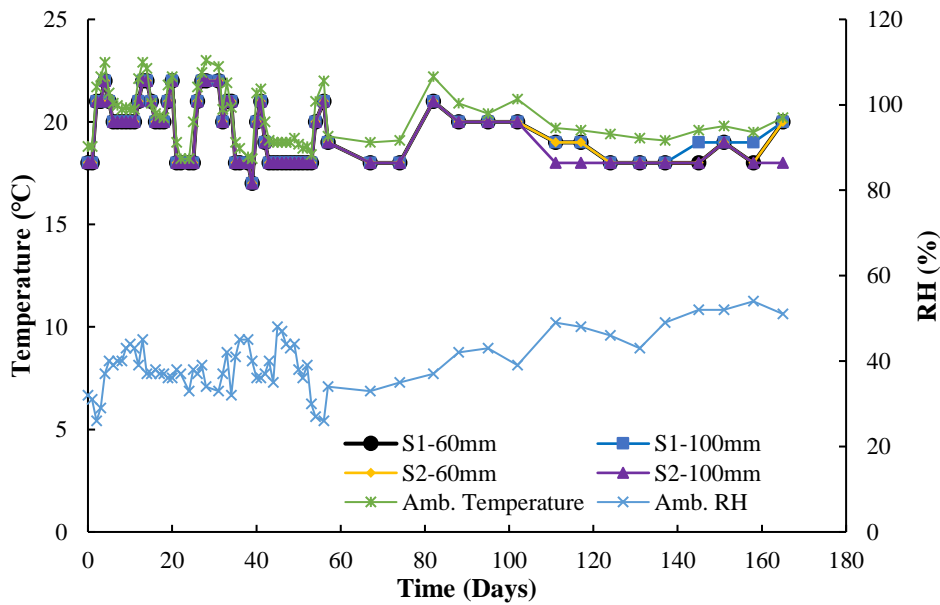
Figure 2.7 Internal temperature evaluation in S1 and S2 Cubes at 60 mm and 100 mm depths with ambient humidity and temperature.

To assess the effectiveness of pre-made holes, it was decided to drill (with a rotary drill machine) two additional holes (i.e. 15 mm depth in the S1 cube and 60 mm in the S2 cube) near the existing holes. Additionally, the existing humidity sensor (at 60 mm depth) in the S2 cube was uninstalled, and the new sensor (Rapid RH 5.0) was reinstalled after roughening the bottom surface of the hole and removing the cement paste residue with a suction air pump. This

was done to eliminate the possibility of moisture being trapped under the rich cement layer at the bottom surface of the hole. It can be seen in Fig. 2.6 (S2-60 mm line) that the reinstalled sensor after 82 days measured 95 % humidity. This confirms that the cement paste had created a rich layer at the bottom of the hole; when it was removed, the humidity started to drop gradually.

Figs. 2.8 and 2.9 show the evolution of RH and temperature in the newly drilled holes (with Rapid RH L6 sensor) and existing holes (with Rapid RH 5.0 sensor) with reinstalled sensors after roughening the bottom of the hole, respectively. RH at 15 mm depth changes faster than at 60 mm depth. However, the RH in the premade and drilled holes is the same, meaning that both types of sensors (Rapid RH L6 and Rapid RH 5.0) yield the same results, and the installation methodology is appropriate.

Ideally, RH is expected to drop gradually with time as specimens dry. However, around 15 % of the drying surface area of the cubes is covered by the sensor's caps resulting in slow drying, and there was no significant change in ambient humidity (i.e., average humidity = 50 %).
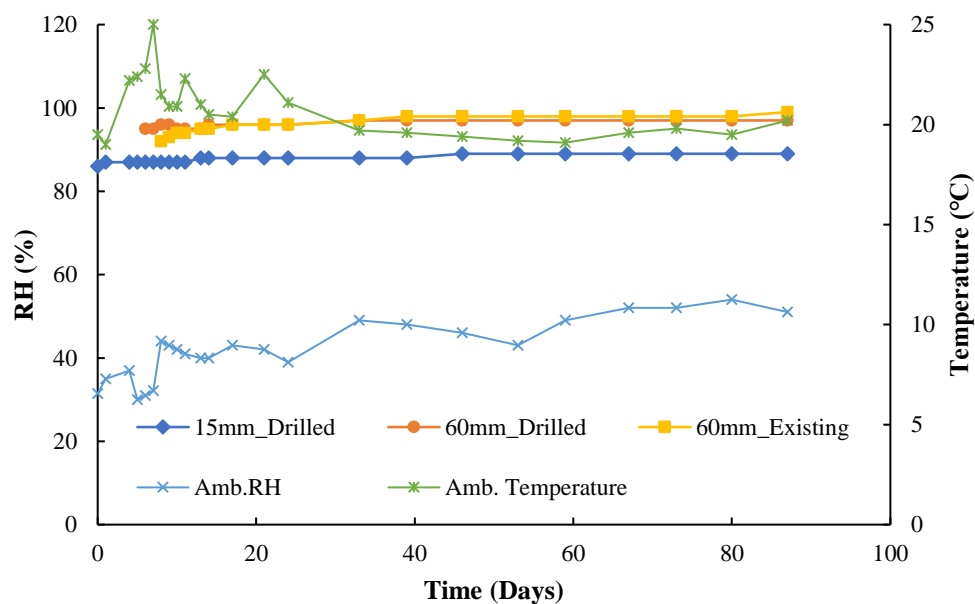
Figure 2.8 RH evaluation in new drilled and existing holes at different depths with ambient humidity and temperature.
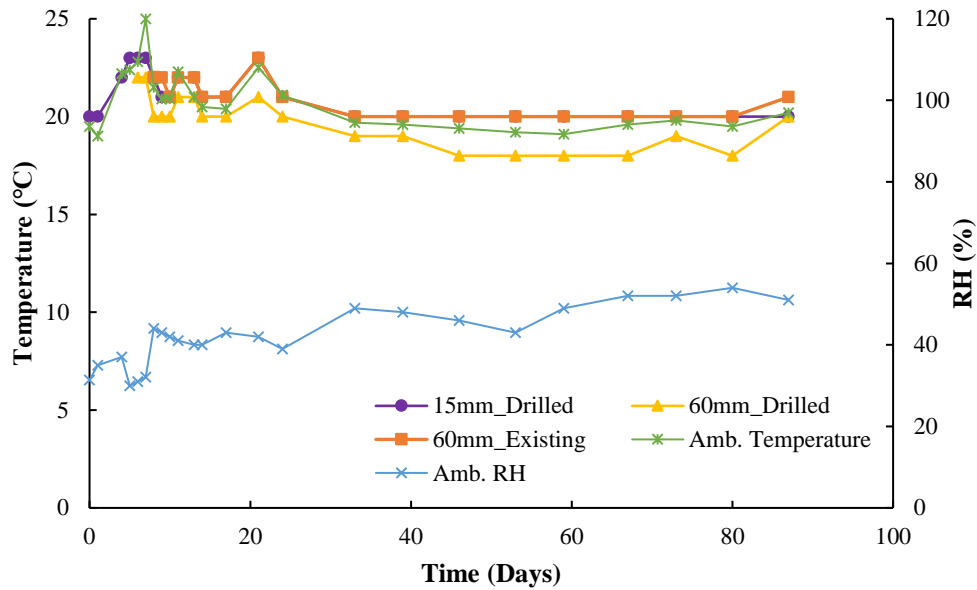
Figure 2.9 Temperature evaluation in new drilled and existing holes at different depths with ambient humidity and temperature.

To assess RH at shallow depths, two holes (at 10 mm and 20 mm depth) were drilled in a new specimen (dummy cube, no specific data is available about mix and curing age). This was done as it was necessary not to reduce further the surface area of existing cubes. The Rapid RH 5.0 sensors were installed, and the cube was stored in the same conditions. This cube was not sealed but had all surfaces exposed. Furthermore, a rubber cork was used instead of the plastic caps provided to minimise the exposed surface loss. The wedge shape of the cork fitted in easily and ensured proper opening and sealing, as shown in Fig. 2.10.
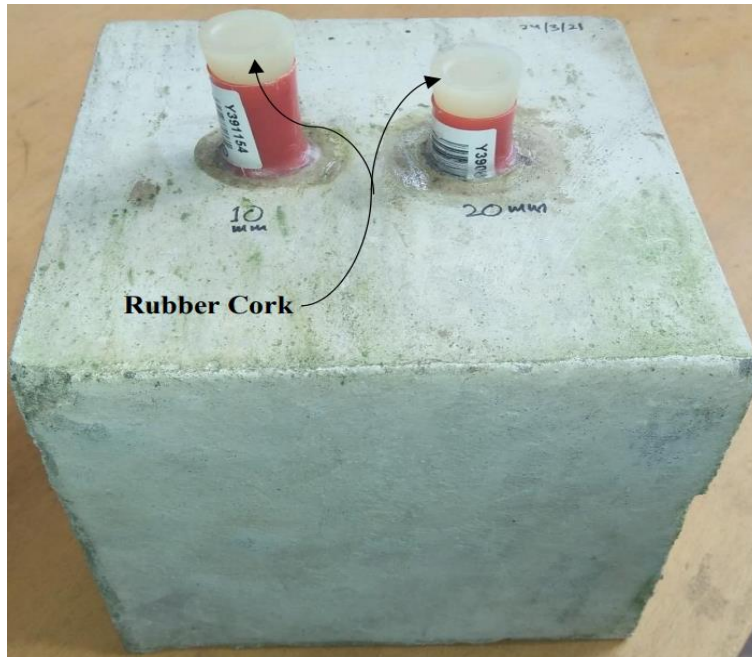
Figure 2.10 Dummy cube with Rapid RH 5.0 sensors at 10 mm and 20 mm depths.

RH and temperature readings were recorded in all cubes for 87 days. The humidity and temperature results are shown in Figs. 2.11 and 2.12, respectively. The dummy cube was already dried, so the first RH measurement recorded was 80 %. As expected, the top surface dried faster than at 20 mm depth. Initially, the specimen dries gradually at 20 mm depth and then stabilises, but as expected, more fluctuation in humidity was observed at a depth of 10 mm.

The ambient temperature also slightly impacts the humidity of the specimens, as observed in other specimens. There is no temperature difference at different depths, meaning the temperature is uniformly distributed throughout the specimen. However, the temperature at any depth is directly related to ambient temperature. As ambient temperature changes, so do the temperature at different depths.
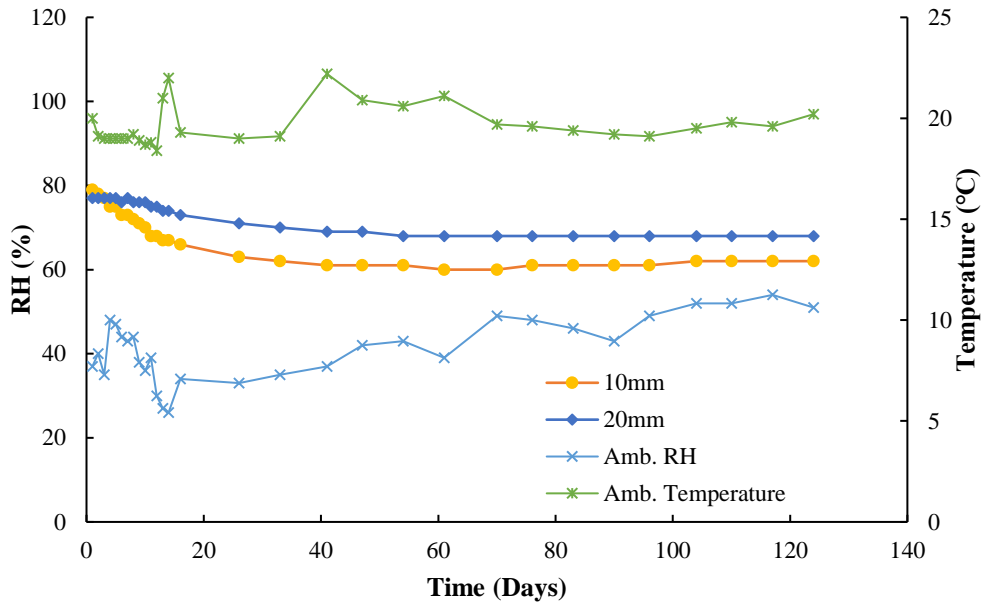
Figure 2.11 RH evaluation in 10 mm and 20 mm depths in dummy cube with ambient humidity and temperature.
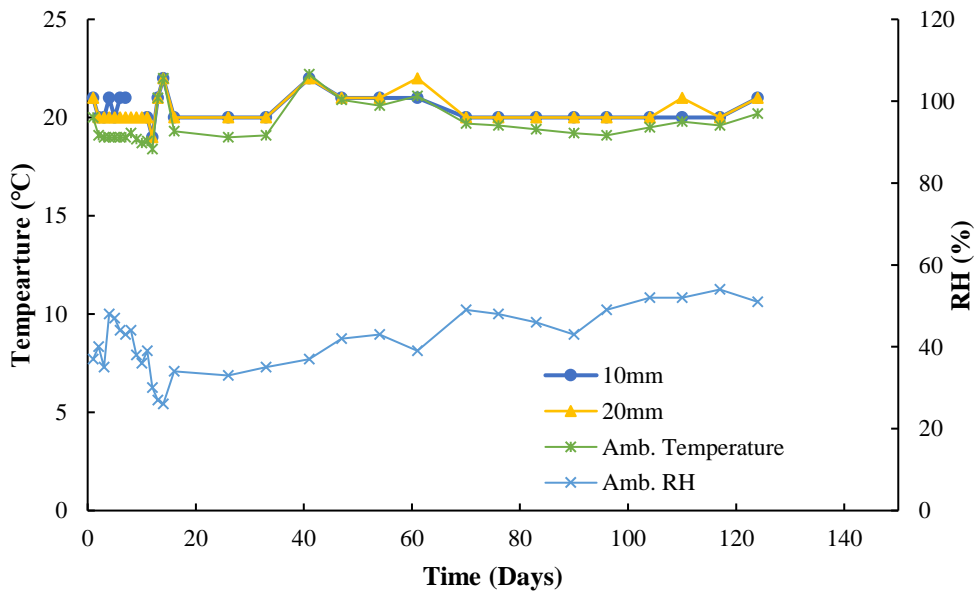
Figure 2.12 Temperature evaluation in 10 mm and 20 mm depths in dummy cube with ambient humidity and temperature.

2.4.3 Shrinkage Measurements

Figs. 2.13, 2.14 and 2.15 show the DEMEC gauge results at 10 mm, 30 mm, and 70 mm depths.
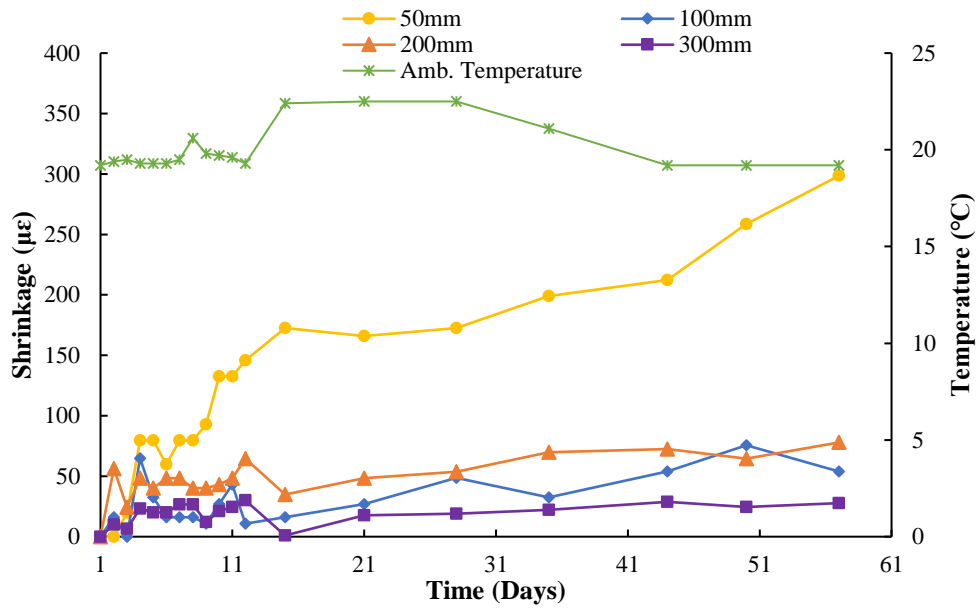
Figure 2.13 Shrinkage measurements at 10 mm depth.
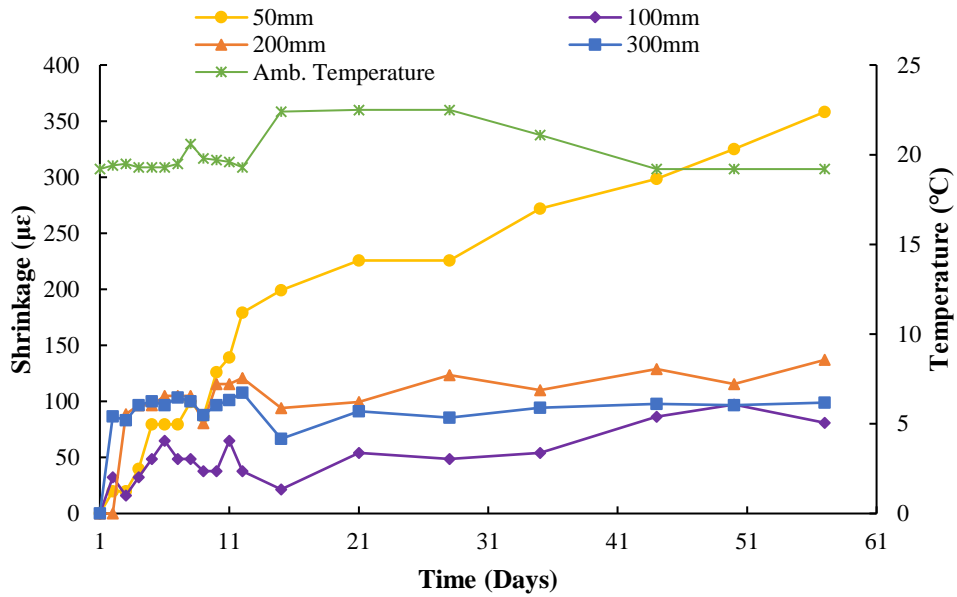
Figure 2.14 Shrinkage measurements at 30 mm depth.
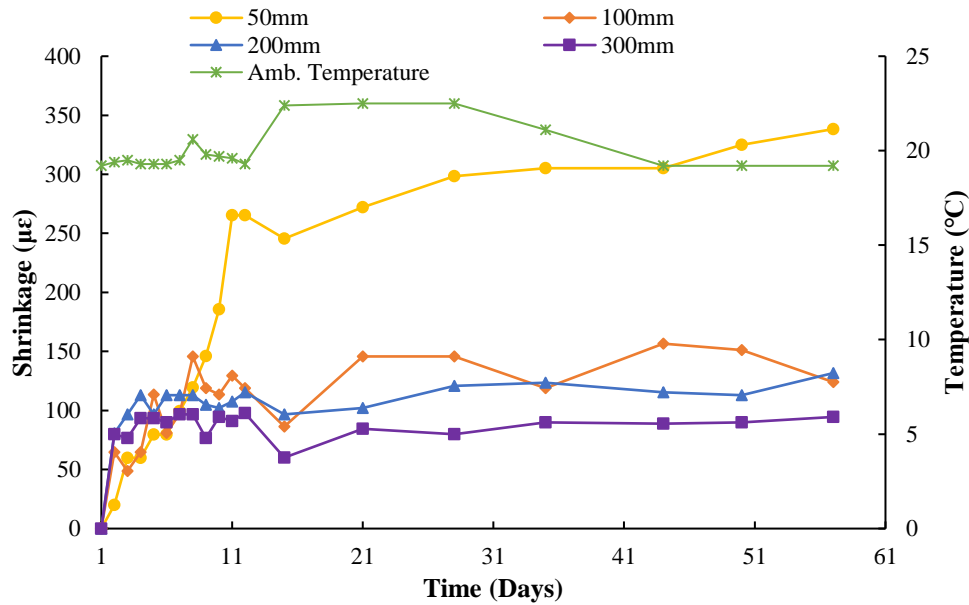
Figure 2.15 Shrinkage measurements at 70 mm depth.

All the gauges follow the same trend of shrinkage except the 50 mm gauge. This gauge shows a higher shrinkage than other gauges, probably due to wrong calibration or faulty gauge, so it was discarded for further measurement. The remaining gauges (100, 200 and 300 mm) were calibrated (see Section 2.5) with a specially developed rig to check the deviation of the gauges from standard measurements.

Shrinkage is affected by both the temperature and humidity of the ambient environment. An increase in temperature induces positive thermal strains, resulting in a lower shrinkage value. For example, shrinkage drops when the temperature changes from 19.3 °C to 22.4 °C on the 12th day. On average, shrinkage (of 100, 200 and 300 mm gauges) reduces to 18 $\mu\varepsilon$, 28 $\mu\varepsilon$ and 30 $\mu\varepsilon$ at 10, 30 and 70 mm depths, respectively. To determine the drying shrinkage more accurately, thermal expansion must be subtracted from the observed values. At the same time, specimens in a higher humidity environment can swell due to water absorption and cement chemical reactions, resulting in the expansion of specimens. However, in this study, the measured average ambient humidity is around 45 % which always causes moisture diffusion from the specimen, hence, leading to shrinkage strains. Sharp humidity fluctuations for a short

period of time are not expected to affect shrinkage measurements, as diffusion happens very slowly, and moisture takes time to travel from the deeper layer to the surface, as also observed in the experiments.

2.5 Calibration of DEMEC Gauges

All the gauges were re-calibrated with a specially designed rig, as shown in Fig. 2.16. The rig has one end fixed with a DEMEC disk. The end can be adjusted according to the required gauge length. The other end is moveable and attached to a digital Vernier Calliper (standard calibration device).

The calliper has a precision of 0.001 mm, while the DEMEC gauges can measure a minimum of 0.002 mm. The DEMEC gauge and calliper results are shown in Figs. 2.17, 2.18 and 2.19.

Figure 2.16 Calibration rig.
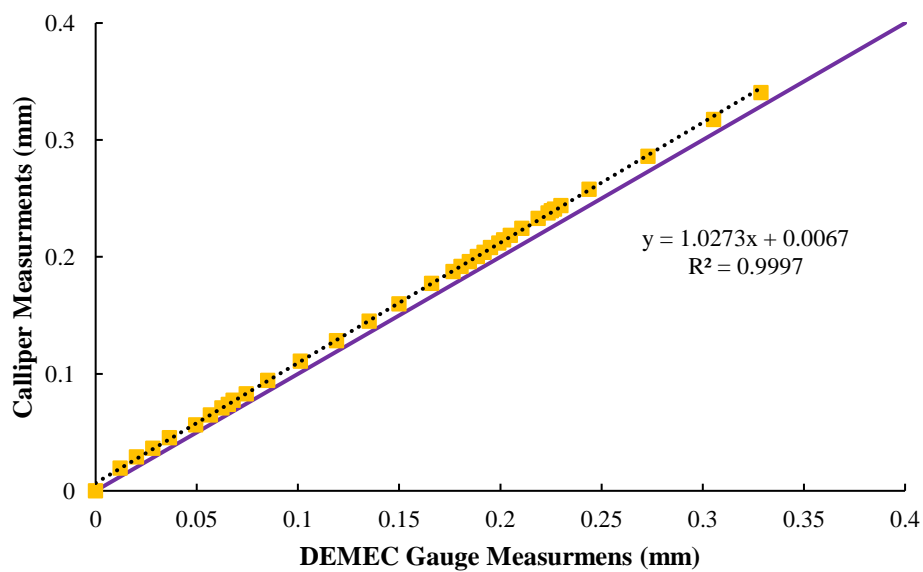
Figure 2.17 Calibration results of 100 mm gauge.
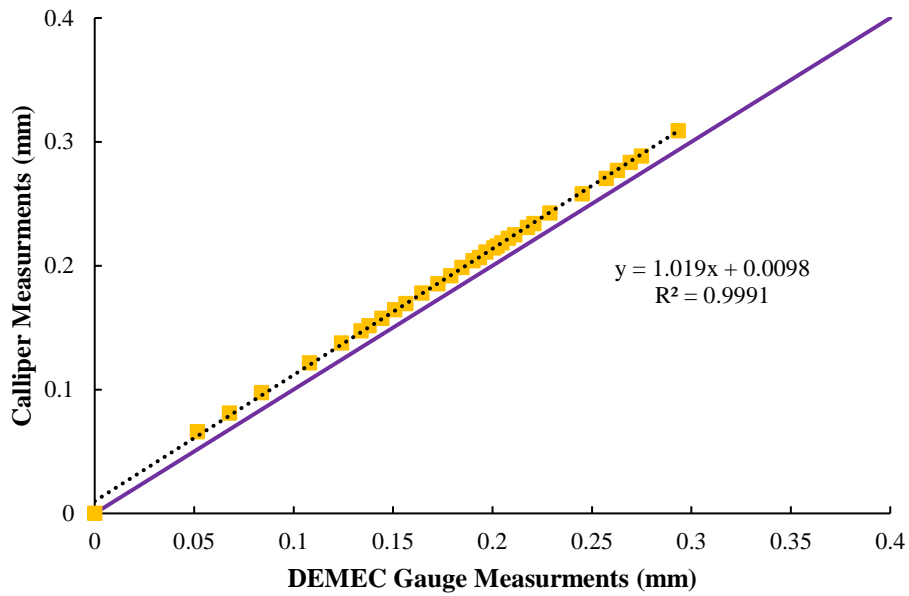
Figure 2.18 Calibration results of 200 mm gauge.
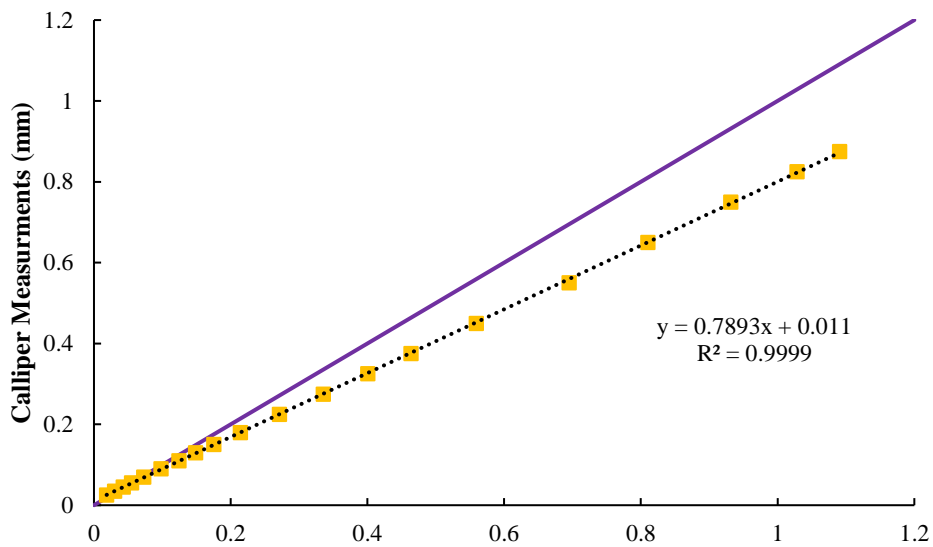
Figure 2.19 Calibration results of 300 mm gauge.

The calibration factor of 1.0273, 1.019 and 0.7893 is multiplied with measured values (of the real prisms) of the 100, 200 and 300 mm gauges, respectively.

2.6 Summary

In this pilot study, specimens were cast and RH sensors were installed to check installation methodology and measurement reliability. The adopted methodology worked well with a few modifications, including changing the sealing cap with a rubber cork and roughening the bottom of the installation hole to remove the rich layer of cement paste before sensor installation.

Additionally, the DEMEC gauges were re-calibrated, and correction factors were determined to adjust the measured shrinkage values. Further, these factors will be used for shrinkage analysis in the research specimens.

Chapter 3: Numerical Determination of Moisture Diffusivity in Concrete

Author's contribution statement

Shanker Lal Meghwar: Conceptualization, Methodology, Running FEA analysis, Writing-original draft, Editing, Formatting, Investigation and Visualization.

Kypros Pilakoutas: Supervision, Review and editing, Investigation, and Technical suggestions.

Giacomo Torelli: Supervision, Review and editing, Investigation, and Technical suggestions.

Maurizio Guadagnini: Supervision, Review and editing, and Formatting.

Abstract

Accurate modelling of moisture diffusion is essential, as it dominates the drying process in concrete and governs the development of shrinkage strains that affect the short- and long-term deformation and cracking behaviour of structural elements. Key models available in the literature use porosity as the main parameter to predict the diffusivity of the material. Although physically sound, this approach is difficult to apply in practice, as the in-situ determination of concrete porosity is challenging. To address this, the present study uses readily available quantities (namely w/c ratio and concrete maturity) as primary material modelling parameters and investigates the effects of pore relative humidity and ambient temperature on the diffusivity properties of concrete using inverse numerical analysis and available experimental data. As a result, a diffusion modelling approach that can be readily used in practical applications is proposed and verified through finite element analyses. The results show that numerical predictions are in good agreement with experimental data. Specifically, the model is capable of capturing the effects of w/c ratio, concrete maturity and thermal conditions on the evolution of the moisture profile within drying concrete elements. The model can be used to determine drying shrinkage strains with a high degree of accuracy, thereby allowing for a more realistic assessment of crack evolution in drying concrete elements and its effects on overall structural performance.

3.1 Introduction

Moisture content and distribution play an important role in the structural performance of concrete elements, as they affect directly their durability (Saeidpour and Wadsö, 2016), freeze-thaw resistance, fire spalling, creep and shrinkage behaviour (Kim and Lee, 1998).

The determination of the evolution of moisture distribution with time is complex due to the dynamic nature of the cement matrix, micro-structure, hydration processes, and environmental exposure (Arfvidsson and Claesson, 2000). Two possible moisture loss mechanisms can be identified in solid networks (Sherwood, 1929): (i) vaporization at a point beneath the surface followed by diffusion through the porous medium to the surface and then out into the air and (ii) liquid diffusion towards the surface followed by vaporization at the surface and finally diffusion into the environment. It is generally difficult to distinguish between the two mechanisms as they can develop simultaneously. In unsaturated concrete (with pore relative humidity, RH between 15 % to 95 %) moisture movement is often considered to be driven by the diffusive process only (Bažant and Najjar, 1972; Kodikara and Chakrabarti, 2005). If this assumption is accepted, moisture diffusivity can be used to represent both bulk water and vapour diffusion.

Vapour diffusion is generally faster in early-age concrete due to higher free available moisture. In general, the diffusion process is affected by environmental temperature and humidity and concrete porosity. While higher temperatures can cause faster diffusion, and higher environmental humidity typically results in lower moisture gradients between the concrete and the surrounding environment, thus leading to slower diffusion. Free water partially diffuses into the environment through capillary action due to the moisture gradient between concrete and the environment, while the remaining water is consumed by the hydration process or can remain trapped in the non-interconnected pores of the concrete. The latter mechanism can affect and slow down the diffusion process over time. Although a model describing moisture

diffusion as a function of temperature, RH and concrete porosity has been proposed by Kang et al. (2012), a reliable estimate of porosity is extremely difficult as it is affected by several parameters, including water-to-cement ratio (w/c), aggregates content, hydration, the width of the interfacial transition zone (ITZ), as well as their complex interactions. Models that can capture accurately the diffusion mechanisms in concrete through easily measurable parameters, like w/c ratio and concrete maturity, would enable the development of more reliable assessment methods for crack development and structural performance of drying concrete elements.

This study proposes a general modelling approach that considers concrete diffusion in terms of readily available material parameters and environmental conditions. The proposed approach can account for porosity indirectly and implements the use of Bazant and Najjar's (1972) model (also used in Model Code 2010, MC-10) to predict diffusion at different w/c ratios and concrete maturity levels. The diffusivity parameters suggested by the MC-10 and Kang et al. (2012) are also assessed through a series of inverse numerical analyses.

3.2 Literature Review

3.2.1 Moisture and Shrinkage Phenomenon

Shrinkage of solid networks can be attributed to the development of four main mechanisms driven by capillary pressure (due to surface tension and interfacial tension in fluids), osmotic pressure (due to concentration gradient), disjoining pressure (produced by the presence of solid-liquid interface), and moisture stress/moisture potential (partial Gibb's free energy of liquid available in pores) (Scherer, 1990). In hardened concrete, the dominant shrinkage-inducing mechanism is capillary pressure (Powers, 1960). During drying, water evaporation from a surface causes a pressure gradient within the concrete matrix that leads to diffusion through its porous medium (Ytterberg, 1987a). The loss of moisture from the finer capillary pores (2.5 to 50 nm size) of hydrated cement paste (Mehta, 1986) results in negative pressure in the pore water (Grasley et al., 2006), which pulls the pore walls closer and causes

33

compressive forces on the surrounding matrix; and thus an overall contraction of the material (Scherer, 1990).

Drying shrinkage in concrete normally takes place simultaneously with autogenous shrinkage. Autogenous shrinkage results from the hydration of cement, which causes an initial rise in temperature and leads to the development of pores and volume loss through contraction (Destrée et al., 2016; Zhang et al., 2013a). With time, hydrates form and cover the space between cement particles and reduce the size of capillary pores (Takiya et al., 2015), thus reducing the diffusivity of concrete.

Shrinkage contraction is generally resisted by internal and external restraints and can result in differential shrinkage. Internally, shrinkage of the cement matrix is resisted by aggregates and reinforcement and can lead to micro and meso-cracks (Al-Kamyani et al., 2018b). Externally, the restrain provided to an element by adjacent structural members (e.g. walls, columns etc.) or by the soil (Hossain and Weiss, 2004) can lead to large movements and macro-cracks (TR-34, 2003). Meso and macro cracks open channels that offer preferential paths for fluid flow, thereby further facilitating drying. The presence of water in cracks can also lead to further physical damage due to, for instance, freeze-thaw phenomena. Moreover, cracks can facilitate the ingress of aggressive substances that can damage concrete chemically (e.g., chloride and sulphate attacks) and corrode the reinforcement, thus reducing durability and potentially leading to structural failures.

Differential shrinkage in concrete can also result from non-uniform moisture distribution. This can be caused by moisture exchange with the environment through exposed surfaces (Rollings, 1993), which is generally accelerated by high-velocity wind, high temperatures, low humidity levels, sunlight etc. Although moisture movement is a 3-dimensional phenomenon (ACI-360R, 2010), 1-dimensional models are suitable to describe moisture movement in elements such as

slabs-on-grade (SoGs) (Jafarifar et al., 2014; Kim and Lee, 1998; M. Asad et al., 1997) or thin shell structures. However, an accurate assessment of the evolution of moisture distribution within the material is needed for a reliable assessment of shrinkage-induced cracking, curling and warping stresses and their effects on strength and durability.

3.2.2   Moisture Modelling

Moisture distribution in concrete has been studied for many years, with the earliest drying models adopting the linear diffusion theory. In a linear drying model, the diffusion coefficient does not depend on the moisture conditions (Pickett, 1946; Carlson, 1937). However, Sakata (1983), Akita et al. (1997), Xu et al. (2009) and Jafarifar et al. (2014) observed that concrete diffusivity depends on water content, making diffusivity a nonlinear phenomenon. Bažant and Najjar (1971) used Fick's law and postulated that diffusion in concrete is a function of RH (or relative vapour pressure) as given in Eq. (3.1).

$$\frac{\partial H}{\partial t} = div \; (D(H) \; grad \; H) \tag{3.1}$$

Where t = time, $D(H)$ = diffusion coefficient function of RH and $H =$ RH

Bažant and Najjar (1972) also proposed that moisture distribution in concrete is strongly non-linear and can be expressed in terms of either moisture content or RH. However, moisture content or RH are not equivalent quantities.

When concrete is exposed to drying in the presence of hydration, such as in the case of early-age concrete, expressing Fick's law in terms of water content is generally not a practical choice (Bažant and Najjar, 1972; Mensi et al., 1988). This is because the distribution of pores (available for water evaporation) becomes non-uniform as hydration continues, making the water content at a particular time not only a function of evaporation but also hydration. Hence, when the water content is used as a reference variable, the total evaporable water needs to be

separated from the water consumed by hydration to model diffusivity. Furthermore, the water content can only be measured as an average over a volume, normally through concrete slices (Jafarifar et al., 2014) and the exact water content at a particular point is practically impossible to determine.

RH is generally regarded as a more suitable parameter than moisture content to model diffusion in concrete. An advantage of using RH as a reference humidity parameter is that it can be easily measured experimentally at a specific location/depth using commercially available RH probes. Moreover, the change in RH due to self-desiccation (in sealed specimens) is negligible (i.e., it stays approximately ≥ 97 % for higher water-to-cement ratios) and can be neglected even if hydration is not yet completed ((Copeland and Bragg, 1955) cited in (Bažant and Najjar, 1972)). Finally, for the boundary conditions (Robin boundary condition) considered in Eq. (3.2) (usually expressed in terms of ambient humidity and RH), the rate of moisture exchange between the environment and the surface is directly related to the gradient of Gibbs' free energy per unit evaporable water, which is the actual driving force of diffusion.

$$D \left(\frac{\partial H}{\partial x} \right)_s = f(H_e - H_s) \tag{3.2}$$

Where f is the surface film factor or convective moisture transfer coefficient that considers wind velocity, surface temperature and surface roughness; H_e is the environmental humidity; H_s is the RH at the surface or near the surface in the interior of the concrete.

The relationship between diffusion coefficient and RH is given in Eq. (3.3) (Bažant and Najjar, 1972).

$$D(H) = D_1 \cdot \left(\alpha_o + \frac{1 - \alpha_o}{1 + \left(\frac{1 - H}{1 - H_c} \right)^n} \right) \tag{3.3}$$

Where; D_1 is the maximum diffusivity at $H = 1$, α_o is the ratio of minimum to maximum diffusivity, and H_c is the RH at $D(H) = 0.5(\alpha_0 + 1)D_1$.

Model Code 2010 (MC-10) adopted Bazant and Najjar's model for isothermal conditions by assuming $n = 15$, $\alpha_o = 0.05$, $H_c = 0.80$ and $D_1 = \frac{D_{1,0}}{f_{cm}-8}$, while $D_{1,0} = 1 \times 10^{-8} \frac{m^2}{s}$.

Both the models proposed by Bažant and Najjar (1972) and the formulation suggested by Model Code 2010 neglect the effects of hydration, pore structure evolution and environmental conditions. However, experimental evidence shows that these parameters significantly affect the diffusivity properties of early-age concrete (Kang et al., 2012). In addition, according to Abyaneh et al., (2015) and Abyaneh, (2015) at the microstructure level, diffusivity is further affected by the complex interaction between the individual ingredients of the cement matrix.

To account for the effect of environmental conditions, Bazant and Thonguthai (1978) proposed a model that considers the diffusion coefficient to be an explicit function of RH and ambient temperature of concrete (see Eq. (3.4)).

$$D(H,T) = D_1 \cdot f_1(H) \cdot f(T)$$ (3.4)

$$f(T) = exp\left[\frac{Q}{R}\left(\frac{1}{293} - \frac{1}{T + 273}\right)\right]$$

More recently, Kang et al. (2012) further extended this model by including the effects of degree of hydration, non-homogeneity, and porosity of concrete as follows:

$$D(H,T,\emptyset_{te}) = D_1 \cdot f_1(H) \cdot f_2(T) \cdot f_3(\emptyset_{te0})$$ (3.5)

Where; $D(H,T,\emptyset_{te})$ diffusion coefficient function of RH, temperature, and porosity of concrete and D_1 maximum $D(H)$ for $H = 1$,

$$f_1(H) = \alpha + \frac{1-\alpha}{1+\left(\frac{1-H}{1-H_c}\right)^4} \qquad \text{For H < 1}$$

$$f_1(H) = 1 \qquad \text{For H} \geq 1$$

$$f_2(T) = \left(\frac{293}{T+273}\right)^{1.5} \cdot exp\left[\frac{Q}{R}\left(\frac{1}{293} - \frac{1}{T+273}\right)\right]$$

$$f_3(\emptyset_{te}) = \left(\frac{\emptyset_{te}}{\emptyset_{te,28}}\right)^m$$

α is the ratio of minimum to maximum diffusivity, T is the temperature in ⁰C, Q is the activation energy for migration of water along with the adsorption layer in the capillary pores, R is the universal gas constant, $\emptyset_{te,28}$ is the porosity at equivalent age of 28 days and $\emptyset_{te}$ is the porosity at an equivalent time t_e.

Kang et al. (2012) model, though comprehensive, depends on the porosity of early-age concrete, which is difficult to assess both experimentally and analytically. This is because porosity is a function of several parameters including the w/c ratio, degree of hydration and width of the interfacial transition zone (Abyaneh et al., 2016). Furthermore, porosity is affected by aggregate content, its gradation, shape, and physical/chemical characteristics. The complex interaction between the above-mentioned parameters makes it difficult to predict porosity a-priory (Abyaneh et al., 2013). Therefore, there is a need for the development of a simplified, yet reliable diffusion model that is easy to use and predicts well moisture distribution in different types of concrete.

3.3 Numerical Investigation

This section discusses the numerical methodology used in this study. It starts by presenting the diffusion model implemented in the Finite Element Analysis (FEA) package that is adopted to predict 1-dimensional drying of available experimental data from the literature is presented and

commented upon. Subsequently, the inverse analysis approach used to determine optimal diffusion model parameters is presented along with the adopted optimisation criteria.

3.3.1 Moisture Modelling

The moisture distribution analysis is performed in the FEA-based software ABAQUS (ABAQUS, 2019). The package offers a heat transfer finite element framework that is here adopted to model moisture diffusion, exploiting the formal analogy between Fourier's law for heat conduction (see Eqs. (3.6) and (3.7)) and Fick's law of diffusion (see Eqs. (3.8) and (3.9)).

$$F = -k \cdot \frac{dT}{dx} \tag{3.6}$$

$$\frac{\partial T}{\partial t} = \left(\frac{k}{c \cdot \rho}\right) \cdot \frac{\partial^2 T}{\partial x^2} \tag{3.7}$$

Where F is the heat flux, k is the thermal conductivity, $\frac{\partial T}{\partial x}$ is the temperature gradient, $\frac{\partial T}{\partial t}$ is the temperature change with time, c is the specific heat capacity and ρ is the material density.

$$J = -D \cdot \frac{dH}{dx} \tag{3.8}$$

$$\frac{\partial H}{\partial t} = D \cdot \frac{\partial^2 H}{\partial x^2} \tag{3.9}$$

Where J is the diffusion flux, $\frac{\partial H}{\partial x}$ is the RH gradient, and $\frac{\partial H}{\partial t}$ is the RH change with time.

Specifically, the heat transfer framework is here used to model moisture transfer by assuming the main variable in Eqs. (3.6) and (3.7) to be moisture (in terms of RH) rather than temperature. Accordingly, it is assumed that $D = \frac{k}{c \cdot \rho}$. This means that the coefficient of diffusion or moisture conductivity is analogous to thermal conductivity when $c \cdot \rho = 1$, and heat flux is equivalent to moisture flux.

3.3.2 Numerical Models

Numerical analyses were performed on concrete prisms $100 \times 100 \times 300$ mm (Fig. 3.1a) to simulate the experimental specimens tested by Kang et al. (2012). The concrete mix used in the original experiments had a w/c ratio equal to 0.50. Values of RH were measured after one day of water curing at three different ambient temperatures (20 °C, 50 °C and 80 °C), and constant ambient humidity (50 %), at three different depths (i.e., 20 mm, 50 mm and 150 mm from the top surface) up to 74 days of equivalent age. Different numerical analyses were performed for each of the test environments using the diffusion coefficient derived through the relevant inverse analysis as discussed in the next section.
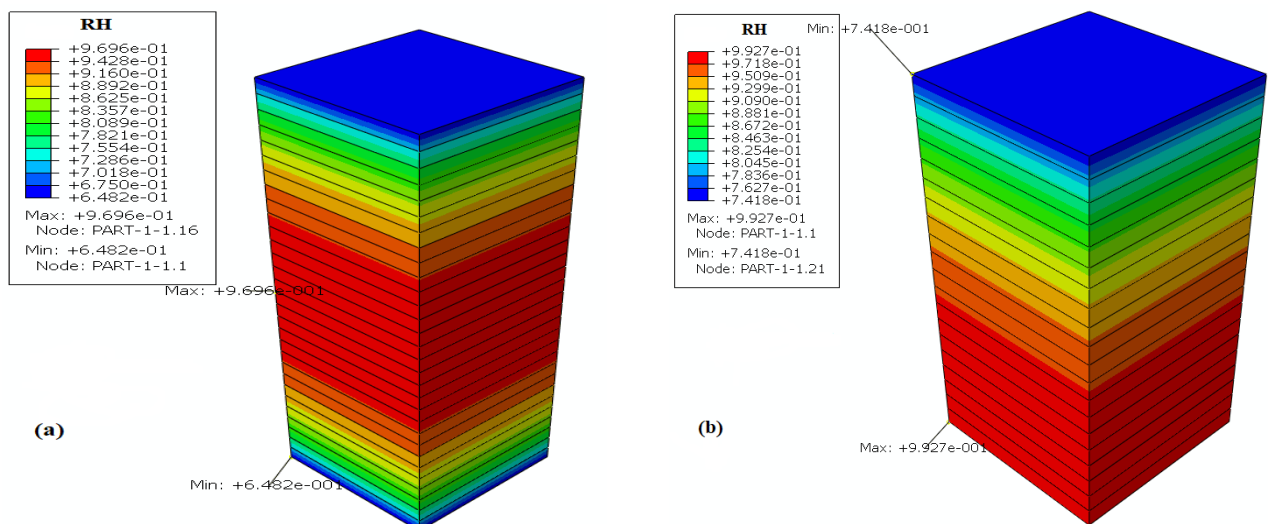
Figure 3.1 Finite element analysis results for: (a) Kang et al. (2012), and (b) Kim et al. (1999) experimental specimens.

Similarly, for the experimental results by Kim and Lee (1999), numerical modelling was performed on concrete prisms $100 \times 100 \times 200$ mm (Fig. 3.1b). The test specimens were cast using different types of concrete mixes with a mean compressive strength of 76 MPa, 53 MPa and 22 MPa at 0.28, 0.40 and 0.68 w/c ratios, respectively. The specimens were water cured for up to 3 and 28 days. Values of RH were measured at three different depths (30 mm, 70 mm and 120 mm from the top surface) up to 200 days and at two ambient conditions (20 °C temperature and 50 % humidity).

The effect of hydration on RH is also considered in this study and the humidity change due to self-desiccation, which was estimated based on tests on sealed specimens (Kim and Lee 1999 and Kang et al. 2012), is subtracted from that of drying specimens before comparing the experimental data with the numerical results.

The specimens tested by Kim and Lee (1999) were modelled by sealing all sides of the specimens except the top, from where diffusion could occur by applying the convection boundary condition (i.e. Robin boundary condition). On the other hand, when modelling the experiments by Kang et al. (2012), diffusion was allowed to occur only from the top and bottom sides.

The RH of concrete was set to be 100 % at the start of every simulation, and this value dropped nonlinearly through the depth as moisture was lost to the environment by diffusion and convection. A mesh sensitivity analysis was also performed to assess the effect of mesh size on moisture distribution. It was found that mesh size along the depth does not significantly affect moisture distribution for the considered mesh refinement levels. Hence, 10 mm thick single elements were used along with the depth (i.e., $10 \times 100 \times 100$ mm). An 8-noded linear heat transfer (i.e., an equivalent moisture transfer) brick element (i.e., DC3D8) was selected to obtain moisture at each nodal point of the element. All the parameters used in the FE analyses are summarized in Table 3.1.

Table 3.1: FEA parameters.

Reference	Specimen Size (L×W×t) (mm)	Initial Conditions	Boundary Conditions	FEM Element Type	Ambient Conditions
Kang at el. (2012)	$100 \times 100 \times 300$	RH = 100 %	All surfaces sealed except the top	DC3D8	RH = 50 % T = 20 ℃, 50 ℃ and 80 ℃
Kim and Lee (1999)	$100 \times 100 \times 200$	RH = 100 %	All surfaces sealed except the top and bottom	DC3D8	RH = 50 % T = 20 ℃

41

3.3.3   Inverse Analysis

Convective (*f*) and diffusion (*D*) coefficients were back-calculated using the aforementioned experimental results of Kang et al. (2012) and Kim and Lee (1999). For the initial values of the diffusion coefficient, the models proposed by MC-10 and Kang et al. (2012) were adopted as given in Eqs. (3.3) and (3.5) at temperatures of 20 °C, 50 °C and 80 °C. For the experimental results of Kim and Lee (1999) and Kang et al. (2012), only the MC-10 values were used to perform moisture modelling at different w/c ratios and temperatures.

The model parameters were obtained through an inverse analysis of the experimental data. The criterion used to select the optimal parameter values was based on the minimisation of the cumulative absolute relative error in the area difference under the RH time history curves at individual depths. The absolute relative error was calculated by using simple numerical integration, as given in Eq. (3.10).

$$\boldsymbol{Absolute\ Error} = \left. \sum_{i=0}^{z-1} \left[\left| \underbrace{\int_{x_i}^{x_{i+1}} f(x)\, dx}_{\substack{\text{Experimental} \\ \text{Area under} \\ \text{curve}}} - \underbrace{\int_{x_i}^{x_{i+1}} g(x)\, dx}_{\substack{\text{Numerical} \\ \text{Area under} \\ \text{curve}}} \right| \right] \middle/ z \right. \tag{3.10}$$

Where *z* is the total number of divisions of the curves (i.e., the number of considered experimental and numerical points), *f(x)* is the area under the experimental curve and *g(x)* is the area under the numerical curve.

3.4 Numerical Results

3.4.1   Experimental Results of Kang et al. (2012)

Following a sensitivity analysis showing that the most influencing parameters in Eq. (3.3) are D_1, *n* and H_c these were calibrated based on the available experimental data to minimise errors in the predictions. The MC-10 suggested parameters (i.e. *n=15*, H_c=0.80 and D_1=86.4 *mm²/day)* were used as an initial estimate.

Fig. 3.2 compares the predicted RH variation to the experimental results obtained by Kang et al. (2012) at three different ambient conditions (20 °C, 50 °C and 80 °C temperature at 50 % humidity). The associated errors, determined using Eq. (3.10), are summarised in Table 3.2, while the back-calculated diffusion coefficients are shown in Fig. 3.3. The numerical predictions agree well with the experimental results, thus indicating that the diffusion coefficient values estimated based on the given w/c ratio, curing age and environmental conditions can capture accurately the moisture profiles.
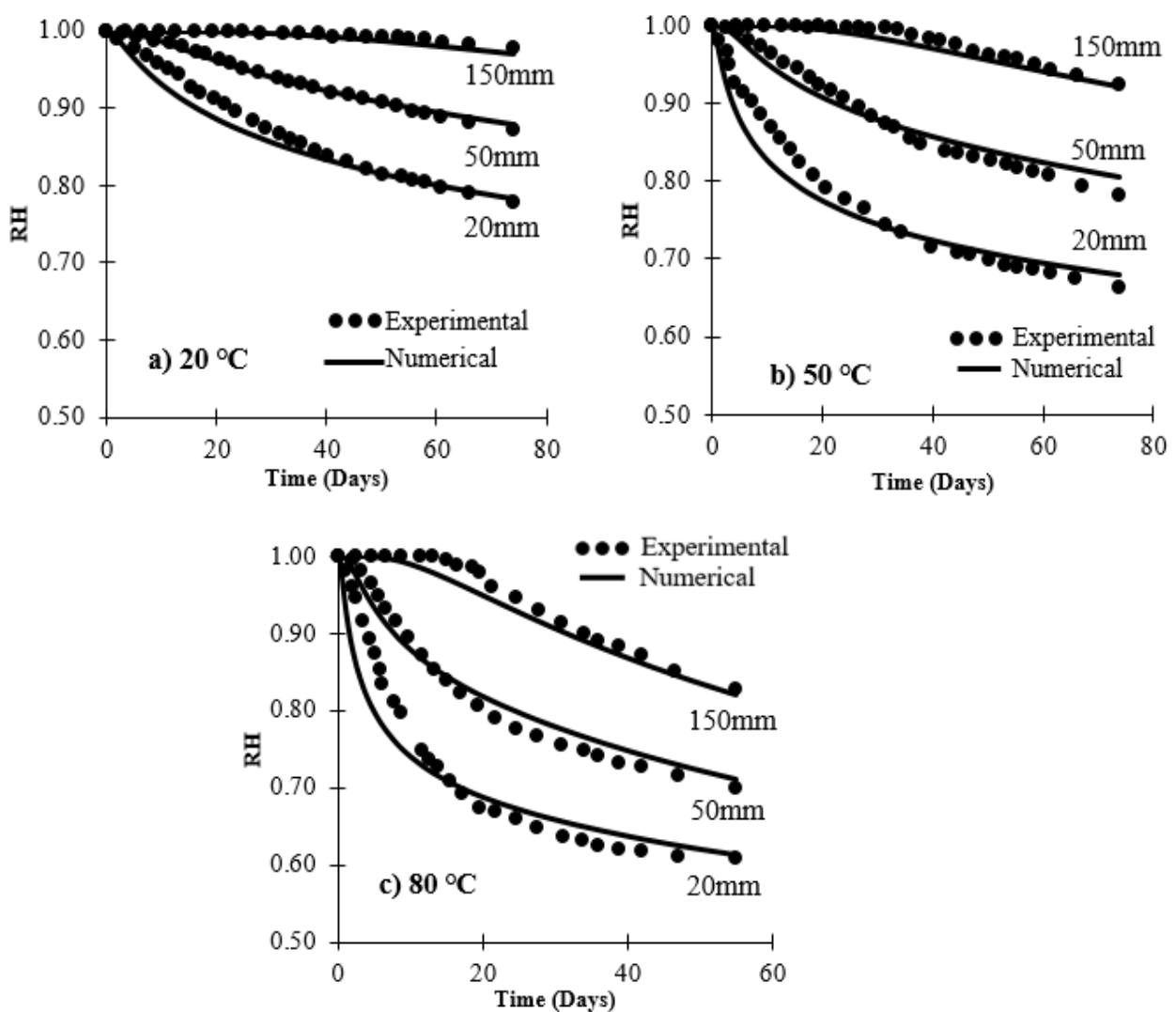
Figure 3.2 Comparison between numerical and experimental values of RH at: (a) 20 °C, (b) 50 °C, and (c) 80 °C.
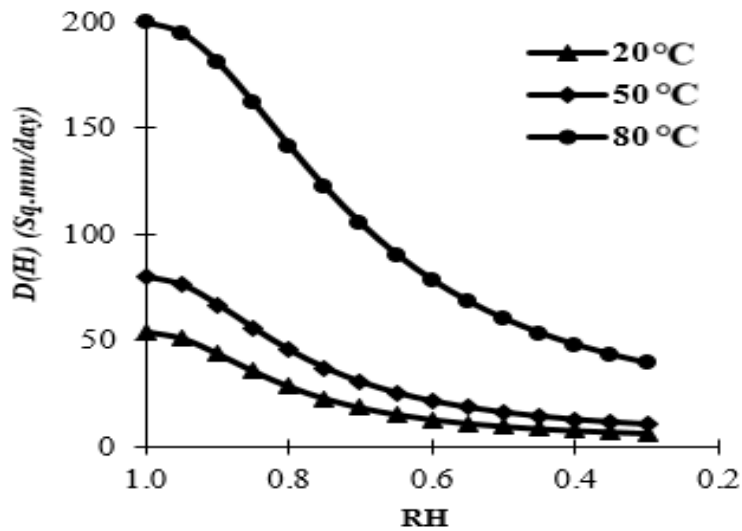
Figure 3.3 Back calculated diffusion coefficient using Model Code-10 at 20 °C, 50 °C and 80 °C.

A value of $\alpha = 0.05$ was used in this study as recommended in MC-10, while a constant value of $n = 2$ was found suitable for the different temperatures considered in this study. On the other hand, the n values suggested by MC-10 and Bazant and Najjar (1972) (i.e. $n = 15$ and $n = 4$, respectively) do not capture the behaviour and trends at all temperatures. In addition, the results of this analysis indicate that H_c cannot be taken as constant as recommended by MC-10 and Kang et al. (2012) but decreases gradually with increasing temperature (see Fig. 3.4a), and the diffusion coefficient, D_1 increases significantly with temperature as seen in Fig. 3.4(b). It should be noted that MC-10 uses just one value of concrete diffusivity for isothermal conditions. However, it is clear from the results that constant diffusivity cannot adequately represent all concretes at different temperatures. The convective coefficient, f, also increases significantly with increasing temperature (see Fig. 3.4(c)), as higher ambient temperatures result in faster rates of convection from the top exposed surface.

Table 3.2: Optimised (for Eq. (3.10)) Model Code-10 parameters based on Kang at el. (2012) dataset.

Trial Name	Back Calculated Variables				Kang at el. D_1 (mm²/day)	Relative Absolute Error at examined depths		
	D_1 (mm²/day)	H_c	n	f (mm/day)		20 mm	50 mm	150 mm
Num: 20°C	54.24	0.80	2	01	54.24	0.31	0.02	0.03
Num: 50°C	80.00	0.78	2	14	54.24	0.82	0.03	0.07
Num: 80°C	200.00	0.70	2	20	54.24	0.60	0.19	0.06
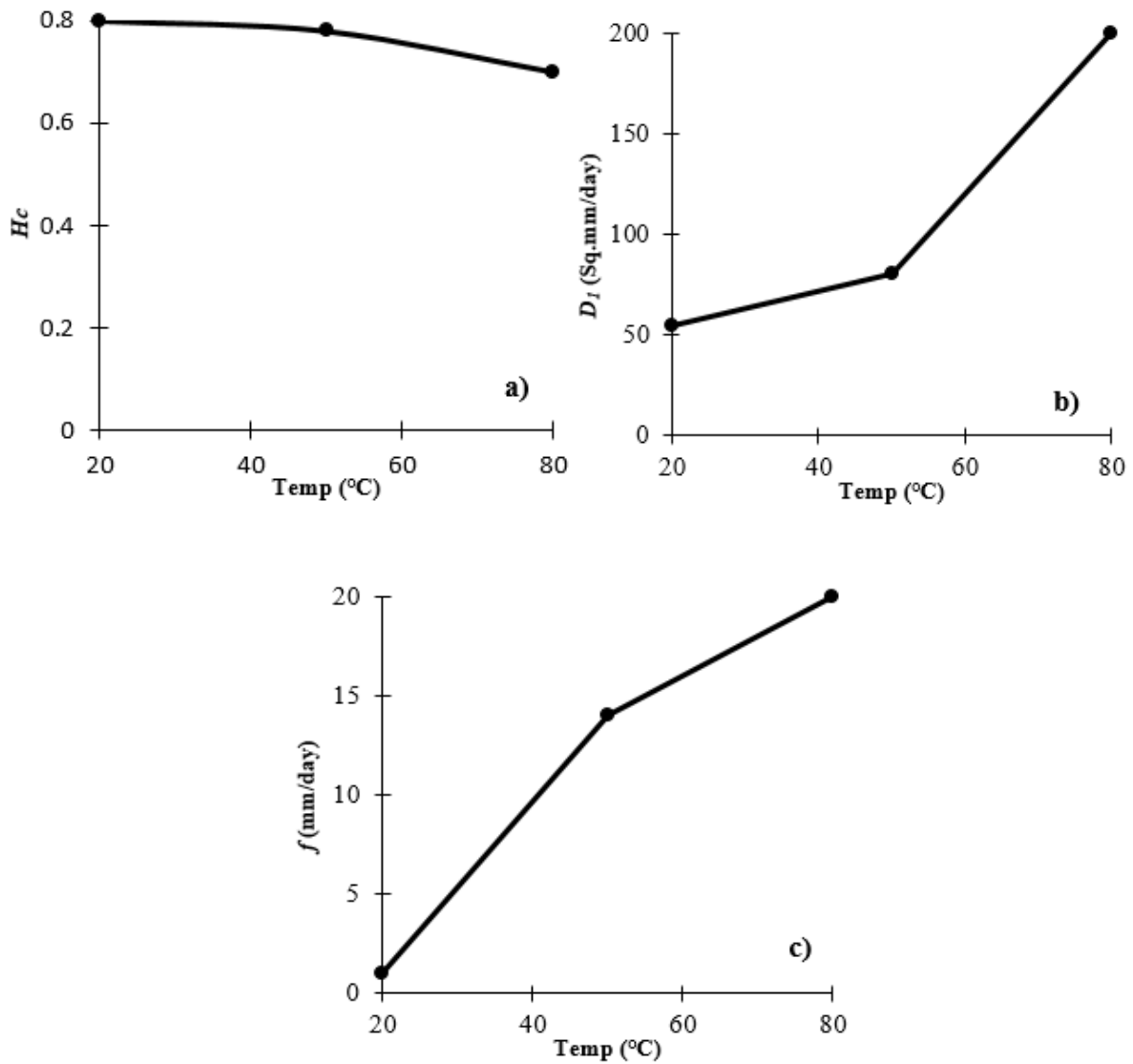
Figure 3.4 Optimized: (a) *Hc*, (b) diffusion coefficient D_1, and (c) convective coefficient *f* at different temperatures.

3.4.2 Experimental Results of Kim and Lee (1999)

Figs. 3.5, 3.6 and 3.7 show the comparison of predicted moisture distribution for the experimental results by Kim and Lee (1999), while Fig. 3.8 shows the variation of the diffusion coefficient as calculated through inverse analysis. The figures show that the optimised parameters capture moisture distribution with a high degree of accuracy. The values adopted for *n* and α were the same as those used when predicting the results by Kang et al. (2012)

above. As the tests were performed at a constant temperature, a constant value of $H_c = 0.80$, as suggested by MC-10, was found to approximate well the experimental results.
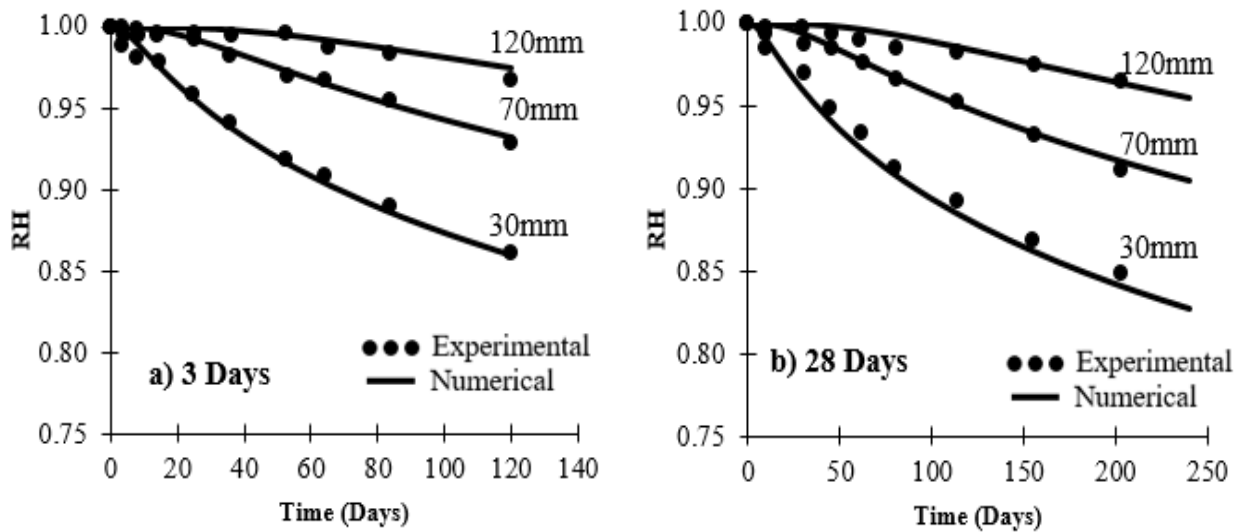
Figure 3.6 Comparison of moisture distribution at 0.28 w/c ratio: (a) 3 days, and (b) 28 days.
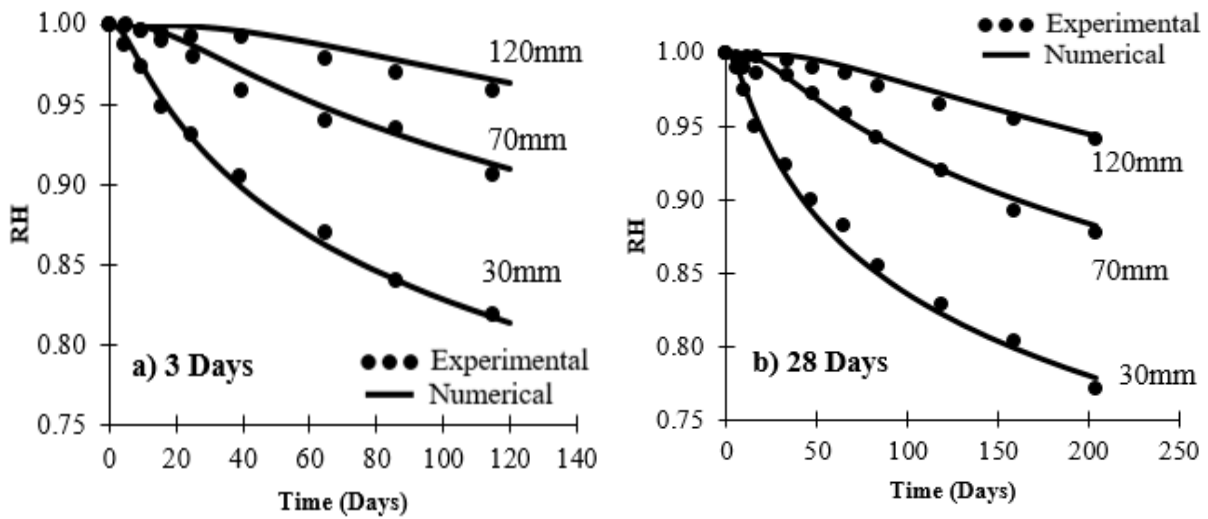
Figure 3.5 Comparison of moisture distribution at 0.40 w/c ratio: (a) 3 days, and (b) 28 days.
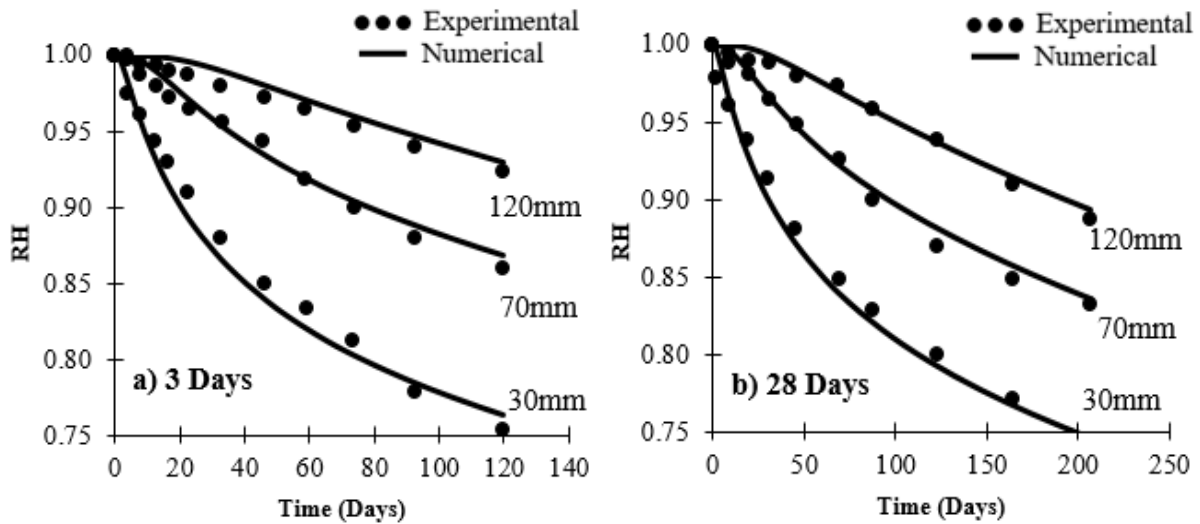
Figure 3.7 Comparison of moisture distribution at 0.68 w/c ratio: (a) 3 days and (b) 28 days.
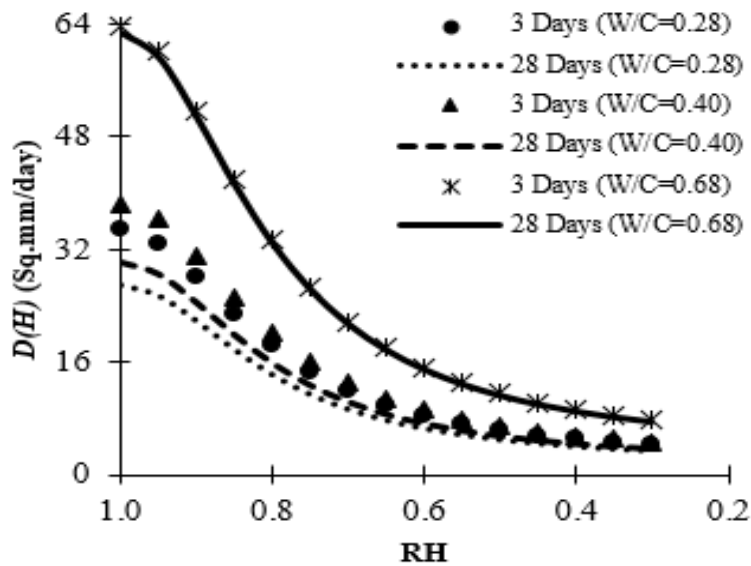
Figure 3.8 Back calculated diffusion coefficient at different w/c ratios and different curing ages.

The effect of the different parameters examined in the original experimental study (i.e. w/c ratio and steam curing age of concrete) on the diffusion coefficient is shown in Fig. 3.9(a) and summarised in Table 3.3. The significant increase in the diffusion coefficient for w/c higher than 0.4 can be attributed to the fact that larger amounts of water in early-age concrete typically lead to higher porosity. Interestingly, the diffusivity is only marginally affected by curing age, which indicates that the densification of the porous structure with time is not as important as the w/c ratio. A similar trend was reported by Kang et al. (2012), who also found that in fresh

47

concrete diffusivity is higher due to the higher amount of free water available to diffuse. Diffusivity decreases with time, however, and eventually stabilizes after the curing period as porosity reaches equilibrium.
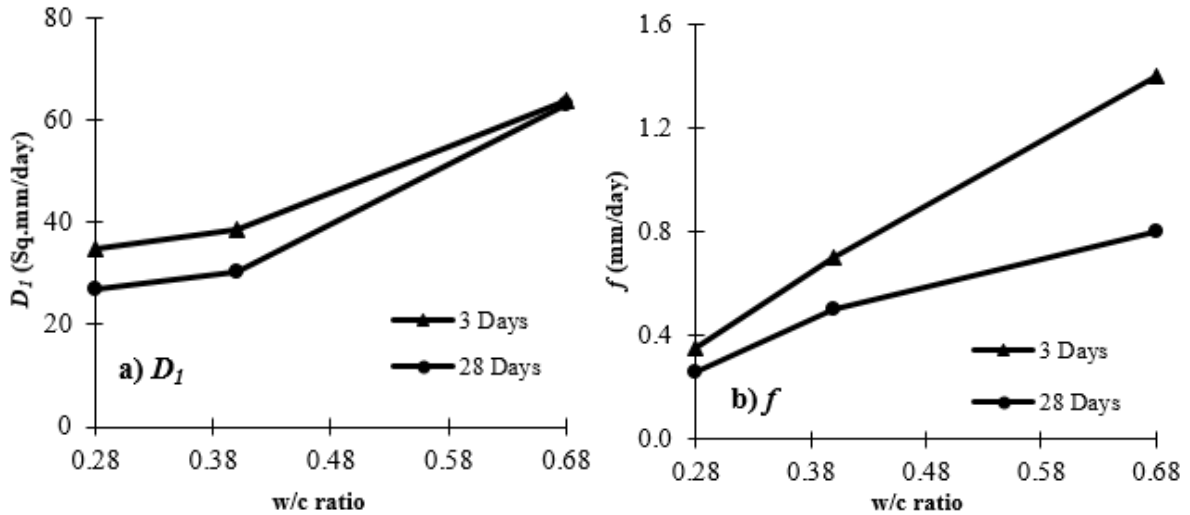
Figure 3.9 Optimized: (a) diffusion coefficient D1, and (b) convective coefficient f at different w/c ratios.

The observed increase in the value of the convective coefficient, *f*, with w/c ratio (Fig. 3.9b) can be attributed to the higher amounts of available free water for higher water content, and the higher amount of pores near the surface, which results in higher convection at the exposed surfaces.

Table 3.3: Optimised (for Eq. (3.10)) Model Code-10 parameters based on Kim and Lee's (1999) dataset.

Trial Name	Back Calculated Variables				CEB-FIP-10	Kang at el. D_1	Relative Absolute Error at examined depths		
	D_1 (mm²/day)	H_c	n	*f* (mm/day)	D_1 (mm²/day)	(mm²/day)	30 mm	70 mm	120 mm
0.28 w/c, 3Days	34.80	0.8	2	0.35	-	48.48	0.01	0.03	0.05
0.28 w/c, 28Days	27.00	0.8	2	0.26	12.72	48.48	0.11	0.07	0.12
0.40 w/c, 3Days	38.40	0.8	2	0.70	-	50.40	0.18	0.09	0.04
0.40 w/c, 28Days	30.24	0.8	2	0.50	19.20	50.40	0.28	0.36	0.06
0.68 w/c, 3Days	63.60	0.8	2	1.40	-	68.88	0.33	0.03	0.20
0.68 w/c, 28Days	62.88	0.8	2	0.80	61.68	68.88	0.40	0.22	0.24

3.5 Modified Diffusion Coefficient Model

A model capable of expressing the diffusion coefficient as a function of both material and environmental parameters is proposed in this study as described below. A single material parameter, *a*, is used to represent the overall effect of concrete porosity and capture the combined effect of the w/c ratio and concrete maturity. This parameter was found to increase linearly with increasing w/c ratio and decrease with increasing maturity. This can be attributed to the fact that higher w/c ratios can initially result in higher porosity and faster diffusion; while the hydration process at increasing levels of maturity results in the densification of the microstructure and reduced diffusivity, which leads to slower diffusion.

The effects of temperature and RH are described using the environmental parameters, *h* and *g*, respectively. At the reference ambient conditions (i.e., 20 °C temperature and 50% humidity) these values are *h = 1* and $g = b \times H$ (with *b = 3.27* constant in all cases in this study).

The variation of the diffusion coefficient *D(H)* observed through the analysis of the experimental data can be approximated by the exponential function given in Eq. (3.11). A similar approach was also used by Mensi et al. (1988); Wittmann et al. (1989); Granger (1995); Alvaredo (1995); Ayano et al. (1999); Tang et al. (2016); and Torelli et al. (2020) to express diffusion as a function of water content.

(3.11)

$$D(H) = a \cdot e^{b \cdot H} \qquad mm^2/day$$

Where *a* and *b* are parameters that can be adjusted for any type of concrete with different w/c ratios and isothermal conditions. These parameters can be obtained through inverse analysis as given in Table 3.4 (*a* and *b* in this study were obtained from Fig. 3.8). From Table 3.4 it is clear that *a* depends on the w/c ratio and curing age, while *b* can be taken as constant and it is equal to *3.27* for the experiments of Kim and Lee (1999). However, there are no universally accepted analytical or empirical equations for the determination of these model parameters. For instance,

Mensi et al. (1988) proposed the use of $a = 1.042 \times 10^{-13}$ and $b = 0.05$ for concrete mixes with different w/c (i.e., w/c = 0.45 and 0.58) at ambient conditions (T = 20 °C and humidity = 50 %).

Table 3.4: Summary of coefficients (*a* and *b*) at different w/c ratios and constant 20 °C temperature and 50 % humidity.

w/c ratio	Curing Age (Days)	*a*	*b*	R^2
0.28	3	1.33	3.27	0.98
0.28	28	1.03	3.27	0.98
0.40	3	1.47	3.27	0.98
0.40	28	1.15	3.27	0.98
0.68	3	2.43	3.27	0.98
0.68	28	2.40	3.27	0.98

The effect of temperature on diffusion is introduced through the use of a temperature-dependent parameter following the Arrhenius equation (Eq. (3.12)). While the combined effect of temperature, RH, w/c ratio and concrete maturity (Eq. (3.13)) is taken into account by implementing a similar approach to that proposed by Bazant and Thonguthai (1978) (see Eq. (3.4)).

$$f(T) = h \cdot e^{\left[\frac{Q}{R}\left(\frac{1}{293} - \frac{1}{T+273}\right)\right]} \tag{3.12}$$

$$D(H, T) = D(H) \cdot f(T)$$

$$D(H, T) = a \cdot e^{b.H} \cdot h \cdot e^{\left[\frac{Q}{R}\left(\frac{1}{293} - \frac{1}{T+273}\right)\right]}$$

$$D(H, T) = a \cdot h \cdot e^{b.H + \left[\frac{Q}{R}\left(\frac{1}{293} - \frac{1}{T+273}\right)\right]}$$

$$D(H, T) = d \cdot e^{g} \tag{3.13}$$

Where,

$$d = a \cdot h$$

$$h = \left(\frac{293}{T + 273}\right)^{n}$$

$$g = b \cdot H + \frac{Q}{R}\left(\frac{1}{293} - \frac{1}{T+273}\right)$$

Where h is a scaling parameter that decreases almost linearly with temperature as seen in Fig. 3.10(a). A value of $n = 4$ was found to represent all the examined temperature ranges (up to 80 °C). A similar factor was also used by Kang et al. (2012) and Granger, (1995), but with different values (i.e. $n = 1.5$ and $n = 1$, respectively).

The minimum energy, Q, needed to start a hydration reaction (i.e. activation energy in *J/mol*) can be obtained through Eq. (3.14), as recommended by RILEM (cited in (Klemczak and Maciej Batog, (2016)).

$$Q(T) = 33536 \frac{J}{mol} \qquad for\ T \geq 20\ °C \tag{3.14}$$

$$Q(T) = 33536 + 1455\ (20 - T) \frac{J}{mol} \qquad for\ T < 20\ °C$$

And R is the universal gas constant in $\frac{J}{mol \cdot K}$.

a) h

b) a
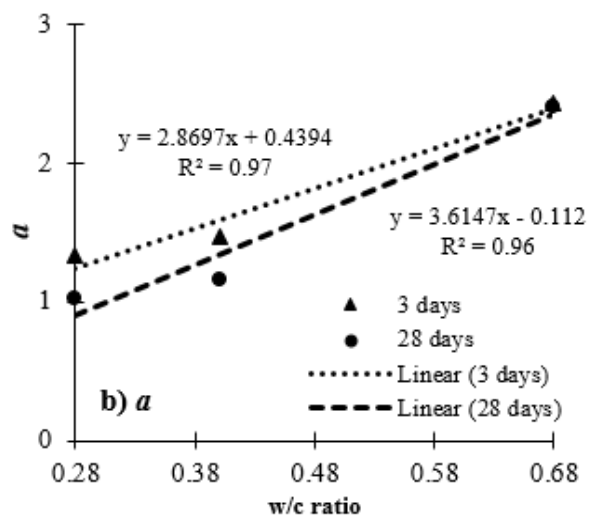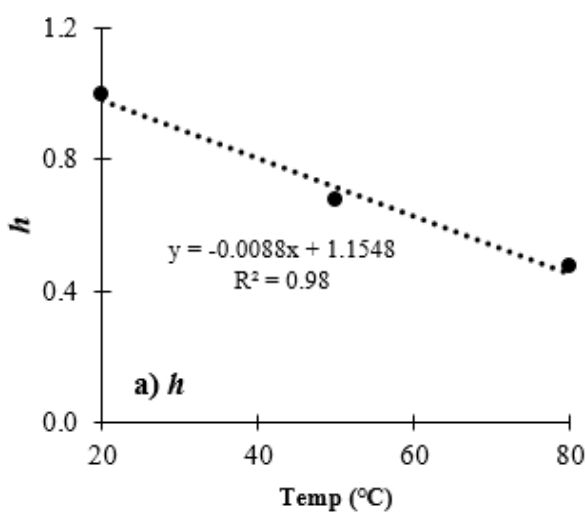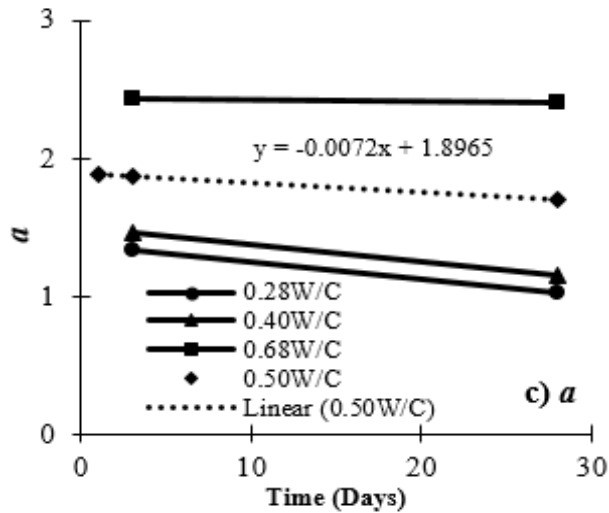
Figure 3.10 Variation in: (a) h at different ambient temperatures, (b) *a* at different w/c ratios and (c) *a* at different curing ages.

3.6 Validation of Proposed Model and Discussion

To validate the proposed approach, a numerical analysis was performed using ABAQUS (2019) to model the experiments carried out by Kang et al. (2012) at different temperatures. The value of *a = 1.9* adopted in the analysis was obtained by using a linear interpolation between the values of the three known w/c ratios (see Table 3.4 and Fig. 3.10(b)) and then extrapolating at the curing age of 1 day (see Table 3.4 and Fig. 3.10(c)).

Fig. 3.11 compares the numerical predictions with the experimental moisture distribution at different temperatures. Fig. 3.12 shows the diffusion coefficient used in the numerical analysis as given by Eq. (3.13). Table 3.5 shows a summary of the coefficients used during the validation of the proposed model and relative absolute errors compared to the experimental results.

The results highlight the limitations of the existing models and the capabilities of the proposed formulation. The values of D_1 suggested by MC-10 are found to be much lower than those derived through the methodology proposed in this paper (Table 3.3). Underestimating D_1 can

lead to underestimations of the drying rate of concrete elements, which in turn can result in an underestimation of shrinkage, shrinkage gradients, and associated mechanical performance (e.g. shrinkage-induced cracking). Hence, using the values of D_l suggested by MC-10 can potentially lead to unsafe structural assessments. Further, MC-10 suggests the use of predefined constant values for $n = 15$, and $H_{c,} = 0.80$, irrespective of the type of concrete at isothermal conditions. However, these parameters influence porosity and rate of diffusion and the results of this study suggest that they markedly depend on temperature, curing age and w/c ratios.
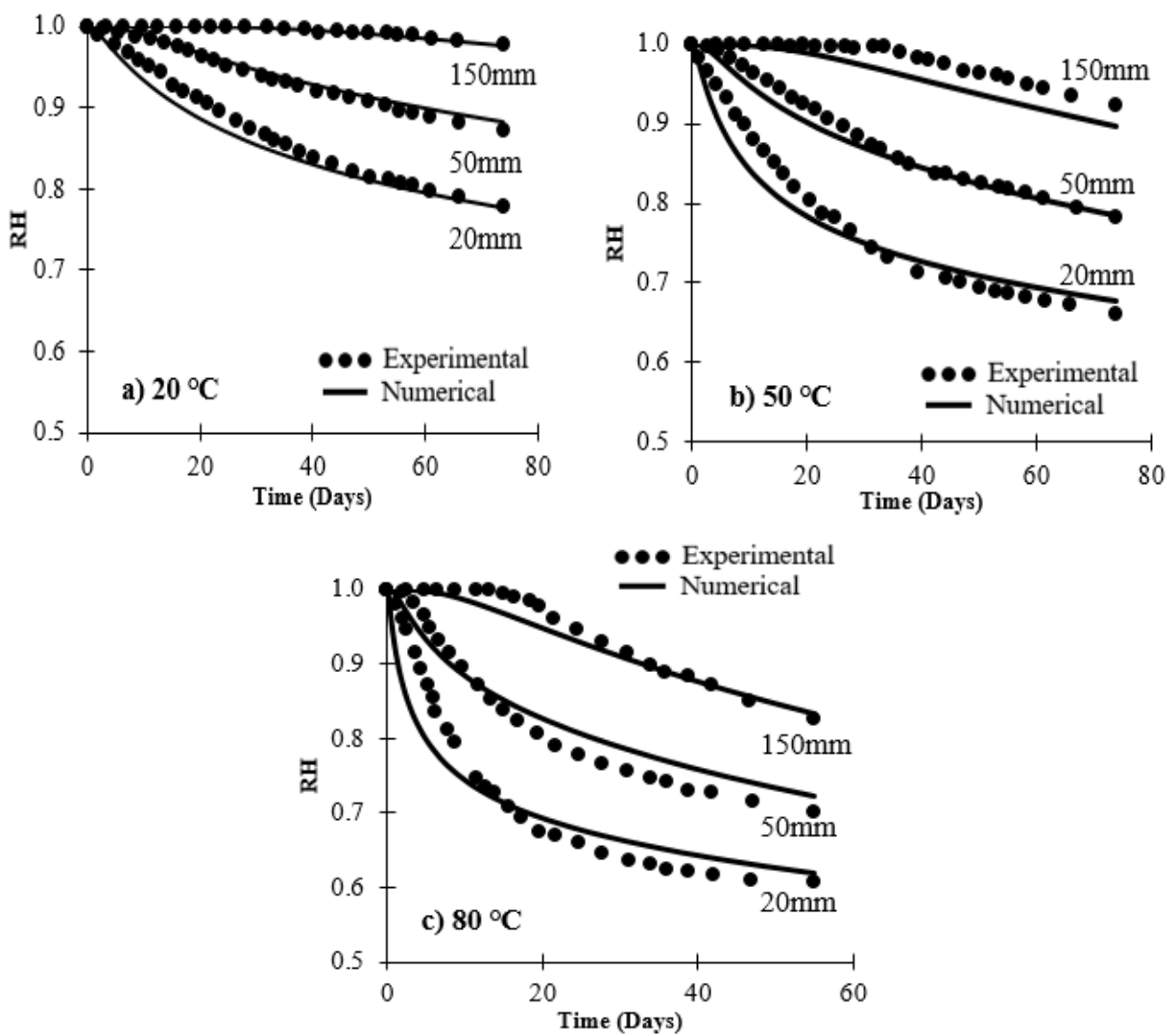
Figure 3.11 Comparison of moisture distribution at: (a) 20 °C, (b) 50 °C and (c) 80 °C using the proposed model.
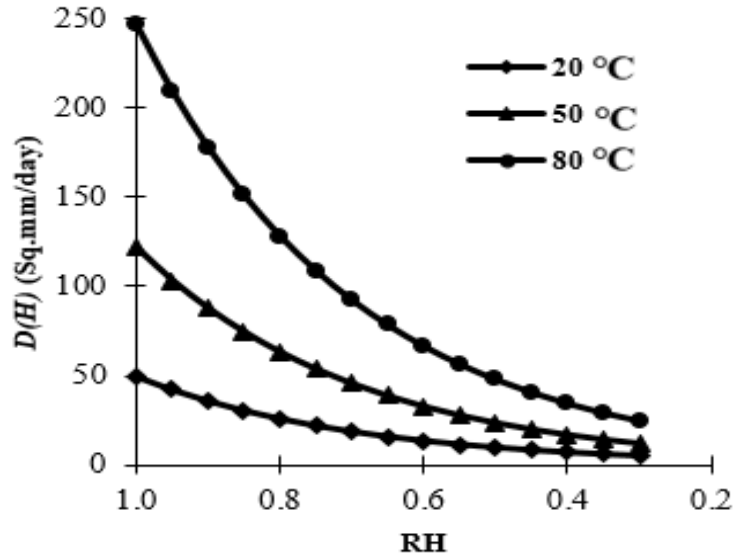
Figure 3.12 Diffusion coefficient at different temperatures using the
proposed model.

Table 3.5: Summary of coefficients at different temperatures, w/c=0.50 and 50 % humidity.

| Temperature (°C) | a | b | h | Relative Absolute Error at examined depths | | |
				20 mm	50 mm	150 mm
20	1.9	3.27	1.00	0.62	0.13	0.22
50	1.9	3.27	0.68	0.22	0.10	0.13
80	1.9	3.27	0.47	1.39	0.28	0.10

Kang et al. (2012) used Bazant and Najjar (1972) suggested parameters (i.e., $n = 4$, $H_c = 0.78$, and $\alpha = 0.05$) as constants and performed inverse numerical analysis to calibrate the porosity and D_1. For a given constant temperature, the calibrated D_1 value increases with increasing w/c ratio, as also observed in the present study (see Table 3.3). However, Kang et al. (2012) found higher values for the diffusion coefficients at lower w/c ratios compared to this study (using inverse analysis and the diffusion coefficient formulation suggested by MC-10, Eq. (3.3)), probably due to coupling effects (between porosity, temperature and RH), and different surface factor (f) values. Furthermore, Kang et al. (2012) used the same diffusion coefficient for the two curing ages under examination (i.e., 3 and 28 days), and calibrated porosity (i.e., $m = 3$).

This approach, however, disregards the fact that the rate of diffusion at an early age can be higher than at later ages as there is generally more free water available to diffuse through larger pore sizes (Cook and Hover, 1999). The model proposed in this study addresses this shortcoming by correlating porosity with concrete maturity and w/c ratio, thus enabling a more reliable estimate of the diffusion coefficient (Fig. 3.12) and a more accurate prediction of the experimental humidity profiles (see Fig. 3.11).

Overall, the diffusion model proposed by Bazant and Nijjar (1972), which has also been adopted in MC-10, is easily applicable and can predict the moisture distribution in concrete as a non-linear function of RH. However, the suggested values for the key parameters (n, H_c, and D_1) do not appear to be suitable for different concrete types and need to be calibrated based on experimental data (Table 3.2 and 3.3). Moreover, at different environmental conditions, the suggested constant diffusion coefficients cannot be used due to the dependency of diffusivity on temperature. On the other hand, the model by Kang et al. (2012) considers the effect of porosity (back-calculated), temperature and RH explicitly and can be adequately simplified by approximating porosity from the w/c ratio and concrete maturity, as shown by this study. The model can easily be used for any type of concrete by changing only two parameters and gives accurate predictions of the experimentally measured moisture distribution.

The numerical results obtained in this study show that the proposed model is generally capable of capturing the effects of w/c ratio, concrete maturity and thermal conditions on the evolution of the moisture profile within drying concrete elements. The model appears to slightly over-predict the early drying in early-age concrete at higher temperatures and under-predict the prolonged drying near the surface of the specimens. The difference between the measured and predicted values can be attributed to different factors, including the non-homogenous pore development (Kang at el. 2012), changes in chemical composition (Schneider et al., 1982; Endait and Wagh, 2020; Naus and Graves, 2006), and coupling effects (hygro-thermal coupling

effect). Although these factors cannot be captured individually by the model, the proposed simplified model is capable of predicting the variation in RH at different depths with an appropriate degree of accuracy for all of the examined parameters and environmental conditions. More detailed experimental studies are required to further validate the proposed modified model based on different ambient environmental conditions (i.e., temperature, humidity, wind speed, and atmospheric pressure at high altitudes), concrete maturities, ultra-high-performance concretes, and binding materials (such as fly ash, GGBFA etc.).

3.7 Conclusions

This study utilised the inverse numerical analysis technique to predict moisture distribution based on two available diffusion models (i.e., MC-10 and Kang et al., 2012) and proposes a modified diffusion model that considers the effect of concrete RH, temperature, w/c ratio and maturity. Based on the results of this study, the following conclusions can be drawn.

1. The diffusion coefficient increases significantly with increasing w/c ratio, and temperature, while it decreases marginally with increasing maturity.

2. The material parameters proposed by Model Code-10 can lead to a large underestimation of shrinkage strains. As a result, the magnitude and extent of shrinkage-induced phenomena, such as the development of cracking and curling stresses and deterioration phenomena, can be largely underestimated, for example, for slabs-on-grade.

3. A modified model is proposed to accurately assess moisture profiles for different temperatures (up to 80 ℃), concrete maturity and w/c ratios. The model can be easily implemented in current practice to carry out a more reliable assessment of crack development and structural performance of drying concrete elements.

Declarations

Funding

Availability of Data

Although the entire data is presented in the paper, ABAQUS CAE/2019 finite element model can be provided by authors if needed.

Chapter 4: Hygro-mechanical Analysis of Drying Shrinkage of Recycled Tyre Steel Fibre Reinforced Concrete

Meghwar, S.L., Pilakoutas, K., Guadagnini, M., and Torelli, G., (2022). Hygro-mechanical Analysis of Drying Shrinkage of Recycled Tyre Steel Fibre Reinforced Concrete: ***to be submitted***

Author's contribution statement

Shanker Lal Meghwar: Conceptualization, Methodology, Running lab experiments and FEA analysis, Writing-original draft, Editing, Formatting, Investigation and Visualization.

Kypros Pilakoutas: Supervision, Review and editing, Investigation, and Technical suggestions.

Maurizio Guadagnini: Supervision, Review and editing, Investigation, and Technical suggestions.

Giacomo Torelli: Supervision, Review and editing, and Formatting.

Abstract

Non-uniform moisture and aggregate distributions can cause differential shrinkage and curvature in concrete elements, such as slabs. Shrinkage gradients lead to curling and warping stresses that result in tensile cracking, which can lead to serviceability failure and long-term durability issues. Understanding the moisture transport and shrinkage behaviour and their coupling is essential to predict these stresses. This study uses experimental and numerical analysis for plain and recycled tyre steel fibre reinforced concrete (RTSF-FRC) to study the moisture and shrinkage phenomenon. First, the diffusivity model is validated, and then diffusion is coupled with the shrinkage model to predict drying shrinkage strains. The proposed methodology can be used for reliable assessment of shrinkage strains and stresses in concrete structures like slabs-on-grade (SoGs) and enhance the robustness, long-term safety, and sustainability of concrete structures.

Keywords: Differential Shrinkage; Shrinkage Curvature; Drying Shrinkage; Moisture Transport; Numerical Analysis; Diffusivity

4.1 Introduction

Shrinkage results from inevitable time-dependent changes in the volume of concrete and can cause cracking in restrained concrete members (Bentz and Jensen, 2004). Volume changes in concrete are due to consolidation and the evaporation of bleeding water (plastic shrinkage) from fresh concrete, hydration of cement (autogenous shrinkage) and loss of water trapped in the pores of hardened concrete (drying shrinkage) (Jeong et al., 2012). Four basic mechanisms cause solid network shrinkage (Scherer, 1990)**:** *disjoining pressure*, the presence of solid-liquid interface; *moisture stress*, partial Gibb's free energy of liquid in the pores; *osmotic pressure* caused by the concentration gradient and; *capillary pressure*, surface tension and interfacial tension in fluids.

Capillary pressure is the most common mechanism that causes drying shrinkage in concrete (Powers, 1960). When water evaporates from an exposed surface during drying, it creates a pressure difference inside the concrete matrix, allowing moisture to diffuse through the porous medium (Ytterberg, 1987a). The moisture loss from the finer capillary pores (2.5 to 50 nm size) of hydrated cement paste causes a negative pressure in the pore fluid (Grasley et al., 2006), which pulls the pore walls closer together and induces compressive forces on the surrounding matrix, resulting in overall material contraction (Scherer, 1990; Destrée et al., 2016; Zhang et al., 2013b).

Shrinkage contraction is resisted by internal and external restraints and can result in differential shrinkage. Internally, aggregates and reinforcement resist cement matrix shrinkage, which can result in micro and meso-cracks (Al-Kamyani et al., 2018a). External restraints such as adjacent structural members (e.g., walls, columns, etc.) or the subgrade soil (Hossain and Weiss, 2004) can cause large deflections and macro-cracks (TR-34, 2003). Meso and macro cracks create channels that provide favourable fluid flow pathways, making drying even easier. Water in the cracks can cause additional physical damage as a result of freeze-thaw cycles. Furthermore,

60

cracks can allow aggressive substances to enter the concrete matrix, causing chemical damage (e.g., chloride and sulphate attacks) and reinforcement corrosion, decreasing durability and eventually leading to deterioration mechanisms.

Differential shrinkage in concrete can also be caused by non-uniform moisture distribution. This is invariably caused by moisture exchange with the environment through exposed surfaces (Rollings, 1993) that is amplified by high-velocity wind, high temperatures, low humidity levels, sunlight, and other factors. Even though moisture movement is a three-dimensional process (ACI-360R, 2010), in structures like slabs-on-grade (SoG) or thin shells, it is primarily unidirectional (Jafarifar et al., 2014; Kim and Lee, 1998; M. Asad et al., 1997). SoGs are normally constructed on impermeable membrane sheets (TR-34, 2010), which force the moisture to diffuse in one direction through the exposed top surface. The exposed surface dries faster than the bottom surface, where concrete internal pore relative humidity (RH) remains almost 100% for a long time. This causes a moisture gradient to develop, leading to differential shrinkage strains and stresses. Due to these stresses, SoG tends to curl or warp (Goel et al., 2007), and the outer edges can lift. Curling leads to loss of ground support and induces additional stresses and, ultimately, cracking/failure in critical regions (Ytterberg, 1987c; Destrée et al., 2016).

The deleterious effects (i.e., cracking) of drying shrinkage can be limited by including fibres to constrain the shrinkage contractions (Destrée et al., 2016; Gribniak et al., 2013). Randomly distributed fibres can also provide an increased flexural, shear and punching performance (Al-Kamyani et al., 2018a). Recycled tyre steel fibres (RTSFs) have emerged as promising low-carbon alternative to manufactured steel fibres. The fibres effectively control both micro- and meso-cracks, owing to the variability of their lengths (Younis, 2014), as well as provide better toughness and post-cracking performance (Jafarifar et al., 2016; Hu et al., 2019; Isa, 2021).

However, a major challenge with the design of concrete elements against shrinkage-induced cracking is the lack of experimental evidence that simultaneously quantifies the time-evolution of drying phenomena and the resulting shrinkage strains. Indeed, the majority of the available experiments are either characterizing the drying properties of plain concrete (Kang et al., 2012; Kim and Lee, 1999; Nilsson, 2002; Zhou et al., 2011; Zhang et al., 2012; Xin et al., 1995; Bakhshi et al., 2012; Qin and Hiller, 2014; Aquino et al., 2004; Shen et al., 2017) or the shrinkage strains that develop upon drying (Kim and Lee, 1998; Jafarifar et al., 2014; Al-Kamyani et al., 2018a; Younis and Pilakoutas, 2016; Qian et al., 2020). The only available work that simultaneously quantified drying profiles and shrinkage strains was performed on sliced concrete elements (Ayano et al., 1999), and solid concrete prisms (Liang and Wei, 2019; Zhang et al., 2017; Wei et al., 2016; Zhang et al., 2010). Although Ayano et al. (1999) were able to provide an estimation of the time-evolution of the drying profile by simply monitoring the weight of single slices, that approach provides limited insight into the behaviour of real (i.e. continuous, non-sliced) elements. On the other hand, Liang and Wei, (2019), Zhang et al. (2017), Wei et al. (2016), and Zhang et al. (2010) provide limited information on moisture gradient and resulting shrinkage strain profile as RH was only measured at a single location at the core of the prisms and strains were only measured along the longitudinal axis of the prisms. However, existing research shows that the drying of concrete is typically non-uniform (Al-Kamyani et al., 2018b; Kim and Lee, 1998). Hence, shrinkage strains developing at any point of a drying specimen are typically affected not only by the local value of RH at the considered point, but also by the RH of neighbouring areas. The simultaneous measurement of moisture and drying shrinkage profiles along the depth of a concrete element is thus essential to accurately quantify the drying process. Furthermore, no systematic experiments were performed to quantify the effects of fibres on both the drying and the shrinkage behaviour of

fibre reinforced concrete, hence preventing the development of validated models and effective designs against drying shrinkage.

This study aims to simultaneously quantify the non-uniform drying and differential shrinkage processes in continuous (non-sliced) plain concrete elements. Additionally, it aims to systematically investigate the effects of RTSFs on both the drying and the shrinkage properties of fibre reinforced concrete. The work combines shrinkage experiments on plain and recycled tyre steel fibre reinforced concrete (RTSFRC) with advanced numerical simulations. Specifically, an experimental programme was performed to simultaneously monitor the drying of three concrete mixes and the associated shrinkage strains of 15 specimens kept in temperature-controlled conditions for up to 318 days. Concrete drying was monitored at different depths by measuring RH with dedicated probes, while shrinkage strains were simultaneously measured using a number of demountable mechanical (DEMEC) gauges. A series of numerical analyses (pure hygral and coupled hygro-mechanical analyses) were performed to model the experimentally observed drying and shrinkage behaviour to gain additional insights into the driving mechanisms.

4.2 Mathematical Modelling

4.2.1   Moisture Modelling

Over the years, many studies have been carried out to quantify moisture distribution. While the earliest models (Carlson, 1937; Pickett, 1946) considered diffusion as a linear phenomenon, more recent models (Sakata, 1983; Akita et al., 1997; Xu et al., 2009; Jafarifar et al., 2014) consider diffusion as a non-linear function of water content. However, Bažant and Najjar (1971) considered Fick's law of diffusion and postulated that diffusion is a non-linear function of moisture distribution in terms of RH, as given in Eq. (4.1). The RH is considered a more representative parameter for various reasons discussed elsewhere (Meghwar et al., 2022). The basic equation of moisture distribution in concrete is:

$$\frac{\partial H}{\partial t} = div\ (D(H)\ grad\ H) \tag{4.15}$$

Where t = time, $D(H)$ = diffusion coefficient function of RH and H = RH

Meghwar *et al.* (2022) proposed a modified diffusion coefficient model, Eq. (4.2), which is also adopted in this study to model the experimental RH distribution.

$$D(H,\ T) = d \cdot e^{\ g} \qquad mm^2/day \tag{4.2}$$

Where

$$d = a \cdot h$$

$$h = \left(\frac{293}{T + 273}\right)^n$$

$$g = b \cdot H + \frac{Q}{R}\left(\frac{1}{293} - \frac{1}{T + 273}\right)$$

a, b and n are fitting parameters for different types of concrete, h is a scaling parameter, T is the temperature in degrees Celsius, Q is the activation energy for migration of water along with the adsorption layer in the capillary pores, and R is the universal gas constant.

4.2.2 Drying Shrinkage Modelling

Similar to moisture modelling, shrinkage modelling in concrete pavements has also been investigated for a long time. Several studies (Bishop, 2001; Pettersson, 1998; Eisemann and Leykauf, 1990; Losberg, 1978) considered shrinkage to be mainly due to temperature gradients and restraint to the free movement of the concrete structures. However, other studies added that concrete pavements (outdoor SoG and concrete overlays) can be subjected to various other environmental conditions like rain, summer-winter temperature cycles, etc. Hence, shrinkage

is due to the combined effect of temperature, moisture, and external and internal restraints (Mateos et al., 2020; Leonards and Harr, 1959a). Drying shrinkage is a long-term process that, in most practical cases, dominates the other components of shrinkage. For example, temperature change in early-age concrete is high due to the hydration process; but with curing and maturity, it stabilises quickly. As indoor SoG do not experience a huge change in ambient temperature, the dominant differential shrinkage is due to the non-uniform moisture distribution and internal and external restraints (Zhang et al., 2018; Jafarifar et al., 2014; Jeong et al., 2012).

The total strain at a time (t) and along the depth (y) of the drying specimens can be calculated using the principle of superposition (Orta and Bartlett, 2014b). The total strain of a drying specimen $\varepsilon(y,t)$ is given by Eq. (4.3) and is a combination of total mechanical strain $\varepsilon_{ms}(y,t)$, free drying shrinkage strain $\varepsilon_{fs}(y,t)$, creep strain $\varepsilon_{cs}(y,t)$, autogenous shrinkage strain $\varepsilon_{as}(y,t)$ and temperature strain $\varepsilon_{ts}(y,t)$.

$$\varepsilon(y, t) = \varepsilon_{ms}(y, t) + \varepsilon_{fs}(y, t) + \varepsilon_{cs}(y, t) + \varepsilon_{as}(y, t) + \varepsilon_{ts}(y, t) \tag{4.3}$$

Creep strain is ignored in this study since the self-weight of the tested specimens is small, and no external load is applied. The total strain change $\Delta\varepsilon(y,t)$ and change in autogenous shrinkage strain $\Delta\varepsilon_{as}(y,t)$ with time are measured experimentally in controlled conditions. To model, the total shrinkage Eq. (4.4) is used.

$$\Delta\varepsilon_{ms}(y, t) + \Delta\varepsilon_{fs}(y, t) = \Delta\varepsilon(y, t) - [\Delta\varepsilon_{as}(y, t) + \Delta\varepsilon_{ts}(y, t)] \tag{4.4}$$

The change in autogenous shrinkage and thermal strains $\Delta\varepsilon_{ts}(y,t)$ is directly subtracted from the total measured strain change to remove the effect of self-desiccation and temperature. Although the experimental measurements were taken in controlled conditions (namely 20°C), fluctuation

in temperature was observed, which directly affected shrinkage strain measurements. Eq. (4.5) is used to compute thermal strains, which are subtracted from the total measured strain.

$$\Delta\varepsilon_{ts}(y,t) = \alpha(T_t - T_r) \tag{4.5}$$

Where

α, coefficient of thermal expansion $12\,{}^{\mu\varepsilon}/_{\circ_C}$ (fib, 2013a); T_t is the temperature at time t; T_r is the reference temperature when the first experimental value is observed.

Change in free drying shrinkage $\Delta\varepsilon_{fs}(y,t)$ is modelled in the finite element-based software Abaqus CAE (ABAQUS, 2019). Abaqus uses a *heat transfer* framework to model heat flux and temperature. The heat transfer model can also be coupled with a mechanical model to compute the thermal strains, i.e., Eq. (4.6) and the material constitutive model, i.e., Eq. (4.7), to compute the mechanical stresses, $\sigma(y,t)$. Stresses are induced in the specimens due to stiffness, $E_c(t)$, and the strain component of non-uniform shrinkage.

$$\frac{\partial\varepsilon_{ts}}{\partial t} = \alpha\frac{\partial T}{\partial t} \tag{4.6}$$

$$\sigma(y,t) = E_c(t) \times \Delta\varepsilon_{ms}(y,t) \tag{4.7}$$

The $\Delta\varepsilon_{fs}(y,t)$ is modelled in Abaqus by exploiting the formal analogy between Eqs. (4.6) and (4.8). It is assumed that the rate of change of ε_{fs} is proportional to the rate of change of RH (Orta and Bartlett, 2014a; Bazant and Chern, 1985).

$$\frac{\partial\varepsilon_{fs}}{\partial t} = k_{sh}(H)\frac{\partial H}{\partial t} \tag{4.8}$$

$k_{sh}(H)$ is the hygral contraction coefficient (HCC) as a function of humidity. According to (Jafarifar et al., 2014; Ayano and Wittmann, 2002), HCC can be approximated by a power function, as given in Eq. (4.9).

$$k_{sh}(H) = -\beta \times [H_0 - H(t)]^{\gamma-1} \qquad (4.9)$$

β and γ are constant parameters, H_0 is relative humidity at the start of drying (i.e., 1.0), and $H(t)$ is humidity at time t.

4.3 Experimental Study

4.3.1 Materials and Mix Proportions

One plain mix and two recycled tyre steel fibres (RTSF) mixes were used to cast prism and cube specimens. The specimens were water cured for 7 days. The mix proportions used, shown in Table 4.1, are typical of SoGs in the UK (Alshammari et al., 2023; Hu, 2018). Locally sourced aggregates were used in the mix, and basic tests were performed to check the quality of aggregates, as reported in Table 4.2.

Table 4.1 Concrete mix design.

Materials	Plain	F30	F40
Cement CEM II 32.5R (kg/m^3)	335	335	335
W/C ratio	0.55	0.55	0.55
Water (kg/m^3)	185	185	185
Sand (kg/m^3)	847	847	847
Gravel-10 mm (kg/m^3)	491	491	491
Gravel-14 mm (kg/m^3)	532	532	532
SP (ltr/m^3) Sika ViscoCrete 30HE (UK)	1.5	1.5	2.584
RTSF (kg/m^3)	0	30	40

Table 4.2 Physical properties of fine and coarse aggregates.

Test Parameters	Sand	Coarse Aggregates	
		10mm	14mm
Water absorption (%)	1.23	0.91	0.88
Specific Gravity	3.21	2.5	2.6

To check the strength and diameter of RTSF, individual fibres from 11 samples of RTSF, each comprising 10 fibres for a total of 110 fibres, were tested in tension (see **Appendix B**). The tests were performed in accordance with EN ISO 6892-1:2016. The initial cross-sectional area

of each fibre was taken as the mean of two measurements carried out in two perpendicular directions using a digital micro-meter with knife edges to an accuracy of 0.01 mm. The mean strength and diameter of all samples were found to be 2909 MPa, with a standard deviation of 166 MPa and 0.32 mm, with a standard deviation of 0.04 mm, respectively. Fig. 4.1 presents the histogram of tensile strengths from all the tested specimens.

4.3.2 Instrumentation for Moisture and Shrinkage Measurements

Generally, two methods are used to determine unidirectional moisture movement in concrete (Jafarifar et al., 2014), i.e., probe-type sensors embedded in the concrete and gravimetric method. The embedded RH sensor method is selected in this study as discussed in (Meghwar et al., 2022).
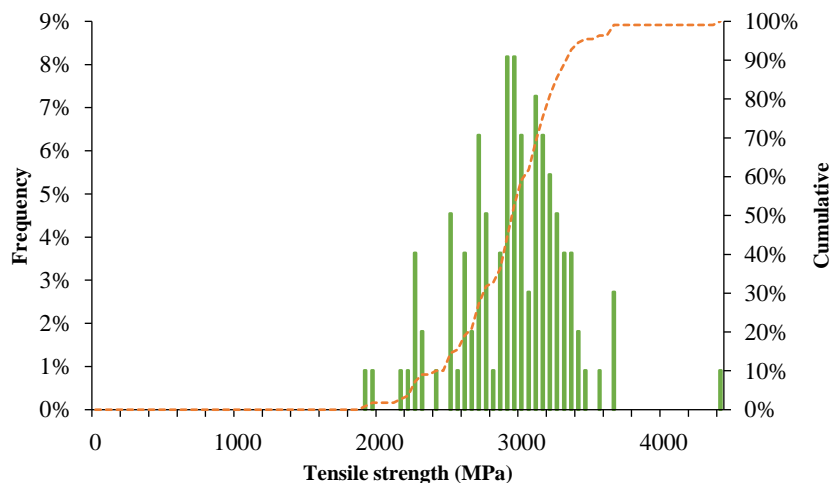
Figure 4.1 Cumulative strength distribution for RTSF individual fibres.

The *Rapid RH L6*[®] (Wagnermeters, 2019b) and *Rapid RH 5.0*[®] (Wagnermeters, 2019a) humidity and temperature sensors manufactured by *Wagnermeters*[®] are used in this study. The *Smart Logger*[®] (Wagnermeters, 2018) was used to log the ambient conditions (i.e., humidity and temperature) in the controlled room where specimens were stored. The sensor was specially designed according to ASTM F2170 (ASTM, 2019) for use in concrete floors to monitor RH and temperature variations with time.

Demountable mechanical (DEMEC) strain gauges are used to measure shrinkage strains. To improve the quality of measurements, three gauges with different gauge lengths (i.e., 100 mm, 200 mm and 300 mm) are used for monitoring shrinkage. Three measurements were taken with each gauge, and the average shrinkage is reported herein.

The RH sensors and DEMEC discs were installed after 7 days of curing. After installing the sensors, the specimens were left for 24 hours in the controlled room before taking the first readings. This time was necessary as the RH sensors need 24 hours (as recommended by the manufacturer) to achieve equilibrium conditions with the internal RH of the specimens and to allow time for the DEMEC to adhere properly on the surface of the specimens. Shrinkage, RH and temperature readings were taken every day for the first two weeks after sensor installation, and once a week thereafter.

4.3.3   Experimental Design

The size of specimens needs to satisfy both parameters, moisture and shrinkage. For free shrinkage measurements, BS EN 12617-4 (EN, 2002) recommends the use of prisms of $40 \times 40 \times 160$ mm, whilst ASTM C157 (ASTM C157/157C, 2008) recommends prisms with dimensions equal to $76 \times 76 \times 286$ mm. However, to eliminate the effect of boundary conditions on fibre and aggregate distributions, prisms of $150 \times 150 \times 500$ mm (see Fig. 4.2a), which are typical for flexural testing, were selected for this study. The added benefit is that, at the end of RH and shrinkage measurements, the same prisms can be tested in three-point bending to determine the effect of fibre and curing age on the flexural tensile strength of RTSF-reinforced concrete.

In total, five prisms were cast for each mix (plain, F30 and F40). Three prisms were used for all surface drying, one prism for drying from only one surface (with four RH sensors) and the remaining prism was completely sealed (with only one RH sensor). For all surface exposed

specimens, one prism was equipped with four RH sensors, whilst the other prisms had only DEMEC points for shrinkage measurements. For the plain mix, one additional prism was cast to assess the effect of curing on autogenous shrinkage. This prism was demoulded after 24 hours of casting, completely sealed and stored in the controlled room. Table 4.3 summarizes the details of design parameters, where the (Y) and (N) symbols indicate whether a particular parameter is considered or not, respectively.

All surface-exposed (ASE) specimens were designed to achieve uniform drying. The completely sealed (CS) specimen was intended to determine autogenous shrinkage. The one surface exposed (OSE) specimens were used to mimic the exposure of one-dimensional drying, such as in SoG. The aluminium tape was used for sealing the specimens.

To evaluate the compressive strength of all the mixes, a further 40 cubes ($100 \times 100 \times 100$ mm) were cast and tested at 4, 7, 14, 28, 56, 90 and 128 days after casting.

(a)
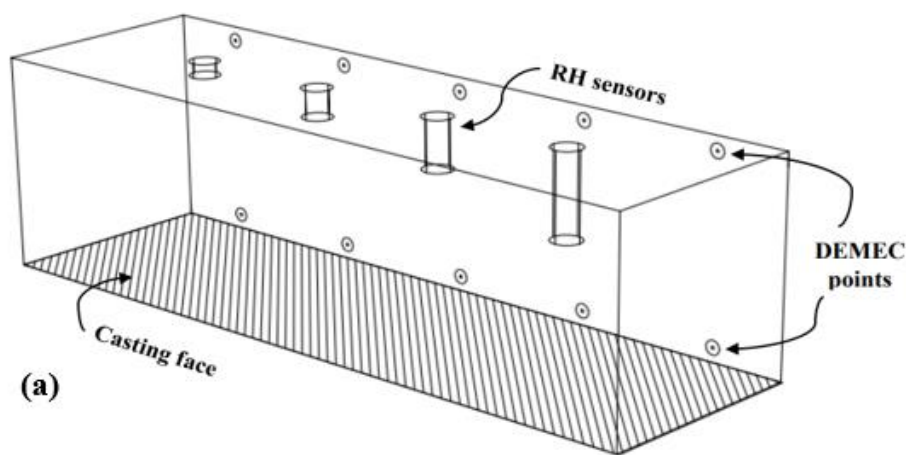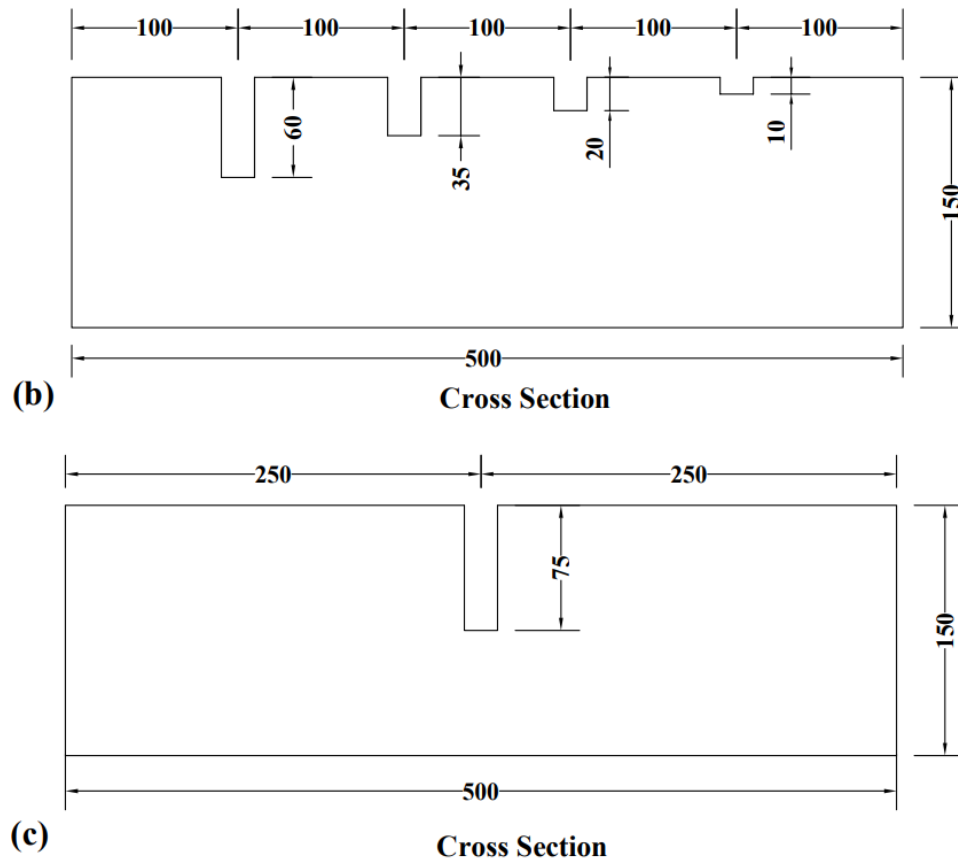
Figure 4.2 Geometry of the Specimen and RH sensor locations: (a) 3D prism; (b) OSE and ASE prisms; and (c) CS prism. All dimensions in mm.

Table 4.3 Specimens configuration and measured parameters.

Parameters	Completely Sealed (CS) with a hole	One Surface Exposed (OSE) with holes	All Surfaces Exposed (ASE) with holes	All Surfaces Exposed (ASE) no holes
Shrinkage Measurements	Y	Y	Y	Y
RH and Temperature Measurements	Y	Y	Y	N
Number of Specimens	1	1	1	2
Holes for Sensors	1 at centre	4 at different depths	4 at different depths	No holes

4.3.4 Moisture and Shrinkage Specimens

Figures 4.2a and 4.2b show the prisms' geometry and the RH sensors' location. Four depths (10, 20, 35 and 60 mm) were selected for RH and temperature monitoring. The sensors used in

71

this study were designed for large-scale SoG, and it was not feasible to locate them at less than 10 mm depth. The maximum depth of 60 mm was selected as the depth at which drying was expected to reach within the timeframe of the measurements. Fig. 4.2c shows the location of the RH sensor in the completely sealed specimen. The RH is measured at the centre (75 mm) of the specimen. Fig. 4.3 shows photos of the arrangement of the RH sensors and DEMEC discs in the observed specimens.

The study on free and restrained shrinkage by (Al-Kamyani et al., 2018b; Younis, 2014) showed a strong boundary effect, particularly on the surface. Hence measurements were taken on the top and bottom sides, 10mm away from the edges. Only in the plain mix (ASE), the shrinkage of two prisms was monitored on the sides to check if the shrinkage gradient differed in any way.

Figure 4.3 Instrumented test specimens: (a) CS with one RH sensor; (b) ASE with four RH sensors; (c) OSE with four RH sensors; (d) ASE without sensors

4.4 Experimental Results

4.4.1 Compressive strength and Flexural Modulus of elasticity

The compressive strength was determined according to BS EN 12390-3:2009 (see **Appendix C**). The elastic modulus was indirectly measured from the load-deflection curve of the three-point bending test by assuming linear elastic behaviour (see Eq. 4.10). The linear part of the load-deflection curve (from 20-30 % to 40-60 % of maximum bending load) was used in calculating the flexural modulus.

$$E_{fm} = \frac{PL^3}{48I\delta} \tag{4.10}$$

Where $\frac{P}{\delta}$ is the slope (N/mm) of the linear part of the load-deflection curve; L is the clear span (mm) between supports; I is the second moment of area (mm^4), and δ is the central deflection (mm) of the prism.
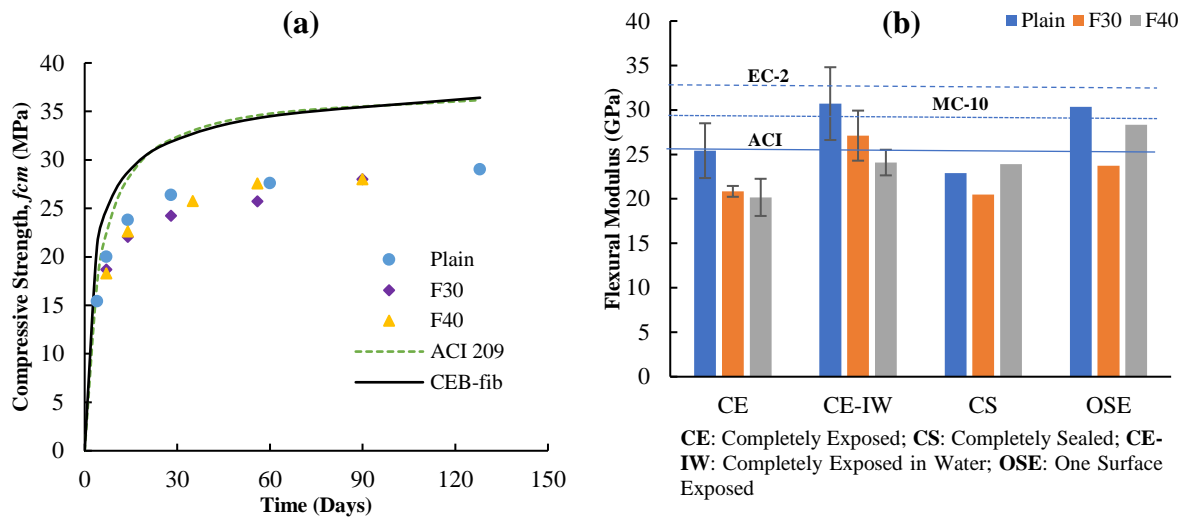
Figure 4.4 Experimental and predicted properties of concrete: (a) Cylinder compressive strength and (b) Young's Modulus of Elasticity.

The experimental values of strength and flexural modulus of elasticity are summarised in Fig. 4a and Fig. 4b, respectively, along with the predictions of design models (fib, 2013b; ACI Committee 209, 2008; CEN, 2004), see Appendix G. While the examined design codes tend to overestimate the compressive strength and flexural modulus, ACI yields more reasonable predictions of flexural modulus. The measured value of elasticity is in the range of 20168 to 30712 MPa. Though the modulus is expected to increase slightly with an increasing amount of RTSF, this is not clearly seen here, most likely due to consolidation issues also reported by others (Suksawang et al., 2018; Lee et al., 2015). The CE-IW specimens have the highest stiffness, as expected due to prolonged curing. OSE specimens gave a higher value of elasticity than CS, possibly because of less shrinkage-induced damage (and thus less degradation of elasticity). Surprisingly, CS gives a lower value of E_{fm} than OSE and CE-IW specimens, but this might be due to possible torsional effects connected to the presence of holes. As described in section 3.3, CS and OSE specimens were cast with four holes to embed the sensors at different locations.

4.4.2 RH Measurement

Figs. 4.5, 4.6 and 4.7 show RH measurements at different depths in OSE, and ASE specimens of plain, F30 and F40 concrete, respectively. As expected, the ASE specimens show a faster loss in RH than OSE. Due to the size of the specimens and boundary conditions, the rate of drying near the surface is faster than in the core of the specimens.

Moisture diffusion near the surface is affected by the ambient environmental humidity. RH at 10 mm depth fluctuates as the RH of the ambient environment fluctuates, as shown in Figs. 4.5(a), 4.6(a), and 4.7(a). This is due to the combined effect of boundary conditions (i.e., moisture convection or Robin boundary conditions) and diffusion. Moisture diffuses from the concrete surface to the environment through convection, which is mathematically expressed as the convection coefficient (Meghwar et al., 2022). The convection-diffusion depends on the RH gradient between the ambient environment and the exposed surface of concrete, as well as the surface conditions (i.e., rough, smooth etc.).

RH measurements are not affected by slight changes in temperature. The minimum and maximum ambient temperatures recorded were 17 ℃ and 23 ℃, respectively. However, the diffusion rate may vary if the temperature change is significant, as reported by (Meghwar et al., 2022; Kang et al., 2012; Bazant and Thonguthai, 1978).
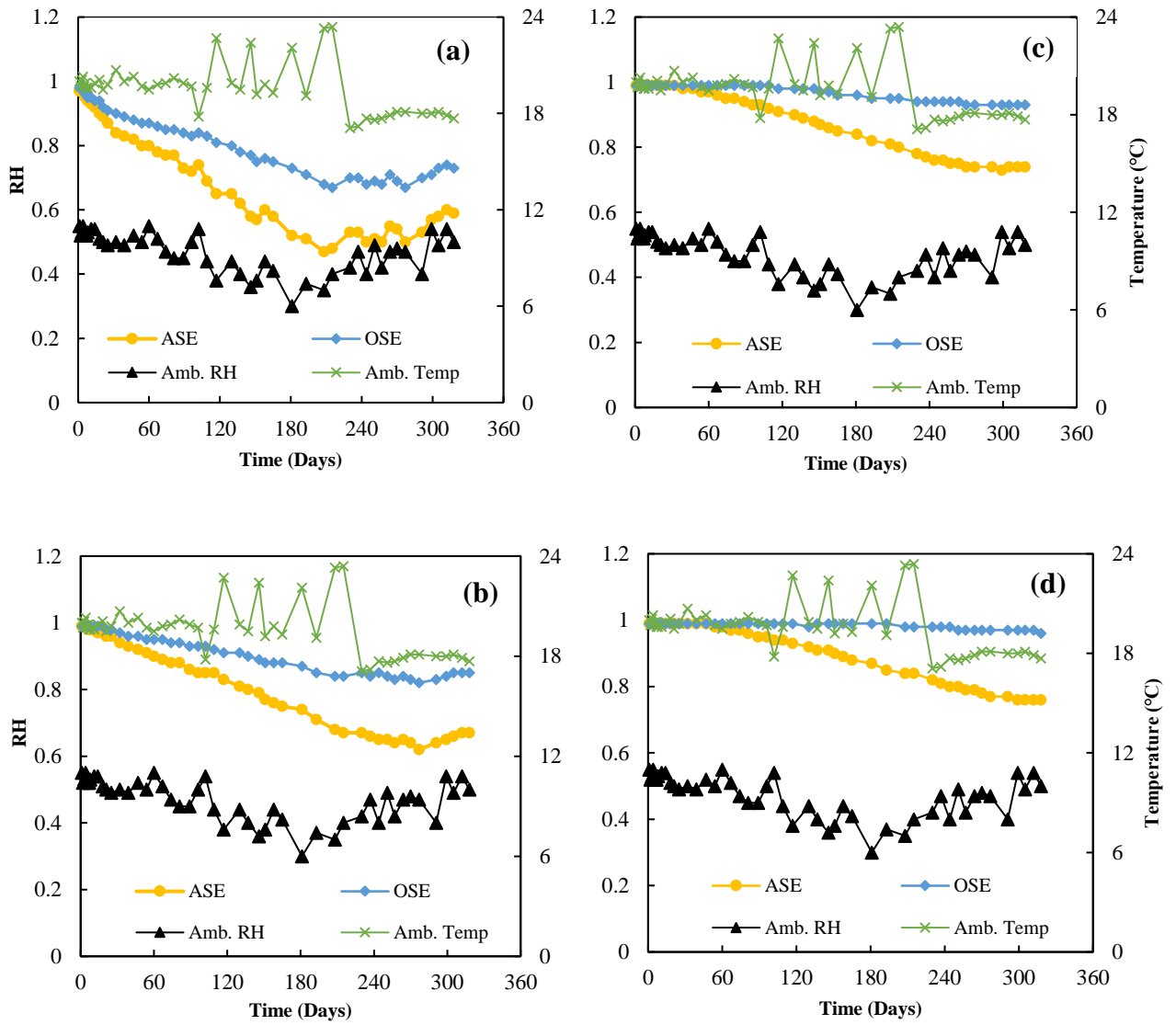
Figure 4.5 RH evolution in ASE and OSE plain concrete specimens at a depth of: (a) 10 mm; (b) 20 mm; (c) 35 mm and (d) 60 mm.
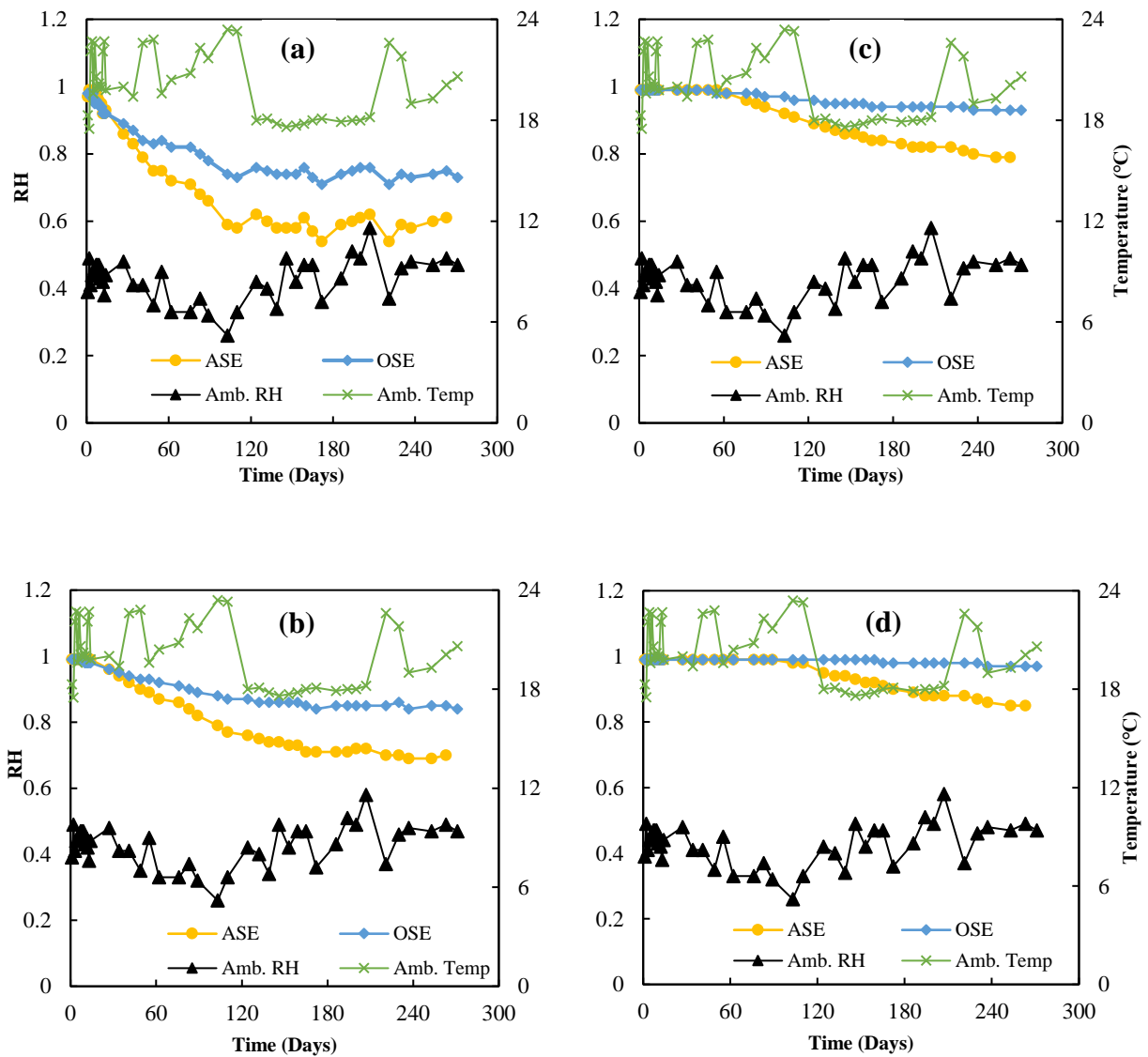
Figure 4.6 RH evolution in ASE and OSE F30 concrete specimens at a depth of: (a) 10 mm; (b) 20 mm; (c) 35 mm and (d) 60 mm.
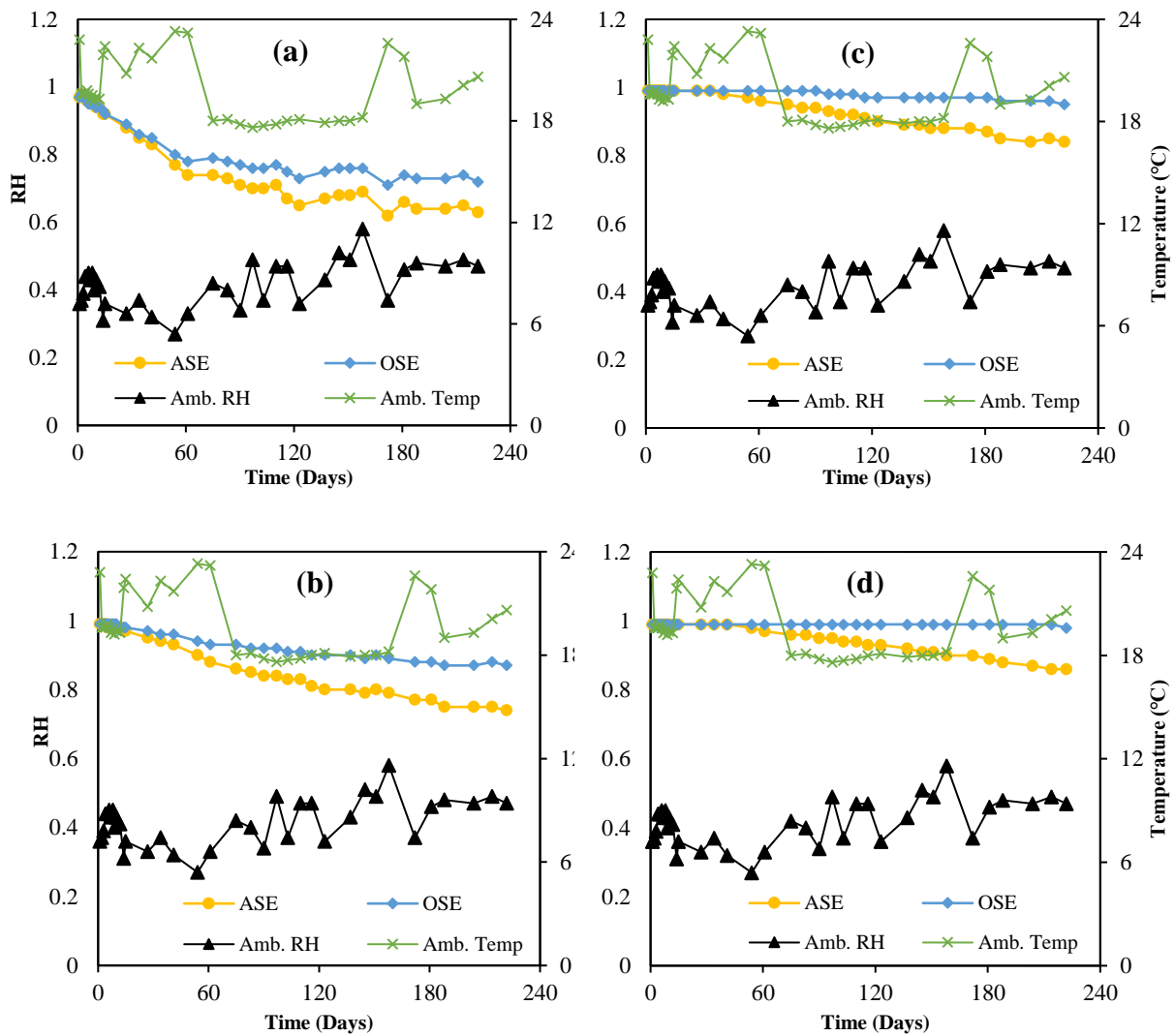
Figure 4.7 RH evolution in ASE and OSE F40 concrete specimens at a depth of: (a) 10 mm; (b) 20 mm; (c) 35 mm and (d) 60 mm.

4.4.3   Shrinkage Measurements

Figs. 4.8, 4.9 and 4.10 show net drying free shrinkage (total measured shrinkage minus autogenous and thermal shrinkage) of ASE, OSE and autogenous shrinkage in CS specimens, respectively. The total shrinkage of all the specimens is given in **Appendix D.** It is clear from the results that shrinkage is affected by the combined effect of ambient temperature and humidity. The temperature variation means that the increase in shrinkage is not monotonic, but shrinkage does slow down with time, and there is a clear difference between the results from the top (T) and bottom (B) surfaces.

Figure 4.8 Drying shrinkage of ASE specimens.

Figure 4.9 Drying shrinkage of OSE specimens.

Figure 4.10 Autogenous shrinkage of CS specimens.

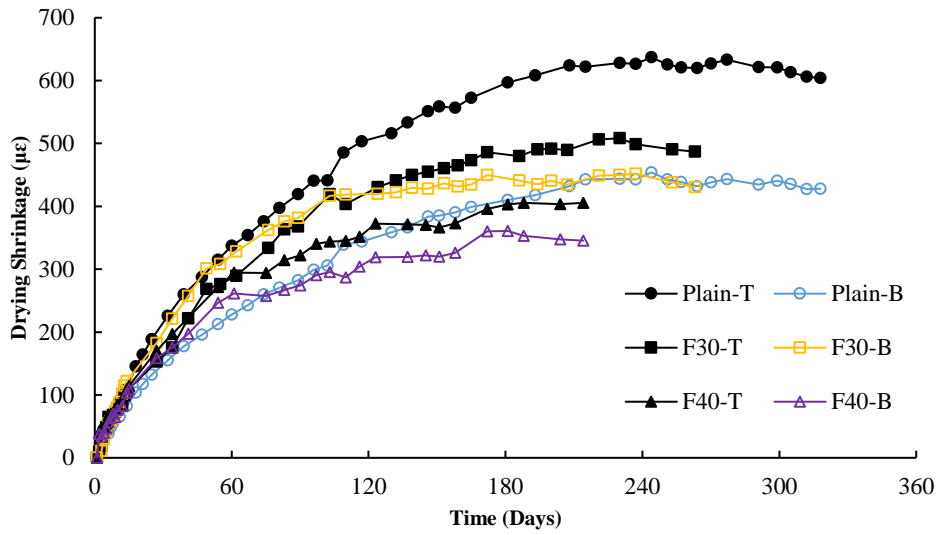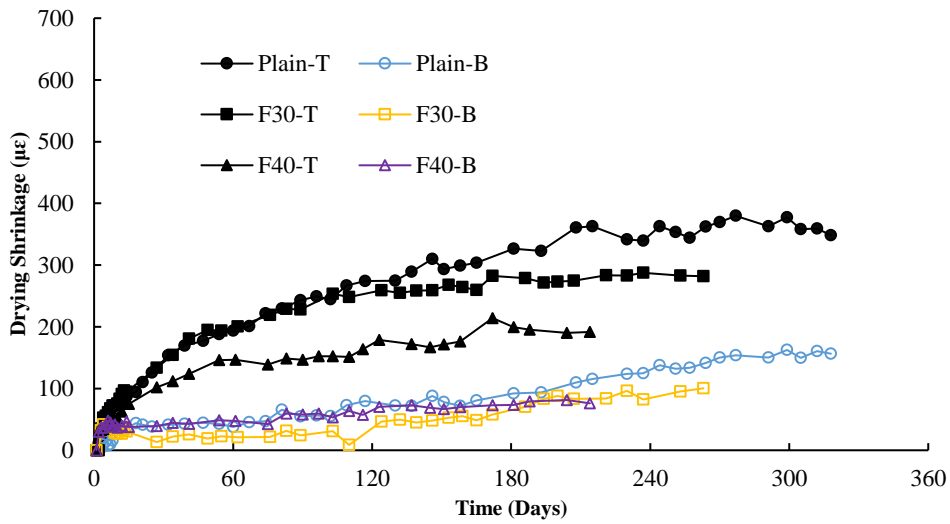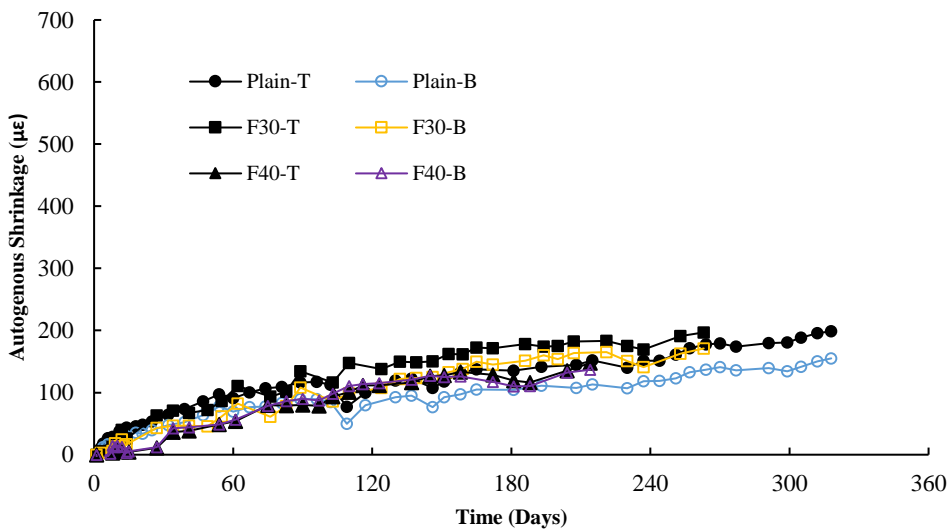Overall, the shrinkage gradient (from top to bottom) in plain concrete is higher than in F30 and F40 mixes; it is also higher in OSE than in ASE specimens. This is partly due to the fact that a) aggregates settle more easily under their weight in plain mixes; b) the casting surface is expected to be a bit weaker due to the bleeding of water during the vibration of the specimens (Jeong et al., 2015); and (c) boundary conditions, as OSE is drying from the top surface only which results in higher shrinkage than the sealed surfaces. This means that the specimens have differential stiffness and, hence, resist shrinkage differentially across the depth (Al-Kamyani, 2018; Kim and Lee, 1998).

In fibre reinforced mixes, the fibres prevent the aggregates from settling during vibration, resulting in a lower shrinkage gradient. Fibres also appear to provide additional internal restraint as less overall shrinkage is observed in mixes F30 and F40 than in plain concrete.

4.4.4 Comparison of shrinkage results and prediction models

Figs. 4.11 and 4.12 show a comparison of autogenous (of CS) and drying shrinkage (of ASE) with theoretical predictive models (Eurocode 2; Model Code 2010; ACI 209; JSCE and B4). The Eurocode, Model Code, JSCE and B4 models under-predict the autogenous shrinkage, as also reported in (Marušić and Štirmer, 2016; Yoo et al., 2011; Zhang et al., 2003; Vinkler and Vítek, 2017b; Vinkler and Vítek, 2017a). Further details of these models can be found in Appendix G. All the models consider only the effect of cement on autogenous shrinkage except the B4 model. The B4 considers the aggregate effect along with the water-to-cement ratio. However, boundary conditions, aggregate distribution and internal restraint due to fibres also affect shrinkage (both autogenous and drying shrinkage).
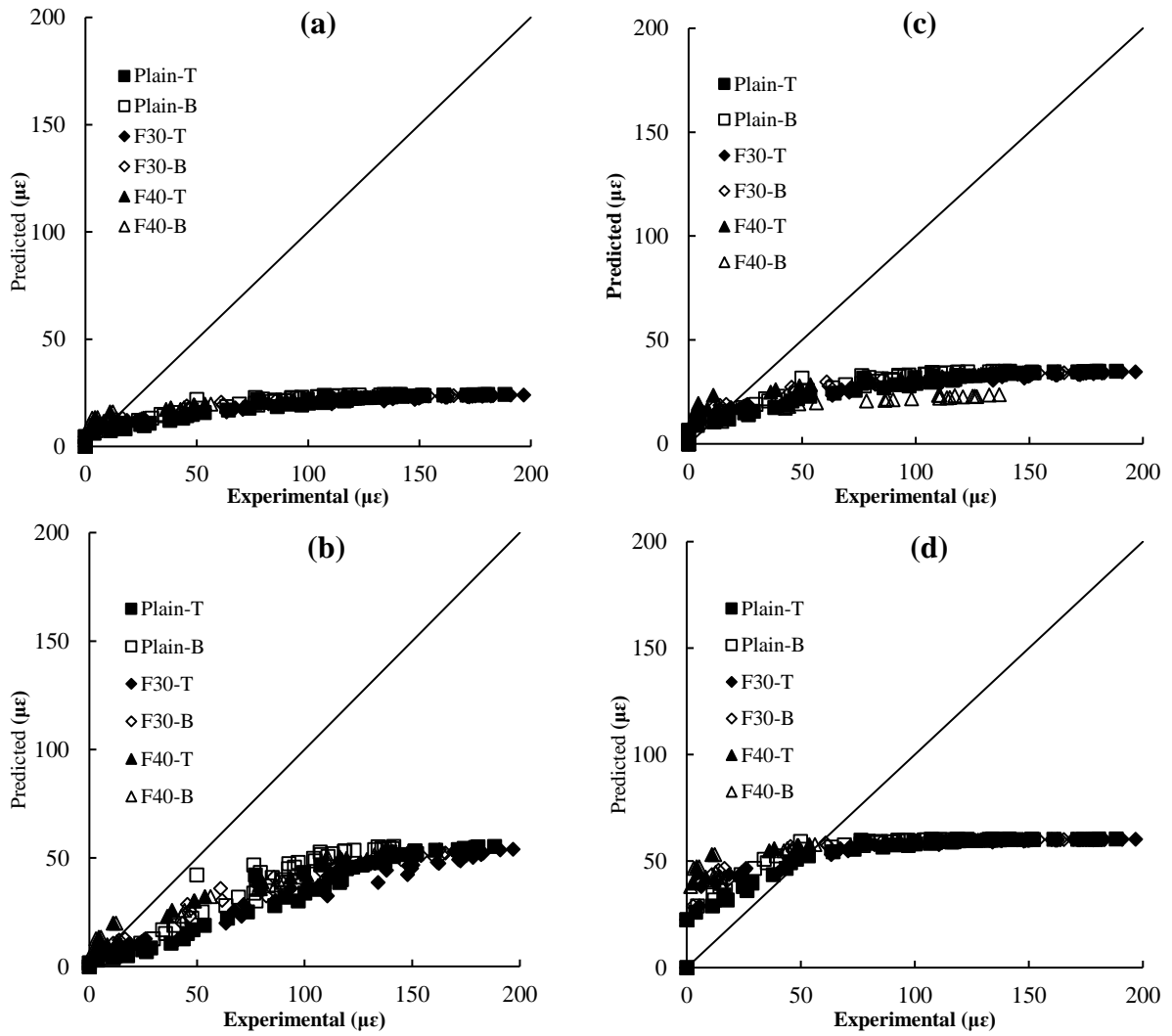
Figure 4.11 Comparison between prediction models and experimental data of autogenous shrinkage, (a) Eurocode 2; (b) JSCE; (c) Model Code 2010 and (d) B4.
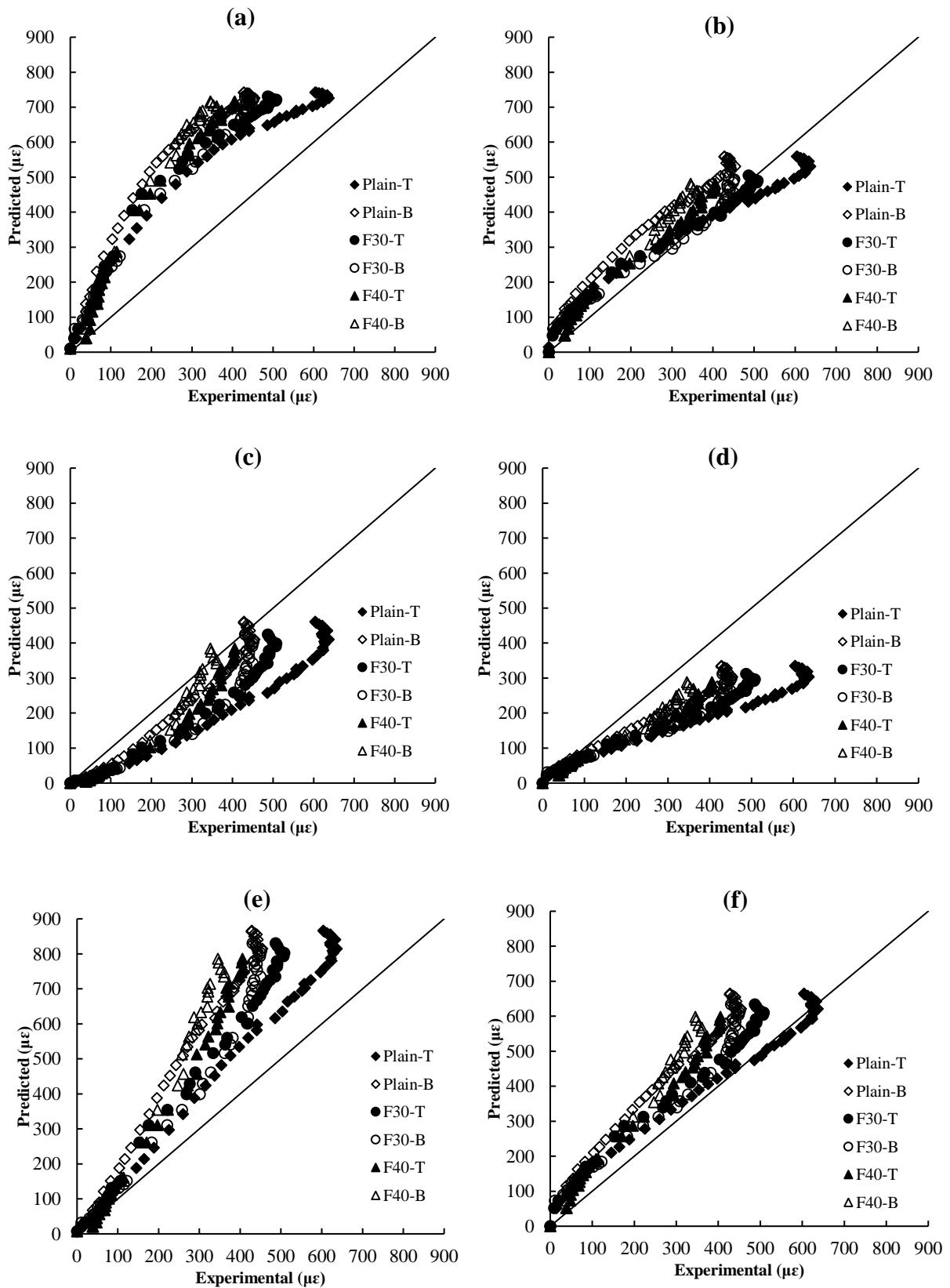
Figure 4.12 Comparison between prediction models and experimental data of drying shrinkage, (a) Eurocode 2; (b) Model Code 2010; (c) ACI 209; (d) B3; (e) JSCE and (f) B4.

Eurocode 2, JSCE, and B4 models over-estimate, and ACI 209 and B3 underestimate the drying shrinkage of all mixes. The Model Code offers the best estimates. However, no code considers the effect of fibres on the shrinkage of concrete, nor differential shrinkage due to the non-uniform distribution of the aggregates.

4.5 Numerical Modelling

Numerical modelling is performed using ABAQUS CAE 2021. For hygro-mechanical analysis, first hygral analysis is performed on 1-dimensional (1D) and 3-dimensional (3D) diffusion specimens to simulate the experimental OSE and ASE specimens, respectively. The procedure of hygral analysis is discussed elsewhere (Meghwar et al., 2022). Mechanical analysis is performed in the second step using the *Static General Package* of the software. The hygral model is coupled with mechanical analysis to calculate drying shrinkage during this analysis.

The concrete damage plasticity (CDP) model (see section 5.2) is used during shrinkage and curvature analysis to capture the tension-softening behaviour of RTSF reinforced concrete. The CDP model is calibrated through an inverse analysis technique (Hu et al., 2019) against experimentally obtained load-deflection curves (from three-point bending tests).

4.5.1 Hygral Modelling

A 3D deformable solid, 8-node linear brick type element was used for modelling. DC3D8 and C3D8R element types were used for hygral and mechanical analysis, respectively. A mesh sensitivity analysis was also performed to assess the effect of mesh size on moisture distribution and shrinkage. It was found that mesh size along the depth does not significantly affect moisture distribution and shrinkage for the considered mesh refinement levels. However, the tension softening part of the material constitutive model (i.e., CDP) is highly mesh dependent (see section 4.5.2). Hence, to avoid a mismatch of meshes in different models and

to maintain computational efficiency and numerical accuracy, a 5mm uniform mesh is adopted in all the models.

Fig. 4.13 compares the experimental results (E) of humidity distribution at different depths with drying time and the numerical predictions (A). The figures show that the calibrated parameters of diffusion coefficient (see Eq. 4.2 and Fig. 4.14), as summarized in Table 4.4, capture moisture distribution with high accuracy. The diffusion coefficient of ASE specimens is higher than OSE. As ASE specimens are exposed from all surfaces, diffusion is 3D while a 1D mechanism is predominant in OSE specimens. Thus it is likely that 3D diffusion is not uniform in all directions. Non-uniformity can be due to the different natures of the cast surface, complex pore structure distribution, and non-uniform aggregate distribution.

Table 4.4 Hygro-mechanical calibrated parameters.

Concrete Mix	Shrinkage parameters		Hygral parameters								
			OSE Specimens				ASE Specimens			
	β	γ	a	b	f (mm/day)	n	a	b	f (mm/day)	n
Plain	0.0025	0.88	0.12	3.27	0.2	4	0.27	3.27	0.5	4
F30	0.0020	0.88	0.12	3.27	0.2	4	0.27	3.27	0.5	4
F40	0.0010	0.88	0.12	3.27	0.2	4	0.27	3.27	0.5	4

As RH drops faster near the surface than in the core of the specimen because moisture takes time to diffuse from the core of the specimens. This creates the RH gradient that can result in differential shrinkage, which is further intensified by the non-uniform stiffness of concrete.

Fig. 4.15 shows numerical prediction results based on the implementation of the diffusion parameters suggested in MC-10 (see Table 4.5). These parameters lead to an under-estimation near the surface (10mm) and an over-estimation of moisture at depths greater than 20mm. This can result in under-prediction of overall shrinkage induced curvatures.
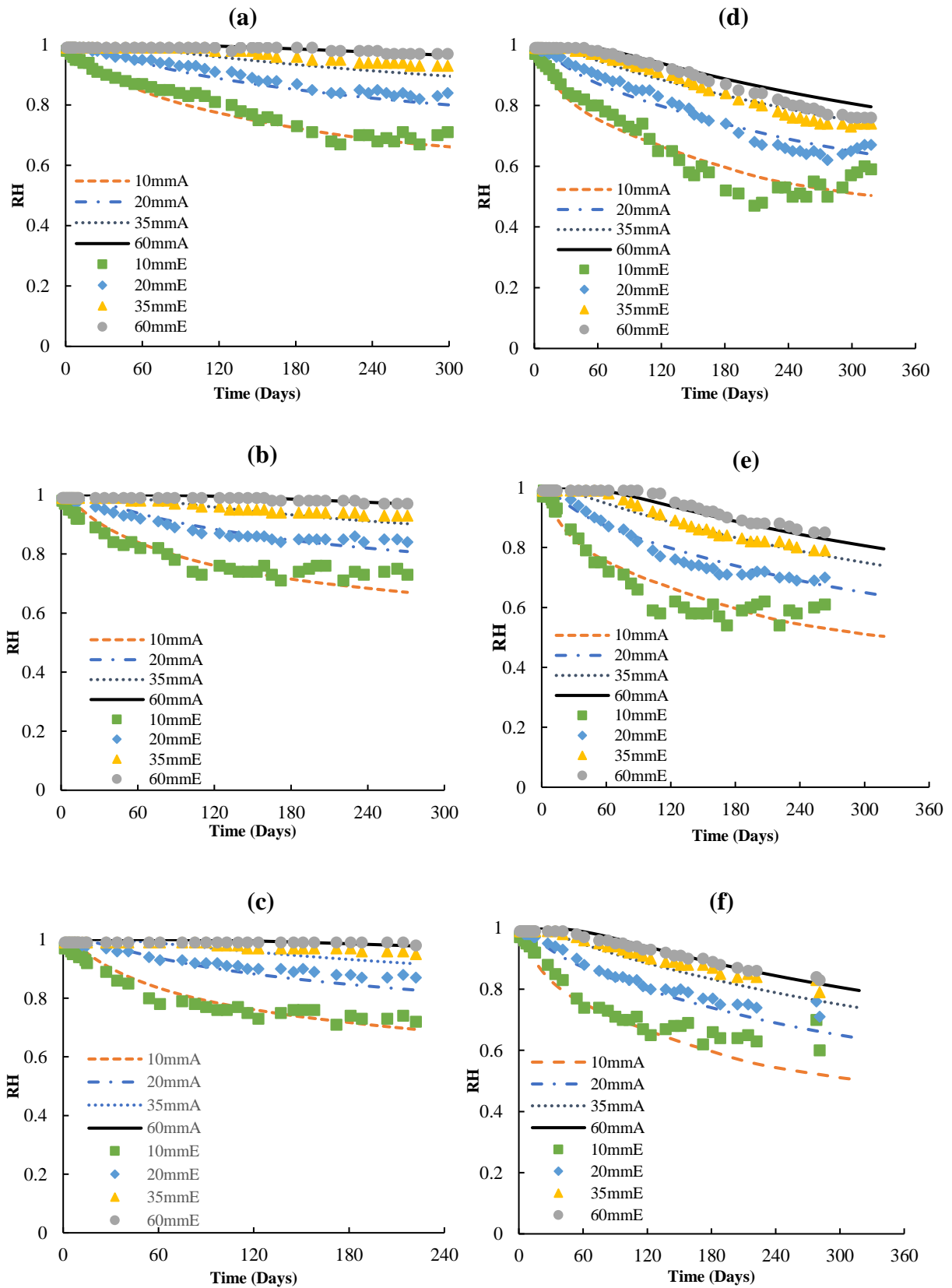
Figure 4.13 Comparison of Experimental and Numerical Moisture Distribution in, (a) OSE Plain, (b) OSE F30, (c) OSE F40, (d) ASE Plain, (e) ASE F30, and (f) ASE F40 specimens.
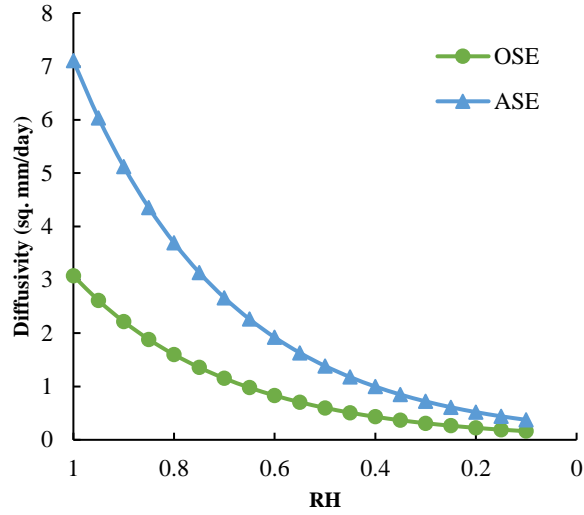
Figure 4.14 Back calculated diffusion coefficient.
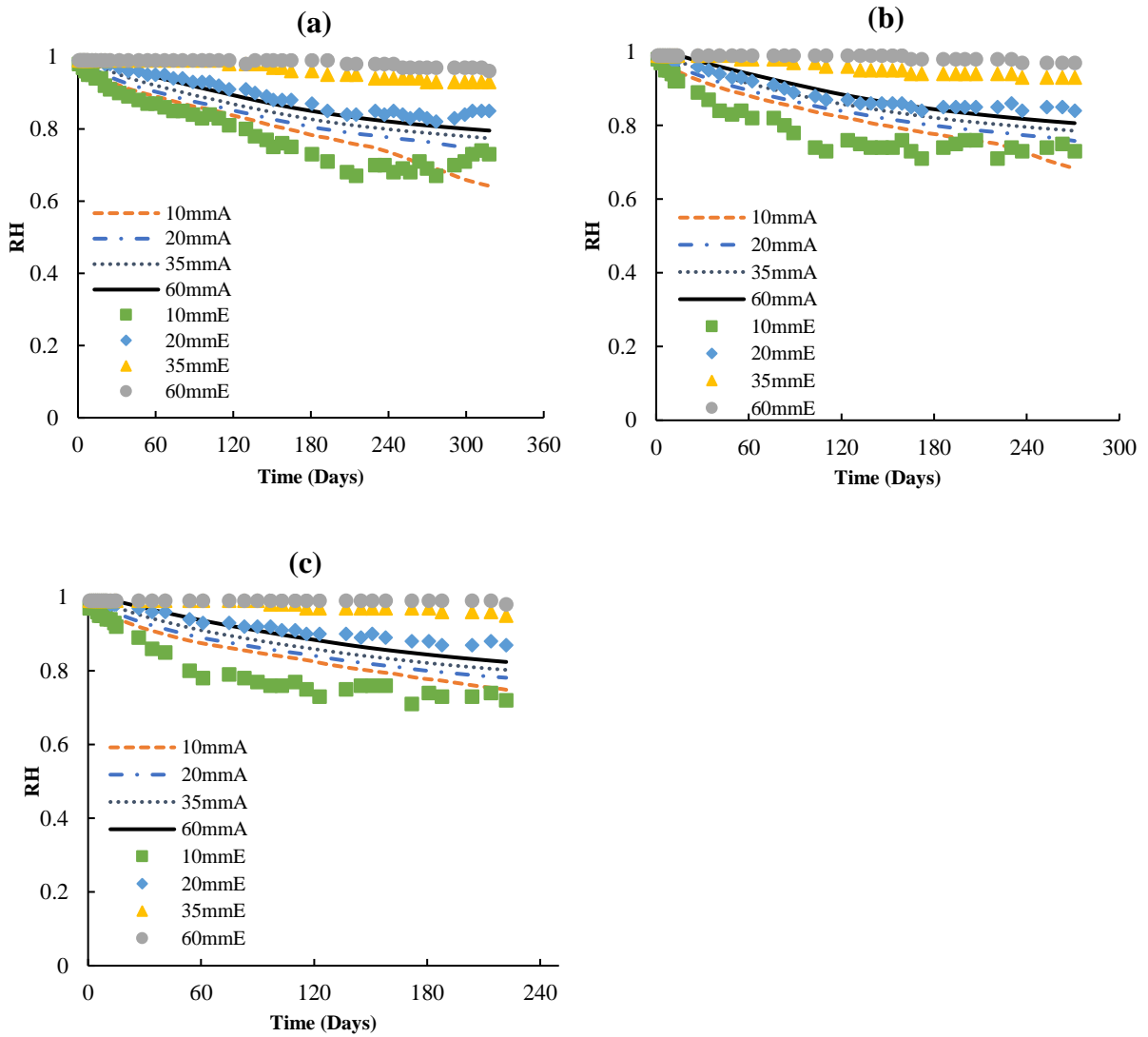
Figure 4.15 Comparison of experimental and Model Code 2010 predicted moisture distribution for: (a) Plain, (b) F30, and (c) F40 mixes.

86

Table 4.5 Model Code 2010 diffusion parameters

Parameters	$D_{1,0}\ (m^2/s)$	$f_{ck0}(MPa)$	H_c	n	α
MC-10 Diffusion Parameters	11×10^{-9}	10	0.80	15	0.05

4.5.2   Calibration of Concrete Damage Plasticity Model

After shrinkage and RH measurements, all the prisms are notched and tested in three-point bending according to RILEM TC 162-TDF, as shown in Fig. 4.16. Details of an individual prism are given in **Appendix E**. The load-deflection curves of experimental prisms (OSE) are calibrated by varying the CDP model parameters (i.e., inverse analysis).

Figure 4.16 Three-point bending: (a) test set-up, and (b) specimen geometry.

Figure 4.17 Abaqus FE model

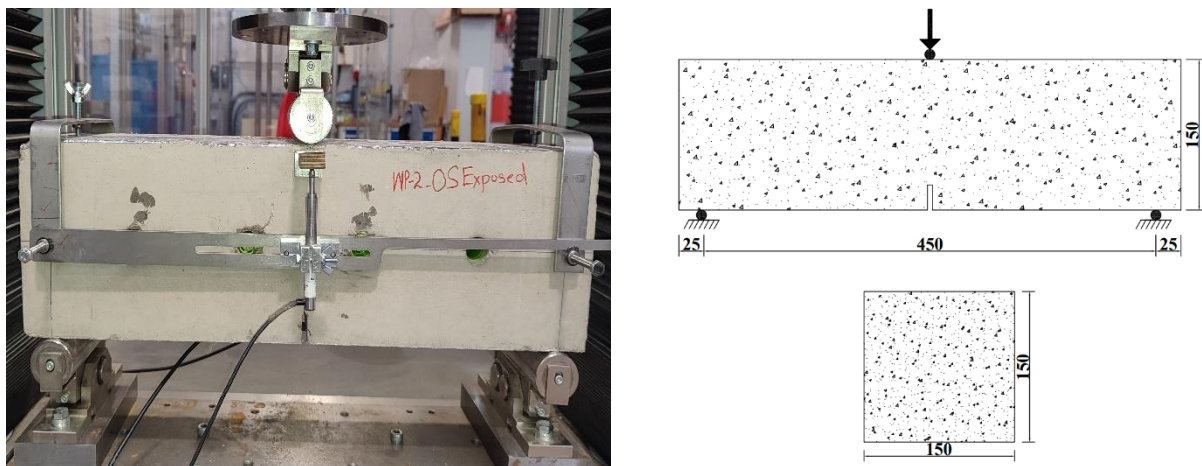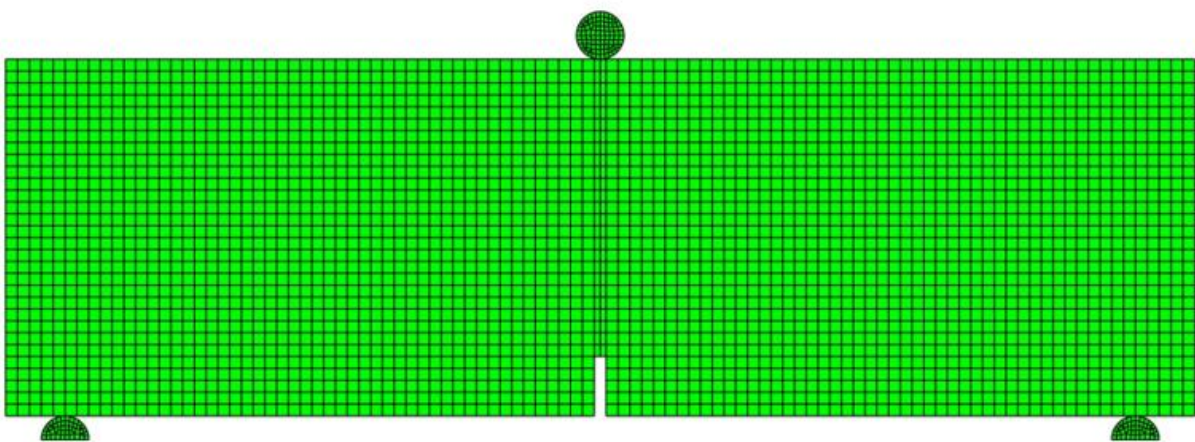Numerical analysis is performed on a two-dimensional (2D) deformable planar shell element and 4-node bilinear plane stress quadrilateral element (CPS4R), as shown in Fig. 4.17. The CDP model input parameters include the inelastic $\sigma - \varepsilon$ relationship in uniaxial compression and tensile behaviour and multiaxial yield and flow parameters (see Table 4.6). According to (Hu et al., 2019), compressive strain remains in the linear elastic region in FRC prisms (with 140 kg/m^3 steel fibres) under flexural loading. Hence, to simplify the analysis, elastic characteristics (according to MC-10) are used in compression. The multilinear $\sigma - \varepsilon$ characteristics in tension are back calculated (see Figs. 4.18b and 4.19b) from the experimental load-deflection curves. Figs 4.18a and 4.19a shows the numerically calibrated load-deflection curves for OSE specimens, along with the experimental data and predictions according to MC-10 and RILEM (see Appendix G). The use of the back calculated $\sigma - \varepsilon$ relationship accurately fits the experimental load-deflection, while MC-10 and RILEM over predict the load-deflection which is also observed by (Isa et al., 2021; Hu et al., 2019; Tlemat et al., 2006). Details of other calibrated load-deflection curves are given in **Appendix F**.
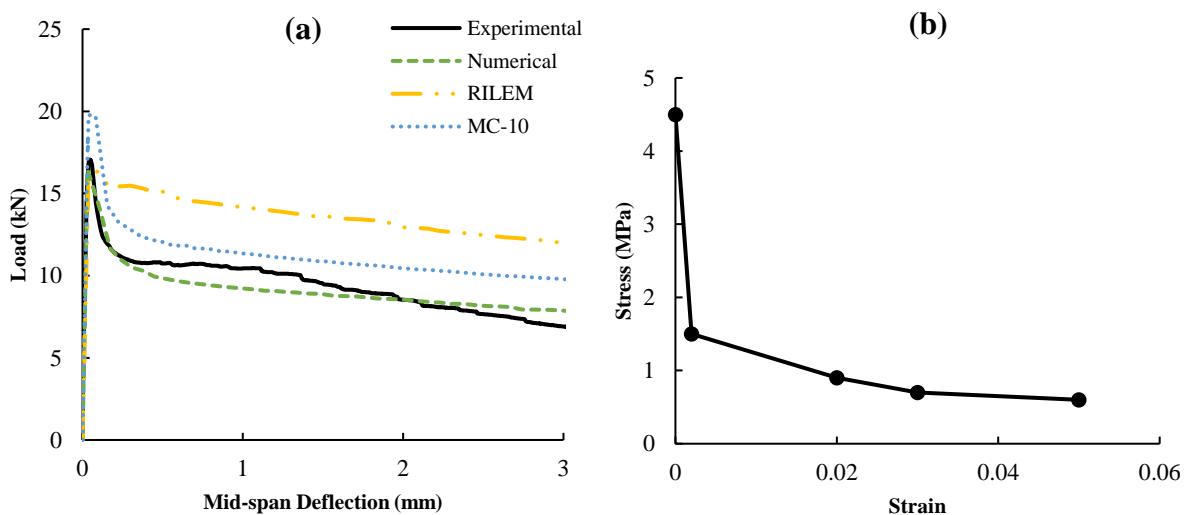

Figure 4.18 Inverse analysis results for OSE-F30 mix; (a) load-deflection curve, and (b) back calculated multilinear $\sigma - \varepsilon$ in tension.

Table 4.6 FE modelling CDP parameters.

	Eccentricity	σ_{b0}/σ_{c0}	K_c	Viscosity parameter	Poisson ratio
Dilation angle					
31	0.1	1.16	0.667	0.00002	0.18
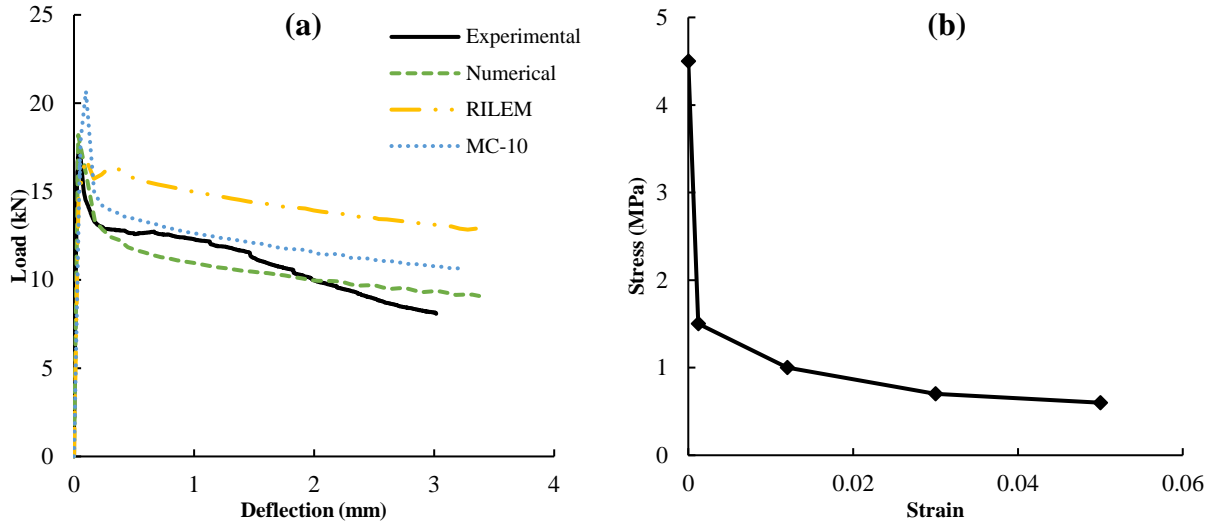
Figure 4.19 Inverse analysis results for OSE-F40 mix; (a) load-deflection curve, and (b) back calculated multilinear $\sigma - \varepsilon$ in tension.

As expected, a mesh sensitivity analysis shows that varying mesh size does not affect the elastic part of the load-deflection curve. However, the strain softening part of the curve is highly mesh dependent as energy dissipation decreases with decreasing size of the mesh (Isa et al., 2021). To avoid the mesh dependency, the characteristics length concept can be used (i.e., the ultimate cracking strain is multiplied by the ratio of the characteristics length of the experimental specimen to the characteristics length of the mesh).

4.5.3 Hygro-mechanical Modelling

Numerical analysis was performed only on OSE specimens. The OSE specimens have a higher shrinkage gradient, so it was expected that, as a result, concrete might crack on the top surface during the analysis. To investigate the effect of shrinkage gradient on the mechanical performance, both uniform and differential stiffness of concrete along the depth (see section 5.4) are examined.

The constant parameters, β and γ of HCC in Eq. 4.9, are calibrated by inverse analysis using experimental shrinkage results. The calibrated parameters are given in Table 4.4. Fig. 4.20 shows the HCC of all the mixes. HCC of the plain mix is higher than for F30 and F40 mixes, as also observed by (Jafarifar et al., 2014). This can be attributed to the higher shrinkage in plain mixes, different aggregates distributions and pore structures, as well as the restraining effect of fibres.
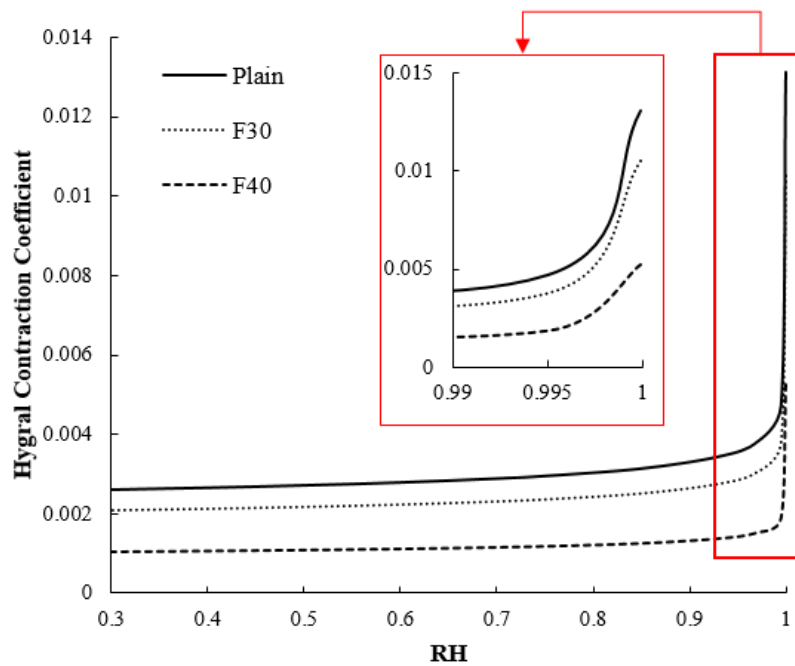
Figure 4.20 Hygral contraction coefficient.

Based on the calibrated parameters of HCC, the numerical predictions of OSE specimens are compared against the experimentally measured shrinkage results in Fig. 4.21. The numerical results at the top surface reasonably follow the experimental results' trend. However, at the bottom surface, the numerical analysis predicts moderate expansion in all OSE specimens, something not seen in the experiments, possibly due to imperfect sealing of the bottom surface. Differential drying results in a shrinkage gradient that can cause mechanical stresses. The compressive strains induced at the top are internally resisted by the adjacent layers, which results in surface tensile stresses. These tensile stresses travel down from the exposed surface to 35 mm as the concrete dries deeper with time (see Fig. 4.22).

As the bottom surface does not dry, it is not predicted to shrink. However, the combined effect of shrinkage curvature and internal restraint (due to fibres and aggregates) result in tensile stresses at the bottom of the prism as well (Jafarifar et al., 2014), which leave the centre of the prism in compression. In practice, these tensile stresses are amplified further by the additional restraining effect of the ground, side walls, internal columns and applied loads, which can impose an eccentric external tensile force along the depth. It is important that this is accounted for in the design of SoG, as it will cause cracks to appear at lower applied loads.
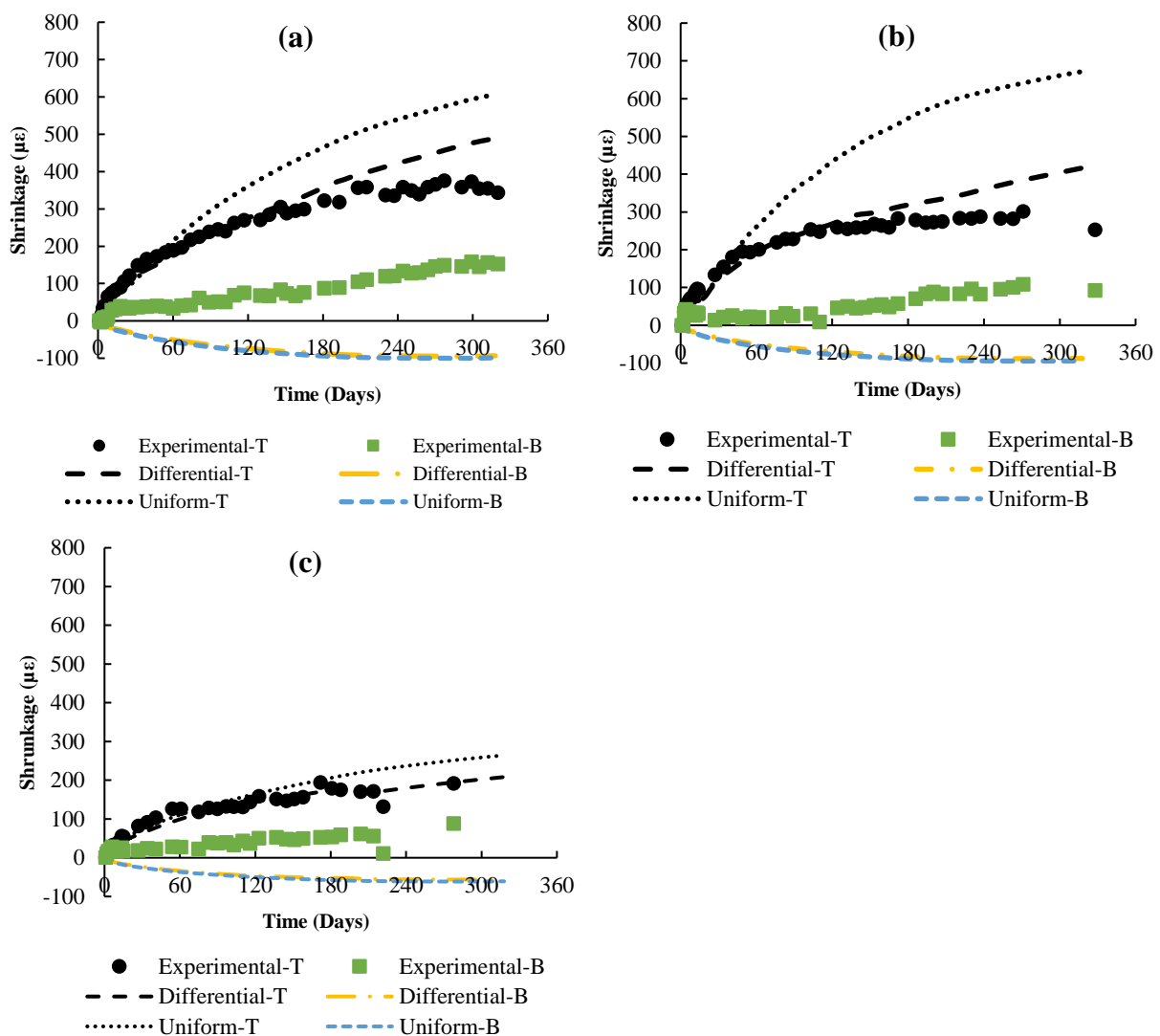

Figure 4.21 Numerical and experimental drying shrinkage of OSE specimens, (a) Plain; (b) F30 and (c) F40.
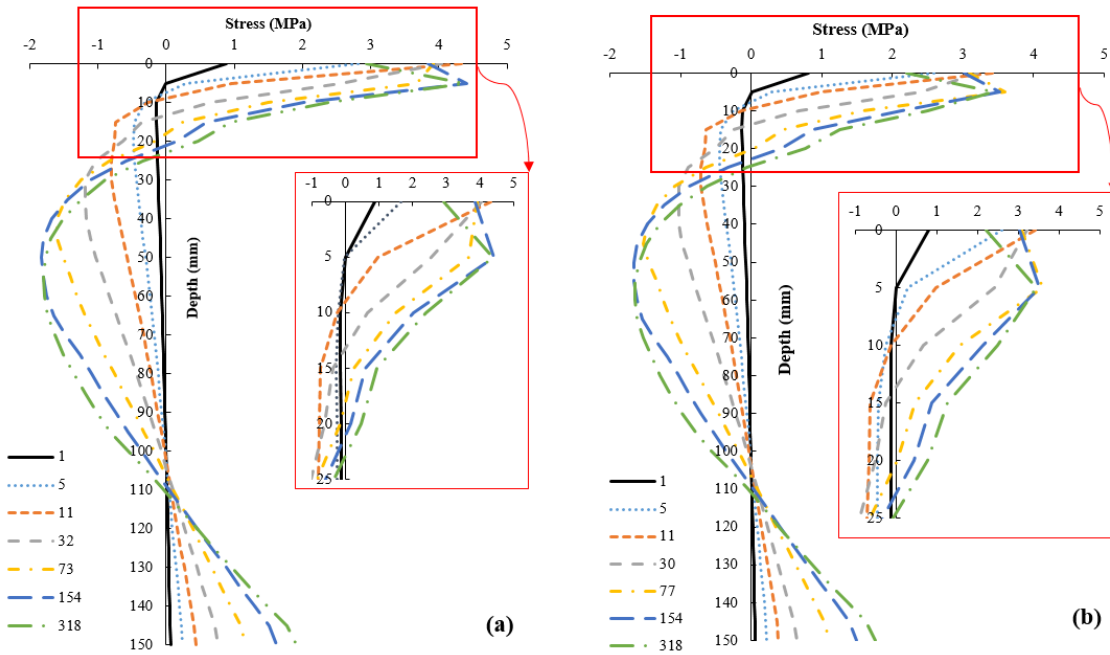
Figure 4.22 Stress distribution along depth at different time intervals in F40 concrete; (a) uniform and (b) differential stiffness.

4.5.4   Numerical Modelling of Shrinkage Curvature

Curvature (k_{exp}) can be determined by dividing the difference in shrinkage strain from the top (ε_t) to the bottom (ε_b) of the prism by the distance between them (i.e., 130 mm). Curvature in structural concrete is attributed to non-uniform shrinkage and creep strains, uneven aggregate distribution and eccentricity of steel reinforcement from the geometric centroid of the concrete section (Gilbert, 2001; Gribniak et al., 2007; Jeong et al., 2015; Younis, 2014). However, in plain and FRC concrete SoGs, non-uniform aggregate and moisture distributions also need to be considered. In this section, the effect of moisture distribution and concrete stiffness on curvature is analysed and compared with the theoretical curvature model of Al-Kamyani *et al.*, (2018), see Eq. 4.11, and numerical curvature models for plain and FRC.

The effect of non-uniform aggregate distribution on concrete aggregates is determined by using models proposed by Al-Kamyani *et al.*, (2018). The non-uniform distribution causes higher stiffness at the bottom than the top (concrete casting surface) of the concrete cross-section (**see**

92

Fig. 4.23). The calibrated *e* of Eq. 4.11 is used to calculate the *dE*. During curvature and

shrinkage analysis, non-uniform (NU) and uniform (U) stiffness are examined separately to

investigate the cracking and its effect on curvature.
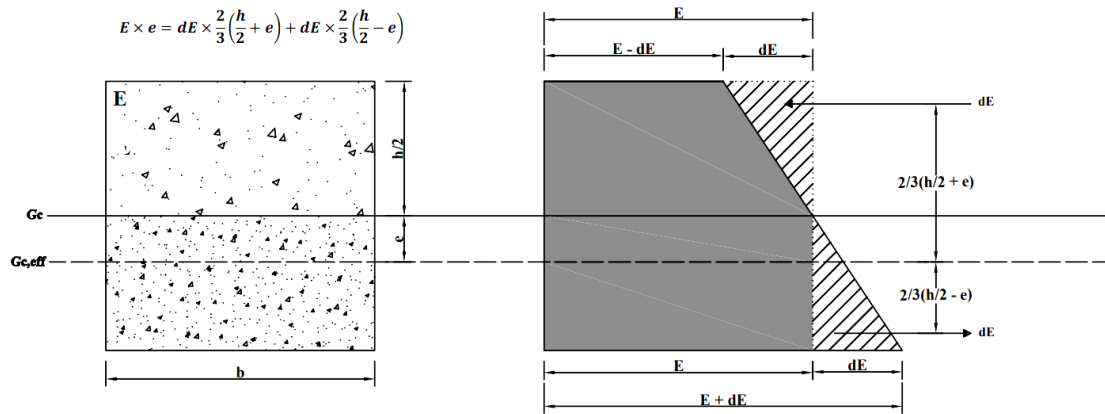
Figure 4.23 Typical plain concrete cross-section and section analysis.

The numerical shrinkage evaluation was calculated by back-calculating the hygral contraction

coefficient (HCC), see section 5.3.

$$k_{cs}(t) = \frac{\varepsilon_{cs}(t) \times A_c \times e}{I_g} \tag{4.11}$$

Where

$$e = G_c - G_{c,ef}$$

$$G_{c,ef} = G_c - k \cdot \frac{C^2 B}{\rho^2 F} \cdot \frac{hS}{D}$$

$$I_g = \frac{bh^3}{12}$$

$k_{cs}(t)$ is the theoretical curvature; $\varepsilon_{cs}(t)$ is free drying shrinkage (is the average of the top and

bottom shrinkage of the specimens); A_c is the total area of concrete; e is the eccentricity; G_c is

the geometric centroid (i.e., $h/2$); $G_{c,ef}$ is the effective centroid of concrete stiffness; I_g is the

second moment of area; b width of the specimen; h is the overall depth of the specimen; C is

the amount of coarse aggregates; B is the amount of binder; ρ is the density of concrete; S is the amount of slump; F is the amount of fine aggregates; k is the calibration factor; and D is the size of coarse aggregates.

4.5.4.1   Curvature results

All values used to calculate the theoretical curvature are given in Table 4.7. Figs. 4.24, 4.25 and 4.26 show the experimental, theoretical and numerical evaluation of the curvature of OSE and ASE specimens. The curvature model proposed by Al-Kamyani *et al.*, (2018) is calibrated by optimizing the calibration factor, k. The model accurately captures the experimental curvature evaluation. Shrinkage induced curvature in the prisms evolves with time as shrinkage progresses, which is also observed in (Younis, 2014; Al-Kamyani et al., 2018c; Jeong et al., 2012). However, in plain (both OSE and ASE), F30 and F40 (only OSE) mix, the experimental curvature drops gradually after 200, 110 and 172 days, respectively. This drop was presumed to indicate the onset of surface cracking, but no visible cracks were observed in the experiments.

Table 4.7 Al-Kamyani et al. (2018) curvature parameters.

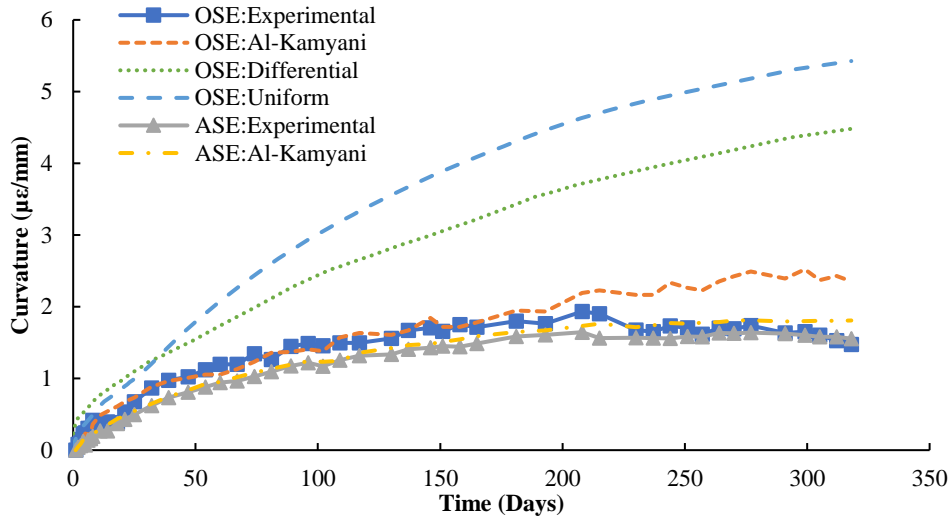| Curvature Parameters	Plain	F30	F40
C (kg/m^3)	1023	1023	1023
B (kg/m^3)	335	335	335
P (kg/m^3)	2339	2360	2389
S (mm)	200	50	40
h (mm)	150	150	150
F (kg/m^3)	847	847	847
D (mm)	14	14	14
k for OSE	0.1	0.53	0.55
k for ASE	0.03	0.05	0.055

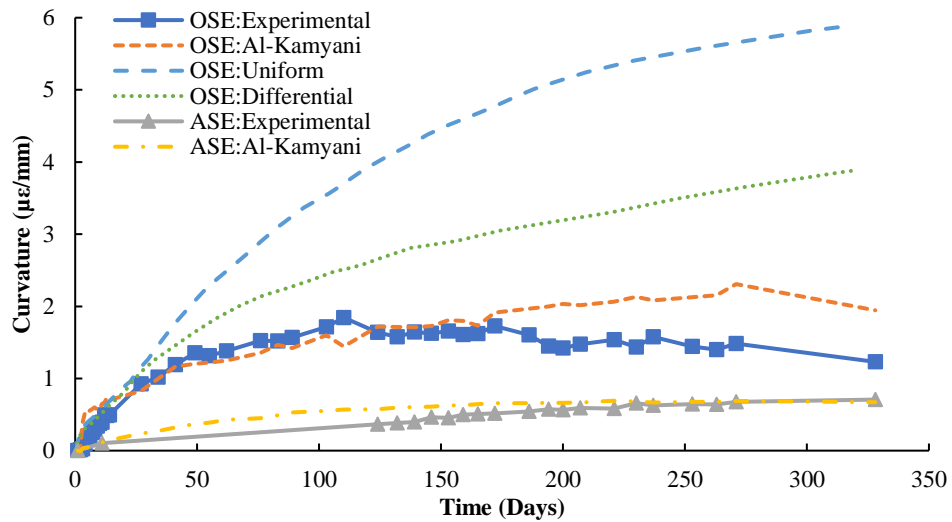Figure 4.24 Curvature prediction in OSE and ASE of plain concrete mix.

Figure 4.25 Curvature prediction in OSE and ASE of F30 concrete mix.

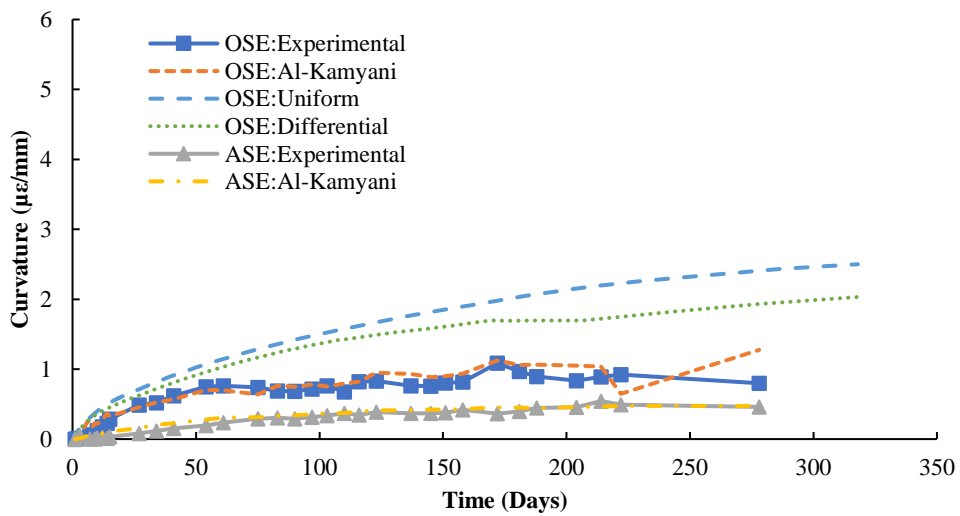Figure 4.26 Curvature prediction in OSE and ASE of F40 concrete mix.

4.5.4.2 Drying Shrinkage and Cracking

In the CDP model, the inelastic strain (IE) or cracking strain can be used to estimate the crack width over an effective length. IE is plotted at critical regions (i.e., at the centre of the top surface) of the OSE specimens in Fig. 4.27 for plain, F30 and F40 mixes. IE is highest in the plain mixes, and it is higher in non-uniform than uniform stiffness specimens. This is because the plain mix has higher shrinkage and stiffness. It can be seen in Fig. 4.27 that at the top surface, IE stabilizes quickly after reaching a maximum value in all samples, whilst this stabilisation is slower in deeper layers. Though the IE values indicate the initiation of cracking in concrete, these values do not escalate sufficiently to result in a sudden drop in stress; hence, any cracks are likely to be small and relatively well-controlled.

Cracking occurs when internal stresses due to drying reach the concrete's tensile capacity. Cracks occur at the top surface and propagate inside the concrete with time. After cracking at the top, internal stresses redistribute and travel inside the concrete as the drying front travels down from the exposed surface of the specimens (see Fig. 4.22). Cracking occurs slightly earlier in the non-uniform stiffness specimens (see Table 4.8) and penetrates up to 20mm, 15mm and 10mm, in plain, F30 and F40 mixes, respectively.

Table 4.8 Onset of cracking time (in Days) in different mixes along depths.

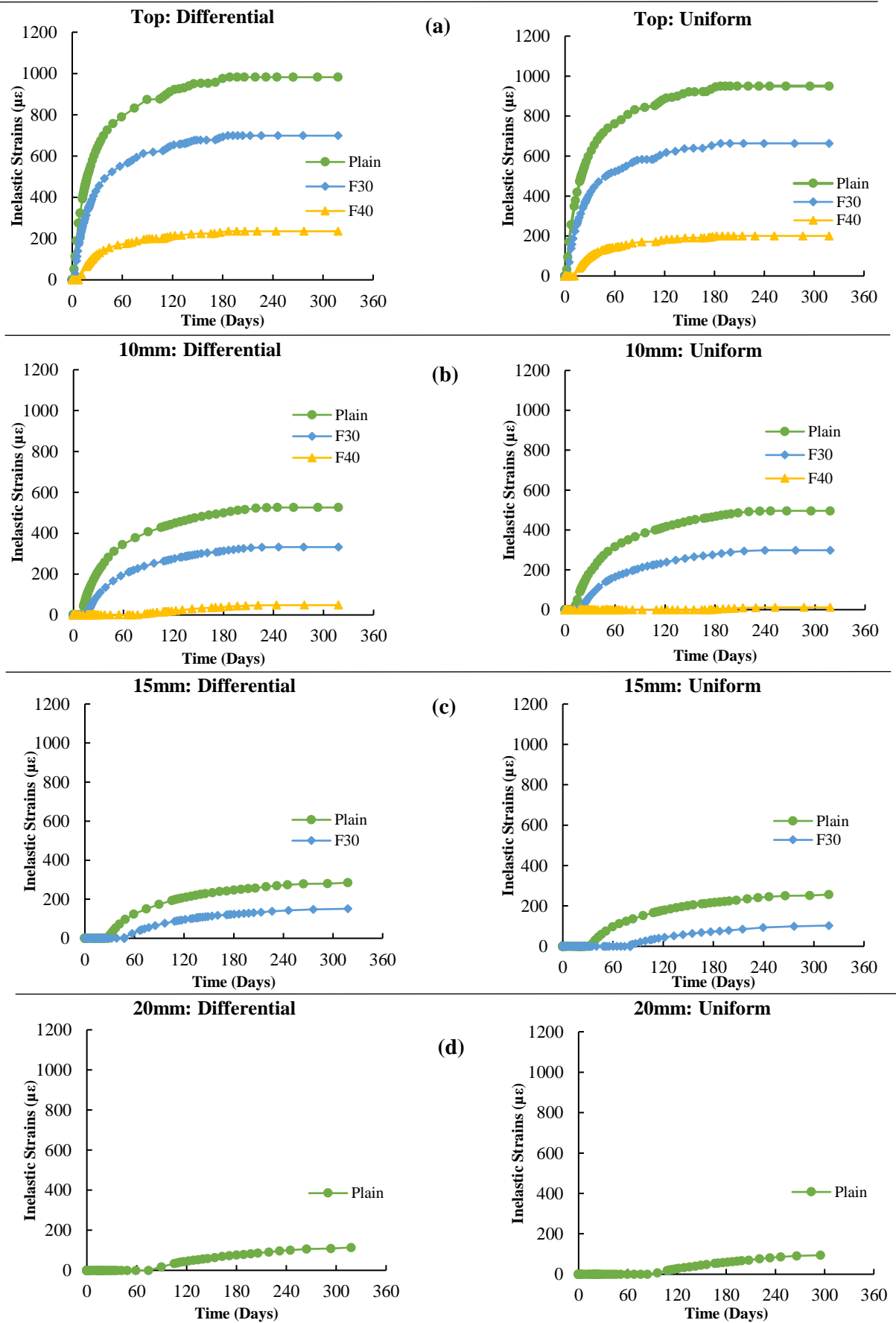| Depth	Plain		F30		F40	
	Uniform	Non-Uniform	Uniform	Non-Uniform	Uniform	Non-Uniform
Top	1.47	1.00	3.32	2.21	11.22	7.48
10 mm	11.22	9.35	18.82	15.44	172.9	76.97
15 mm	31.75	28.15	80.6	47.65	-	-
20 mm	83.94	74.28	-	-	-	-

Figure 4.27 Inelastic strain at the centre of Plain, F30 and F40 specimens with non-uniform and uniform stiffness distribution at (a) top, (b) 10 mm, (c) 15 mm, and (d) 20 mm.

Figs. 4.28, 4.29 and 4.30 show the 3D stress development with depth over time of plain, F30 and F40 concrete with uniform stiffness. The stress drop near the surface confirms that the concrete is cracking and that the cracking propagates down the depth slowly with time. Nonetheless, as the IE strain is not increasing after it reaches its maximum and then stress is reducing, this is an indication of stress relaxation as deeper drying releases the stress at the top surface. This is a further indication that these cracks are unlikely to develop into visible cracks.

The figures also show that the tensile stress at the bottom of the prism is high but not high enough to cause cracking. For equilibrium, the centre of the prism is always in compression, which increases over time as the tensile stresses also increase. The implication of this stress distribution is that, in practice, cracking is likely to develop further with loading (both at the top and bottom of an SoG) and at a much earlier stage than would be expected if the drying stresses were not considered. Nonetheless, these cracks cannot penetrate very deep, as the middle of the section is under compression. Hence, the stress development due to drying shrinkage changes the way the slab will behave under load, and due consideration needs to be given in design.

Figure 4.28 3D Stress distribution of plain concrete with uniform stiffness.
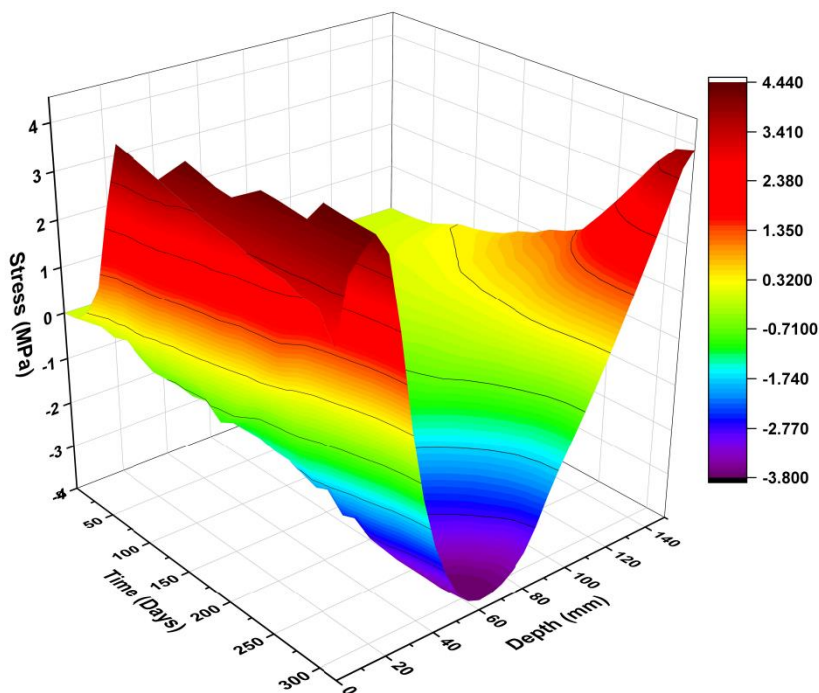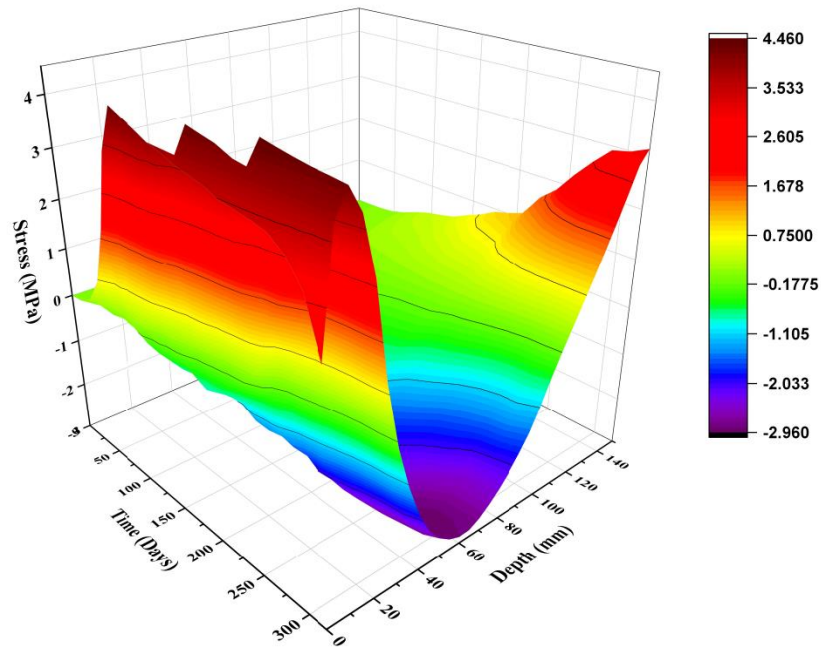
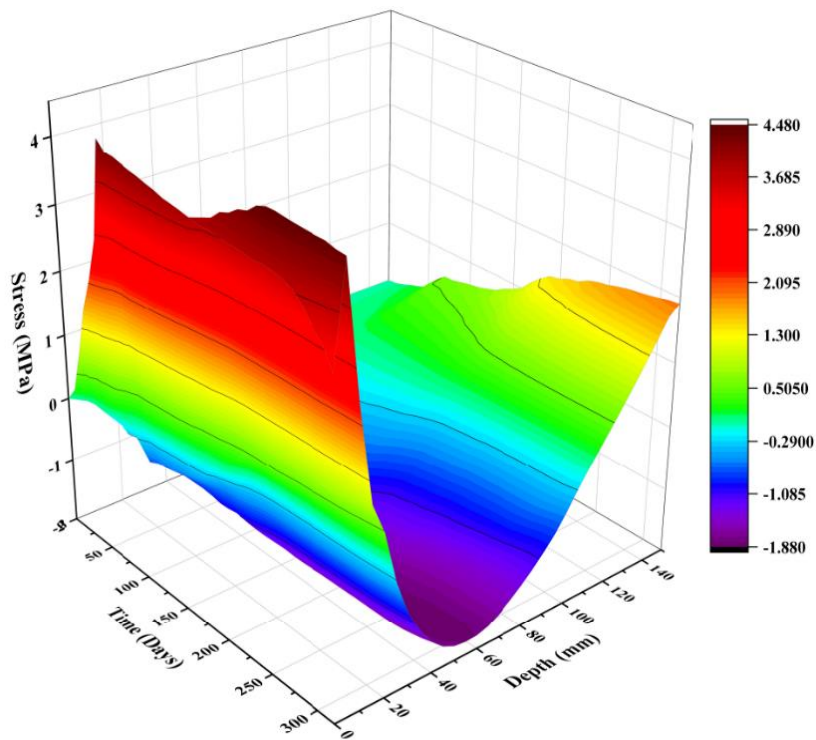Figure 4.29 3D Stress distribution of F30 concrete with uniform stiffness.

Figure 4.30 3D Stress distribution of F40 concrete with uniform stiffness.

4.6 Discussion and Conclusion

This study investigated moisture distribution and free differential shrinkage in plain and fibre

reinforced concrete and cracking due to shrinkage curvature. The adopted numerical modelling

approach (i.e., hygro-mechanical modelling) yields a better prediction of the drying shrinkage and associated cracking. Though these cracks are likely to be small, their impact is higher at the top surface, particularly for the plain mixes, as they are likely to develop rapidly as loads are applied. In addition, the concrete casting surface is more prone to cracking as a result of non-uniform slab stiffness due to aggregate settlement.

Design codes like Eurocode 2 and Model Code 10 do not consider the effect of differential shrinkage curvature. At the same time, the UK's Concrete Society updated Technical Report 34 completely neglects the effect of drying shrinkage and curvature in SoGs. Omitting the shrinkage induced stresses will lead to underestimation of concrete cracking and lead to serviceability issues. To accommodate cracking specifically in SoGs, the nominal moment carrying capacity in the critical regions (i.e. at the top drying surface and an interface between the slab and subgrade) should be reduced. However, further experimental and numerical studies are still required to investigate the exact reduction level required in the tensile capacity due to the differential shrinkage of the concrete.

Based on experimental and numerical modelling, the following specific conclusions can be drawn:

1. Plain and fibre reinforced concrete dry similarly with slightly faster diffusion in SFRC mixes, possibly due to more entrained air. However, 1D diffusion is slower than 3D diffusion in all the mixes. The faster diffusivity is due to different boundary conditions and non-uniform pore and aggregate distribution.

2. Numerical analysis can predict with high accuracy the moisture distribution if the appropriate diffusion coefficient is used. Coupling the hygral model with the mechanical model (i.e., hygro-mechanical analysis) yields a better prediction of shrinkage strains.

3. Plain concrete shrinks faster than SFRC mixes. It is likely that fibres provide additional restraint to shrinkage.

4. Differential shrinkage is higher in plain concrete than in SFRC mixes. Aggregates in plain mixes tend to settle at the bottom more, resulting in denser concrete in the bottom half of the prism. The non-uniform distribution of aggregates causes non-uniform shrinkage. In SFRC mixes, fibres prevent the aggregates from settling down, resulting in less additional shrinkage curvatures.

5. Design codes underestimate autogenous shrinkage and do not consider the effect of differential shrinkage. Non-uniform shrinkage can cause additional stresses that can lead to higher stresses and deformations in structural members. Structural members such as SoG, which usually dry from the top only, are more prone to shrinkage cracks and curling deformations (i.e., lifting up of edges).

Chapter 5: State-of-the-Art Review of Slabs-on-Grade and Numerical Modelling

The first part of this chapter critically reviews the literature on curling stresses and differential shrinkage in slabs-on-grade (SoG). It discusses design aspects and limitations of current design guidelines for SoG, specifically in the United Kingdom. In the second part of this chapter, numerical modelling is performed on a typical full-scale SoG to investigate the critical parameters that dominate the complex behaviour of SoG when drying shrinkage effects are considered.

5.1 Curling Stresses in SoG

According to ACI-360R, (2006), *curling* is *'the distortion of an originally essentially linear or planar member into a curved shape, such as the warping of a slab due to differences in temperature or moisture content in the zones adjacent to its opposite faces'*. The code also defines *warping*, which is the 'deviation of a slab or wall surface from its original shape, usually caused by either temperature or moisture differentials or both within the slab or wall'. Both of these terms are used interchangeably and commonly referred to as *curling*. The primary cause of curling is differential shrinkage through the depth of SoG. The top exposed surface of SoG is more prone to shrinkage than the bottom surface, as it is commonly free to dry faster and has a higher unit water content at the time of the final set. The entire length of the slab does not lift as a result of curling, but the part near the edge of the slab does, as shown in Fig. 5.1. The curled length is called *critical length* (L_{cr}), and it is defined as the length from the edges of the slab where the internal stresses arising from the non-uniform shrinkage are equal and opposite to the stresses resulting from the self-weight of the unsupported end section of the slab (Eisemann and Leykauf, 1990).
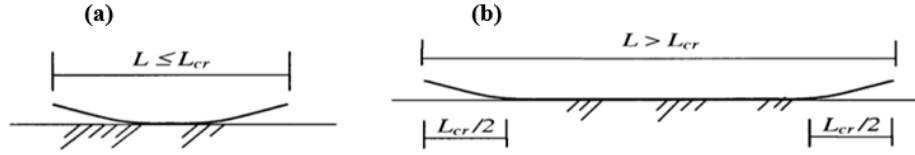
Figure 5.1 Critical length (L_{cr})) of the slab; (a) total length of the slab less than or equal to (L_{cr}); (b) total length of slab greater than (L_{cr}).

The loss of contact between the slab and the ground caused by curling can be prevented by making a certain length (the critical length) of the slab thicker. However, this induces tensile cracks on the surface due to the higher level of restraint at the ends (Ytterberg, 1987c). In addition, the shrinkage strains are further restrained by side walls, inner columns, applied loads, ground friction etc. which cause tensile strains that ultimately lead to inelastic or tensile cracking on the surface of the concrete (TR-34, 2013).

5.2 Mathematical Models of Curling Stress

Various analytical and empirical models of curling stresses due to shrinkage, critical length of slab and upward deflection of the end have been proposed by different researchers. For example, Eisemann and Leykauf, (1990) and Pettersson, (1998) (cited in Bishop, (2001)), showed that the critical length depends on h, the depth of the slab; α_c, coefficient of thermal expansion; $\varDelta T$, temperature gradient at the top and the bottom surfaces of the slab; E_c, the elastic modulus of concrete; ε_s, drying shrinkage strain at the top; h_d, depth of slab; ρ_c, density of concrete; g, acceleration due to gravity and f, load factor as given in Eqs. (5.1), (5.2) and (5.3) (derived based on SI units).

$$L_{cr}(in\ mm) = 167.h.\sqrt{\alpha_c.\Delta T.E_c} \tag{5.1}$$

$$L_{cr}(in\ mm) = 409.6.h.\sqrt{\frac{t.\varepsilon_s.(h-h_d).E_c}{h}} \tag{5.2}$$

$$L_{cr}(in\ mm) = \sqrt{\frac{4.\alpha_c.E_c.\Delta T.h}{5.\rho_c.\ g.\ f}} \tag{5.3}$$

103

This curling can be upward or downward depending on positive or negative temperature or moisture gradient (Hiller and Roesler, 2010). The study carried out by ACI-325 (1956) and Leonards and Harr (1959) cited in Ytterberg (1987a) recognised two modes of slab curling as given in Fig. 5.2 (after ACI-325, 1956). Structural design guidelines of the ACI 360R Committee on Design of Slab on Ground adopt these deflection modes.
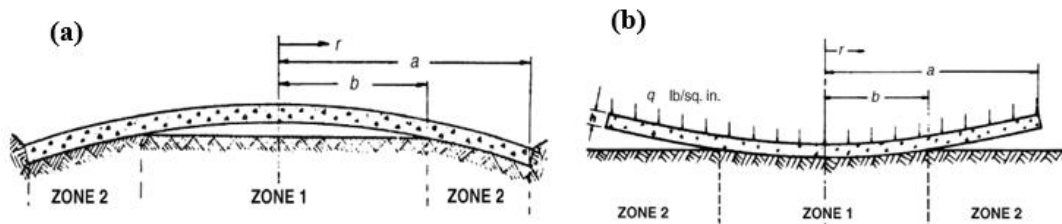

Figure 5.2 Curling of slabs; (a) highway slab during day time when the sun warms the top surface, (b) indoor slab due to moisture differential between the top and bottom of the slab.

Fig. 5.2 (a) depicts the positive gradient due to temperature difference at the top and bottom of the slab, especially exposed to sunshine. This behaviour is typical in highway concrete pavements where ambient environmental conditions frequently fluctuate every day with hot (daytime) and cold (night-time) cycles. During the day, the top surface is hotter than the bottom surface (positive temperature gradient of 3 $^\circ$F/inch), and during the night, vice versa (negative temperature gradient of 1 $^\circ$F/inch) (Ytterberg, 1987b).

Indoor slabs, such as warehouse ground slabs or industrial ground slabs, are not much affected by sun heat but are affected by moisture movement. The moisture content at the bottom surface is higher than at the top. This is due to the use of impermeable polyethene sheets at the bottom. The sheets are provided underneath the slab before construction, as recommended in TR34 (2013) design guidelines to (a) avoid the friction between the subgrade and slab for unrestricted movement and (b) prevent the cement gel of the concrete from penetrating inside the ground, which can degrade the quality of the concrete. The moisture gradient causes differential

shrinkage strains, higher at the top than the bottom, resulting in upward slab curling at the edges, as shown in Fig. 5.2(b).

Destrée Yao and Mobasher (2015) carried out a parametric study using a 1D finite difference model of sequential cracking and opening of restrained SoG. The study concluded that a higher level of restraint from either friction or fibres inside the concrete or higher bond strength reduced the predicted crack opening by restricting the movement of cracked slab sections. Similarly, a study carried out by Nicholson (1981) on three full-scale slabs (54 x 13 ft) cast on three different bases (i.e. impervious polyethene, pervious sand, and sand-cement treated base) investigated the shrinkage and cracking behaviour of the slabs. It was observed that the slab on the impervious base had more plastic shrinkage cracks due to the evaporation of extra bleeding water from the top-only surface that led to faster drying of the top surface. The slab tended to curl, while early-age strength gain was less than the developed tensile stresses leading to cracks. However, these cracks were lower in the sand base slab because of more even moisture loss due to evaporation from the top and penetration of water inside the sand, enabling the concrete to densify without creating any differential stresses, which prevented curling and resulted in the elimination of plastic shrinkage cracking.

5.3 Differential Shrinkage Cracking

Non-uniform shrinkage strain induces differential stresses inside structural concrete. These stresses are flexural or tensile in nature; if at any stage of concrete maturity, the magnitude of induced stress becomes higher than the tensile strength of the concrete, then concrete can crack (Ytterberg, 1987a). As per ACI-360R (2006) and TR34 (2013), the size of these cracks can be micro or macro depending on the time they appear. At an early age, these cracks are very fine, known as *crazing,* and with time, they progress along the length and width due to drying shrinkage and applied loads and can be seen with the naked eye. Although *crazing* only affects

surface appearance rather than leading to any serviceability or structural issues, macro cracks can severely affect the performance of SoG.

In SoG, cracking is often associated with *restraint shrinkage.* The restraining effect is due to resistance to free movement. According to Destrée, Yao and Mobasher (2015), there are two restraining effects: internal and external. While internal restraint is caused by the non-uniform distribution of aggregates and steel reinforcement (Al-Kamyani, 2018), external restraint is caused by interaction with the ground, side walls and columns (Bishop, 2001; Losberg, 1978; Robins et al., 2003; de Sa et al., 2008). Ground restraint is dominant in SoG as compared to other types of restraint. Restraint induced stresses can be calculated using Eqs. (5.4) and (5.5) (Losberg, 1978).

$$\sigma_t = \omega . \gamma . \mu_s . \frac{L}{2} \qquad (5.4)$$

$$\sigma_{wt} = \frac{E_c}{1 - \nu_c} . \frac{\Delta \varepsilon_t}{2} \qquad (5.5)$$

Where; σ_t pure tensile stress due to ground restraint, ω load correction factor, 1.5 to 1.8 between pure tensile stress and bending tensile stress, γ density of concrete, μ_s coefficient of friction between subgrade and slab, L length of the slab, σ_{wt} warping or curling stress, E_c modulus of elasticity of concrete, ν_c Poisson's ratio and $\Delta \varepsilon_t$ differential shrinkage strain due to temperature gradient at the top and bottom of the slab.

Losberg (1978) suggested adding both stresses (from ground restraint and warping), and the consolidated amount should be subtracted from the tensile strength of concrete during the structural designing of SoG. Though this formulation quantifies both ground restraint and temperature gradient, moisture gradient needs to be accounted for, which is significantly dominant in indoor SoG. The study by G.A. Leonards and Harr (1959) shows curling is due to the combined effect of thermal and hygral or moisture gradient known as the equivalent thermal

gradient (ETG). The ETG considers the total shrinkage strain, ε_{sh} at time t and the coefficient

of thermal expansion α_c, to calculate equivalent shrinkage strain, as given in Eq. (5.6).

$$\text{ETG} = \frac{\varepsilon_{sh}}{\alpha_c \cdot h} \tag{5.6}$$

As the slab thickness is not enough to cause a sufficient temperature gradient, this gradient can

be significant in the early age when concrete starts the hydration process, which releases heat

and increases the internal temperature of the concrete.

Temperature variation and induced strains were observed through temperature and strain

gauges at various slab locations along the length and depth up to 28 days in 5 full-scale slabs

in England by Bishop (2001). Based on field observations and finite element analysis (FEA)

on thermal modelling, it was observed that the temperature gradient was generally small, as the

section of the slab was not enough to generate significant heat inside the concrete. Still, ETG

of 1.5 ⁰C/cm and 0.74 ⁰C/cm was experimentally determined by assuming $\alpha_c =$

$10\ \mu\ strain/^0\text{C}$ for large pour areas and thick and reduced joint spacing, respectively.

Moreover, the stresses from uniform contraction were significantly less than those from

differential contraction. In the longer term, when warping and frictional restraint are accounted

for, the maximum tensile stresses in a slab will likely occur at the top surface. The warping

restraint was more significant than the longitudinal restraint, and the field-measured

longitudinal restraint between gauges was higher than predicted by the current frictional

restraint theory. This means that the curling stresses influence more cracking than uniform

shrinkage restraint stress.

5.4 SoG Design Guidelines

TR 34 (2003) recommends providing a slip membrane to avoid frictional resistance between

the slab and the ground. Further, the TR34 report suggests using a 0.2 restraining factor (RF)

to estimate stress due to external restraint to shrinkage as given in Eq. (5.7), and if the slab is

fully restrained, then RF = 1. To account for curling due to internal restraint, this report suggests the use of the formula proposed by Losberg (1978), see Eq. (5.7). Instead of differential shrinkage due to temperature gradient, the report considers the shrinkage due to moisture gradient (see Eq. (5.8), and considers the creep relaxation factor in both of the stresses.

➢ Uniform stress due to external restraints

$$f_{sh} = \text{RF}. E_{cm,eff} . \varepsilon_{sh}$$ (5.7)

$$E_{cm,eff} = \frac{E_{cm}}{1+\phi}$$

Where

f_{sh} = long-term shrinkage stress

E_{cm} = Secant modulus of elasticity of concrete

ε_{sh} = Free drying shrinkage

$E_{cm,eff}$ = Effective modulus of elasticity

ϕ = Creep relaxation factor (the report suggests, i.e., 2)

➢ Curling stress due to internal restraints

$$f_{cur} = \frac{1}{2} \cdot \frac{E_{cm}}{3} \cdot \frac{\Delta\varepsilon_{sh}}{1-\nu_c}$$ (5.8)

Where

f_{cur} = Curling stress

$\Delta\varepsilon_{sh}$ = Differential drying shrinkage at the top and bottom of the slab

ν_c = Poisson's ratio

Finally, this report concludes that shrinkage stresses due to restraint and loading are complex and suggests subtracting 1.5 N/mm^2 from the tensile strength of concrete while computing the hogging moment capacity of the slab in severe loading areas.

The more recent TR 34 (2013) publication made a significant revision regarding industrial ground floor curling and restraint stresses. This report, however, does not consider the effect of shrinkage-induced stresses but instead emphasises (a) minimising the shrinkage by using suitable concrete mix design, (b) minimising contact with external sources (ground, walls etc.), (c) the use of slip membranes, and (d) adequate provision of joints that can release the induced stresses. In addition, this report recommends sawn joints at 6 m spacing for fabric-reinforced concrete and load transfer joints at 35 m spacing for jointless slabs to avoid the risk of drying shrinkage cracking. At the same time, no sawn joints are recommended for fibre-reinforced concrete due to the high risk of the joints opening, which can lead to the progressive reduction of load transfer capacity and the formation of free edges. This can result in significant deflections, cracking, vertical movement at joints, loss of slab support and joint damage.

However, just ignoring the curling stresses does not mean that they are mitigated completely, but they need to be analysed quantitatively to know the complex behaviour of shrinkage. In pursuing that objective, Jafarifar (2012) conducted experimental and finite element analysis to assess the impact of moisture gradient on curling stresses in concrete pavement ($10086 \times 3360 \times 200$ mm) for up to 365 days. The numerical results showed that due to drying shrinkage, in the top quarter of the cross-section of the pavement, the tensile strength reaches half (50%) of the ultimate tensile strength capacity. On the other hand, TR 34 (2003) recommends reducing by 30% the flexural tensile strength capacity throughout the slab's top half; TR 34 (2013) ignores the effect of drying shrinkage, which is very dominant on the surface.

Similarly, Bishop (2001) performed experimental and 1D numerical modelling (thermal modelling) on early-age (i.e., 28 days) concrete pavements ($40000 \times 40000 \times 225$ mm). The author measured strains and temperature in full-scale slabs at different locations along length and depth using vibrating wires gauges (VW) and thermocouples, respectively. The induced strains were higher three days after casting due to the higher initial temperature caused by cement hydration, which then decreased uniformly. Although the author did full-scale modelling and measured strains at specific locations (e.g., mid of concrete slab, in some cases near edges), local strains may not give a representative result of the shrinkage effect. Moreover, drying shrinkage is a long-term phenomenon, so early-age shrinkage might not inform the expected long-term behaviour of pavements. For theoretical calculations, the author did not consider the effect of temperature and moisture individually but rather equivalent thermal gradient in place of differential shrinkage strains, as suggested by G. A. Leonards and Harr. On the other hand, TR 34 (2003) uses differential shrinkage instead of ETG in the curling stress equation, as given in Eq. (5.8). In comparison, Jafarifar (2012) considered the moisture analysis only without considering the effect of temperature by assuming that the hygral coefficient varies with the properties of concrete and internal moisture content.

The differential shrinkage strains, therefore, are due to both moisture and temperature gradients. At an early age, the thermal strains are dominant, but with time as the concrete dries, the moisture gradient plays a more important role. Due to the provision of the slip membrane underneath SoG, the moisture does not penetrate the ground from the bottom but instead evaporates only from the top surface. This phenomenon will induce a higher moisture gradient, low at the top and high at the bottom (almost 100% RH). Thus, there is a need to quantify the temperature (in the case of early-age concrete) and moisture-induced strains (experimentally and numerically) in full-scale SoG at not only the middle strip but also near the edges to understand the complex long-term behaviour of SoG.

5.5 Numerical Modelling of SoG

FE numerical modelling is performed in Abaqus CAE 2021 on 3D full-scale SoG (i.e., 10000 × 10000 × 150 mm). The 3D modelling approach gives a better approximation than 2D of curled shapes due to differential shrinkage. First hygral analysis is performed, and then time-history moisture data is coupled with the mechanical model (for details, see Chapter 4) to quantify the behaviour of the slab in drying without external loading.

Typical SoG are constructed using FRC with 25-45 Kg/m^3 steel fibres. TR 34 (2013) considers residual flexural strength values (i.e., f_{R1} and f_{R2}) to calculate the moment capacity of FRC SoGs based on RILEM TC 162-TDF. In this study, the RTSFRC with 40 Kg/m^3 of RTSF is used. F40 concrete mix's characteristics properties, stiffness and calibrated CDP material model are used for the analysis.

5.5.1   Modelling Assumptions

As discussed earlier, SoG dries from the top only surface, so all the slab surfaces are sealed except the top, where moisture diffuses to the environment. The calibrated diffusion coefficient and hygral contraction coefficient of the F40 mix (i.e., OSE prism) are used in hygral and shrinkage analysis, respectively. As per the TR34 design recommendation, a minimum depth of 150 mm for the slab and sub-base is selected.

Due to symmetry along the length and width of the slab and sub-base, and to reduce computational time, only a quarter (i.e., 5000 × 5000 × 150 mm) of the slab and sub-base is modelled, as shown in Fig. 5.3.
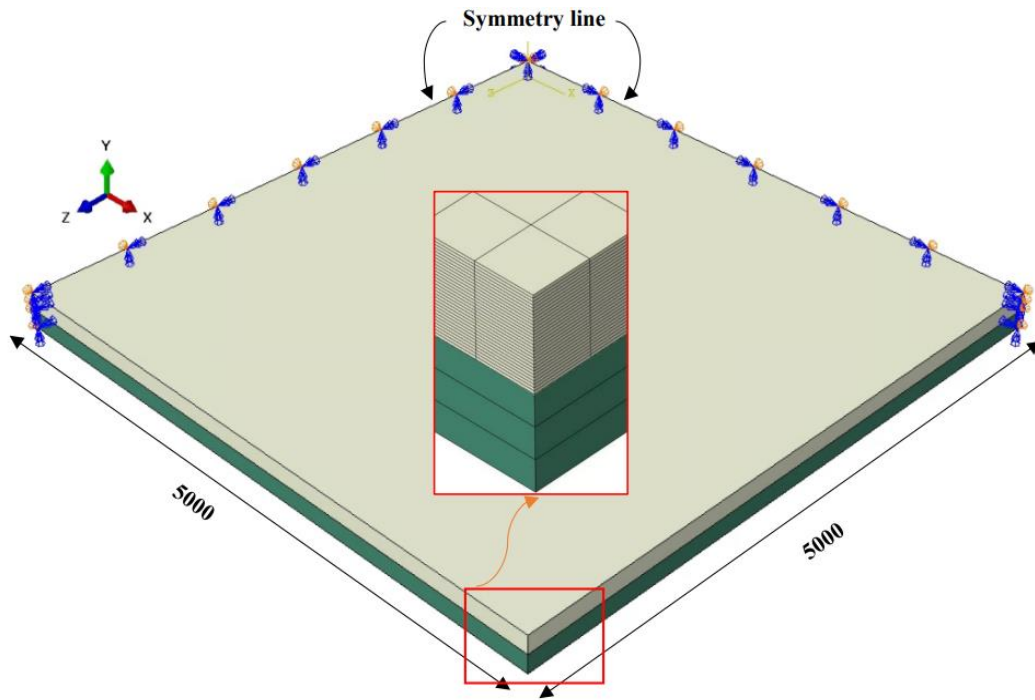
111

Figure 5.3 FEA geometry of the slab.

To model the contact between the slab and sub-base, the Coulomb friction model is adopted. According to the model (as given in Eq. (5.9)), the shear stress is proportional to the contact pressure before sliding surfaces. Once shear stress reaches the critical value, sliding of the surfaces occurs.

$$\tau = \mu \cdot p \tag{5.9}$$

Where τ is the shear stress, μ is the coefficient of friction; and p is the contact pressure.

The coefficient of friction (0.5), critical shear stress (100 kPa), elastic modulus (8 GPa) and Poisson's ratio (0.3) for the sub-base and interface between the slab and sub-base are assumed after (Jafarifar et al., 2016).

The soil underneath the sub-base, also known as subgrade, is modelled according to the Winkler soil model. According to Winkler (1867), the foundation deflection under vertical load is directly proportional to the force without shear transmission to the adjacent layers. This model is defined in terms of the modulus of subgrade (k) of the elastic foundation. According

112

to TR 34 (2003), k varies between 0.01 to 0.1 N/mm^3 for different types of soils. An average value of 0.06 N/mm^3 is adopted in this study.

DC3D8 and C3D8R, 8-node solid brick elements, were used for hygral and mechanical analysis, respectively. During analysis, 5×100 and 50×200 mm (5 and 50 mm along the depth and 100 and 200 mm along length and width) mesh sizes for the slab and sub-base are adopted, respectively. Mesh sensitivity analysis shows that in 1D diffusion problems, the mesh size along the diffusion direction does not significantly affect moisture distribution and is not mesh sensitive in other directions (see Chapter 3). In Chapter 4, shrinkage analysis and CDP material model calibration were done using a 5 mm mesh size. In addition, the slab dries along the depth only, so a 5 mm mesh size along the depth and 100 mm along the length and width is considered appropriate.

5.5.2 Drying Creep

The drying creep of concrete includes micro cracking and intrinsic creep. Micro cracking is associated with microstructural damage due to non-uniform drying. At the same time, intrinsic creep has its own mechanism and depends on the properties of concrete. The tensile stresses are dominant in the design of SoG, hence drying creep here refers to tensile creep.

During numerical modelling, the micro cracking component of the creep is considered by the CDP material model. According to Altoubat and Lange, (2002; and Jafarifar et al., (2016), intrinsic creep occurs in the pre-cracking stage when concrete is elastic. It only releases 7% of the total drying shrinkage strains in the critical regions (i.e. at the top drying surface where shrinkage is high), which is much less than the cracking strains. Hence, the intrinsic component is not considered in the analysis. After cracking, the tensile stresses are released by the crack opening.

5.5.3 Modelling Results

5.5.3.1 Critical Length

Figs. 5.4 and 5.5 show the curling length of the slab from the centre to the edge and the centre to the corner. The edge and corner lift up 3.46 mm and 10 mm, respectively, after 119 days. After that, deflection started to decrease slowly, as shown in Fig. 5.6. This relaxation of the deflection defines the onset of cracking near the edge and corner. Due to the self-weight of the slab, some portion of the deflection is released. The total length from the centre to the edge and corner is 5000 mm and 7071 mm, respectively. After 318 days of drying, 1500 mm and 4384 mm lengths of the edge and corner from the centre are curled up due to differential shrinkage. This is half of the critical length (see Fig. 5.1). Lifting up causes a complete loss of sub-base support, as shown in Fig. 5.7. However, half of the critical length is higher at 119 days due to higher curling of the corner. After this time, cracks occur, which release part of the curling. At this stage, if the curled length is further loaded by any external loads, such as material handling equipment (MHE), it can cause severe cracking.
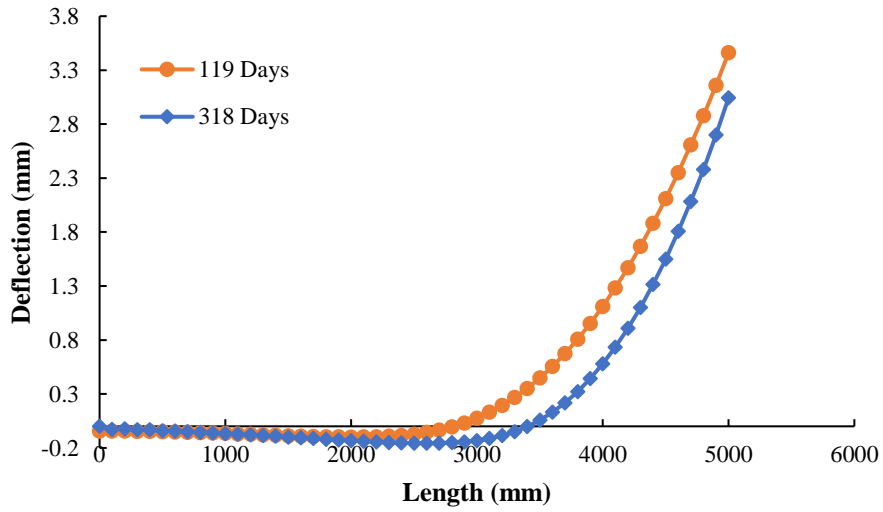
Figure 5.4 Critical length of the edge from the centre of the slab.
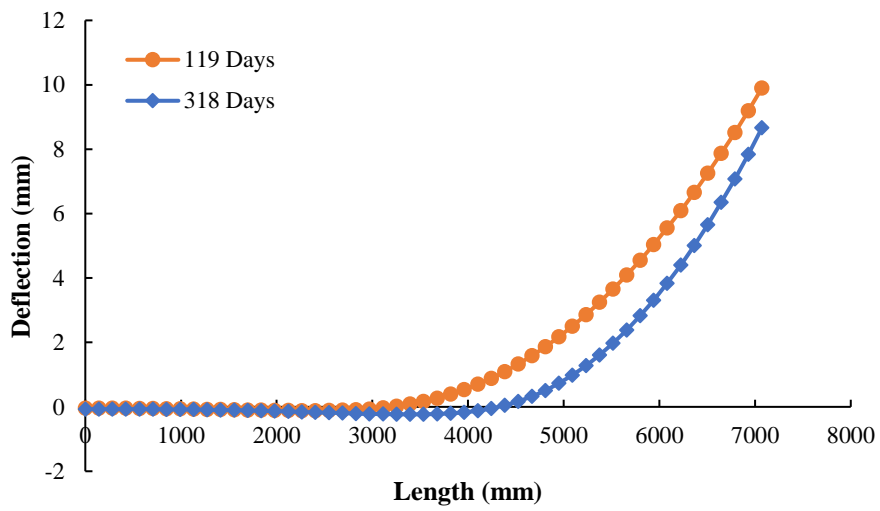
Figure 5.5 Critical length of the corner from the centre of the slab.
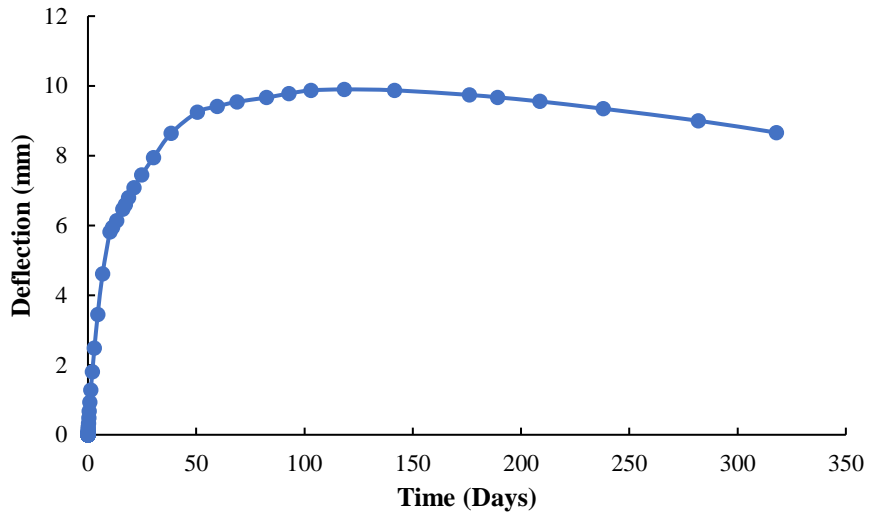
Figure 5.6 Time history deflection of the corner.
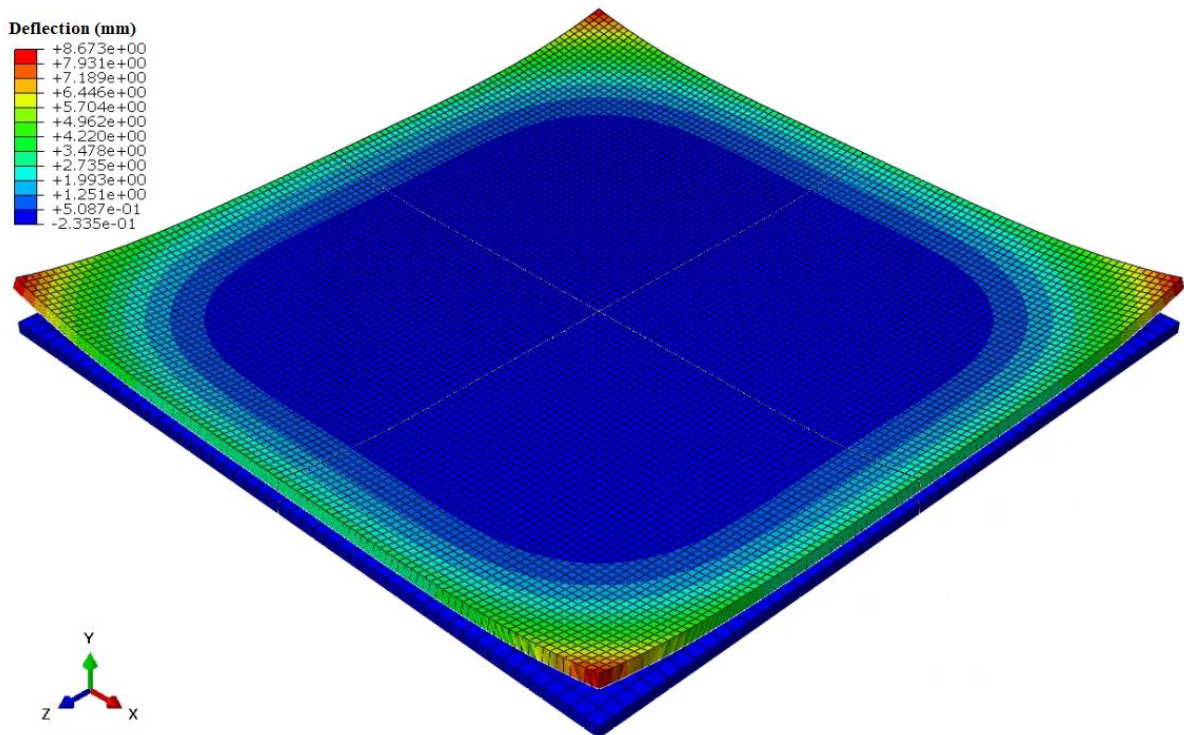
Figure 5.7 Deflected shape of the slab.

116

5.5.3.2 Drying Shrinkage and Cracking

As mentioned in Chapter 4, the inelastic strain (IE) component of the total strain in Abaqus is the cracking strain. IEs (in µε) are plotted along depth at the critical region (i.e., at the centre) as shown in Fig. 5.8. Fig. 5.9 shows the graphical distribution of the strains over the top drying surface. These strains are higher at the centre region than edge and corner because 3000 mm of the length is unsupported, which shifts the cracking at the start of the critical length.

IEs start at the top after 10 days and penetrate inside the slab with time up to 20mm. They are higher at the top than 20mm depth which means cracks are wider at the top. If an external load is applied over the slab at an early age, these cracks will further open up. Specifically, a load applied at the edge or corner can cause severe cracks in the critical regions (where curling has started).
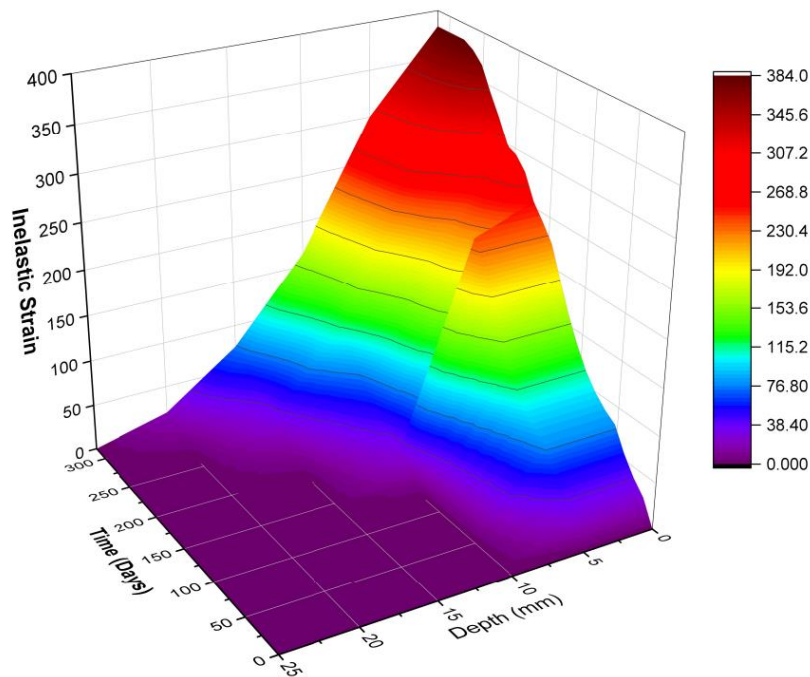
Figure 5.8 Inelastic strain distribution along the depth at the centre of the slab.
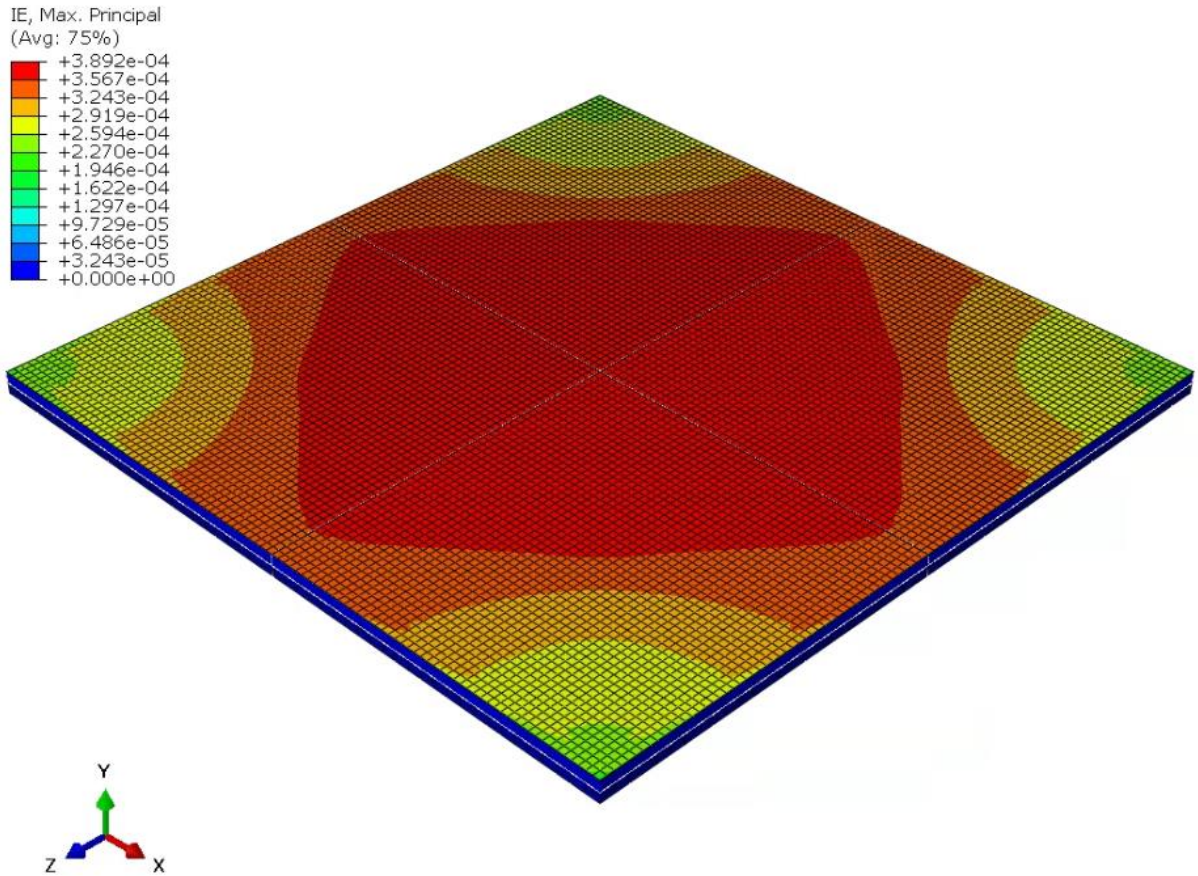
Figure 5.9 Inelastic strain distribution at the top of the slab.

5.5.3.3   Curling Stresses

Fig. 5.10 shows the curling stress distribution along the depth at the corner of the slab. At the top, after 13 days of drying, the stress reaches a maximum value of 4 MPa and then redistributes along the depth. As for the prisms in Chapter 4, this redistribution happens as the drying front travels from the top surface towards the core of the slab.
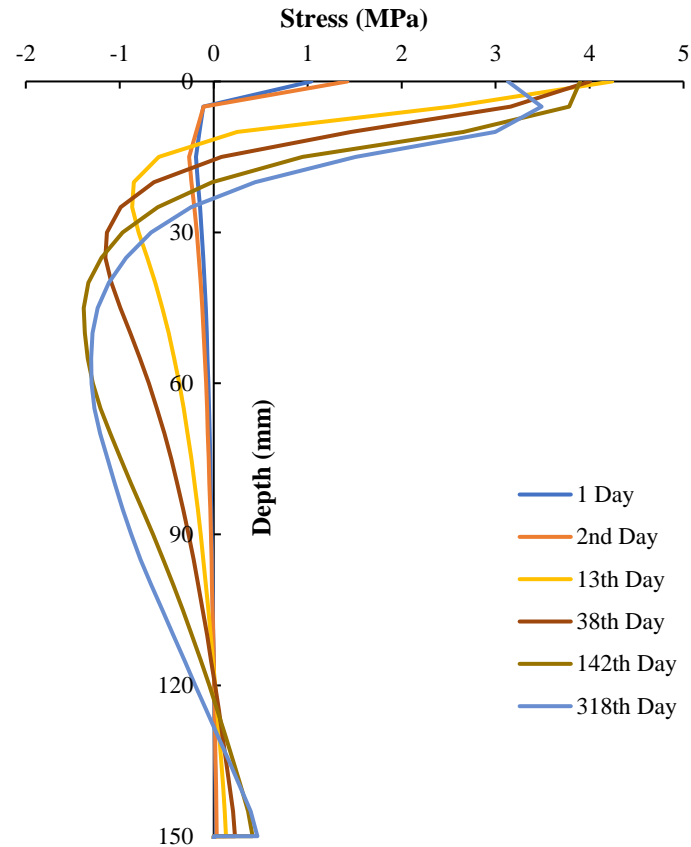
Figure 5.10 Stress distribution with time (in Days) along the depth at the corner.

Figs. 5.11, 5.12 and 5.13 show 3D stress distribution at the centre, the midpoint of the edge and the corner of the slab. The stress values drop at the top after reaching the maximum value, thus confirming cracking, but as the IEs are low, these cracks are likely to be small. The figures also show that tensile stresses travel along the depth up to 50mm, 40mm and 20mm at the centre, edge and corner, respectively. The slab's bottom half mainly has compression at the centre and edge. While underneath the corner, tensile stresses increase with time but are not high enough to cause cracking. However, they can cause cracking if drying continues for a long time and if a load is applied at the corner.
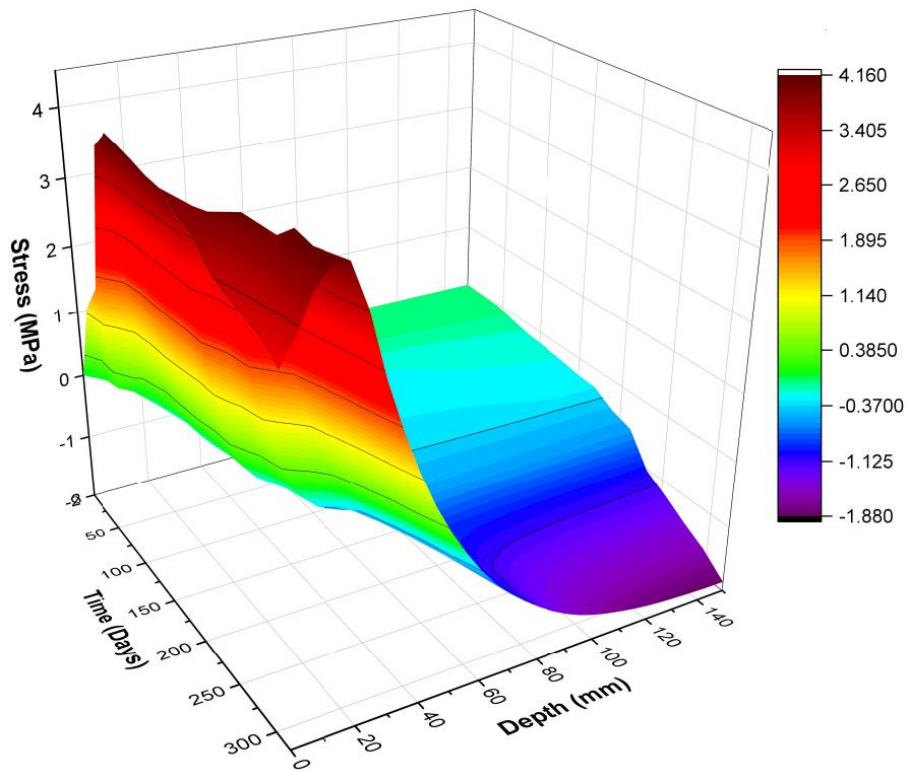
Figure 5.11 3D stresses distributions at the centre of the slab.
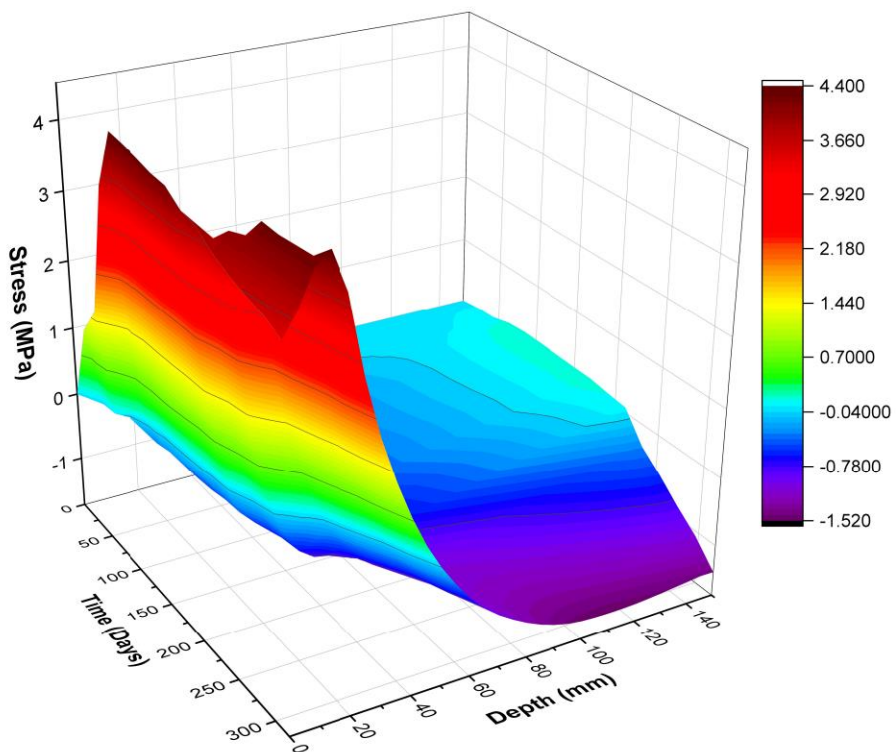
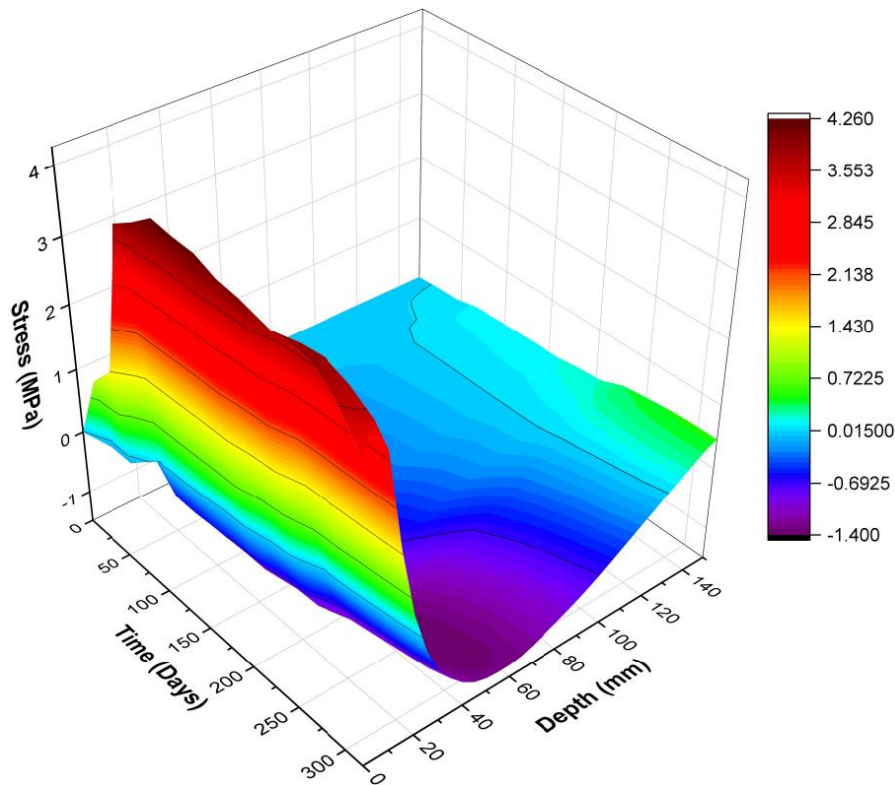Figure 5.12 3D stresses distributions at the midpoint of the edge of the slab.

Figure 5.13 3D stresses distributions at the corner of the slab.

5.6 Summary

Full-scale modelling of SoG based on the calibrated diffusion and shrinkage parameters is performed in this chapter as a case study. The modelling results show that only non-uniform drying can cause cracking on the top surface and 10mm curling of the corners of the slab. If this drying shrinkage is further coupled with structural loading (i.e., hygro-mechanical-structural analysis), the loading will cause serious macro cracking in the critical regions. Further analysis shows that curling stresses are of the magnitude of 4 MPa in critical areas.

The experimental shrinkage observed in F40 concrete (with 20168 MPa stiffness) is in the order of 352με and 272 με (including autogenous shrinkage) at the top and bottom of the prisms, respectively. Based on TR 34 (2003) formulations (see Eqs. (5.7) and (5.8)), this shrinkage can induce 1.2 to 1.5 MPa shrinkage stresses and 1.4 MPa curling stresses without creep. The numerical prediction shows that the induced stresses are of the magnitude of 4 MPa, which is much higher than TR 34's estimation. These tensile stresses travel from the top up to 50mm

121

inside the slab, but they might further penetrate when external loading is applied to the slab. Therefore, it is highly recommended to consider these stresses in the design of the SoG, specifically in the critical regions which are more prone to cracking.

In the numerical modelling, the intrinsic creep is ignored, as previous studies show that it releases 50% of the elastic strains before cracking in the highly distressed regions, which are around 7% of the total strains. This relaxation can result in 7% fewer induced stresses in the numerical predictions. However, further studies are still required to model the SoG with an evaluation of the concrete stiffness and CDP material model parameters. These parameters are time-dependent, so they can affect the behaviour of the early-age concrete. In addition, parametric studies on friction between the slab and sub-base, properties of the sub-base and subgrade will yield a better prediction of the behaviour of SoG.

Chapter 6: Conclusions and Recommendations for Future Research

6.1 Conclusions

This research aimed to quantify the moisture and shrinkage distribution in RTSF-reinforced concrete. A state-of-the-art literature review was carried out to investigate the parameters which cause non-uniform moisture distribution in the concrete. Based on the identified parameters, a modified diffusion model was generated and calibrated using humidity data from the literature. The diffusion model was validated using experimental data obtained from extensive lab work. For almost a year, moisture in terms of relative humidity and shrinkage was monitored in prisms. Finally, numerical modelling of moisture and shrinkage was performed on 3D full-scale slab-on-grade to investigate the drying shrinkage performance of the slab. The main findings of this work are summarized below.

6.1.1 Instrumentation and Pilot Study (Chapter 2)

- The RH sensor installation methodology worked effectively. Inserting steel rods in concrete moulds to create voids results in a rich cement paste at the bottom of the hole, hence preventing moisture movement. The rich cement layer needs to be roughened before sensor installation.

- The ambient temperature and temperature inside the concrete are proportional. No temperature gradient is observed in the specimens.

- Changes in ambient humidity affect RH at shallow depths more than at the core of the concrete.

- Moisture distribution is highly non-linear whether drying is 1D or 3D. 1D drying is slower than 3D due to boundary conditions and the complex nature of the pore distribution.

- Both ambient temperature and humidity affect drying shrinkage. As temperature increases, shrinkage slows down due to thermal expansion. Lower ambient humidity

causes a higher humidity gradient between the environment and concrete, resulting in faster diffusion and more drying shrinkage.

6.1.2 Numerical Determination of Moisture Diffusivity in Concrete (Chapter 3)

- The diffusion coefficient increases significantly with increasing w/c ratio, and temperature, while it decreases marginally with concrete maturity.

- The material parameters proposed by Model Code-10 can lead to a large underestimation of shrinkage strains. As a result, the magnitude and extent of shrinkage-induced phenomena, such as the development of cracking and curling stresses and deterioration phenomena, can be largely underestimated, for example, for slabs-on-grade.

- A modified model is proposed to accurately assess moisture profiles for different temperatures (up to 80 °C), concrete maturity and w/c ratios. The model can be easily implemented in current practice to carry out a more reliable assessment of crack development and structural performance of drying concrete elements.

6.1.3 Hygro-mechanical Analysis of Drying Shrinkage of Recycled Tyre Steel Fibre Reinforced Concrete (Chapter 4)

- Plain and fibre reinforced concrete dry similarly with slightly faster diffusion in SFRC mixes, possibly due to more entrained air. However, 1D diffusion is slower than 3D diffusion in all the mixes. The faster diffusivity is due to different boundary conditions and non-uniform pore and aggregate distribution.

- Numerical analysis can predict with high accuracy the moisture distribution if the appropriate diffusion coefficient is used. Coupling the hygral model with the mechanical model (i.e., hygro-mechanical analysis) yields a better prediction of shrinkage strains.

- Plain concrete shrinks faster than SFRC mixes. It is likely that fibres provide additional restraint to shrinkage.

- Differential shrinkage is higher in plain concrete than in SFRC mixes. Aggregates in plain mixes tend to settle at the bottom more, resulting in denser concrete in the bottom half of the prism. The non-uniform distribution of aggregates causes non-uniform shrinkage. In SFRC mixes, fibres prevent the aggregates from settling down, resulting in less additional shrinkage curvatures.

- Design codes underestimate autogenous shrinkage and do not consider the effect of differential shrinkage. Non-uniform shrinkage can cause additional stresses that can lead to higher stresses and deformations in structural members. Structural members such as SoG, which usually dry from the top only, are more prone to shrinkage cracks and curling deformations (i.e., lifting up of edges).

6.1.4 State-of-the-Art Review of Slabs-on-Grade and Numerical Modelling (Chapter 5)

- Coupling moisture with mechanical modelling yields a reliable assessment of the drying shrinkage performance of the SoG.

- Drying shrinkage alone can induce tensile stresses reaching the tensile strength (4 MPa) at the drying surface; with time, these stresses penetrate inside the slab (up to 50 mm at the centre). Induced stresses can easily cause cracking at the top surface first and then travel inside the concrete (up to 20 mm and 40 mm depth at corner and edge, respectively.

- Due to differential shrinkage, the edges and corners of the slab curl up by 3.46 mm and 10 mm, respectively. The maximum curling occurs at 119 days, and then it drops slowly due to cracking in the critical regions.

- The updated UK design guidelines (i.e., Concrete Society's Technical Report 34) ignore the curling stresses in the slab entirely. However, the numerical analysis shows that differential shrinkage induces curling stresses which causes cracking and lifting of the exterior edges of the slab. These stresses will further increase once the slab experience external static or dynamic loading. Thus it is highly recommended to consider these stresses when designing the slabs, specifically in critical regions.

6.2 Recommendation for Future Work

This study focuses on the drying shrinkage performance of RTSF-reinforced concrete. Initially, the drying shrinkage performance of both lab specimens and full-scale industrial ground floors (i.e., SoG) was planned to be investigated. However, due to disruptions caused by the Covid-19 pandemic and the closure of the labs, it was impossible to physically monitor full-scale slabs in the field. Therefore, this work is mainly based on small-scale lab specimens. Although the drying of concrete and its shrinkage is a long-term phenomenon, the lab specimens are monitored for up to 330 days due to the limitation of time, which is enough to get the overall drying trend in the concrete.

To complement this work, the aspects discussed below should be examined further.

6.2.1 Parametric study on moisture distribution and shrinkage

- The modified diffusion model is calibrated based on limited available humidity data. Only three parameters (concrete maturity, w/c ratio, and ambient conditions) are considered in this study. This work can be extended by considering the effect of aggregate amount, superplasticizers, and different types of cement.

- Only fibre dosage and its effect are considered on moisture and shrinkage distribution in the concrete. This can be further extended by considering different concrete mixes varying from normal concrete to high-strength concretes.

126

- This study monitored drying and autogenous free shrinkage in the 1D prisms with holes of different depths along the length. However, shrinkage in SoG is 2D, so shrinkage should be monitored along both dimensions (i.e., length and width), possibly in the field on full-scale slabs or in controlled laboratory conditions on large-scale prototype slabs (e.g., with different ground conditions and with or without polyethene sheet between the slab and the subgrade to mimic real site conditions).

- The design codes under-predict autogenous shrinkage and do not consider differential shrinkage. The experimental results show that the shrinkage at the top surface is always higher than at the bottom and this gradient decreases with increasing fibre dosage. However, these findings are only based on a selected concrete mix design. Different mixes should be examined to gain a more in-depth understanding of the relationship between shrinkage, curvature and concrete strength.

- Differential shrinkage and curvature are attributed to non-uniform drying and aggregate distribution. Non-uniform drying is monitored in this study, but the effect of aggregate distributions still needs quantification.

6.2.2 Full-scale field measurements and modelling

- In this study, RH and shrinkage are monitored in controlled lab conditions. However, field conditions vary, as do ambient conditions. RH field measurements on full-scale SoG are required to further validate the proposed modified diffusion model.

- Numerical modelling can be performed on different sizes of the SoG to investigate the effect of non-uniform moisture distribution and differential shrinkage on curling stresses. In addition, structural loading can also be applied to check the performance of SoG with shrinkage and without shrinkage.

- Due to non-uniform moisture distribution, SoG tends to curl up, which can induce stresses and result in cracking. The curling of edges can be monitored easily in practice using conventional laser levels. Further, it can be verified using numerical modelling.

6.2.3 Investigation of cracks in SoG

- Non-uniform moisture induces differential shrinkage in structural concrete. Shrinkage gradient causes curvature in plain and FRC concrete. This curvature is further increased due to the non-uniform distribution of aggregates. Shrinkage curvature is neglected in design codes like Eurocode and Model Code. This implies that the moment carrying capacity of SoG is overestimated, which should be reduced to counter the effect of the shrinkage gradient. In this study, numerical modelling is carried out to quantify the curvature by varying the concrete stiffness in the top layers. However, the stiffness of concrete evolves with time, and at an early age, it is significantly lower, which can easily cause cracks. Further work can be done by considering the representative stiffness evolution and aggregate distribution.

- Crack density and width can be monitored using appropriate crack-monitoring tools in full-scale field slabs. Numerical analysis can further verify this to decouple the cracking strains from the total strains.

- Experiments are also needed to determine the extent of tensile creep relaxation.

- Parametric study on slab geometry, concrete mix, different types of structural loading, subgrade stiffness and interaction between the slab and subgrade can help to understand the complex behaviour of the slabs.

References

ABAQUS (2019). CAE Dassault Systèmes Simulia Corporatio:

Abdulaziz Alsaif (2019). *Mechanical Behaviour and Long-Term Performance of Steel Fibre Reinforced Rubberised Concrete*, The University of Sheffield.

Abyaneh, S.D. (2015). *Modelling the effect of microcracks on transport properties of concrete*, Imperial College London.

Abyaneh, S.D., Wong, H.S., and Buenfeld, N.R. (2015). "Modelling the Effect of Microcracks on the Transport Properties of Concrete in Three Dimensions." *CONCREEP 2015: Mechanics and Physics of Creep, Shrinkage, and Durability of Concrete and Concrete Structures - Proceedings of the 10th International Conference on Mechanics and Physics of Creep, Shrinkage, and Durability of Concrete and Concrete Structure*, Vienna, Austria, p. 377–386.

Abyaneh, S.D., Wong, H.S., and Buenfeld, N.R. (2013). "Modelling the transport properties of concrete from three-dimensional mesostructure." *TRANSCEND*, Guildford, UK.

Abyaneh, S.D., Wong, H.S., and Buenfeld, N.R. (2016). Simulating the effect of microcracks on the diffusivity and permeability of concrete using a three-dimensional model: *Computational Materials Science*, Vol. 119, pp. 130–143, DOI: 10.1016/j.commatsci.2016.03.047.

ACI-325 (1956). Design Considerations for Concrete Pavement Reinforcement for Crack Control: *ACI Journal Proceedings*, Vol. 53, No. 4, pp. 337–362.

ACI-360R (2006). Design of Slabs-on-Ground.:

ACI-360R (2010). Design of Slabs-on-Ground - ACI 360R-10.:

ACI Committee 209 (2008). Guide for Modeling and Calculating Shrinkage and Creep in Har~ened Concrete I-Background 1.2-Scope 1.3-Basic assumptions for development of prediction models.:

Akita, H., Fujiwara, T., and Ozaka, Y. (1997). A practical procedure for the analysis of moisture transfer within concrete due to drying: *Magazine of Concrete Research*, Vol. 49, No. 179, pp. 129–137, DOI: 10.1680/macr.1997.49.179.129.

Al-Kamyani, Z.S. (2018). *PhD thesis on Controlling Shrinkage and Crack Widths in RC Structures Using Sustainable Construction Materials*, The University of Sheffield.

Al-Kamyani, Z., Figueiredo, F.P., Hu, H., Guadagnini, M., and Pilakoutas, K. (2018a). Shrinkage and flexural behaviour of free and restrained hybrid steel fibre reinforced concrete: *Construction and Building Materials*, Vol. 189, pp. 1007–1018, DOI: 10.1016/j.conbuildmat.2018.09.052.

Al-Kamyani, Z., Guadagnini, M., and Pilakoutas, K. (2018b). Predicting shrinkage induced curvature in plain and reinforced concrete: *Engineering Structures*, Vol. 176, pp. 468–480, DOI: 10.1016/J.ENGSTRUCT.2018.09.034.

Al-Kamyani, Z., Guadagnini, M., and Pilakoutas, K. (2018c). Predicting shrinkage induced curvature in plain and reinforced concrete: DOI: 10.1016/j.engstruct.2018.09.034.

Alshammari, T.O., Pilakoutas, K., and Guadagnini, M. (2023). Performance of Manufactured and Recycled Steel Fibres in Restraining Concrete Plastic Shrinkage Cracks: *Materials*, Vol. 16, No. 2, p. 713, DOI: 10.3390/ma16020713.

Altoubat, S.A., and Lange, D.A. (2002). The Pickett effect at early age and experiment separating its mechanisms in tension: *Materials and Structures*, Vol. 35, No. 4, pp. 211–

218, DOI: 10.1007/BF02533082.

Alvaredo, A.M. (1995). "Crack Formation Under Hygral or Thermal Gradients." *Fracture mechanics of concrete structures (FraMCoS2)*, Wittmann F ed., Zürich, Switzerland, p. 1423–1441.

Andrew, R.M. (2018). Global CO2 emissions from cement production: *Earth System Science Data*, Vol. 10, pp. 195–217, DOI: 10.5194/essd-10-2213-2018.

Aquino, W., Hawkins, N.M., and Lange, D.A. (2004). Moisture distribution in partially enclosed concrete: *ACI Materials Journal*, Vol. 101, No. 4, pp. 259–265, DOI: 10.14359/13357.

Arfvidsson, J., and Claesson, J. (2000). Isothermal moisture flow in building materials: Modelling, measurements and calculations based on Kirchhoff's potential: *Building and Environment*, Vol. 35, No. 6, pp. 519–536, DOI: 10.1016/S0360-1323(99)00045-1.

ASTM (2019). ASTM F2170-19a Standard Test Method for Determining Relative Humidity in Concrete Floor Slabs Using in situ Probes.:

ASTM C157/157C (2008). "ASTM C157/C157M-08 – Standard Test Method for Length Change of Hardened Hydraulic-Cement Mortar and Concrete." *Annual Book of ASTM Standards*, ASTM International, p. 1–7.

Ayano, T., Sakta, K., and Wittmann, F.H. (1999). Moisture distribution, diffusion coefficient and shrinkage of cmenet-based materials: *Journal of Materials, Construction, Structure and Pavements*, Vol. 45, No. 634, pp. 387–401.

Ayano, T., and Wittmann, F.H. (2002). Drying, moisture distribution, and shrinkage of cement-based materials: *Materials and Structures*, Vol. 35, No. 3, pp. 134–140.

131

Bakhshi, M., Mobasher, B., and Soranakom, C. (2012). Moisture loss characteristics of cement-based materials under early-age drying and shrinkage conditions: *Construction and Building Materials*, Vol. 30, pp. 413–425, DOI: 10.1016/j.conbuildmat.2011.11.015.

Bazant, Z.P., and Chern, J.-C. (1985). Log Double Power Law for Concrete Creep:

Bažant, Z.P., and Najjar, L.J. (1971). Drying of concrete as a nonlinear diffusion problem: *Cement and Concrete Research*, Vol. 1, No. 5, pp. 461–473, DOI: 10.1016/0008-8846(71)90054-8.

Bažant, Z.P., and Najjar, L.J. (1972). Nonlinear water diffusion in nonsaturated concrete: *Materials and Structures*, Vol. 5, No. 25, pp. 3–20, DOI: 10.1007/BF02479073.

Bazant, Z.P., and Thonguthai, W. (1978). Pore pressure and drying of concrete at high temperature: *ASCE Journal of the Engineering Mechanics Division*, Vol. 104, No. 5, pp. 1059–1079.

Bentz, D.P., and Jensen, O.M. (2004). Mitigation strategies for autogenous shrinkage cracking: *Cement and Concrete Composites*, Vol. 26, No. 6, pp. 677–685, DOI: 10.1016/S0958-9465(03)00045-3.

Bishop, J.W. (2001). *The early age behaviour of concrete industrial ground floor slabs*, Loughborough Univerisity, UK.

Carlson, R.W. (1937). Drying shrinkage of large concrete members: *ACI Journal Proceedings*, Vol. 33, No. 1, pp. 327–336, DOI: 10.14359/8421.

CEN (2004). *Eurocode 2: Design of concrete structures, Part 1-1: Materials*.

Cook, R.A., and Hover, K.C. (1999). Mercury porosimetry of hardened cement pastes: *Cement and Concrete Research*, Vol. 29, No. 6, pp. 933–943, DOI: 10.1016/S0008-8846(99)00083-6.

Copeland, L.E., and Bragg, R.H. (1955). "Self-desiccation in portland cement pastes." *Proc. of American Society of Testing Materials*,.

Destrée, X., Yao, Y., and Mobasher, B. (2016). Sequential Cracking and Their Openings in Steel-Fiber-Reinforced Joint-Free Concrete Slabs: *Journal of Materials in Civil Engineering*, Vol. 28, No. 4, pp. 1–2, DOI: 10.1061/(ASCE)MT.1943-5533.0001377.

Donald J. Janssen (1986). Moisture in Portland Cement Concrete.:

Eisemann, J., and Leykauf, G. (1990). "Simplified Calculation of Slab Curling Caused by Surface Shrinkage." *2nd International Workshop on the Theoretical Design of Concrete Pavements*, PIARC Committee on Concrete Roads, Spain, p. 185–197.

EN, B.S. (2002). BS EN 12617-4:2002. Products and systems for the protection and repair of concrete structures-test methods-Part 4: Determination of shrinkage and expansion: *Br Stand Inst. London*,.

EN 12390, B. standard (2009). Testing hardened concrete - Part 3: Compressive strength of test specimens.:

Endait, M., and Wagh, S. (2020). Effect of elevated temperature on mechanical properties of early-age concrete: *Innovative Infrastructure Solutions*, Vol. 5, No. 1, pp. 1–8, DOI: 10.1007/s41062-019-0254-8.

ETRA (2010). The European Tyre Recycling Association (ETRA), Introduction to tyre recycling.:

fib (2013a). "Materials." *fib Model Code for Concrete Structures 2010*, Wiley-VCH Verlag GmbH & Co. KGaA, Weinheim, Germany, p. 74–150.

fib (2013b). "Materials." *fib Model Code for Concrete Structures 2010*, Wiley Online Books, Wiley-VCH Verlag GmbH & Co. KGaA, Weinheim, Germany, p. 74–150.

Gardner, C.-E.N.J., and Weiss, J. (2005). SP-227: Shrinkage and Creep of Concrete.:

Gilbert, I. (2001). Shrinkage, Cracking and Deflection-the Serviceability of Concrete Structures: *Electronic Journal of Structural Engineering*, Vol. 1, No. 1, pp. 15–37, DOI: 10.56748/ejse.1121.

Goel, R., Kumar, R., and Paul, D.K. (2007). Comparative Study of Various Creep and Shrinkage Prediction Models for Concrete: *Journal of Materials in Civil Engineering*, Vol. 19, No. 3, pp. 249–260, DOI: 10.1061/(asce)0899-1561(2007)19:3(249).

Graeff, Â.G. (2011). *PhD thesis on Long-Term Performance of Recycled Steel Fibre Reinforced Concrete for Pavement Applications*, The University of Sheffield.

Granger, L. (1995). *Comportement différé du béton dans les enceintes de centrales nucléaires. Démarche d'analyse et modélisation*.

Grasley, Z.C., Lange, D.A., and D'ambrosia, M.D. (2006). Internal relative humidity and drying stress gradients in concrete: *Materials and Structures*, Vol. 39, pp. 901–909, DOI: 10.1617/s11527-006-9090-3.

Gribniak, V., Kaklauskas, G., and Bacinskas, D. (2007). State-of-art Review on Shrinkage Effect on Cracking and Deformations of Concrete Bridge Elements: *Baltic journal of road and bridge engineering*, Vol. 2, No. 4, pp. 183–193.

Gribniak, V., Kaklauskas, G., Kliukas, R., and Jakubovskis, R. (2013). Shrinkage effect on
short-term deformation behavior of reinforced concrete – When it should not be
neglected: *Materials & Design*, Vol. 51, pp. 1060–1070, DOI:
10.1016/j.matdes.2013.05.028.

Hammond, G.P., and Jones, C.I. (2008). Embodied energy and carbon in construction
materials: *Proceedings of the Institution of Civil Engineers - Energy*, Vol. 161, No. 2,
pp. 87–98, DOI: 10.1680/ener.2008.161.2.87.

Hiller, J., and Roesler, J. (2010). Simplified Nonlinear Temperature Curling Analysis for
Jointed Concrete Pavements: *Journal of Transportation Engineering*, pp. 654–663.

Hossain, A.B., and Weiss, J. (2004). Assessing residual stress development and stress
relaxation in restrained concrete ring specimens: *Cement and Concrete Composites*, Vol.
26, No. 5, pp. 531–540, DOI: 10.1016/S0958-9465(03)00069-6.

Hu, H. (2018). *PhD thesis on Mechanical Properties of Blended Steel Fibre Reinforced
Concrete Using Manufactured and Recycled Fibres from Tyres*, The University of
Sheffield.

Hu, H., Wang, Z., Figueiredo, F.P., Papastergiou, P., Guadagnini, M., and Pilakoutas, K.
(2019). Postcracking tensile behavior of blended steel fiber-reinforced concrete:
Structural Concrete, Vol. 20, No. 2, pp. 707–719, DOI: 10.1002/suco.201800100.

Isa, M.N. (2021). *Mechanical Behaviour of Eco-Efficient Ultra- High Performance Fibre
Reinforced Concrete (E-UHPFRC) and Design of E-UHPFRC Screw Piles By
Muhammad Nura Isa*, The University of Sheffield.

Isa, M.N., Pilakoutas, K., and Guadagnini, M. (2021). Determination of tensile characteristics

and design of eco-efficient UHPC: *Structures*, Vol. 32, pp. 2174–2194, DOI: 10.1016/J.ISTRUC.2021.03.114.

Jafarifar, N. (2012). *PhD thesis on Shrinkage Behaviour of Steel Fiber Reinforced Concrete Pavements.*, The University of Sheffield.

Jafarifar, N., Pilakoutas, K., and Bennett, T. (2014). Moisture transport and drying shrinkage properties of steel-fibre-reinforced-concrete: *Construction and Building Materials*, Vol. 73, pp. 41–50, DOI: 10.1016/j.conbuildmat.2014.09.039.

Jafarifar, N., Pilakoutas, K., and Bennett, T. (2016). The effect of shrinkage cracks on the load bearing capacity of steel-fibre-reinforced roller-compacted-concrete pavements: *Materials and Structures/Materiaux et Constructions*, Vol. 49, No. 6, pp. 2329–2347, DOI: 10.1617/s11527-015-0652-0.

Jeong, J.H., Lim, J.S., Sun, R.J., and Zollinger, D.G. (2012). Modelling of differential shrinkage of pavement slabs: *Proceedings of the Institution of Civil Engineers: Transport*, Vol. 165, No. 1, pp. 3–14, DOI: 10.1680/tran.10.00020.

Jeong, J.H., Park, Y.S., and Lee, Y.H. (2015). Variation of Shrinkage Strain within the Depth of Concrete Beams: *Materials 2015, Vol. 8, Pages 7780-7794*, Vol. 8, No. 11, pp. 7780–7794, DOI: 10.3390/MA8115421.

Kang, S.T., Kim, J.S., Lee, Y., Park, Y.D., and Kim, J.K. (2012). Moisture diffusivity of early age concrete considering temperature and porosity: *KSCE Journal of Civil Engineering*, Vol. 16, No. 1, pp. 179–188, DOI: 10.1007/s12205-012-1445-4.

Kim, J.K., and Lee, C.S. (1999). Moisture diffusion of concrete considering self-desiccation at early ages: *Cement and Concrete Research*, Vol. 29, No. 12, pp. 1921–1927, DOI:

10.1016/S0008-8846(99)00192-1.

Kim, J.K., and Lee, C.S. (1998). Prediction of differential drying shrinkage in concrete: *Cement and Concrete Research*, Vol. 28, No. 7, pp. 985–994, DOI: 10.1016/S0008-8846(98)00077-5.

Klee, H. (2009). Recycling Concrete.:

Klemczak, B., and Batog, M. (2016). Heat of hydration of low clinker cements: Part II - Determination of apparent activation energy and validity of the equivalent age approach: *Journal of Thermal Analysis and Calorimetry*, Vol. 123, No. 2, pp. 1361–1369, DOI: 10.1007/s10973-015-4791-x.

Kodikara, J., and Chakrabarti, S. (2005). Modeling of moisture loss in cementitiously stabilized pavement materials: *International Journal of Geomechanics*, Vol. 5, No. 4, pp. 295–303, DOI: 10.1061/ASCE1532-364120055:4295.

Kundak, M., Lazić, L., and Črnko, J. (2009). CO2emissions in the steel industry: *Metalurgija*, Vol. 48, No. 3, pp. 193–197.

Lee, S.C., Oh, J.H., and Cho, J.Y. (2015). Compressive behavior of fiber-reinforced concrete with end-hooked steel fibers: *Materials*, Vol. 8, No. 4, pp. 1442–1458, DOI: 10.3390/MA8041442.

Leonards, G.A., and Harr, M.E. (1959a). Analysis of concrete slabs on ground: *Journal of the Soil Mechanics and Foundations Division*, Vol. 85, No. 3, pp. 35–58.

Leonards, G.A., and Harr, M.E. (1959b). Analysis of Concrete Slabs on Ground: *American Society of Civil Engineers (ASCE)*, Vol. 85, No. SM3, pp. 35–58.

Liang, S., and Wei, Y. (2019). Methodology of obtaining intrinsic creep property of concrete by flexural deflection test: *Cement and Concrete Composites*, Vol. 97, No. September 2018, pp. 288–299, DOI: 10.1016/j.cemconcomp.2019.01.003.

Losberg, B.A. (1978). Pavements and Slabs on Grade with Structurally Active Reinforcement: *ACI Journal Proceedings*, Vol. 75, No. 12, pp. 647–657, DOI: 10.14359/10977.

M. Asad, Baluch, M.H., and AI-Gadhib, A.H. (1997). Drying shrinkage stresses in concrete patch repair systems: *Magazine of Concrete Research*, Vol. 49, No. 181, pp. 283–293.

Marušić, E., and Štirmer, N. (2016). Autogenous Shrinkage and Expansion Related to Compressive Strength and Concrete Composition: *Journal of Advanced Concrete Technology*, Vol. 14, No. 9, pp. 489–501, DOI: 10.3151/jact.14.489.

Mateos, A., Harvey, J., Bolander, J., Wu, R., Paniagua, J., and Paniagua, F. (2020). Structural response of concrete pavement slabs under hygrothermal actions: *Construction and Building Materials*, Vol. 243, p. 118261, DOI: 10.1016/j.conbuildmat.2020.118261.

Meghwar, S.L., Pilakoutas, K., Torelli, G., and Guadagnini, M. (2022). Numerical Determination of Moisture Diffusivity in Concrete: *KSCE Journal of Civil Engineering*, Vol. 26, No. 9, pp. 1–13, DOI: 10.1007/s12205-022-0985-5.

Mehta, P.K. (1986). *Concrete-Structure, Properties and Materials*, Prentice-Hall.

Mensi, R., Acker, P., and Attolou, A. (1988). Séchage du béton: analyse et modélisation: *Materials and Structures*, Vol. 21, No. 1, pp. 3–12, DOI: 10.1007/BF02472523.

Meyerhof, G.G. (1960). "Bearing Capacity of Floating Ice Sheets." *Journal of the Engineering Mechanics Division Proceedings of ASCE*, ASCE, New York, p. 113–146.

Naus, D.J., and Graves, H.L. (2006). "A Review of the Effects of Elevated Temperature on Concrete Materials and Structures." *Volume 1: Plant Operations, Maintenance and Life Cycle; Component Reliability and Materials Issues; Codes, Standards, Licensing and Regulatory Issues; Fuel Cycle and High Level Waste Management*, ASMEDC, p. 615–624.

Neville, A.. (2011). *Properties of concrete*, Fifth Ed., Pearson Education Limited.

Nicholson, L.P. (1981). How to minimize cracking and increase strength of slabs on grade: *Concrete Construction*, Vol. 26, No. 9, pp. 739–741.

Nilsson, L.O. (2002). Long-term moisture transport in high performance concrete: *Materials and Structures/Materiaux et Constructions*, Vol. 35, No. 254, pp. 641–649, DOI: 10.1617/13972.

Orta, L., and Bartlett, F.M. (2014a). Free shrinkage strains in concrete overlays: *ACI Materials Journal*, Vol. 111, No. 3, pp. 263–271, DOI: 10.14359/51686566.

Orta, L., and Bartlett, F.M. (2014b). Stresses due to restrained shrinkage in concrete deck overlays: *ACI Materials Journal*, Vol. 111, No. 6, pp. 701–710, DOI: 10.14359/51687183.

Pettersson, D. (1998). *Stresses in Concrete Structures from Ground Restraint*, Lund Institute of Technology, Sweden.

Pickett, G. (1946). Shrinkage Stresses in Concrete: *Journal of the American Concrete Institute*, Vol. 17, No. 3, pp. 165–204.

Powers, T.C. (1960). Physical properties of cement paste: *Chemistry of Cement Proceedings of the Fourth International Symposium*, Vol. II, pp. 577–609.

Purnell, P. (2013). The carbon footprint of reinforced concrete: *Advances in Cement Research*, Vol. 25, No. 6, pp. 362–368, DOI: 10.1680/adcr.13.00013.

Qian, X., Yu, C., Zhang, L., Qian, K., Fang, M., and Lai, J. (2020). Influence of Superplasticizer Type and Dosage on Early-age Drying Shrinkage of Cement Paste with Consideration of Pore Size Distribution and Water Loss: *Journal Wuhan University of Technology, Materials Science Edition*, Vol. 35, No. 4, pp. 758–767, DOI: 10.1007/s11595-020-2318-1.

Qin, Y., and Hiller, J.E. (2014). Simulating moisture distribution within concrete pavement slabs: model development and sensitivity study: *Materials and Structures*, Vol. 47, No. 1–2, pp. 351–365, DOI: 10.1617/s11527-013-0065-x.

Robins, P.J., Bishop, J.W., and Austin, S.A. (2003). "Early-age finite element modelling of concrete industrial floors." *Proceedings of the Institution of Mechanical Engineers, part L: Journal of Materials: Design and Applications*,, p. 295–308.

Rollings, R.S. (1993). Curling failures of steel fiber reinforced concrete slabs: *Journal of Performance of Constructed Facilities*, Vol. 7, No. 1, pp. 3–19.

de Sa, C., Benboudjema, F., Thiery, M., and Sicard, J. (2008). Analysis of microcracking induced by differential drying shrinkage: *Cement and Concrete Composites*, Vol. 30, No. 10, pp. 947–956, DOI: 10.1016/j.cemconcomp.2008.06.015.

Saeidpour, M., and Wadsö, L. (2016). The influence of sorption hysteresis on diffusion coefficients represented with different moisture potentials: *Cement and Concrete Research*, Vol. 90, pp. 1–5, DOI: 10.1016/j.cemconres.2016.07.009.

Sakata, K. (1983). A study on moisture diffusion in drying and drying shrinkage of concrete:

Cement and Concrete Research, Vol. 13, No. 2, pp. 216–224, DOI: 10.1016/0008-8846(83)90104-7.

Scherer, G.W. (1990). Theory of drying: *Journal of the American Ceramic Society*, Vol. 73, No. 1, pp. 3–14, DOI: 10.1111/j.1151-2916.1990.tb05082.x.

Schneider, U., Diederichs, U., and Ehm, C. (1982). Effect of temperature on steel and concrete for PCRV's: *Nuclear Engineering and Design*, Vol. 67, No. 2, pp. 245–258, DOI: 10.1016/0029-5493(82)90144-3.

Shen, D., Wang, M., Chen, Y., Wang, T., and Zhang, J. (2017). Prediction model for relative humidity of early-age internally cured concrete with pre-wetted lightweight aggregates: *Construction and Building Materials*, Vol. 144, pp. 717–727, DOI: 10.1016/j.conbuildmat.2017.03.088.

Sherwood, T.K. (1929). The Drying of Solids-II: *Industrial and Engineering Chemistry*, Vol. 21, No. 10, pp. 976–980.

Smithers Rapra (2019). The Future of Tire Manufacturing to 2022: Vol. 44, No. 0, p. 703.

Suksawang, N., Wtaife, S., and Alsabbagh, A. (2018). Evaluation of elastic modulus of fiber-reinforced concrete: *ACI Materials Journal*, Vol. 115, No. 2, pp. 239–249, DOI: 10.14359/51701920.

Suprenant, B.A. (2002). Why Slabs Curl: *Concrete International*, Vol. 24, No. 3, pp. 56–61.

Takiya, H., Watanabe, N., Kozaki, T., and Sato, S. (2015). Effects of water-to-cement ratio and temperature on diffusion of water in hardened cement pastes: *Journal of Nuclear Science and Technology*, Vol. 52, No. 5, pp. 728–738, DOI: 10.1080/00223131.2014.979902.

Tang, S.B., Wang, S.Y., Ma, T.H., Tang, C.A., Bao, C.Y., Huang, X., and Zhang, H. (2016). Numerical study of shrinkage cracking in concrete and concrete repair systems: Vol. 199, pp. 229–244, DOI: 10.1007/s10704-016-0108-8.

Tlemat, I.H. (2004). *PhD thesis on Steel Fibers from Waste Tyres to Concrete; Testing, Modelling and Design*, The University of Sheffield.

Tlemat, H., Pilakoutas, K., and Neocleous, K. (2006). Modelling of SFRC using inverse finite element analysis: *Materials and Structures 2006 39:2*, Vol. 39, No. 2, pp. 221–233, DOI: 10.1617/S11527-005-9010-Y.

Torelli, G., Gillie, M., Mandal, P., Draup, J., and Tran, V.X. (2020). A moisture-dependent thermomechanical constitutive model for concrete subjected to transient high temperatures: *Engineering Structures*, Vol. 210, DOI: 10.1016/j.engstruct.2020.110170.

TR-34 (2003). Concrete industrial ground floors: Thomas Telford Publishing.

TR-34 (2013). TR34 Concrete industrial ground floors.:

Vinkler, M., and Vítek, J.L. (2017a). Drying Shrinkage of Concrete: Experiments and Numerical Models: *Solid State Phenomena*, Vol. 259, pp. 46–51, DOI: 10.4028/www.scientific.net/SSP.259.46.

Vinkler, M., and Vítek, J.L. (2017b). Drying shrinkage of concrete elements: *Structural Concrete*, Vol. 18, No. 1, pp. 92–103, DOI: 10.1002/suco.201500208.

Wagnermeters (2019a). Rapid RH 5.0:

Wagnermeters (2019b). Rapid RH L6:

Wagnermeters (2018). Smart Logger:

Wei, Y., Guo, W., and Zheng, X. (2016). Integrated shrinkage, relative humidity, strength development, and cracking potential of internally cured concrete exposed to different drying conditions: *Drying Technology*, Vol. 34, No. 7, pp. 741–752, DOI: 10.1080/07373937.2015.1072549.

Westergaard, H.M. (1925). Computation of stresses in concrete roads: *Proceedings of the fifth annual meeting of the Highway Research Board*, Vol. 5, No. 1, pp. 90–112.

Westergaard, H.M. (1926). Stresses in Concrete Pavements Computed by Theoretical Analysis: *Public Roads*, Vol. 7, No. 2.

Winkler, E. (1867). *Die Hehre von der Elastizitat und Festigkeit'' (The Theory of Elasticity and Stiffness)*, Dominicus, Prague.

Wittmann, X., Sadouki, H., and Wittmann, F.H. (1989). "Numerical evaluation of drying test data." *Transactions of the 10th international conference on structural mechanics in reactor technology,*, p. 71–79.

Xin, D., Zollinger, D.G., and Allen, G.D. (1995). An approach to determine diffusivity in hardening concrete based on measured humidity profiles: *Advanced Cement Based Materials*, Vol. 2, No. 4, pp. 138–144, DOI: 10.1016/1065-7355(95)90014-4.

Xu, Q., Ruiz, J.M., Chang, G.K., Rasmussen, R.O., and Rozycki, D.K. (2009). Moisture transport model for enhancing FHWA HIPERPAV predictions: *Transportation Research Record*, Vol. 2113, No. 2113, pp. 1–12, DOI: 10.3141/2113-01.

Yoo, D.Y., Min, K.H., Lee, J.H., and Yoon, Y.S. (2011). Autogenous shrinkage of concrete with design strength 60-120 N/mm 2: *Magazine of Concrete Research*, Vol. 63, No. 10, pp. 751–761, DOI: 10.1680/macr.2011.63.10.751.

Younis, K.H. (2014). *PhD thesis on Restrained Shrinkage Behaviour of Concrete with Recycled Materials*, The University of Sheffield.

Younis, K.H., and Pilakoutas, K. (2016). Assessment of Post-Restrained Shrinkage Mechanical Properties of Concrete: *ACI Materials Journal*, Vol. 113, No. 3, pp. 267–276, DOI: 10.14359/51688699.

Ytterberg, R.F. (1987a). Shrinkage and Curling on Slab on Grade-part-1: *Concrete International*, Vol. 9, No. 4, pp. 22–31.

Ytterberg, R.F. (1987b). Shrinkage and Curling on Slab on Grade-part-2: *Concrete International*, Vol. 9, No. 5, pp. 54–61.

Ytterberg, R.F. (1987c). Shrinkage and Curling on Slab on Grade-part-3: *Concrete International*, Vol. 9, No. 6, pp. 72–81.

Zhang, J., Dongwei, H., and Wei, S. (2010). Experimental study on the relationship between shrinkage and interior humidity of concrete at early age: *Magazine of Concrete Research*, Vol. 62, No. 3, pp. 191–199, DOI: 10.1680/macr.2010.62.3.191.

Zhang, J., Han, Y.D., Gao, Y., and Luosun, Y. (2013a). Integrative Study on the Effect of Internal Curing on Autogenous and Drying Shrinkage of High-Strength Concrete: *Drying Technology*, Vol. 31, No. 5, pp. 565–575, DOI: 10.1080/07373937.2012.745869.

Zhang, J., Hou, D., and Gao, Y. (2013b). Calculation of Shrinkage Stress in Early-age Concrete Pavements. I: *Journal of Transportation Engineering*, pp. 961–970.

Zhang, M.H., Tam, C.T., and Leow, M.P. (2003). Effect of water-to-cementitious materials ratio and silica fume on the autogenous shrinkage of concrete: *Cement and Concrete Research*, Vol. 33, No. 10, pp. 1687–1694, DOI: 10.1016/S0008-8846(03)00149-2.

Zhang, J., Wang, J., and Ding, X. (2018). Calculation of shrinkage stress in concrete structures with impact of internal curing: *Engineering Fracture Mechanics*, Vol. 192, pp. 54–76, DOI: 10.1016/j.engfracmech.2018.02.002.

Zhang, J., Wang, Q., and Zhang, J. (2017). Shrinkage of internal cured high strength engineered cementitious composite with pre-wetted sand-like zeolite: *Construction and Building Materials*, Vol. 134, pp. 664–672, DOI: 10.1016/j.conbuildmat.2016.12.182.

Zhang, J., Yuan Gao, ;, and Han, Y. (2012). Interior Humidity of Concrete under Dry-Wet Cycles: *Journal of Materials in Civil Engineering*, Vol. 24, No. 3, pp. 289–298.

Zhou, J., Chen, X., Zhang, J., and Wang, Y. (2011). Internal relative humidity distribution in concrete considering self-desiccation at early ages: *International Journal of the Physical Sciences*, Vol. 6, No. 7, pp. 1604–1610, DOI: 10.5897/IJPS11.108.

Appendix A: Sensor Calibration Certificates

This appendix provides the *Rapid RH 5.0* and *Rapid RH L6* sensor calibration certificates.

These sensors have 1.2% to 2% and 1.8% to 3% traceable accuracy for RH measurements of 0-90% and 90-100%, respectively.

SENSIRION
THE SENSOR COMPANY

Calibration Certification

Name and address of the manufacturer: **Sensirion AG**
Laubisruetistrasse 50
CH-8712 Switzerland

Description: Digital Humidity- and Temperature Sensors

- SHT1x
- SHT3x
- SHTC1
- STS21

- SHT2x
- SHT7x
- SHTW1
- STSC1

The above mentioned products are calibrated to meet the specifications according to the corresponding Sensirion data sheet. Each device is individually tested after its calibration.

Sensirion uses transfer standards for the calibration. These transfer standards are themselves subject to a scheduled calibration procedure. The calibration of the reference itself used for the calibration of the transfer standards is performed by an ISO/IEC 17025 accredited laboratory.

The accreditation body is full member of the International Laboratory Accreditation Cooperation (www.ilac.org). Calibration certificates issued by facilities accredited by a signatory to the ILAC Mutual Recognition Arrangement (MRA) are accepted by all signatories to the ILAC MRA.

This provides traceability of measurement to recognized national standards and to units of measurement realized at the "National Physical Laboratory" (NPL) or other recognized national standards laboratories like "Physikalisch-Technische Bundesanstalt" (PTB) or "National Institute of Standards and Technology" (NIST).

Staefa, November 2015
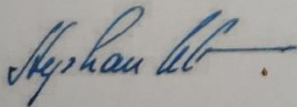
Stephan Weber,
Director,
Head of Quality Management, Sensirion AG
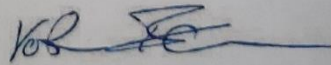
Volker Born
Manager,
Head of Quality Engineering, SensirionAG

Appendix B: RTSF Testing Results

This appendix presents the tensile test results of recycled tyre steel fibers (RTSF) collected at equally spaced intervals during a single production shift. Each sample comprised ten specimens. All specimens included in the report failed within the gauge length. The results from specimens that failed at the grip have been ignored.

Individual fibers from 11 samples of RTSF, each comprising 10 specimens for a total of 110 specimens, were tested in tension. The mean strength and diameter (Diam) of all samples were found to be 2909 MPa, with a standard deviation of 166 MPa and 0.32mm, with a standard deviation of 0.036mm, respectively.

B. 1   Experimental Setup

The tests were performed in accordance with EN ISO 6892-1:2016, except as indicated below.

The test setup is illustrated in Figure B.1. Test pieces with a minimum gauge length of 20 mm were mounted on countersunk snubbing grips with a 1mm radius to increase the probability of failure occurring at the free length of the specimen and produce valid test results. The results from specimens that failed at the grip were ignored. The initial cross-sectional area of each specimen was calculated from the arithmetic mean of two measurements carried out in two perpendicular directions to an accuracy of 0.01mm using a digital micrometre with knife edges.

All tests were performed under displacement control at a displacement rate of 2 mm/min.

Figure B.1 Tensile test setup.

B. 2 Test Results
B.2.1 Sample 1

Table B.1 summarises the main results in terms of diameter, maximum load and tensile strength

for all specimens in Sample 1. Figure B.2 shows the individual tensile strength results against

the mean strength (solid black line), which for Sample 1 is 2627 MPa (standard deviation 355

MPa).

Table B.1 Diameter measurements, maximum load and tensile strength results for Sample 1.

|	Specimen ID	Diam 1 (mm)	Diam 2 (mm)	Mean Diam (mm)	Max Load (N)	Tensile strength (MPa)
Sample 1	G1	0.360	0.361	0.361	191.5	1876
	G2	0.319	0.332	0.326	236.1	2837
	G4	0.332	0.331	0.332	198.1	2295
	G7	0.348	0.346	0.347	270.6	2861
	G10	0.351	0.347	0.349	258.6	2703
	G11	0.316	0.318	0.317	229.3	2905
	G12	0.330	0.329	0.330	230.1	2698
	G13	0.315	0.323	0.319	198.5	2483
	G15	0.332	0.333	0.333	217.0	2499
	G16	0.332	0.338	0.335	274.3	3112
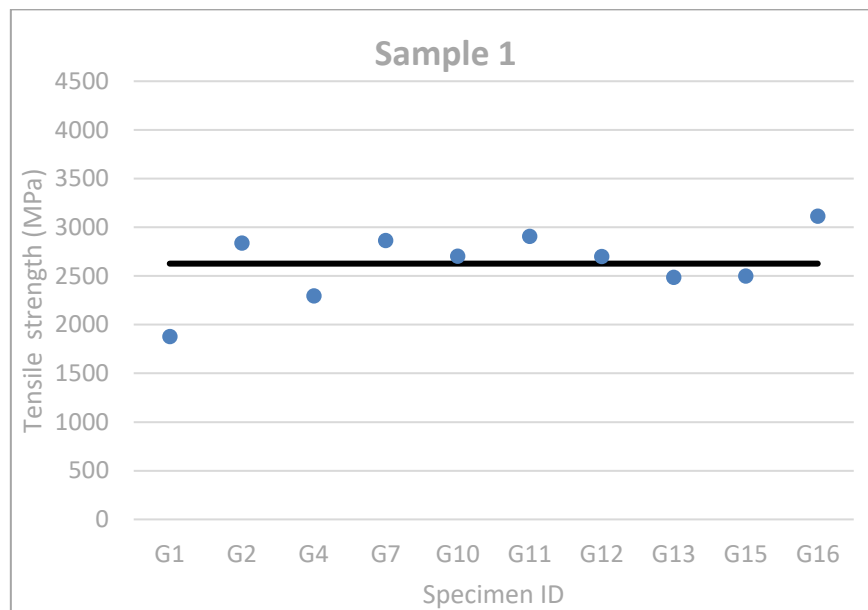
Figure B.2 Individual tensile strength results and a mean value for Sample 1.

B.2.2 Sample 2

Table B.2 summarises the main results in terms of diameter, maximum load and tensile strength for all specimens in Sample 2. Figure B.3 shows the individual tensile strength results against the mean strength (solid black line), which for Sample 2 is 3073 MPa (standard deviation 263 MPa).

Table B.2 Diameter measurements, maximum load and tensile strength results for Sample 2.

|	Specimen ID	Diam 1 (mm)	Diam 2 (mm)	Mean Diam (mm)	Max Load (N)	Tensile strength (MPa)
Sample 2	G17	0.325	0.327	0.326	229.5	2749
	G18	0.331	0.334	0.333	248.5	2862
	G19	0.326	0.325	0.326	257.8	3098
	G20	0.318	0.315	0.317	251.4	3195
	G21	0.225	0.220	0.223	122.0	3136
	G23	0.320	0.322	0.321	261.2	3227
	G24	0.325	0.322	0.324	248.7	3026
	G25	0.329	0.334	0.332	270.4	3133
	G27	0.196	0.197	0.197	109.3	3603
	G28	0.340	0.333	0.337	239.9	2698
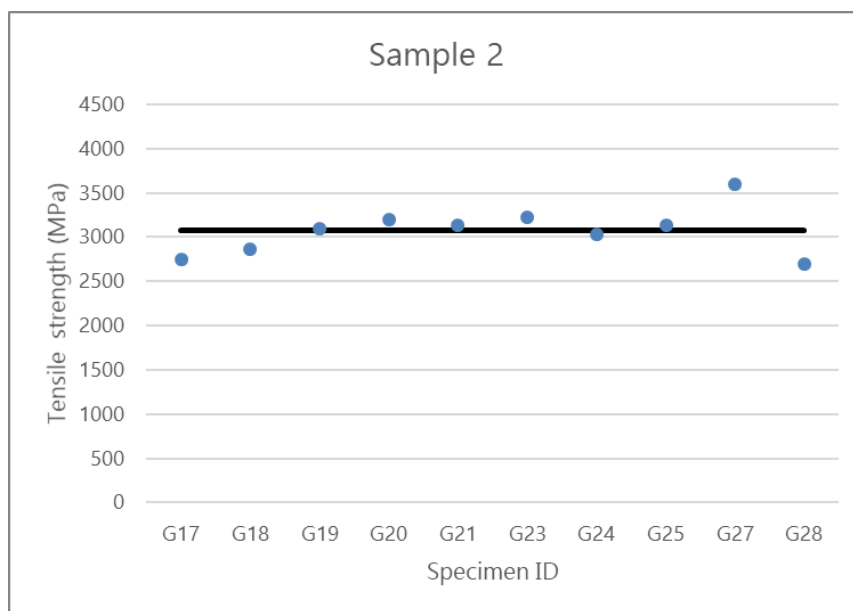
Figure B.3 Individual tensile strength results and a mean value for Sample 2.

151

B.2.3   Sample 3

Table B.3 summarises the main results in terms of diameter, maximum load and tensile strength for all specimens in Sample 3. Figure B.4 shows the individual tensile strength results against the mean strength (solid black line), which for Sample 3 is 2835 MPa (standard deviation 305 MPa).

Table B.3 Diameter measurements, maximum load and tensile strength results for Sample 3.

	Specimen ID	Diam 1 (mm)	Diam 2 (mm)	Mean Diam (mm)	Max Load (N)	Tensile strength (MPa)
Sample 3	G29	0.324	0.329	0.327	249.2	2977
	G30	0.323	0.318	0.321	241.6	2995
	G31	0.320	0.320	0.320	198.5	2467
	G33	0.327	0.313	0.320	199.5	2480
	G34	0.333	0.337	0.335	222.4	2523
	G35	0.333	0.332	0.333	244.4	2814
	G36	0.330	0.329	0.330	221.4	2597
	G38	0.311	0.320	0.316	235.2	3008
	G40	0.300	0.316	0.308	246.6	3310
	G41	0.318	0.309	0.314	245.7	3183
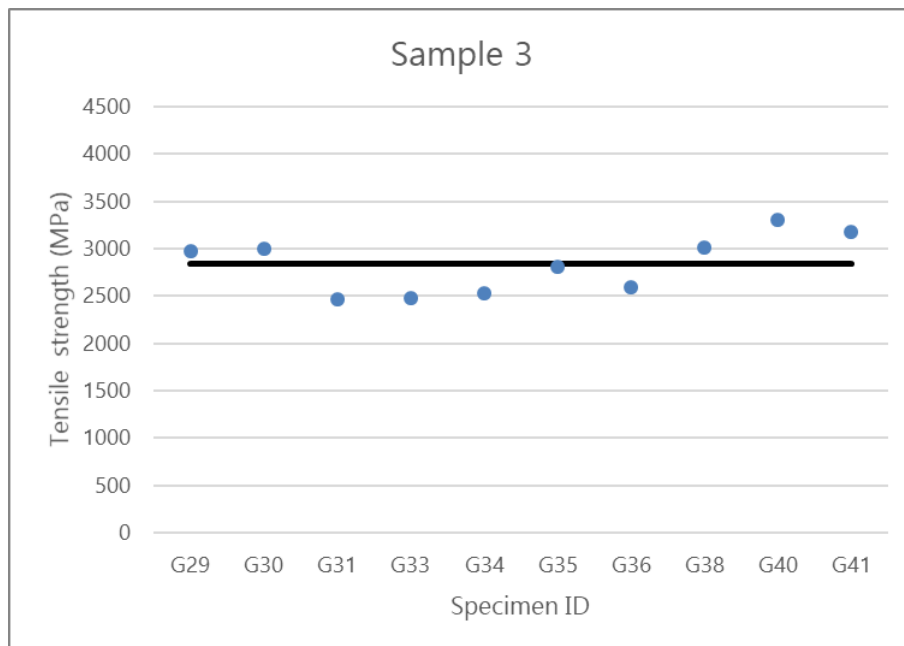
Figure B.4 Individual tensile strength results and a mean value for Sample 3.

152

B.2.4 Sample 4

Table B.4 summarises the main results in terms of diameter, maximum load and tensile strength for all specimens in Sample 4. Figure B.5 shows the individual tensile strength results against the mean strength (solid black line), which for Sample 4 is 2696 MPa (standard deviation 422MPa).

Table B.4 Diameter measurements, maximum load and tensile strength results for Sample 4.

	Specimen ID	Diam 1 (mm)	Diam 2 (mm)	Mean Diam (mm)	Max Load (N)	Tensile strength (MPa)
Sample 4	G42	0.347	0.343	0.345	199.5	2133
	G43	0.325	0.327	0.326	242.1	2900
	G44	0.328	0.323	0.326	222.2	2670
	G45	0.326	0.328	0.327	277.5	3304
	H1	0.348	0.313	0.331	271.3	3162
	H2	0.326	0.326	0.326	187.7	2249
	H3	0.317	0.315	0.316	246.9	3147
	H4	0.374	0.386	0.380	282.0	2486
	H6	0.329	0.341	0.335	235.1	2667
	H7	0.385	0.386	0.386	261.1	2237
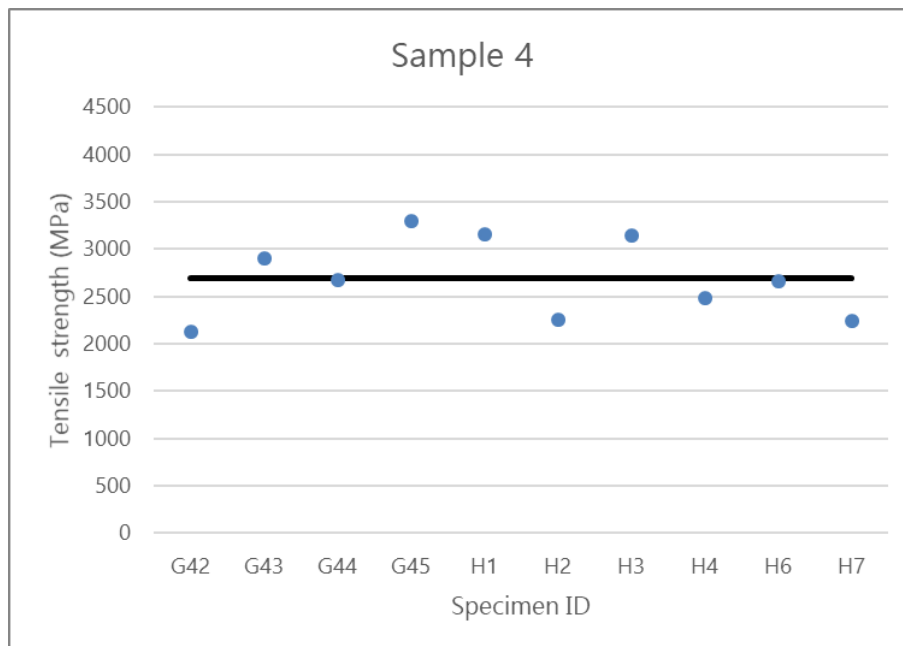
Figure B.5 Individual tensile strength results and a mean value for Sample 4.

153

B.2.5   Sample 5

Table B.5 summarises the main results in terms of diameter, maximum load and tensile strength for all specimens in Sample 5. Figure B.6 shows the individual tensile strength results against the mean strength (solid black line), which for Sample 5 is 2951 MPa (standard deviation 392MPa).

Table B.5 Diameter measurements, maximum load and tensile strength results for Sample 5.

	Specimen ID	Diam 1 (mm)	Diam 2 (mm)	Mean Diam (mm)	Max Load (N)	Tensile strength (MPa)
Sample 5	H8	0.320	0.315	0.318	230.0	2904
	H10	0.324	0.325	0.325	268.6	3247
	H11	0.320	0.323	0.322	249.5	3073
	H12	0.323	0.316	0.320	220.5	2749
	H13	0.337	0.332	0.335	197.7	2249
	H14	0.338	0.345	0.342	262.4	2864
	H16	0.332	0.327	0.330	227.3	2665
	H17	0.200	0.197	0.199	112.2	3626
	H18	0.323	0.323	0.323	227.1	2771
	H19	0.312	0.318	0.315	261.7	3358
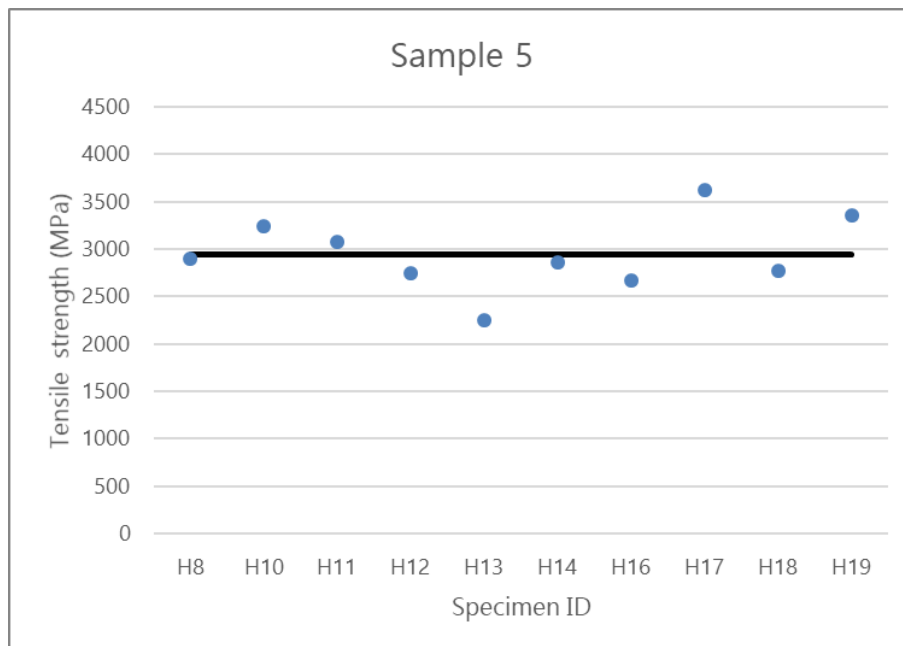
Figure B.6 Individual tensile strength results and a mean value for Sample 5.

B.2.6 Sample 6

Table B.6 summarises the main results in terms of diameter, maximum load and tensile strength for all specimens in Sample 6. Figure B.7 shows the individual tensile strength results against the mean strength (solid black line), which for Sample 6 is 2892 MPa (standard deviation 303MPa).

Table B.6 Diameter measurements, maximum load and tensile strength results for Sample 6.

	Specimen ID	Diam 1 (mm)	Diam 2 (mm)	Mean Diam (mm)	Max Load (N)	Tensile strength (MPa)
Sample 6	H20	0.269	0.263	0.266	133.0	2392
	H21	0.380	0.379	0.380	327.5	2895
	H22	0.335	0.333	0.334	252.6	2883
	H23	0.327	0.327	0.327	272.1	3240
	H24	0.377	0.387	0.382	310.9	2713
	H25	0.315	0.316	0.316	260.8	3335
	H26	0.334	0.330	0.332	230.6	2664
	H27	0.395	0.398	0.397	361.9	2931
	H29	0.309	0.308	0.309	197.7	2645
	H31	0.314	0.313	0.314	248.8	3223
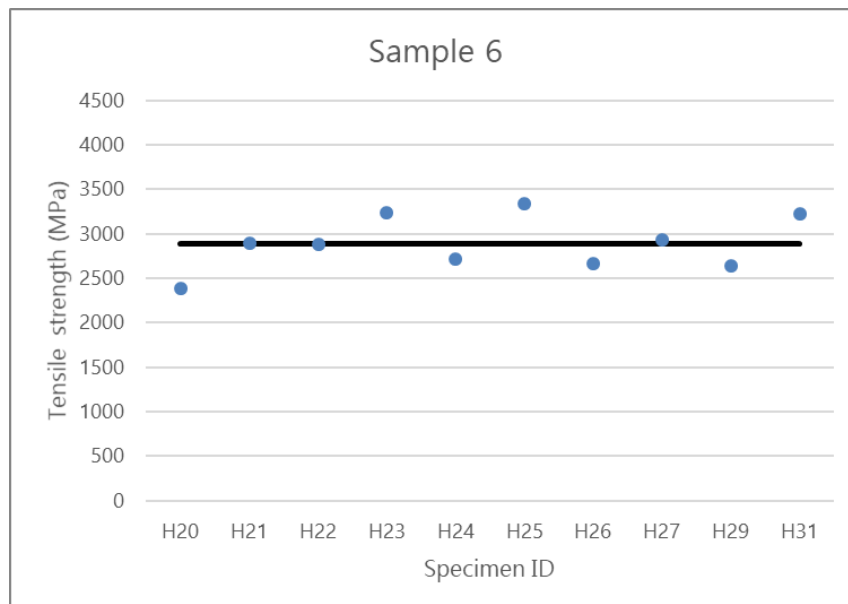
Figure B.7 Individual tensile strength results and a mean value for Sample 6.

B.2.7   Sample 7

Table B.7 summarises the main results in terms of diameter, maximum load and tensile strength for all specimens in Sample 7. Figure B.8 shows the individual tensile strength results against the mean strength (solid black line), which for Sample 7 is 3131 MPa (standard deviation 602MPa).

Table B.7 Diameter measurements, maximum load and tensile strength results for Sample 7.

	Specimen ID	Diam 1 (mm)	Diam 2 (mm)	Mean Diam (mm)	Max Load (N)	Tensile strength (MPa)
	H32	0.310	0.317	0.314	241.8	3133
	H33	0.322	0.329	0.326	302.4	3634
	H35	0.329	0.318	0.324	244.6	2975
	H36	0.209	0.212	0.211	91.3	2623
Sample 7	H37	0.397	0.396	0.397	281.6	2281
	H38	0.326	0.328	0.327	268.1	3192
	H41	0.190	0.198	0.194	101.9	3447
	H42	0.264	0.265	0.265	140.9	2564
	H43	0.307	0.308	0.308	325.6	4384
	H44	0.319	0.327	0.323	252.5	3082
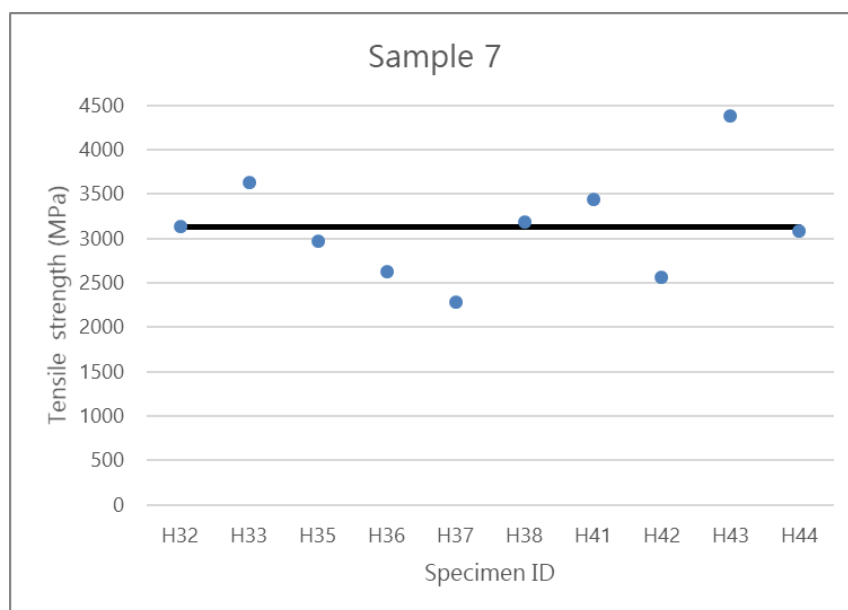
Figure B.8 Individual tensile strength results and a mean value for Sample 7.

B.2.8   Sample 8

Table B.8 summarises the main results in terms of diameter, maximum load and tensile strength for all specimens in Sample 8. Figure B.9 shows the individual tensile strength results against the mean strength (solid black line), which for Sample 8 is 3097 MPa (standard deviation 197 MPa).

Table B.8 Diameter measurements, maximum load and tensile strength results for Sample 8.

	Specimen ID	Diam 1 (mm)	Diam 2 (mm)	Mean Diam (mm)	Max Load (N)	Tensile strength (MPa)
Sample 8	H45	0.316	0.320	0.318	227.4	2863
	H46	0.323	0.317	0.320	237.3	2950
	H47	0.329	0.325	0.327	275.9	3285
	I1	0.336	0.344	0.340	264.9	2917
	I5	0.305	0.325	0.315	245.9	3155
	I6	0.333	0.333	0.333	266.3	3058
	I7	0.314	0.330	0.322	230.9	2835
	I9	0.331	0.337	0.334	288.9	3297
	I11	0.323	0.328	0.326	271.4	3261
	I12	0.316	0.314	0.315	261.3	3353
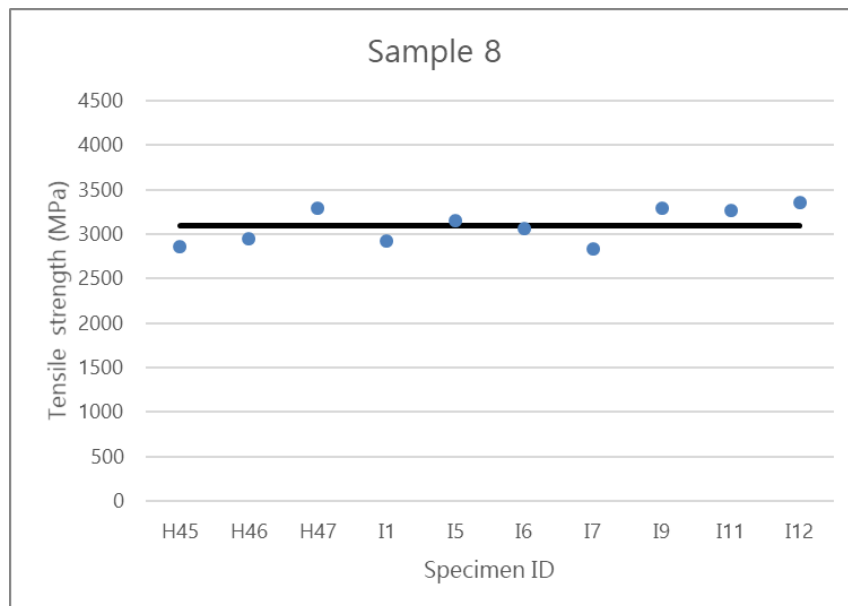
Figure B.9 Individual tensile strength results and a mean value for Sample 8.

157

B.2.9 Sample 9

Table B.9 summarises the main results in terms of diameter, maximum load and tensile strength for all specimens in Sample 9. Figure B.10 shows the individual tensile strength results against the mean strength (solid black line), which for Sample 9 is 2817 MPa (standard deviation 315 MPa).

Table B.9 Diameter measurements, maximum load and tensile strength results for Sample 9.

	Specimen ID	Diam 1 (mm)	Diam 2 (mm)	Mean Diam (mm)	Max Load (N)	Tensile strength (MPa)
Sample 9	I13	0.320	0.333	0.327	214.2	2559
	I14	0.332	0.327	0.330	220.4	2585
	I15	0.335	0.338	0.337	282.6	3178
	I16	0.352	0.348	0.350	212.5	2209
	I17	0.331	0.337	0.334	270.0	3081
	I19	0.211	0.208	0.210	93.7	2716
	I20	0.323	0.325	0.324	244.4	2964
	I21	0.317	0.319	0.318	213.8	2692
	I22	0.375	0.343	0.359	315.0	3111
	I23	0.339	0.338	0.339	276.9	3076
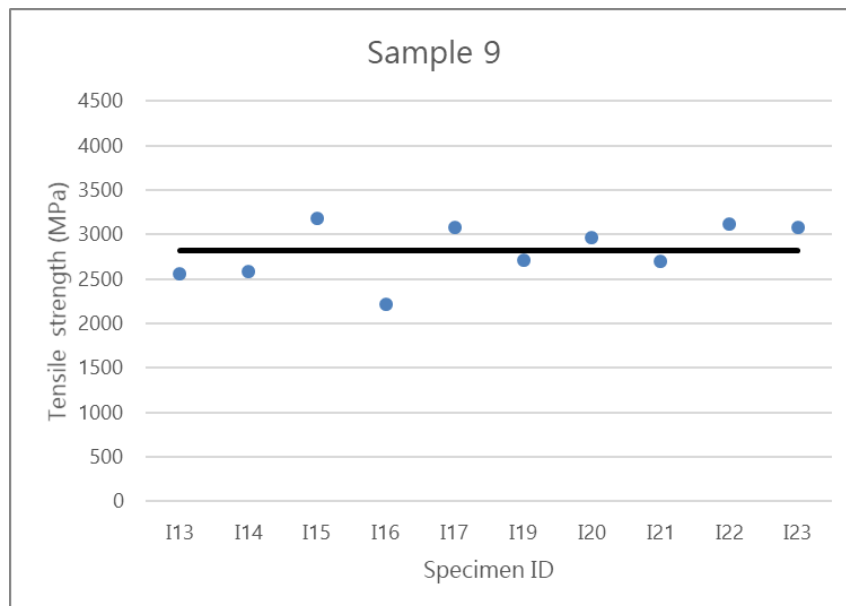
Figure B.10 Individual tensile strength results and a mean value for Sample 9.

158

B.2.10   Sample 10

Table B.10 summarises the main results in terms of diameter, maximum load and tensile strength for all specimens in Sample 10. Figure B.11 shows the individual tensile strength results against the mean strength (solid black line), which for Sample 10 is 2840 MPa (standard deviation 452MPa).

Table B.10 Diameter measurements, maximum load and tensile strength results for Sample 10.

	Specimen ID	Diam 1 (mm)	Diam 2 (mm)	Mean Diam (mm)	Max Load (N)	Tensile strength (MPa)
Sample 10	I24	0.308	0.309	0.309	214.7	2871
	I25	0.318	0.319	0.319	260.0	3264
	I26	0.338	0.337	0.338	296.9	3319
	I28	0.321	0.315	0.318	171.5	2159
	I29	0.308	0.307	0.308	216.6	2917
	I30	0.192	0.193	0.193	55.6	1912
	I31	0.320	0.313	0.317	235.7	2996
	I32	0.325	0.326	0.326	242.9	2918
	I33	0.320	0.327	0.324	244.8	2978
	I34	0.336	0.318	0.327	257.7	3068
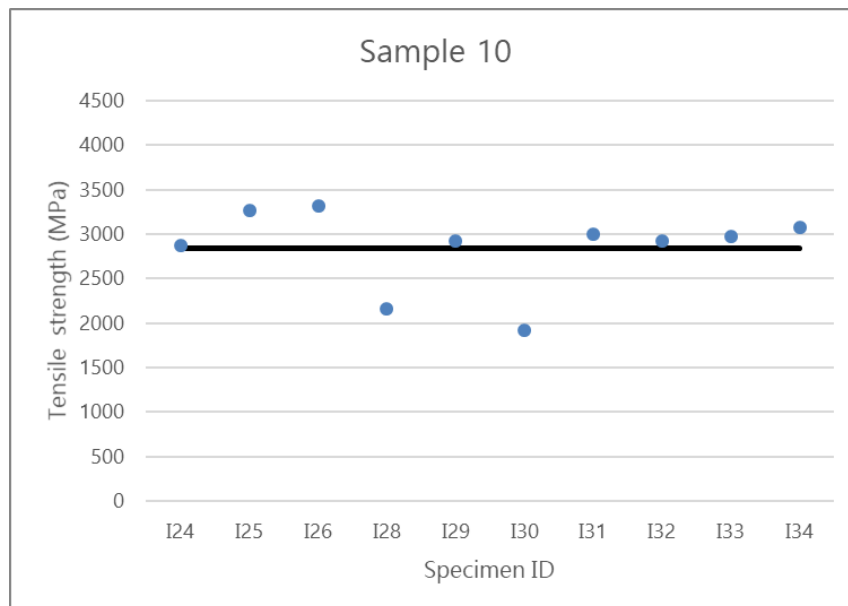
Figure B.11 Individual tensile strength results and a mean value for Sample 10.

B.2.11 Sample 11

Table B.11 summarises the main results in terms of diameter, maximum load and tensile strength for all specimens in Sample 11. Figure B.12 shows the individual tensile strength results against the mean strength (solid black line), which for Sample 11 is 3045 MPa (standard deviation 218 MPa).

Table B.11 Diameter measurements, maximum load and tensile strength results for Sample 11.

	Specimen ID	Diam 1 (mm)	Diam 2 (mm)	Mean Diam (mm)	Max Load (N)	Tensile strength (MPa)
Sample 11	I35	0.311	0.317	0.314	251.3	3245
	I36	0.316	0.317	0.317	239.3	3041
	I37	0.331	0.323	0.327	256.7	3056
	I38	0.337	0.336	0.337	260.5	2928
	I39	0.333	0.331	0.332	245.3	2833
	I41	0.318	0.307	0.313	219.8	2866
	I42	0.311	0.320	0.316	245.0	3134
	I43	0.320	0.328	0.324	292.1	3542
	I44	0.302	0.312	0.307	213.9	2890
	I45	0.334	0.331	0.333	253.0	2914
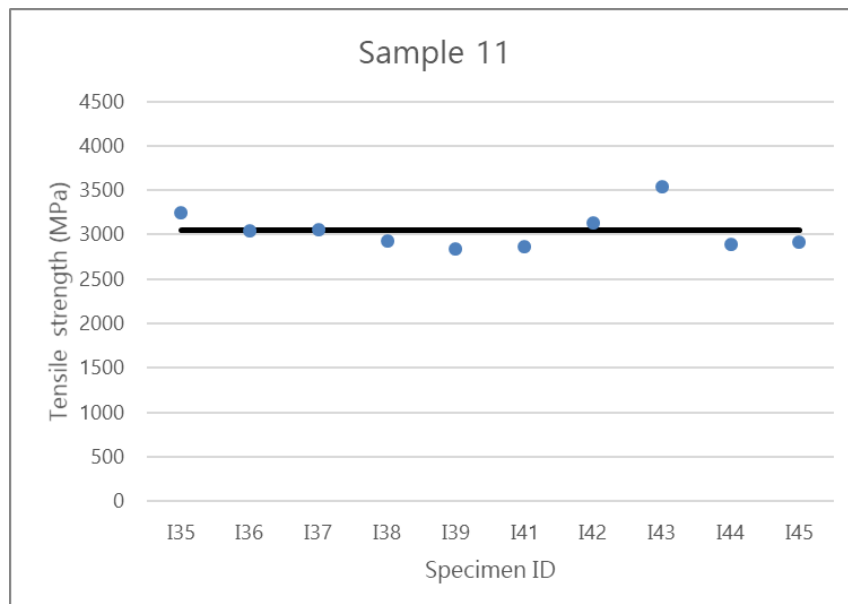
Figure B.12 Individual tensile strength results and a mean value for Sample 11.

B.2.12 All samples

Figure B.13 shows the average tensile strength results of each individual sample against the mean strength of all samples (solid black line), which is 2909 MPa (standard deviation 166 MPa). Figure B.14 presents the histogram of tensile strengths from all tested specimens.
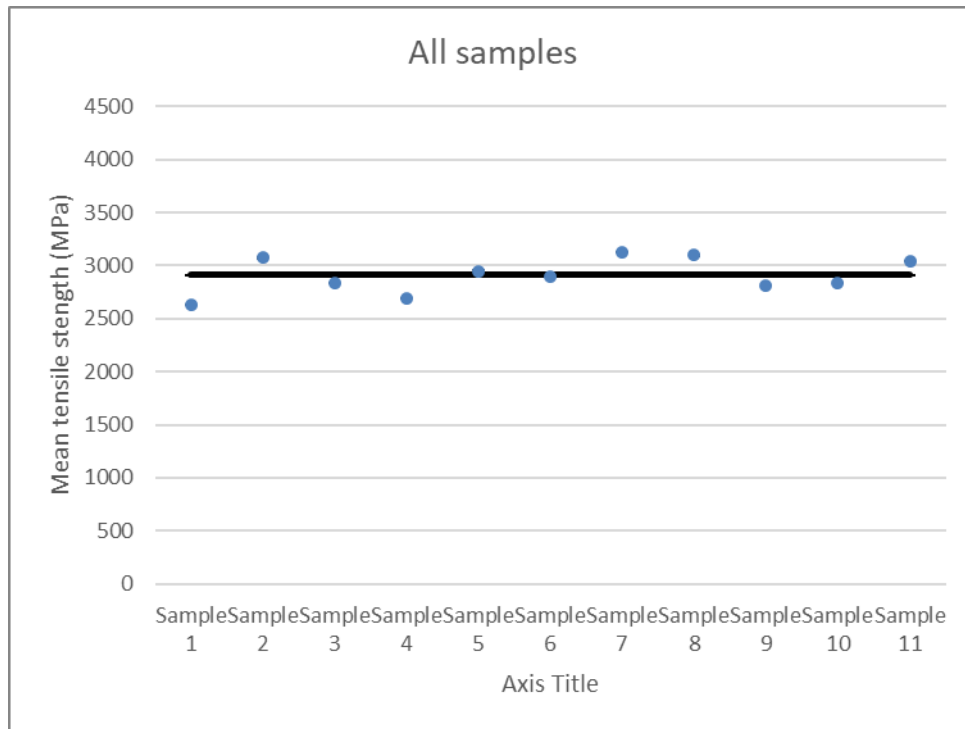
Figure B.13 Mean tensile strength results and a mean value from all Samples.
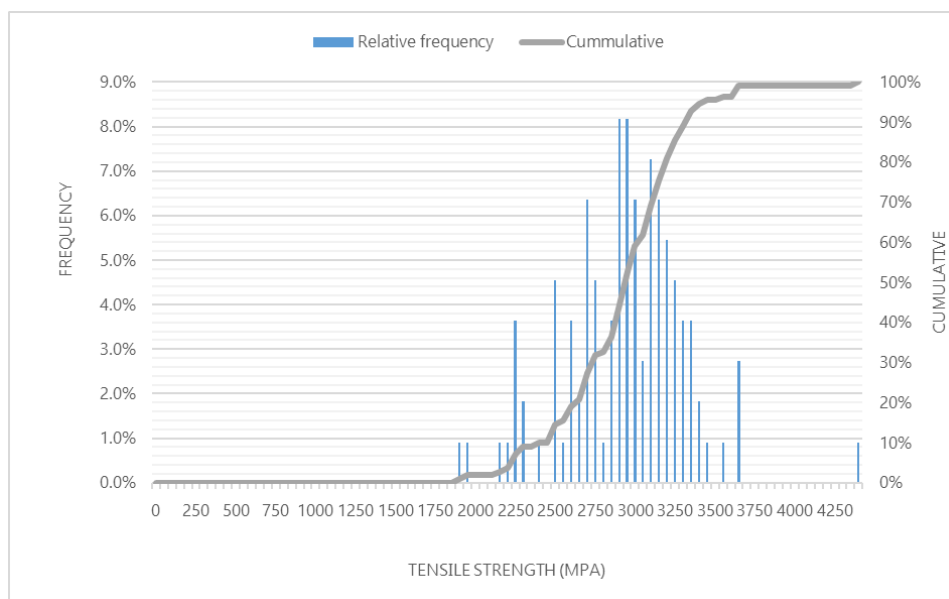
Figure B.14 Histogram of tensile strength results from all specimens.

Appendix C: Compressive and Flexural Strength Results

This appendix summarises compressive strength, mass density, residual flexural values and flexural modulus of plain, F30 and F40 concrete mixes. Three cubes ($100 \times 100 \times 100$ mm) were tested at each curing age, and the average of all (20, 15 and 14 cubes for plain, F30 and F40 mixes, respectively) is reported herein. The residual flexural values ($f_{R,1}$, $f_{R,2}$, $f_{R,3}$, and $f_{R,4}$) were obtained from three-point bending tests (after 389, 339 and 320 days for plain, F30 and F40 mixes, respectively, after casting) of prisms, $500 \times 150 \times 150$ mm. Details of the flexural tests are given in Appendix E.

The flexural capacity of the prisms (all time in water, ASE_W) is not affected by curing time. This means prolonged curing for the considered mix does not benefit the flexural strength.

C.1 Compressive Strength

Plain				F30				F40			
Curing Time	ID	Strength (MPa)	Density (Kg/m^3)	Curing Time	ID	Strength (MPa)	Density (Kg/m^3)	Curing Time	ID	Strength (MPa)	Density (Kg/m^3)
4 Days	1	19.87	2322	7 Days	1	23.10	2343	7 Days	1	22.60	2390
	2	20.60	2326		2	23.70	2352		2	23.40	2383
	3	17.33	2342		3	23.30	2344		3	22.60	2389
Avg.		**19.27**	**2330**	Avg.		23.37	2346	Avg.		22.87	2387
7 Days	1	25.76	2340	14 Days	1	27.10	2356	14 Days	1	28.30	2388
	2	24.45	2343		2	26.80	2357		2	27.70	2390
	3	24.91	2329		3	28.90	2340		3	28.90	2379
Avg.		**25.04**	**2337**	Avg.		27.60	2351	Avg.		28.30	2386
14 Days	1	30.02	2329	28 Days	1	29.93	2361	35 Days	1	32.30	2387
	2	28.92	2347		2	29.96	2361		2	32.60	2389
	3	30.40	2342		3	31.00	2357		3	31.70	2391
Avg.		**29.78**	**2339**	Avg.		30.30	2360	Avg.		32.20	2389
21 Days	1	30.00	2355	56 Days	1	30.75	2365	56 Days	1	34.60	2387
	2	28.38	2336		2	33.52	2352		2	34.30	2381
	3	31.53	2357		3	32.18	2353		3	34.50	2393
Avg.		**29.97**	**2349**	Avg.		32.15	2357	Avg.		34.47	2387
28 Days	1	33.50	2338	90 Days	1	35.10	2360	90 Days	1	35.32	2386
	2	29.58	2330		2	34.50	2353		2	34.92	2392
	3	35.08	2348		3	34.30	2357	Avg.		35.12	2389
Avg.		**32.72**	**2339**	Avg.		34.63	2357				
60 Days	1	33.10	2364								
	2	30.61	2319								
Avg.		**31.86**	**2341**								
128 Days	1	36.80	2336								
	2	35.80	2342								
	3	35.00	2351								
Avg.		**36.30**	**2339**								

C.2 Residual Flexural Strength and Flexural Modulus

Mix	Specimen ID	$f_{cm,cube}$ (MPa)	Flexural Modulus(MPa)	$f_{fct,L}$ (MPa)	Residual flexural Strength (MPa)			
					$f_{R,1}$	$f_{R,2}$	$f_{R,3}$	$f_{R,4}$
Plain	ASE-1	33	27597	4.85	-	-	-	-
	ASE-2		23241	4.92	-	-	-	-
	ASE-WRHS		-	4.54	-	-	-	-
	ASE_W-1		34757	3.90	-	-	-	-
	ASE_W-2		26574	3.78	-	-	-	-
	ASE_W-3		30807	3.86	-	-	-	-
	OSE-WRHS		-	4.20	-	-	-	-
	CS		22881	3.84	-	-	-	-
F30	ASE-1	30.3	20410	5.42	3.32	3.22	2.89	2.38
	ASE-2		21275	4.77	3.59	3.53	3.09	2.73
	ASE-WRHS		24051	6.00	3.46	3.32	3.04	2.57
	ASE_W-1		29593	3.45	2.76	2.64	2.33	1.96
	ASE_W-2		27683	4.08	4.04	3.14	2.47	1.92
	ASE_W-3		24051	3.77	2.84	2.49	2.06	1.72
	OSE-WRHS		23741	4.70	2.97	2.88	2.52	2.21
	CS		20499	4.53	3.06	2.67	2.39	2.00
F40	ASE-1	32.2	22404	5.72	4.41	4.29	3.74	3.26
	ASE-2		18264	5.73	5.37	5.01	4.32	3.64
	ASE-WRHS		19835	5.39	3.99	3.73	3.25	2.84
	ASE_W-1		24823	4.26	4.70	4.39	3.89	3.26
	ASE_W-2		22422	4.02	3.79	3.53	3.05	2.66
	ASE_W-3		25005	4.07	5.00	4.24	3.54	2.91
	OSE-WRHS		28330	4.94	3.62	3.48	3.08	2.66
	CS		23913	5.02	3.71	3.07	2.54	2.09

Appendix D: Total Shrinkage of All the Specimens

This appendix summarizes all the experimental results of total drying and autogenous shrinkage. For each concrete mix (plain, F30 and F40), 1 completely sealed (CS), 3 all-surface exposed (ASE), and 1 one-surface exposed (OSE) prism were used for shrinkage measurements. One additional prism (completely sealed with no curing) for the plain mix only was used for autogenous shrinkage.

Three DEMEC gauges (100, 200 and 300 mm) were used for shrinkage measurements. To improve the accuracy of measurements, three readings were taken on the perpendicular side of the concrete casting surface with each gauge (at 10mm from the top, T and the bottom, B), and the average is reported herein.

Total drying shrinkage of all surface exposed specimens is also compared with design models (ACI 209, Eurocode 2, Model Code 2010, B3, B4 and JSCE). No design code considers drying shrinkage in fiber reinforced concrete.

D.1 Plain Concrete ASE Specimens

Plain (S-1)

Plain (S-2)

Plain (S-3)

Plain Average (S-1, 2 & 3)

D.2 F30 Concrete ASE Specimens

F30 (S-1)

F30 (S-2)

F30 (S-3)

Average F30 (S-1, 2 & 3)

169

D.3 F40 Concrete ASE Specimens

F40 (S-1)

F40 (S-2)

F40 (S-3)

Average F40 (S-1, 2 & 3)
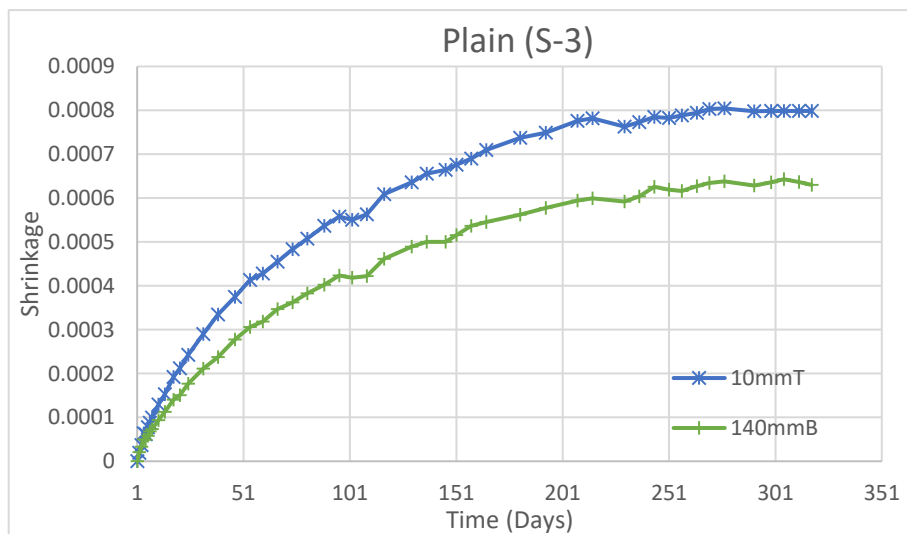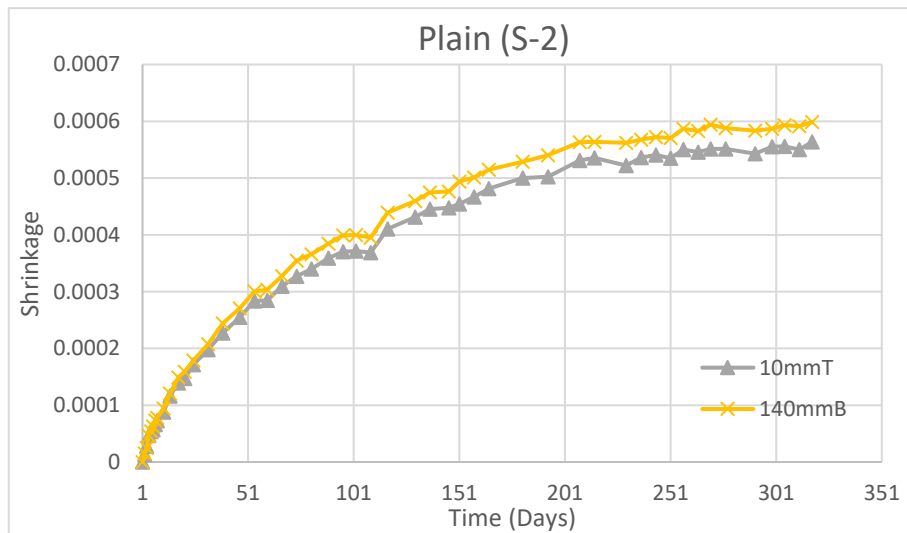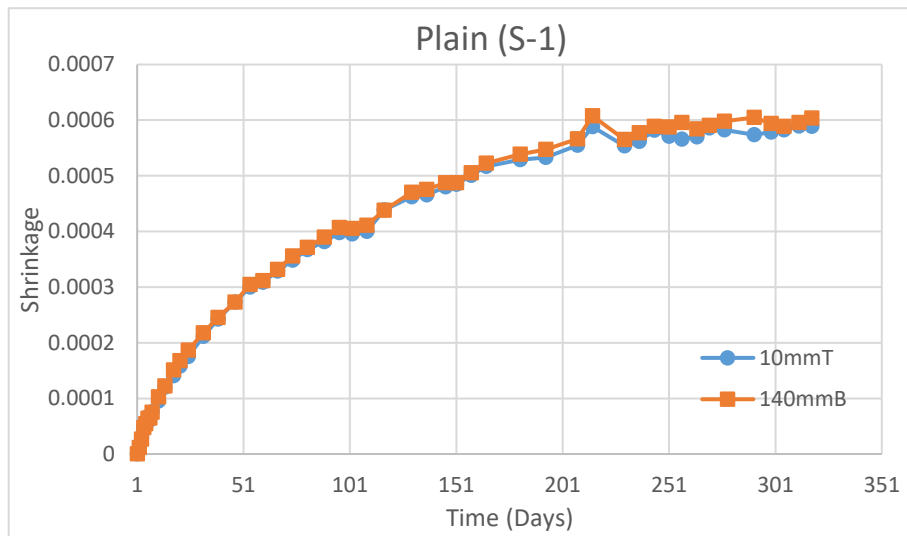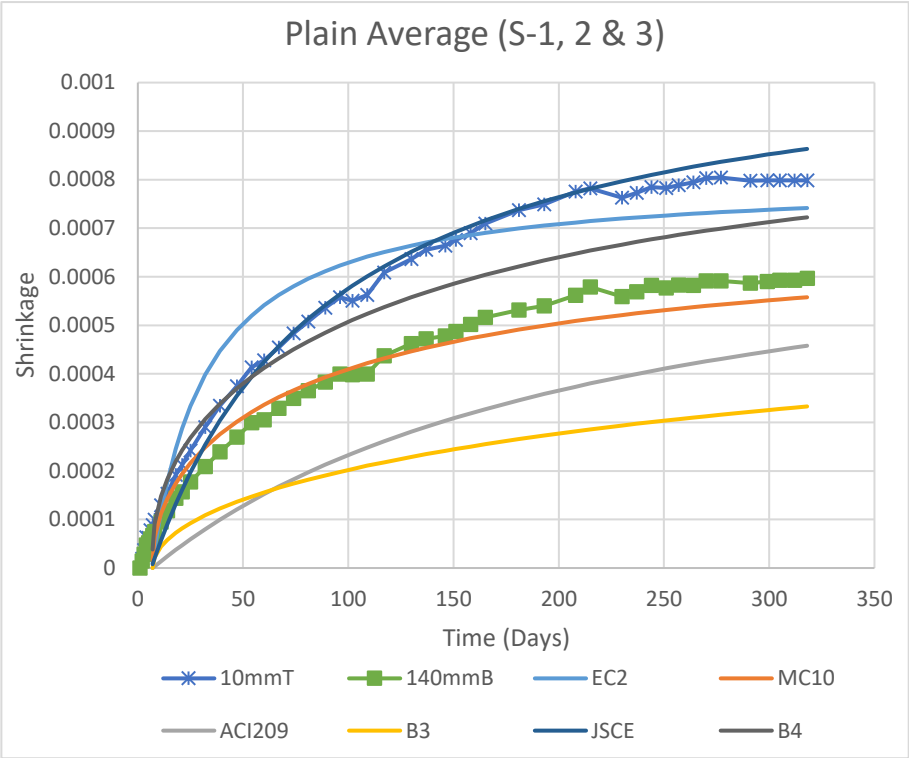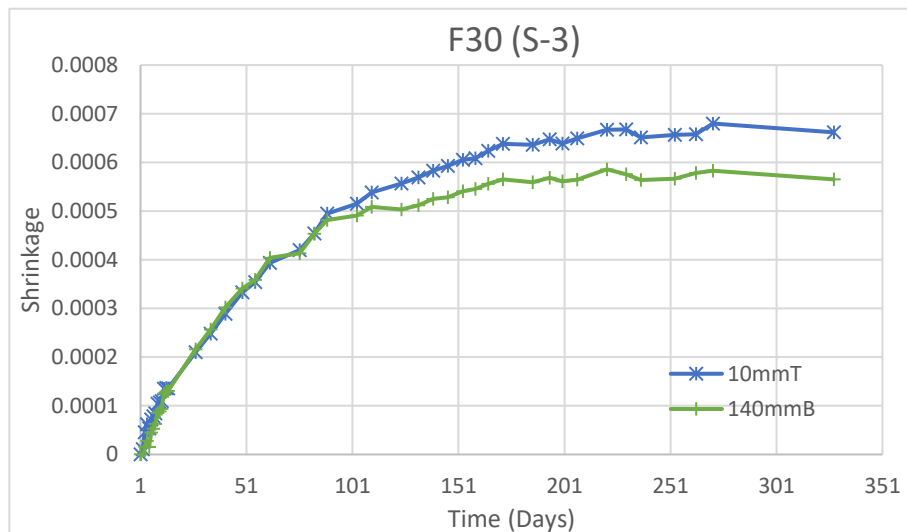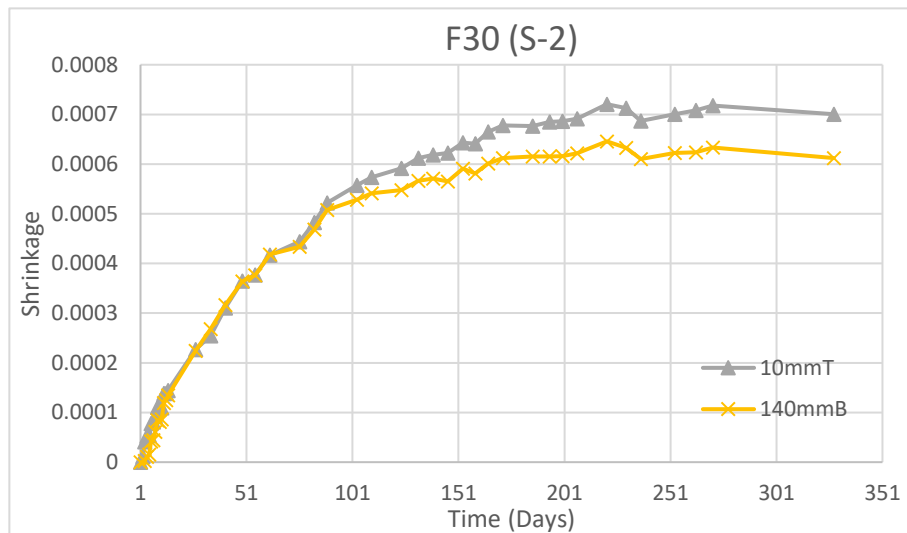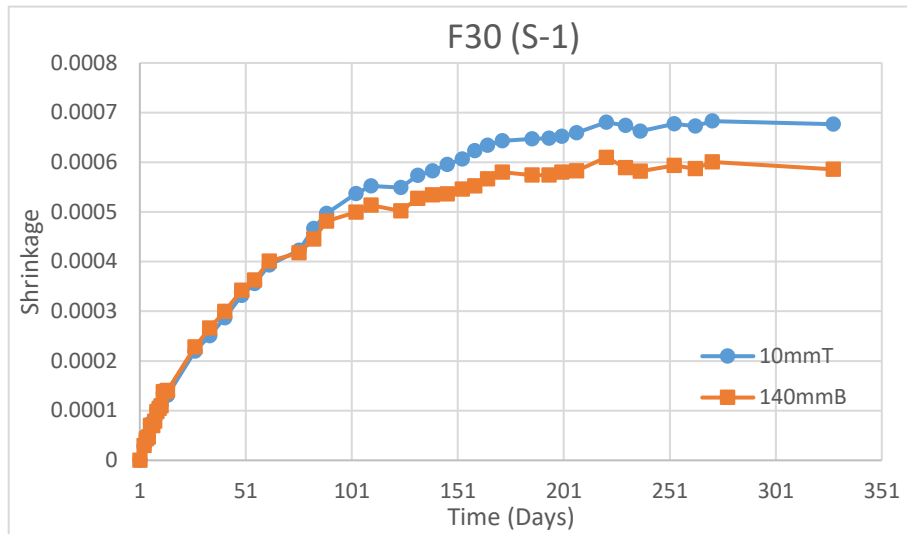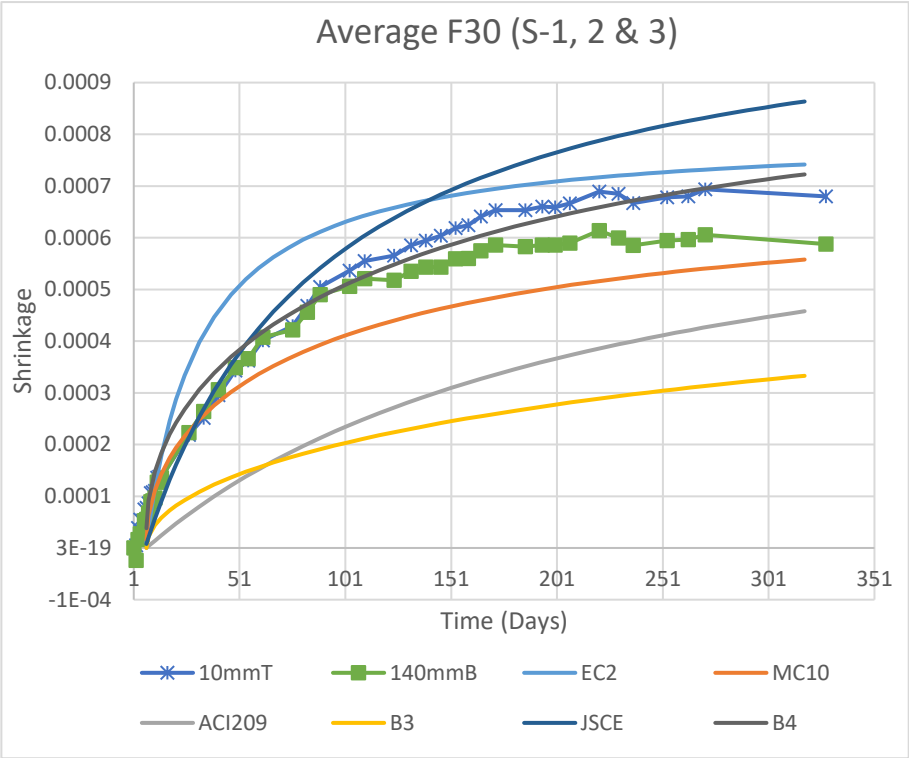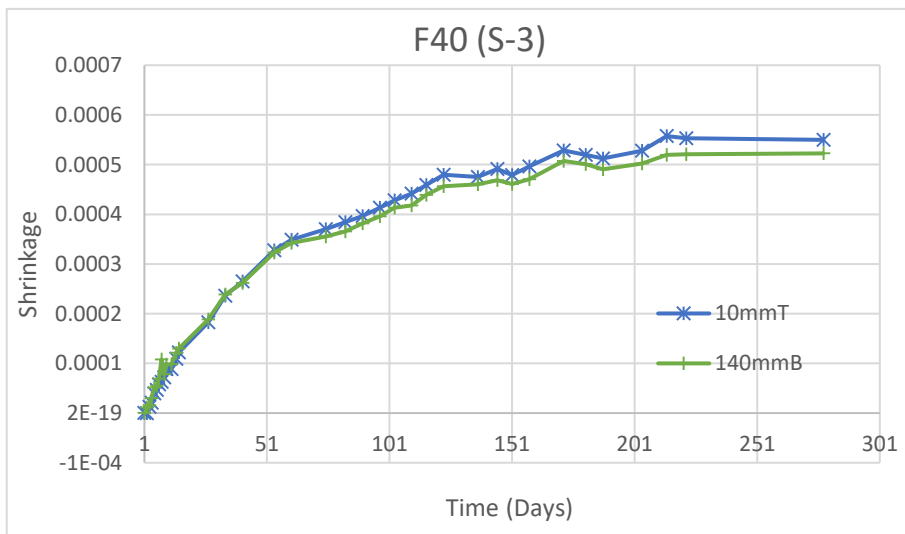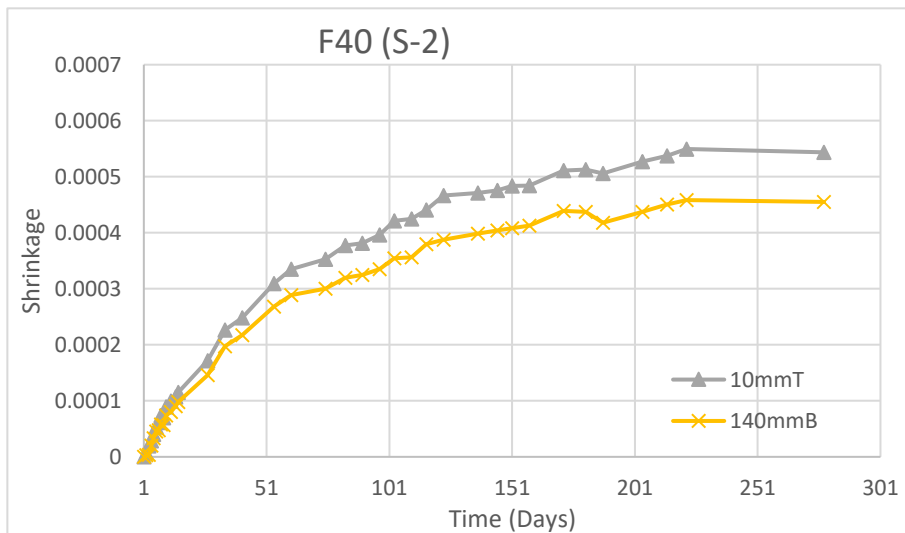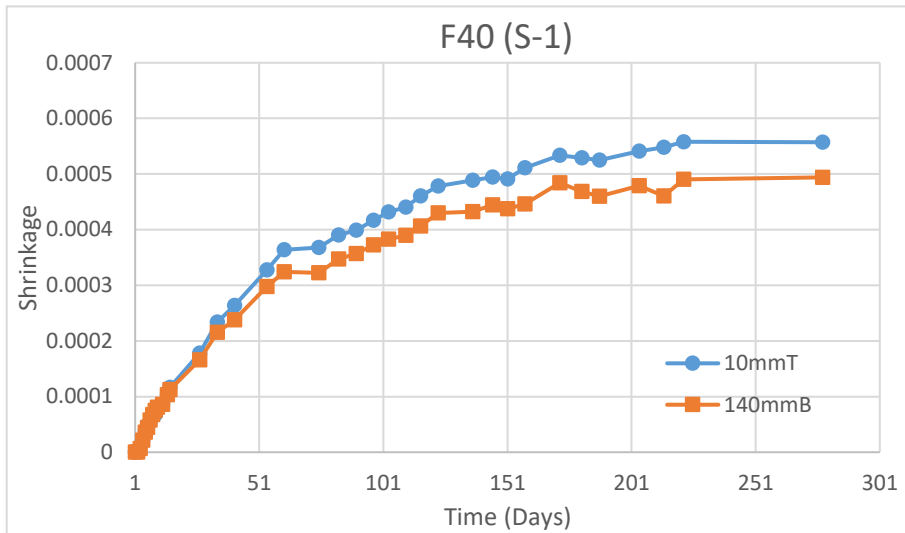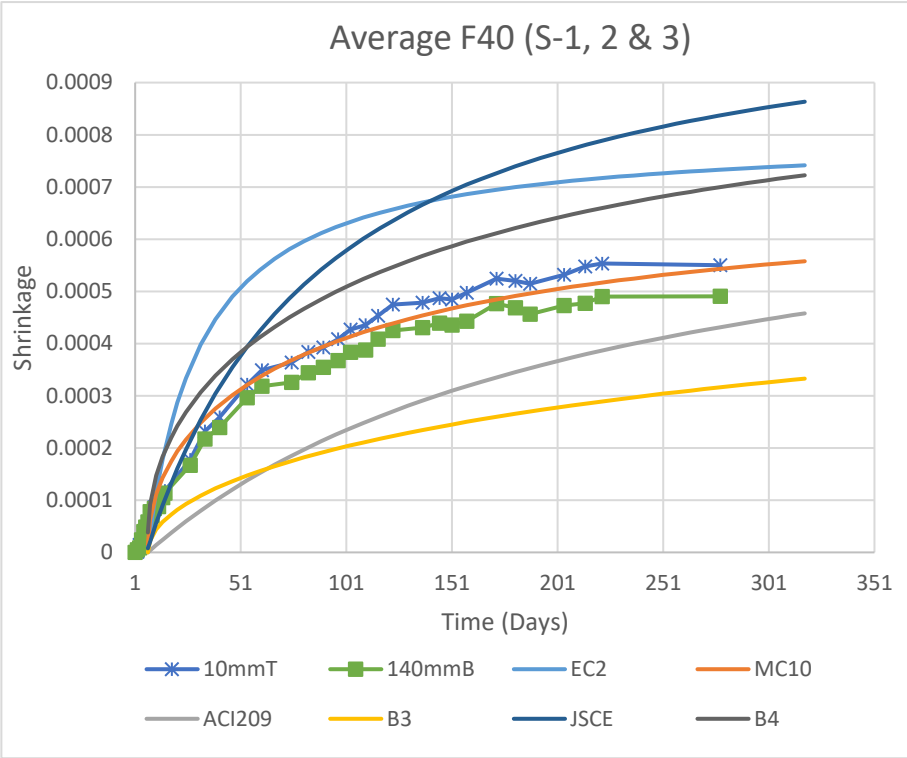
D.4 Plain Concrete OSE Specimens
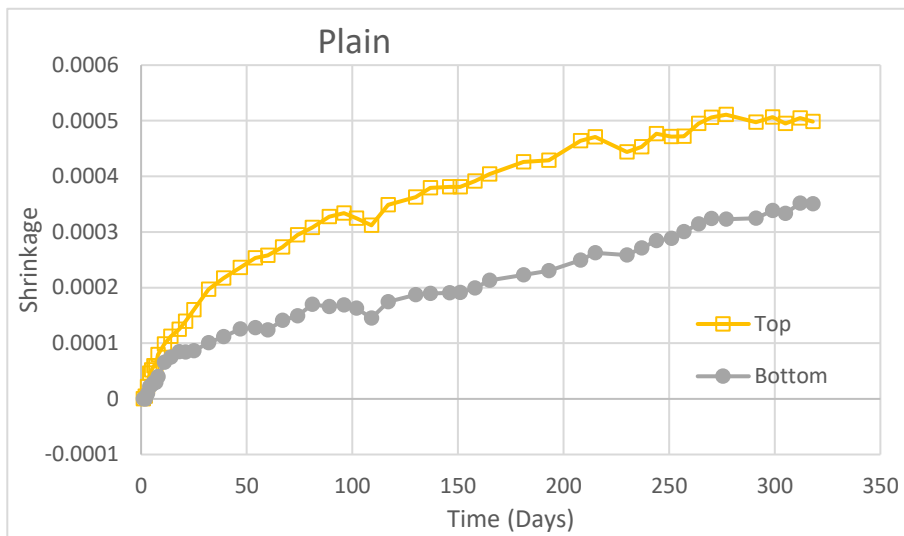
D.5 F30 Concrete OSE Specimen
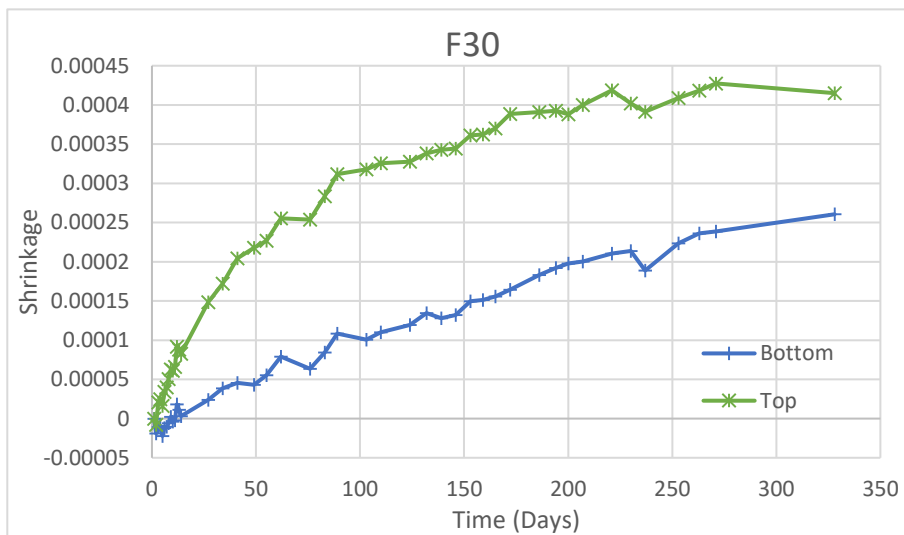
D.6   F40 Concrete OSE Specimen
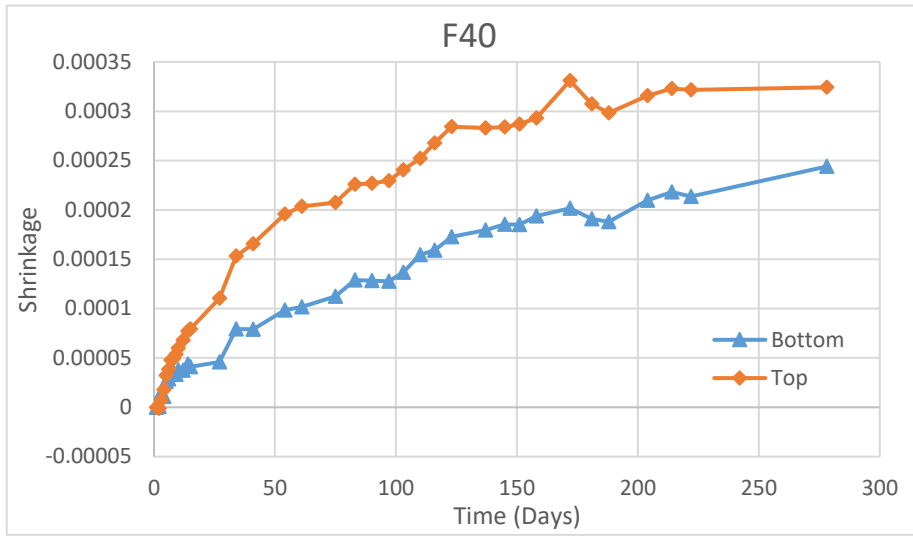
D.7   Plain Concrete CS Specimen
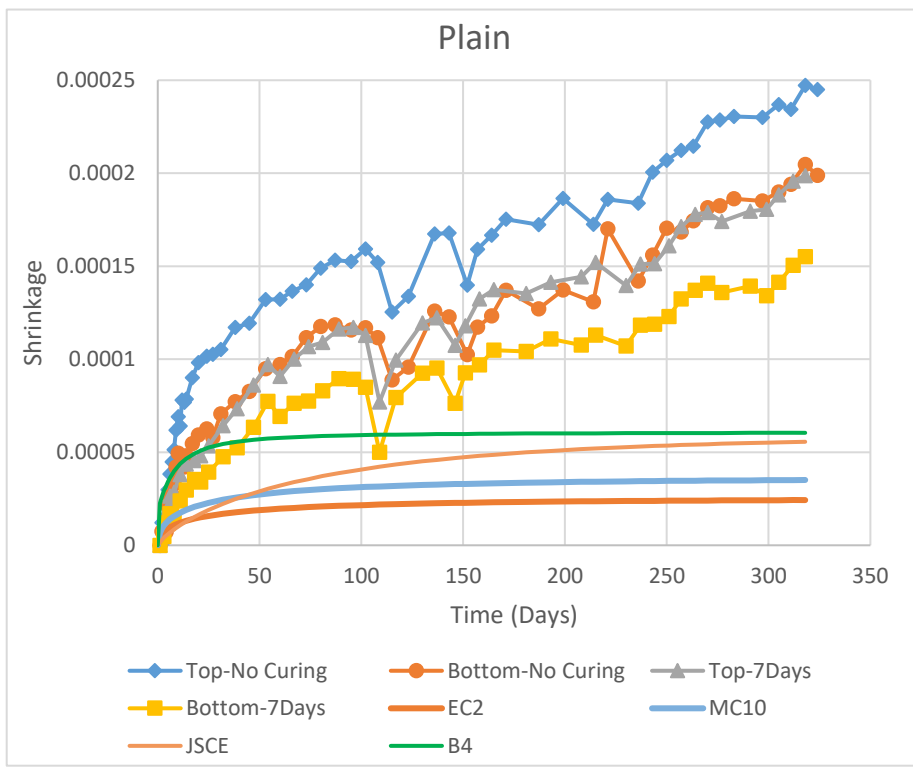
D.8   F30 Concrete CS Specimen
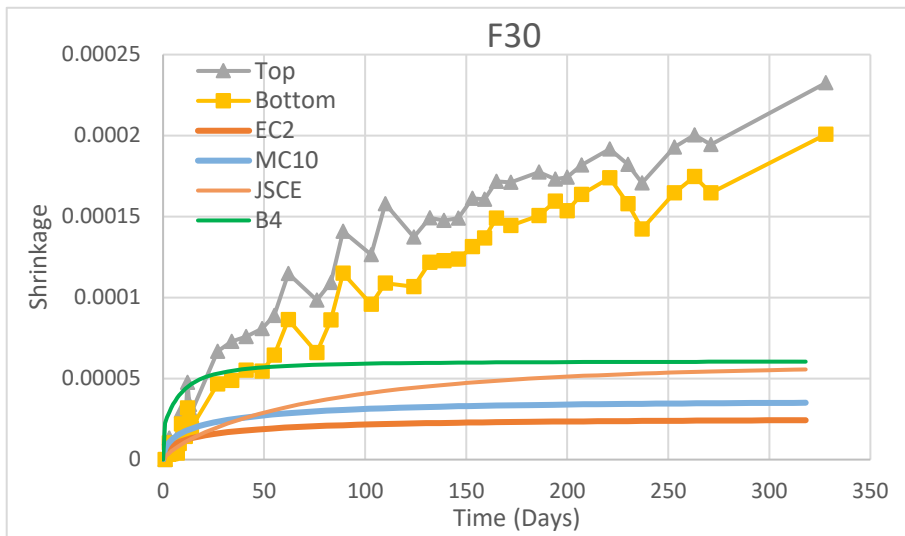
D.9   F40 Concrete CS Specimen
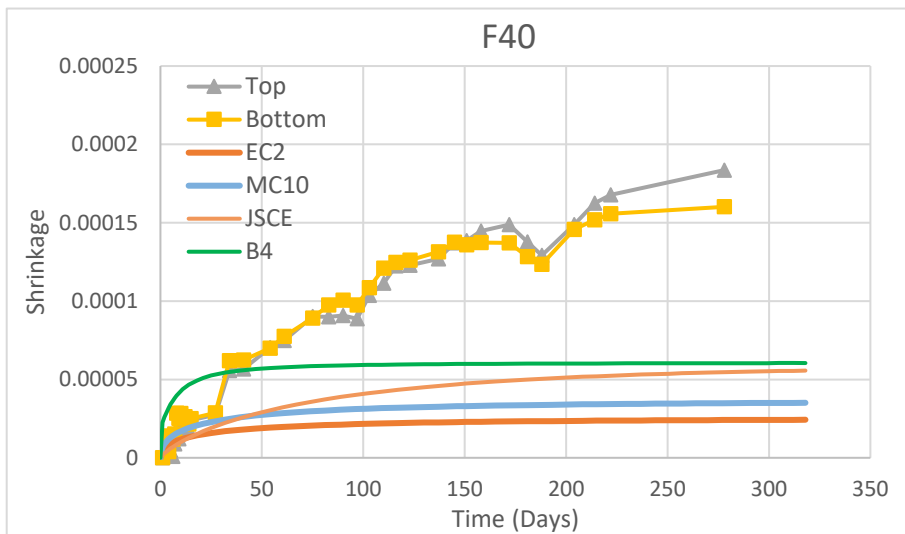
Appendix E: Experimental Three-point Bending Results

This appendix presents experimental load-deflection and crack mouth opening displacement (CMOD) results for all 24 prisms (8 for each concrete mix, Plain, F30 and F40) tested in the three-point bending setup. Sections E.1, E.2 and E.3 summarise the results of plain, F30 and F40 concrete mixes, respectively. Tables in each section summarise each specimen's geometrical parameters and flexural strength. Whilst photographs are taken before and after the testing of the specimens.

E.1 Plain Concrete Mix

Specimen Name	WP1-ASE-1
Depth (mm)	149.5
Width (mm)	150
Notch depth (mm)	127
Flexural Strength, $f_{fct,L}$ (MPa)	4.85
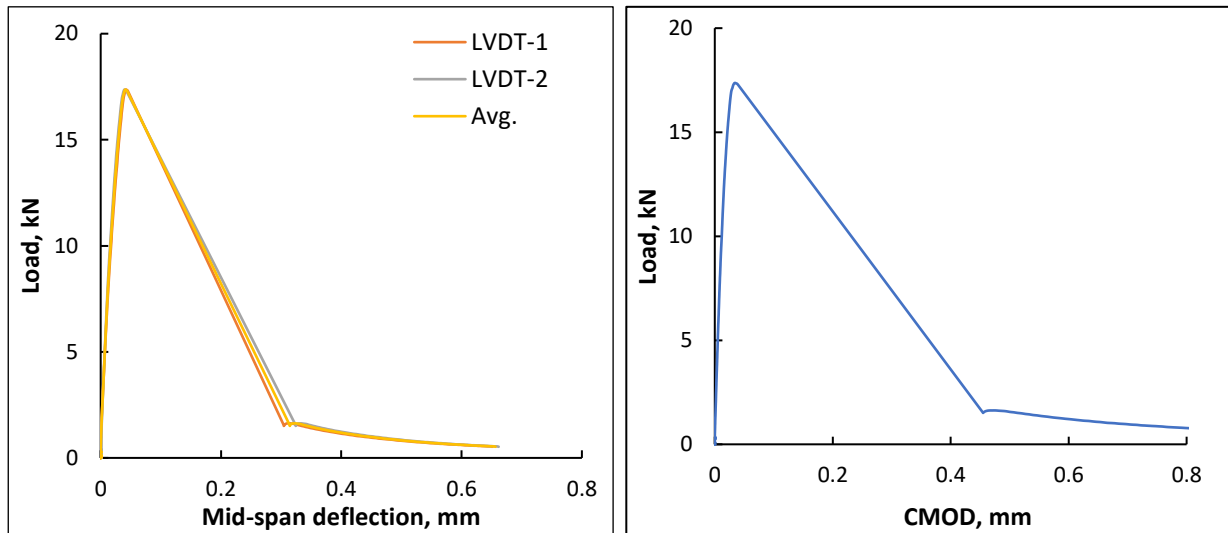
Specimen Name	**WP1-ASE-2**
Depth (mm)	150.5
Width (mm)	150
Notch depth (mm)	126.5
Flexural Strength, $f_{fct,L}$ (MPa)	4.92
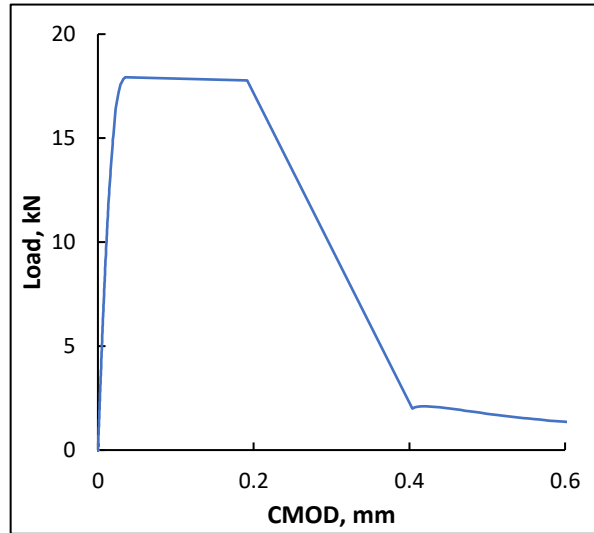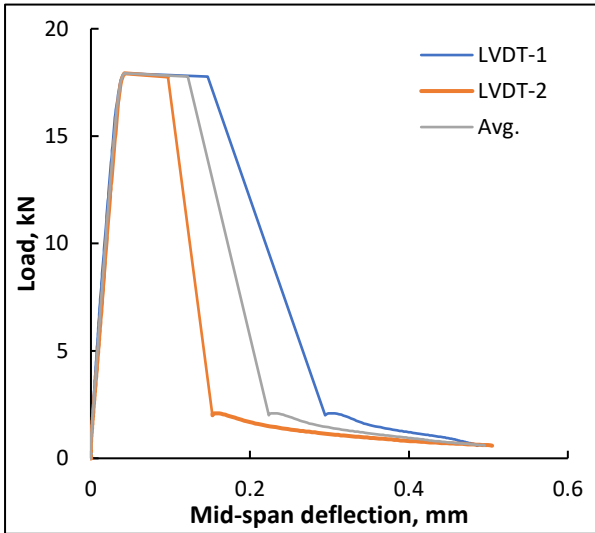
Specimen Name	**WP1-ASE-WRHS**
Depth (mm)	149.5
Width (mm)	150.5
Notch depth (mm)	125.5
Flexural Strength, $f_{fct,L}$ (MPa)	4.54
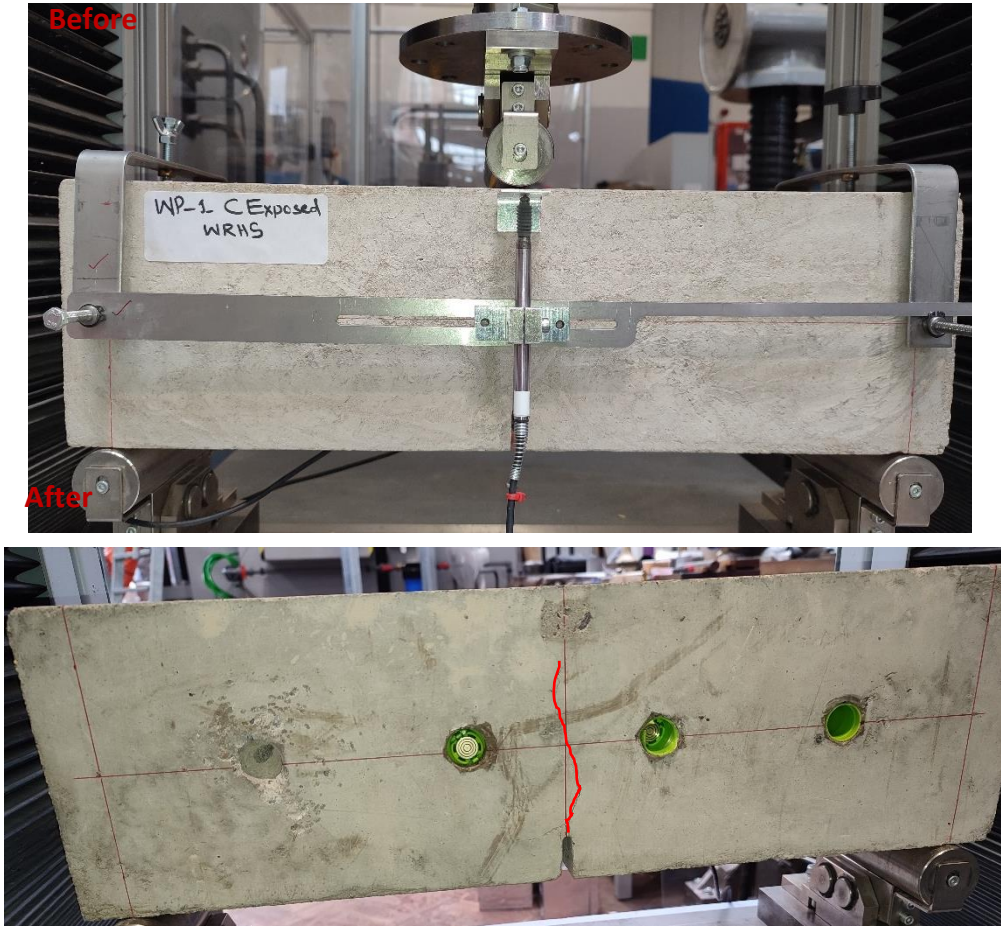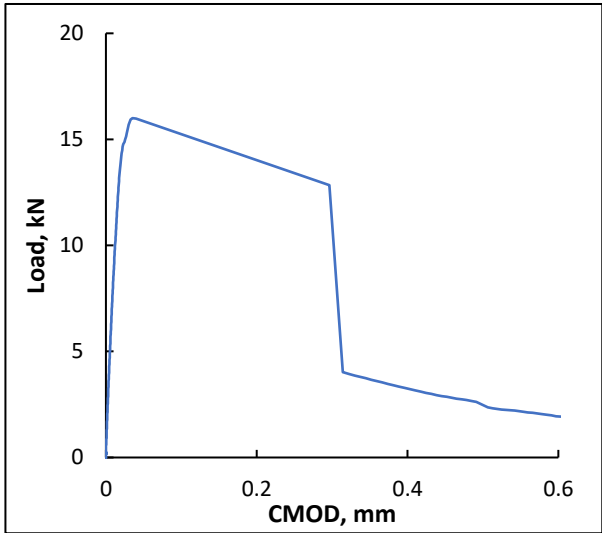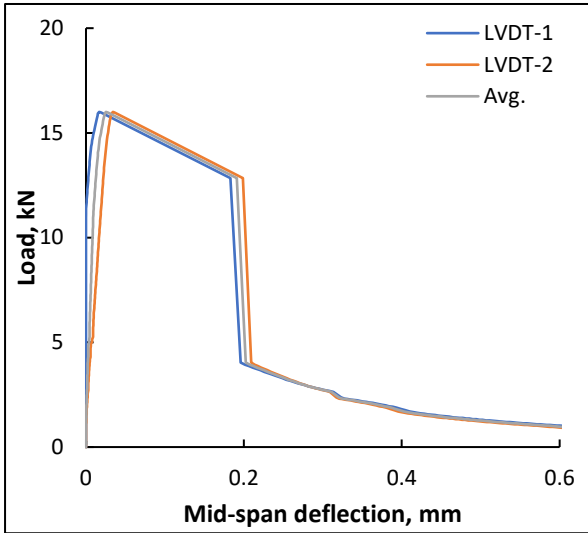
Specimen Name	**WP1-CExposed_IW-1**
Depth (mm)	149.5
Width (mm)	149
Notch depth (mm)	126
Flexural Strength, $f_{fct,L}$ (MPa)	3.90
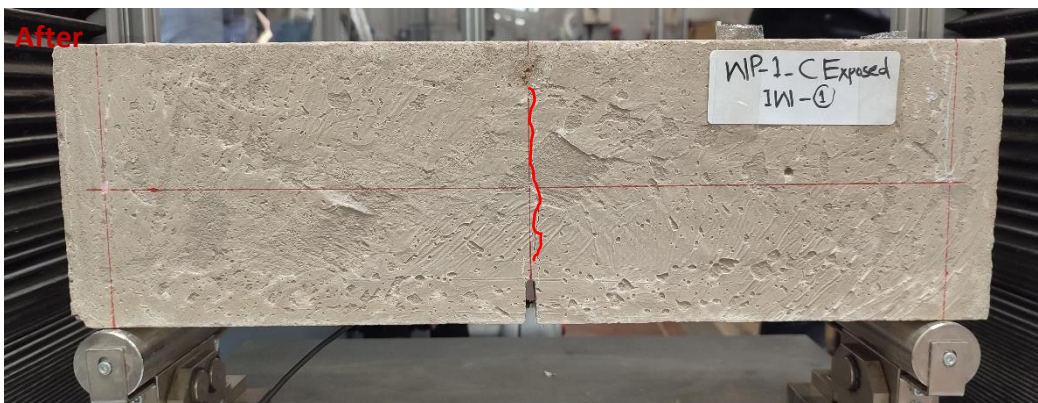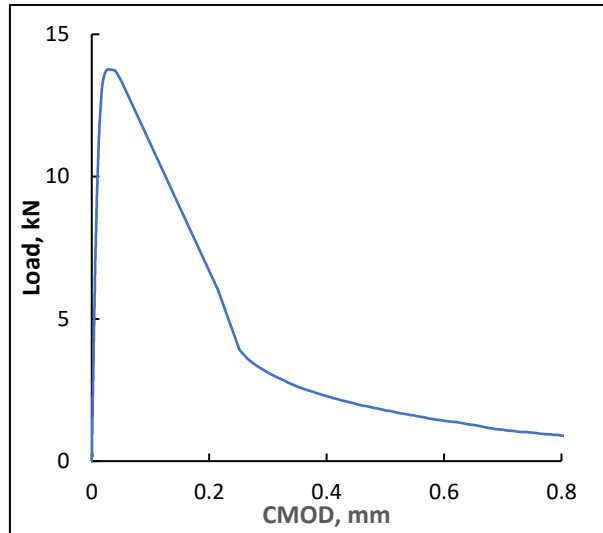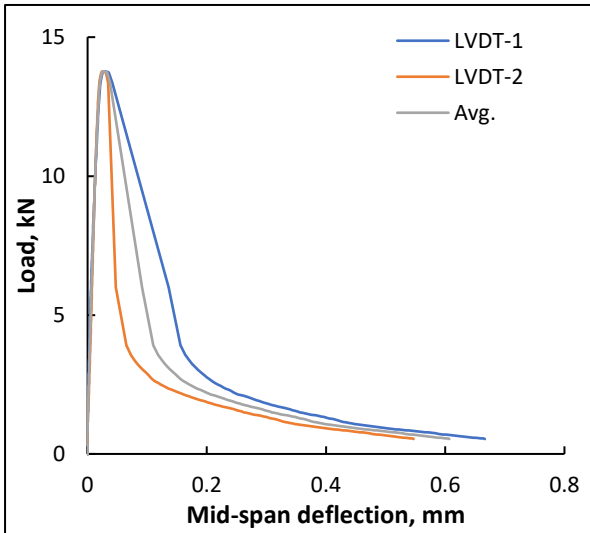
Specimen Name	**WP1-CExposed_IW-2**
Depth (mm)	151
Width (mm)	150
Notch depth (mm)	127
Flexural Strength, $f_{fct,L}$ (MPa)	3.78
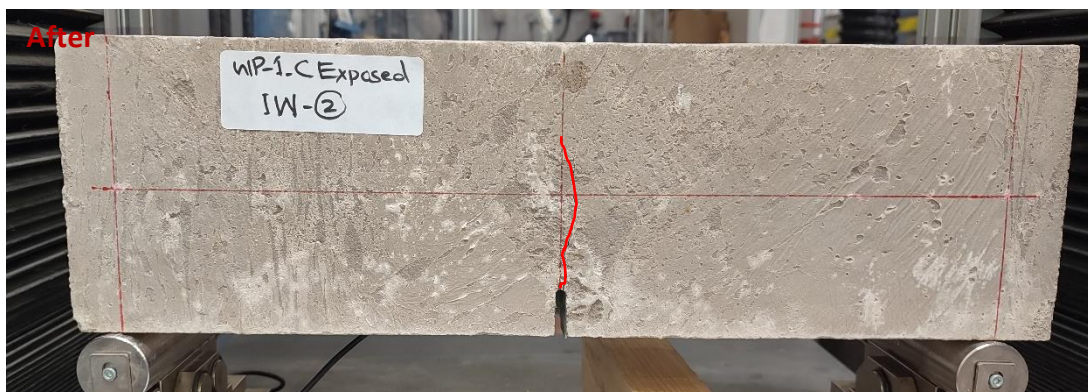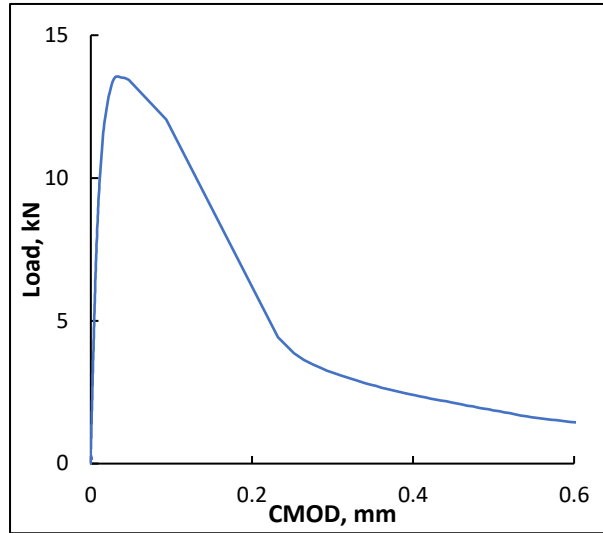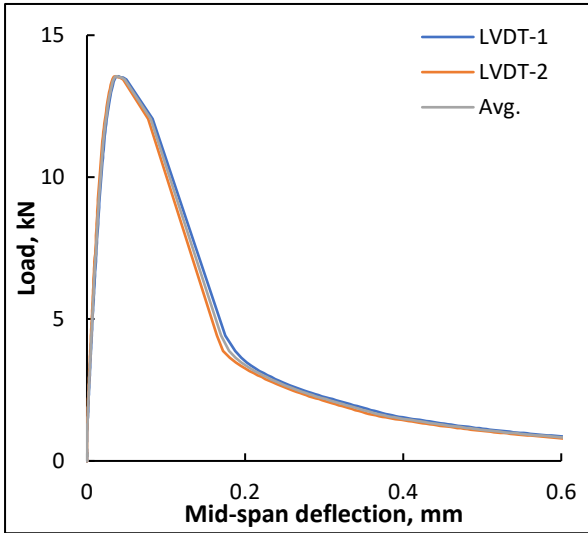
Specimen Name	**WP1-CExposed_IW-3**
Depth (mm)	151
Width (mm)	150.5
Notch depth (mm)	126.5
Flexural Strength, $f_{fct,L}$ (MPa)	3.86
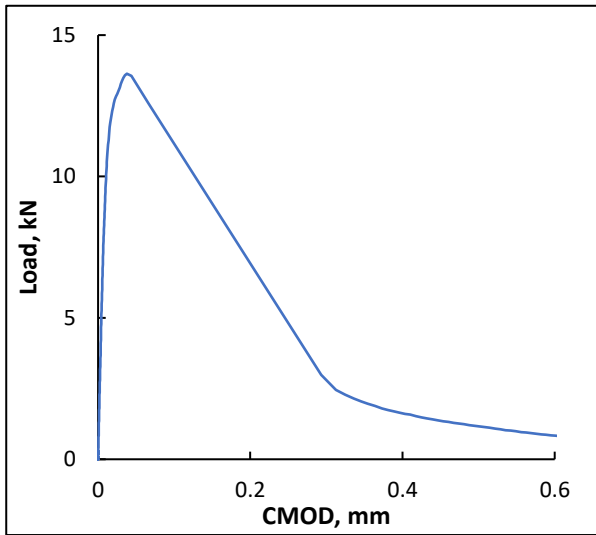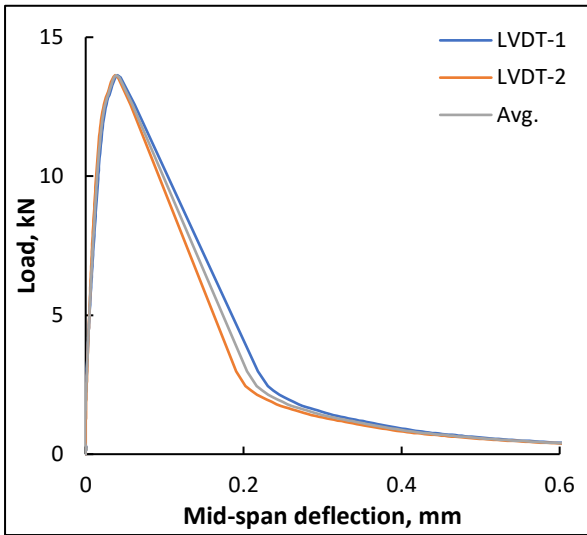
Specimen Name	**WP1-CS**
Depth (mm)	150
Width (mm)	150.5
Notch depth (mm)	126.5
Flexural Strength, $f_{fct,L}$ (MPa)	3.84
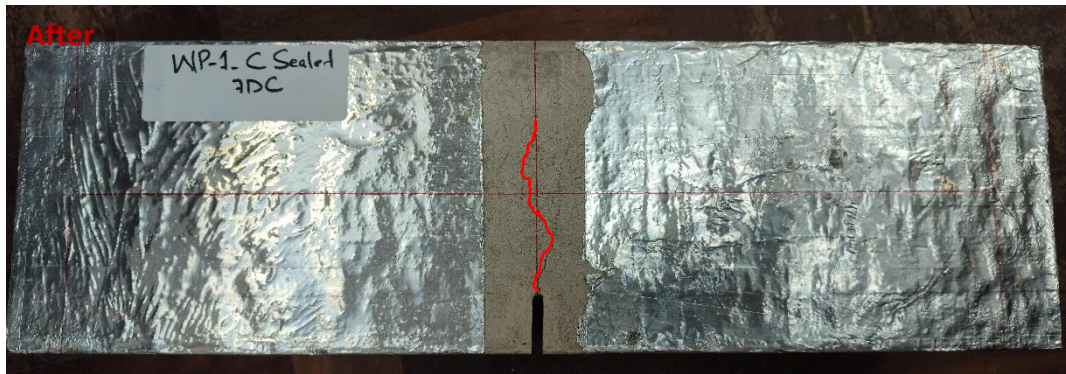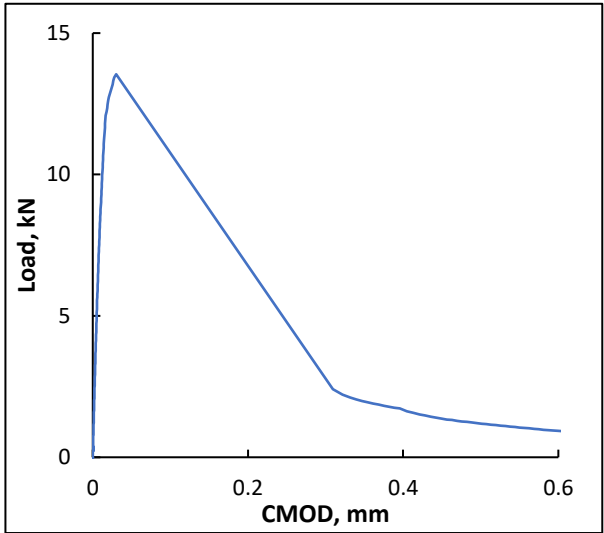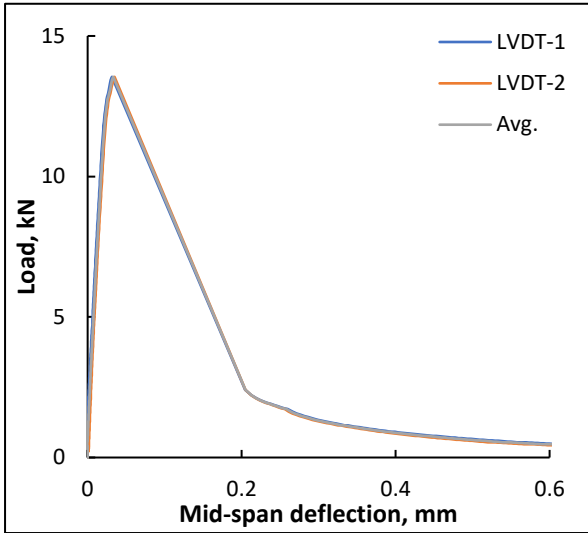
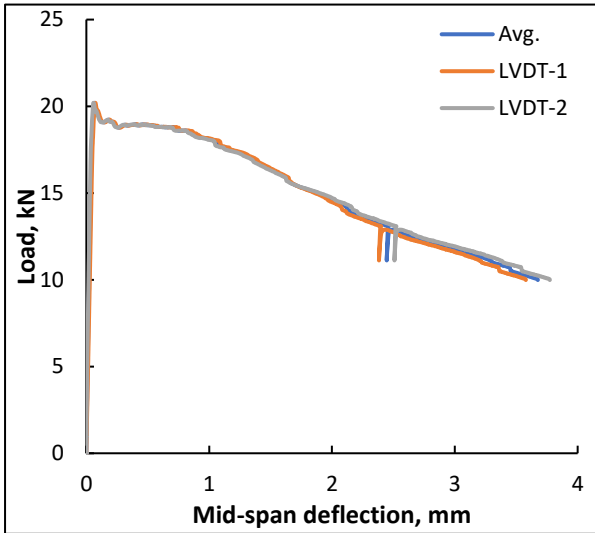| Specimen Name	**WP1-OSE**
Depth (mm)	150
Width (mm)	151
Notch depth (mm)	126
Flexural Strength, $f_{fct,L}$ (MPa)	4.20
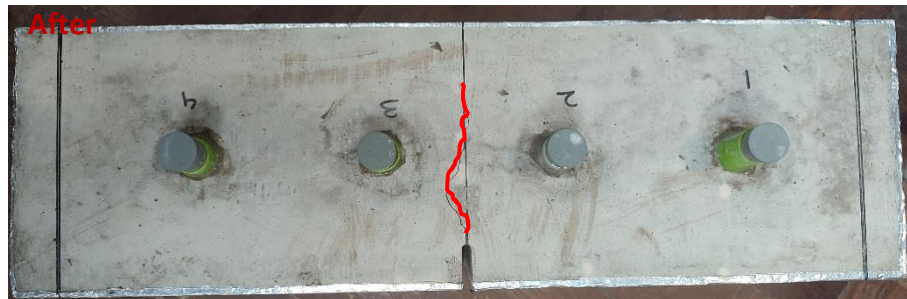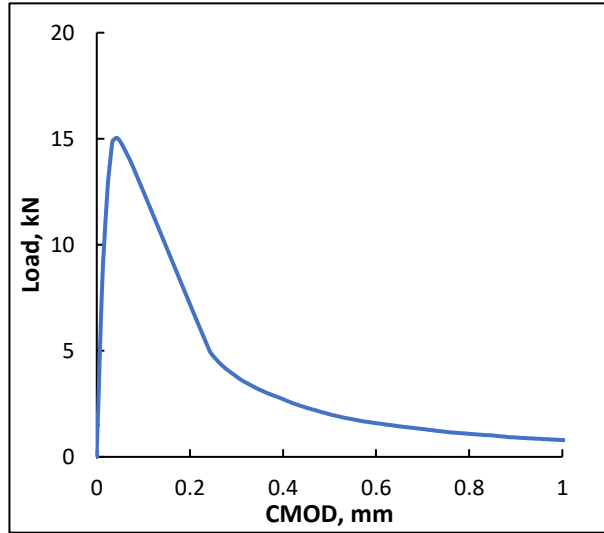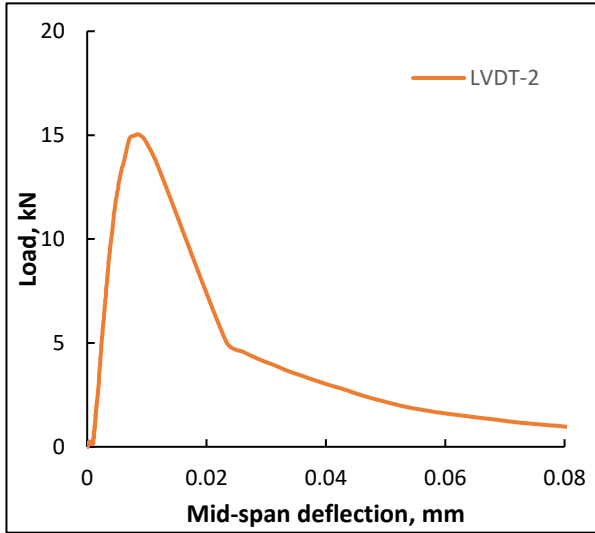
E.2 F30 Concrete Mix

Specimen Name	**WP2-ASE-1**
Depth (mm)	150
Width (mm)	149
Notch depth (mm)	126.5
Flexural Strength, $f_{fct,L}$ (MPa)	5.42
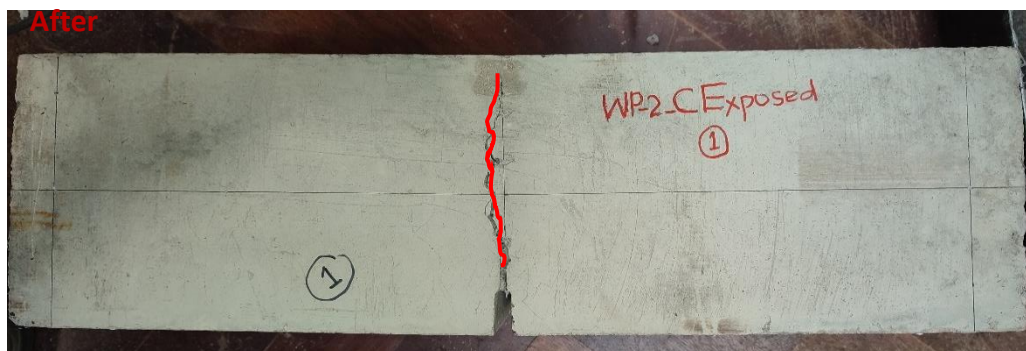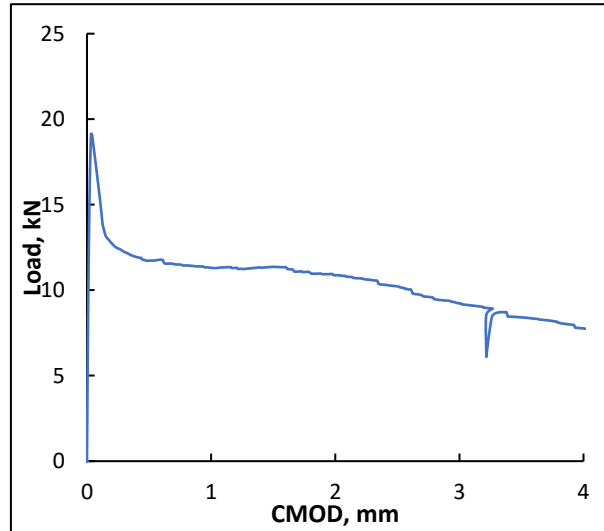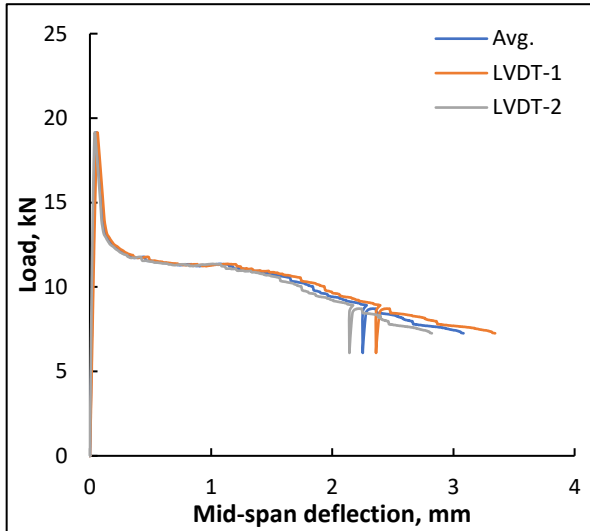
Specimen Name	**WP2-ASE-2**
Depth (mm)	150
Width (mm)	150.33
Notch depth (mm)	125.5
Flexural Strength, $f_{fct,L}$ (MPa)	4.77
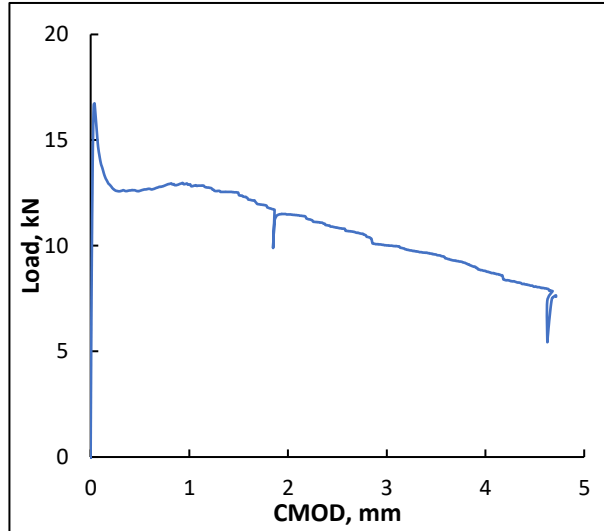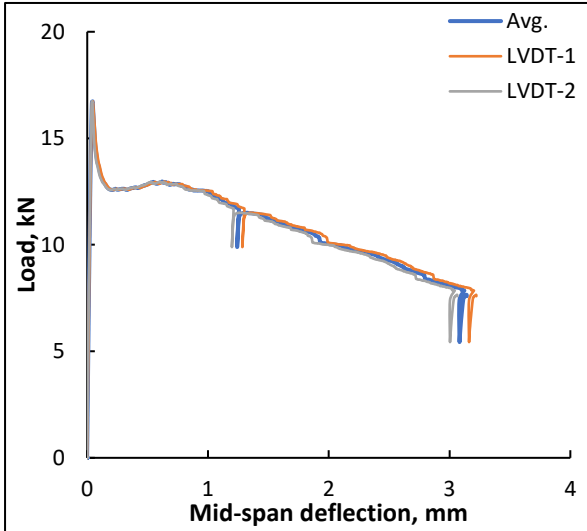
Specimen Name	**WP2-ASE-WRHS**
Depth (mm)	149.67
Width (mm)	151
Notch depth (mm)	127
Flexural Strength, $f_{fct,L}$ (MPa)	6.00
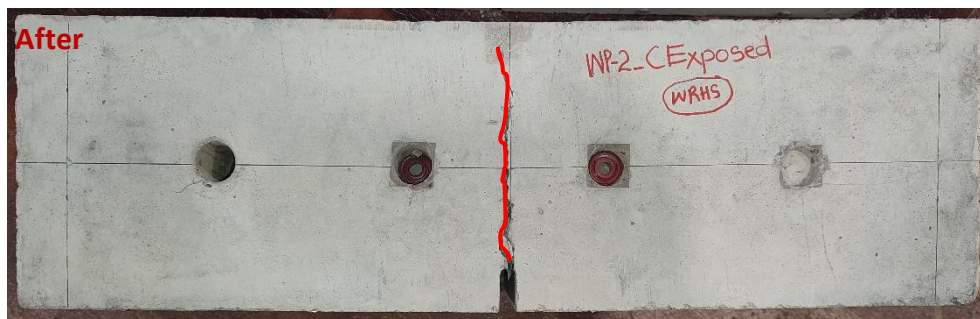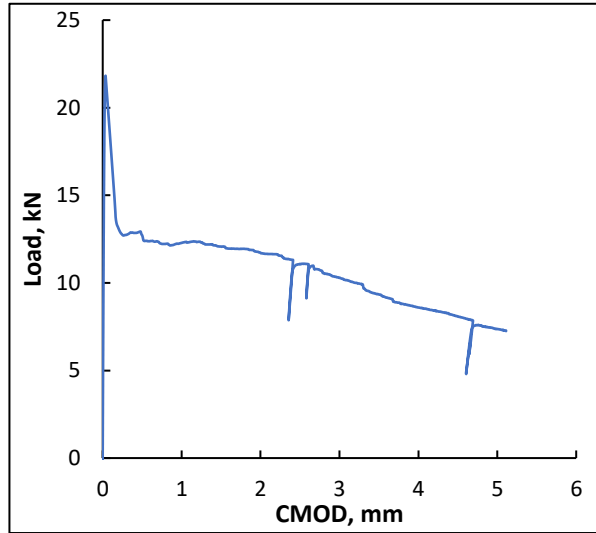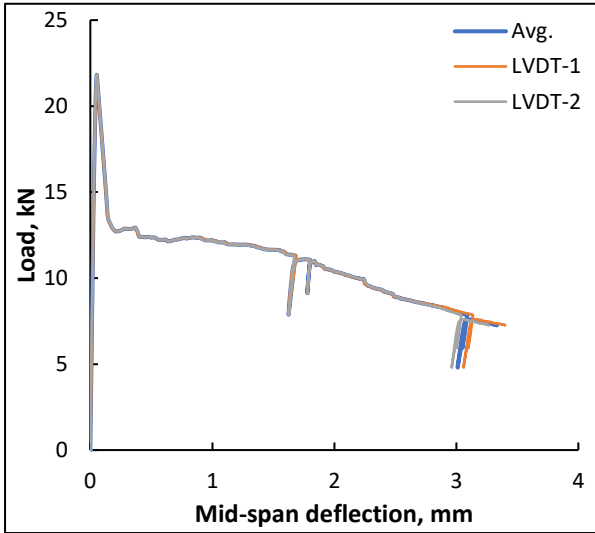
Specimen Name	**WP2-CExposed_IW-1**
Depth (mm)	150
Width (mm)	148.33
Notch depth (mm)	127.5
Flexural Strength, $f_{fct,L}$ (MPa)	3.45
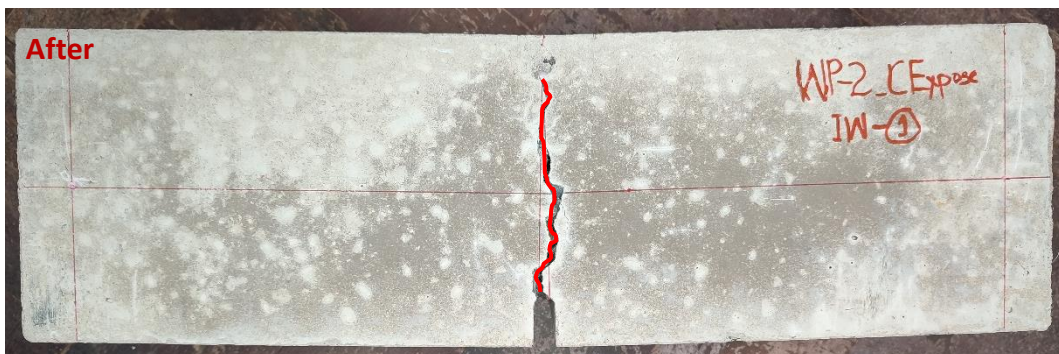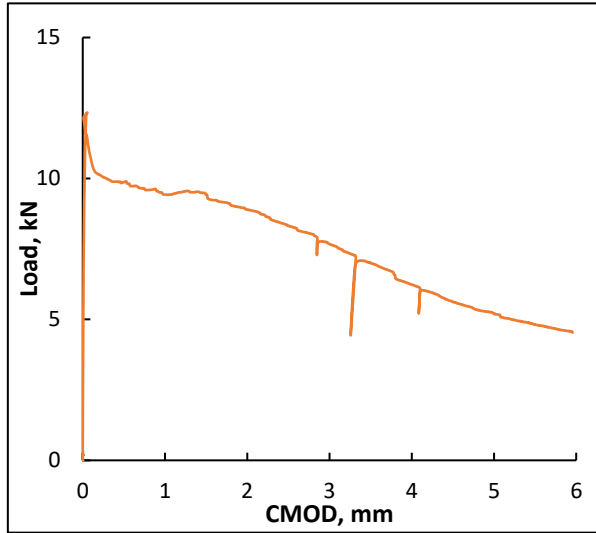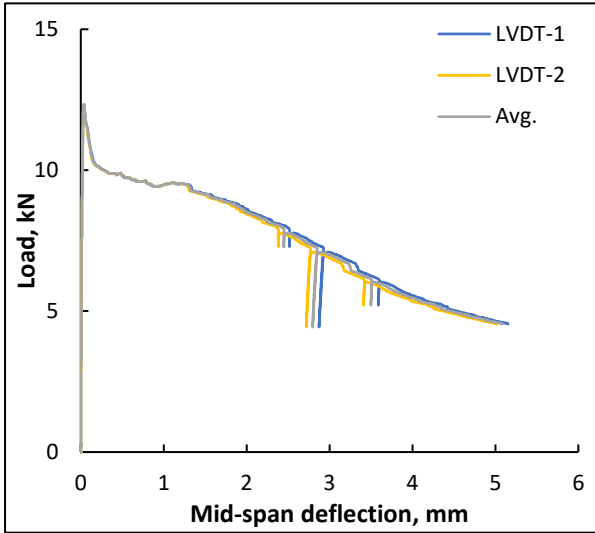
Specimen Name	**WP2-CExposed_IW-2**
Depth (mm)	148.67
Width (mm)	149
Notch depth (mm)	128.5
Flexural Strength, $f_{fct,L}$ (MPa)	4.08
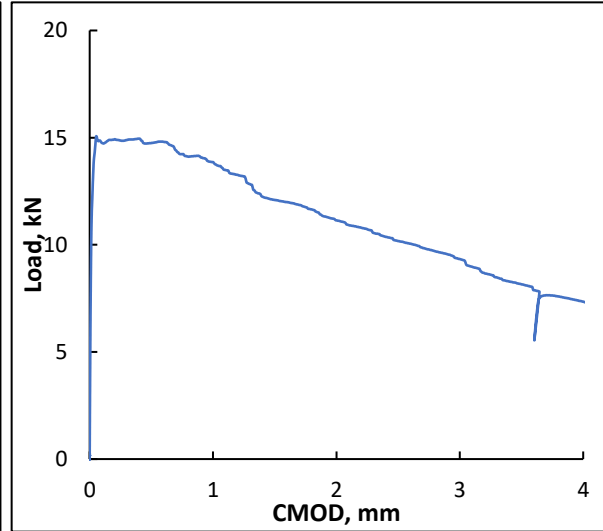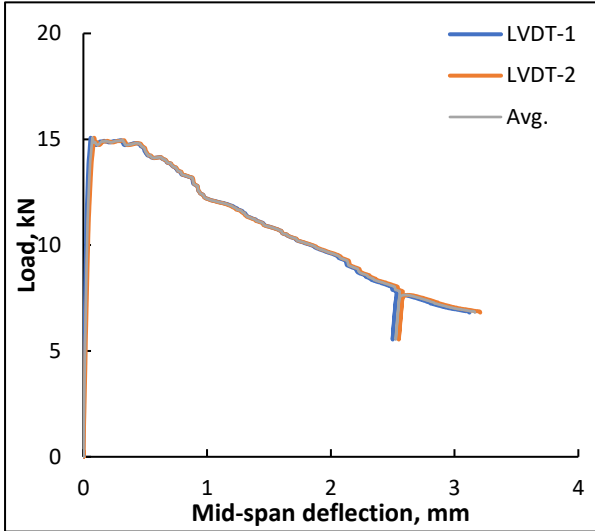
Specimen Name	**WP2-CExposed_IW-3**
Depth (mm)	150
Width (mm)	150.67
Notch depth (mm)	127.5
Flexural Strength, $f_{fct,L}$ (MPa)	3.77
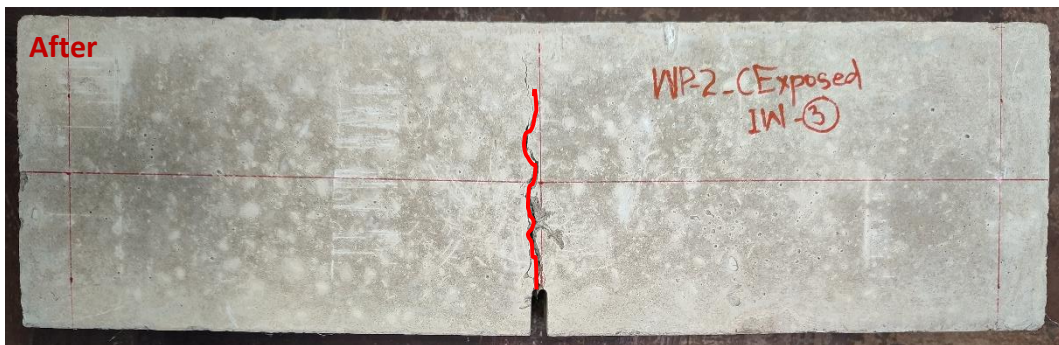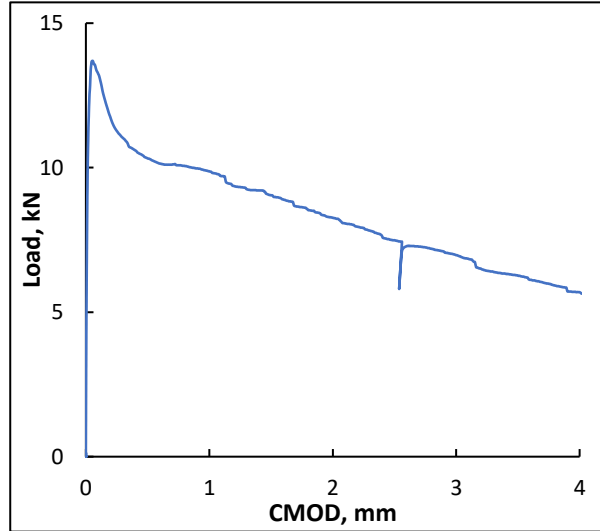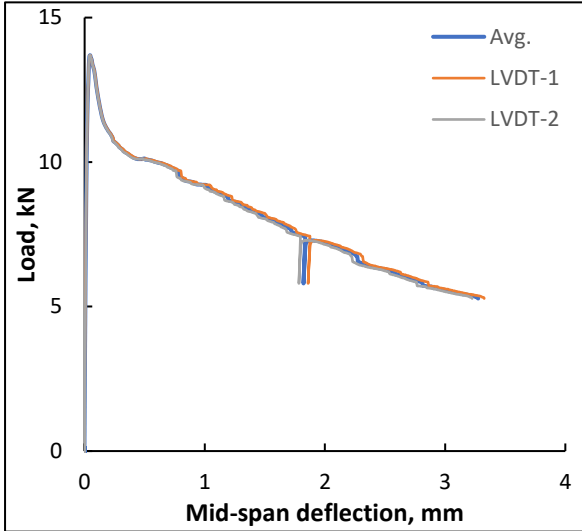
Specimen Name	**WP2-OSE**
Depth (mm)	150
Width (mm)	150.67
Notch depth (mm)	127.5
Flexural Strength, $f_{fct,L}$ (MPa)	4.70
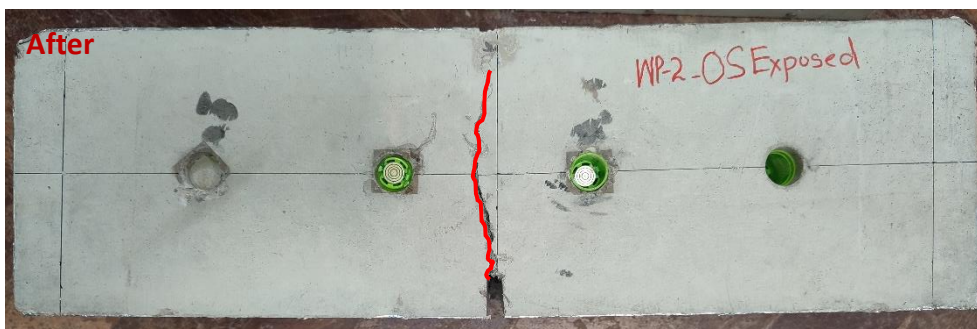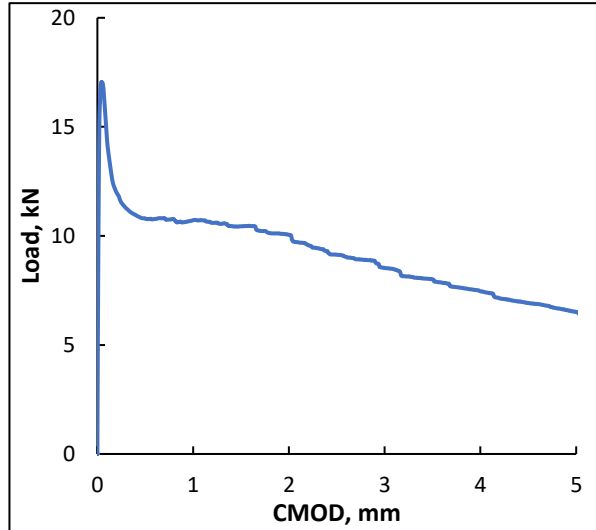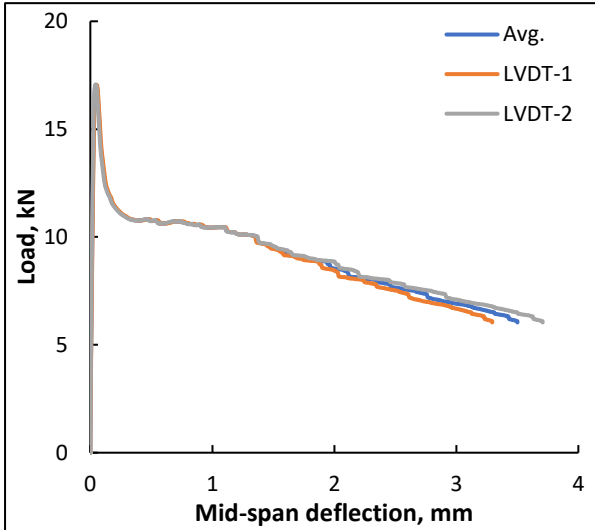
Specimen Name	**WP2-CS**
Depth (mm)	149.33
Width (mm)	150.33
Notch depth (mm)	127
Flexural Strength, $f_{fct,L}$ (MPa)	4.53
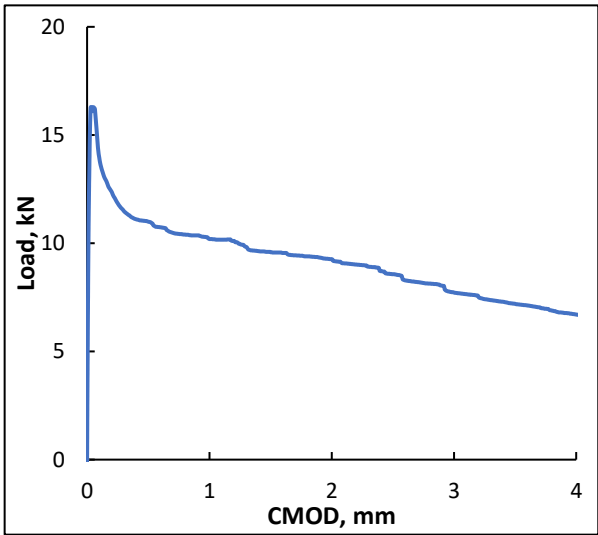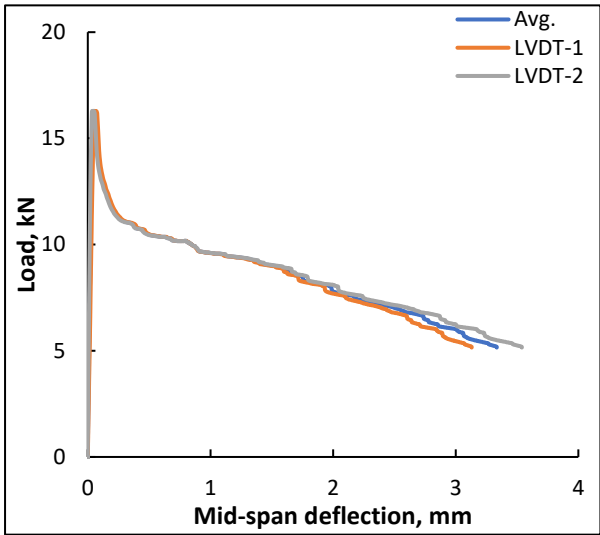
E.3 F40 Concrete Mix

Specimen Name	**WP3-ASE-1**
Depth (mm)	149.67
Width (mm)	150.67
Notch depth (mm)	125
Flexural Strength, $f_{fct,L}$ (MPa)	5.72
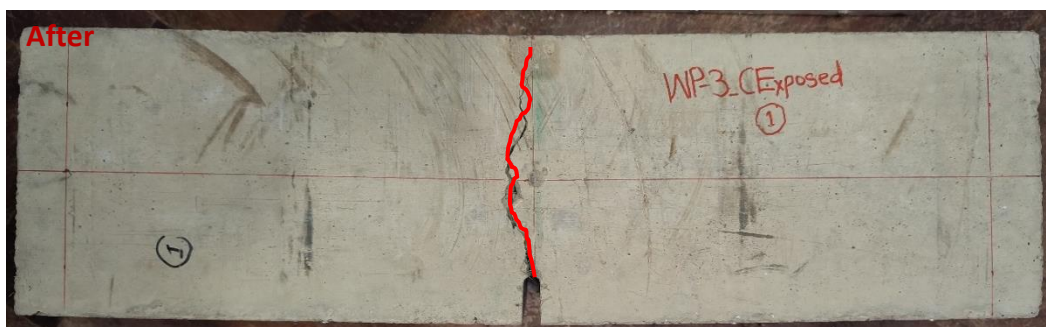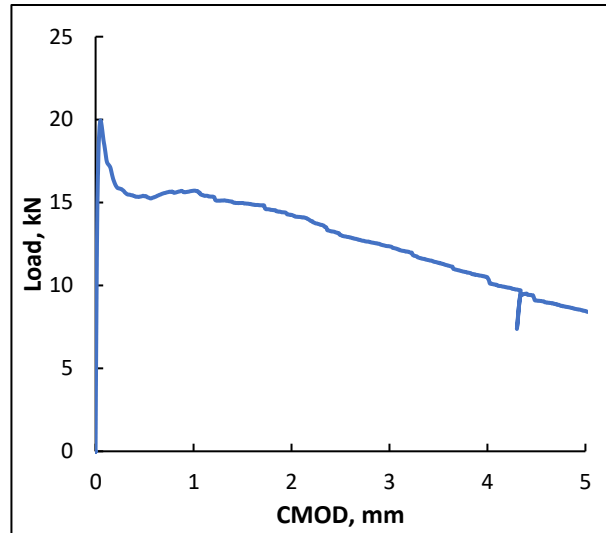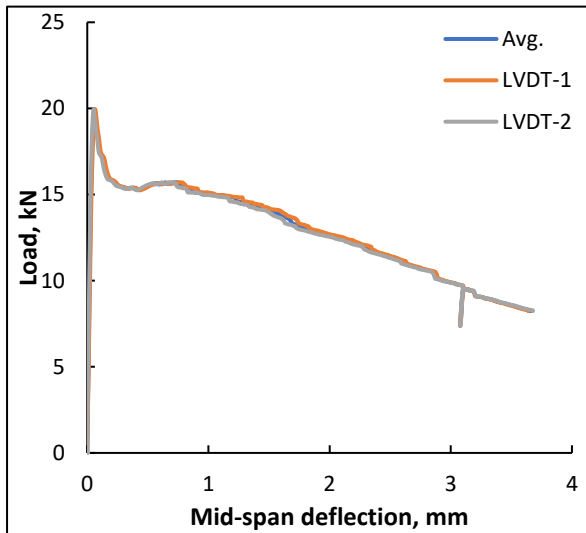
Specimen Name	**WP3-ASE-2**
Depth (mm)	150.33
Width (mm)	150
Notch depth (mm)	126
Flexural Strength, $f_{fct,L}$ (MPa)	5.73
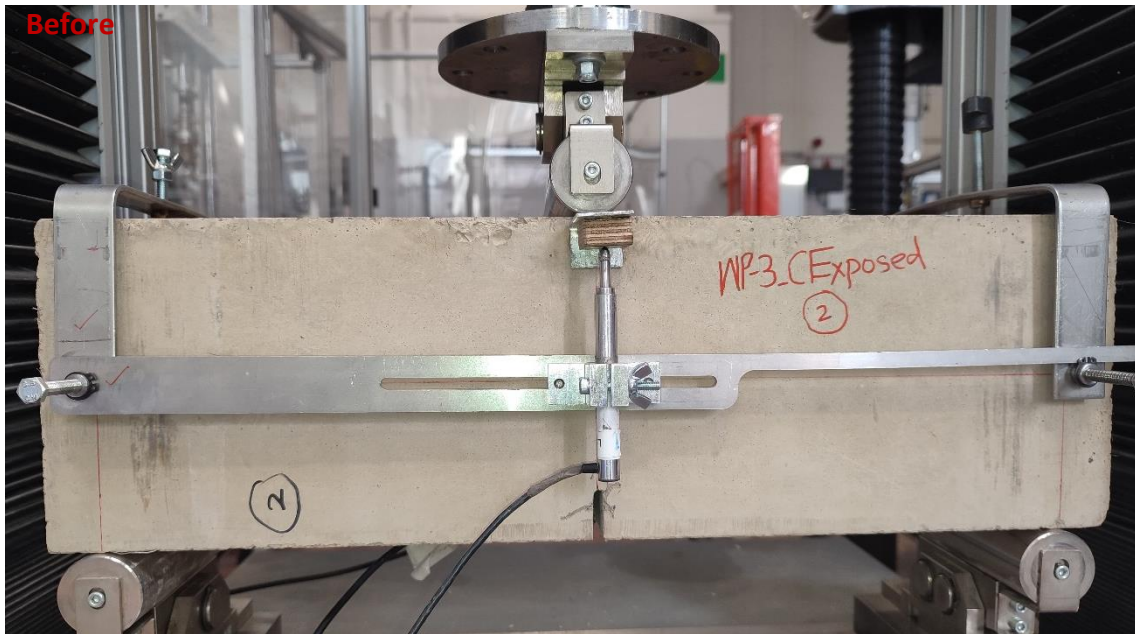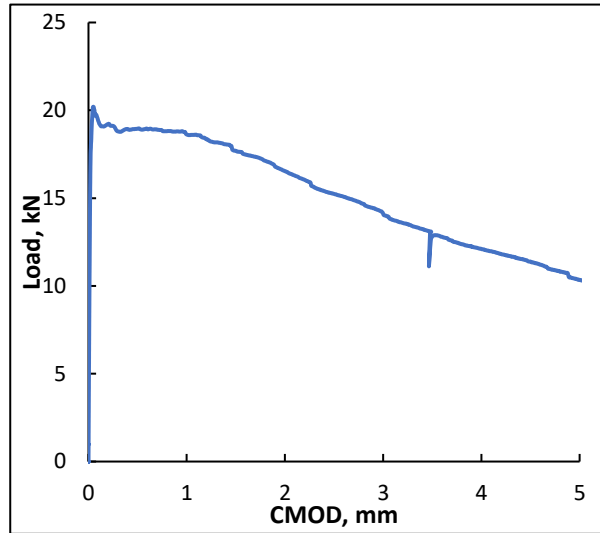
Specimen Name	**WP3-ASE-WRHS**
Depth (mm)	150
Width (mm)	150.33
Notch depth (mm)	126
Flexural Strength, $f_{fct,L}$ (MPa)	5.39
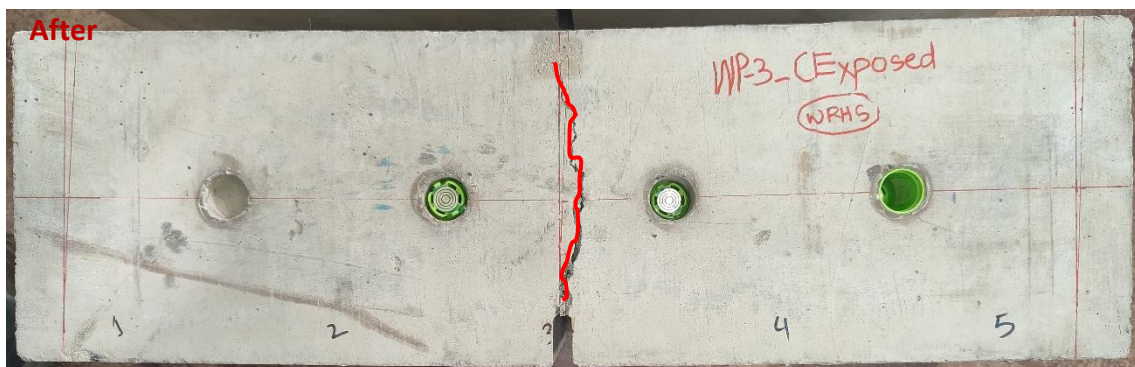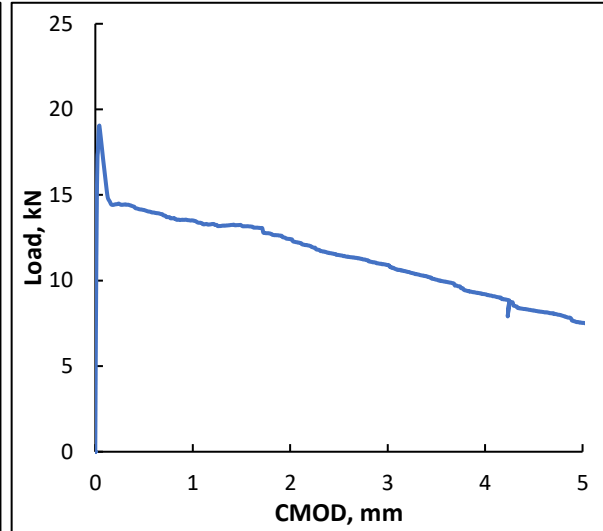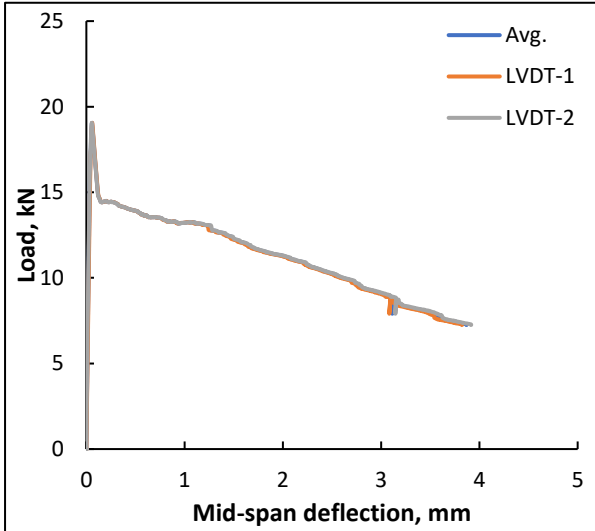
Specimen Name	**WP3-CExposed_IW-1**
Depth (mm)	150
Width (mm)	150.67
Notch depth (mm)	128
Flexural Strength, $f_{fct,L}$ (MPa)	4.27
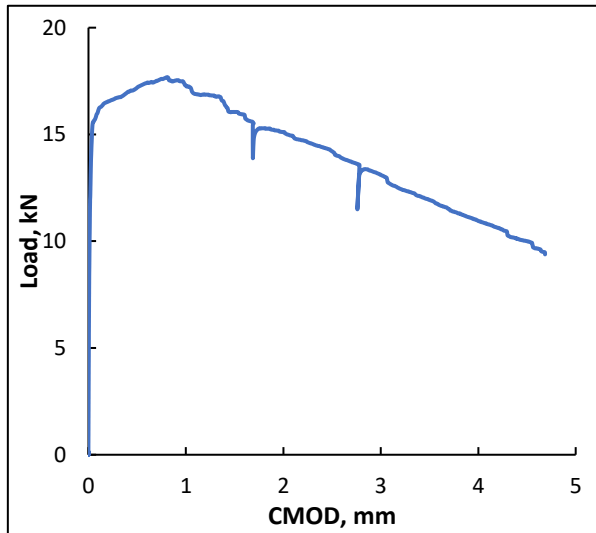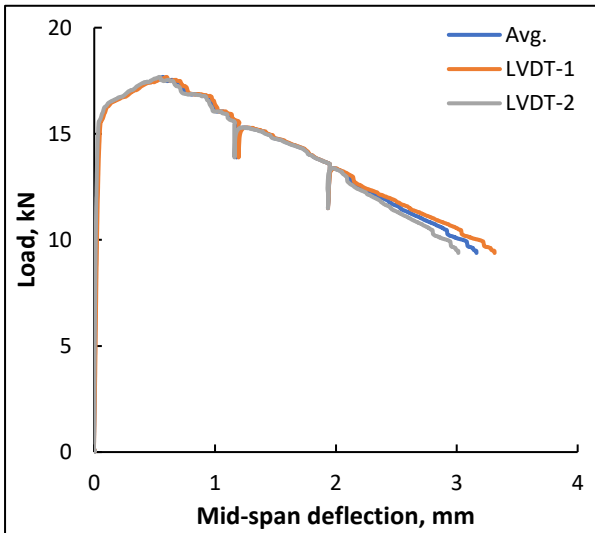
Specimen Name	**WP3-CExposed_IW-2**
Depth (mm)	150
Width (mm)	151
Notch depth (mm)	126.5
Flexural Strength, $f_{fct,L}$ (MPa)	4.02
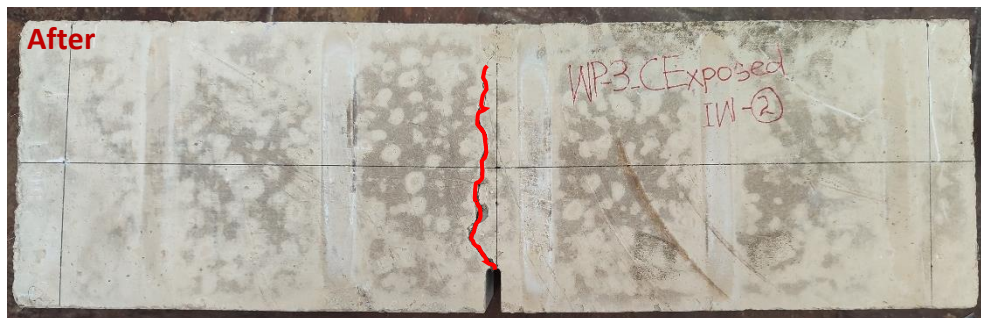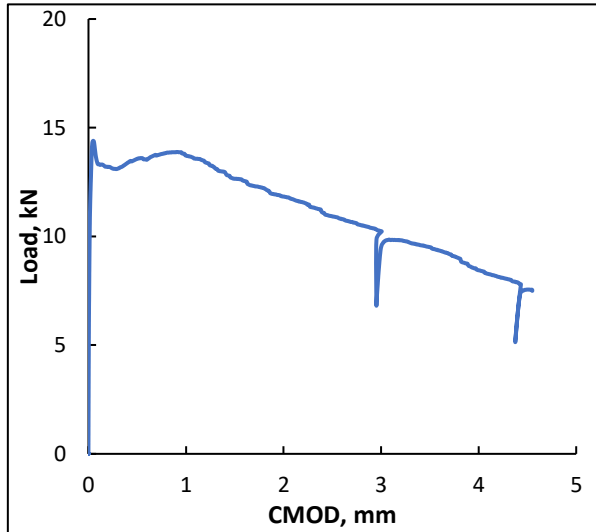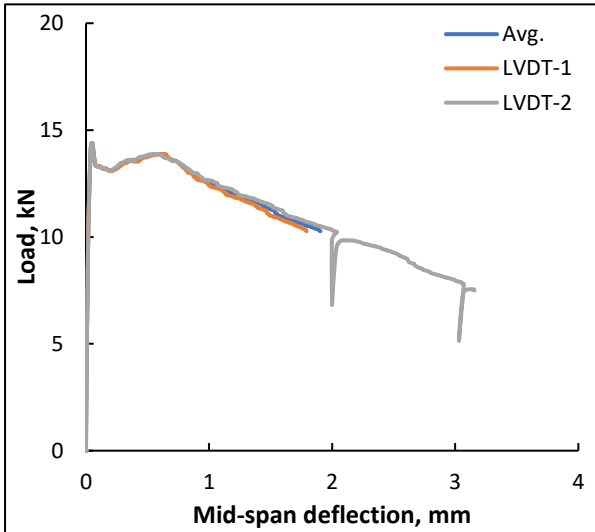
Specimen Name	**WP3-CExposed_IW-3**
Depth (mm)	149.67
Width (mm)	149.33
Notch depth (mm)	127.5
Flexural Strength, $f_{fct,L}$ (MPa)	4.07
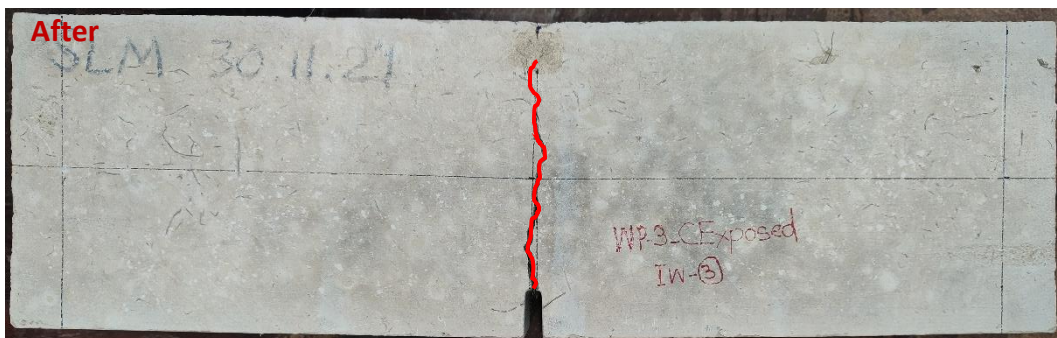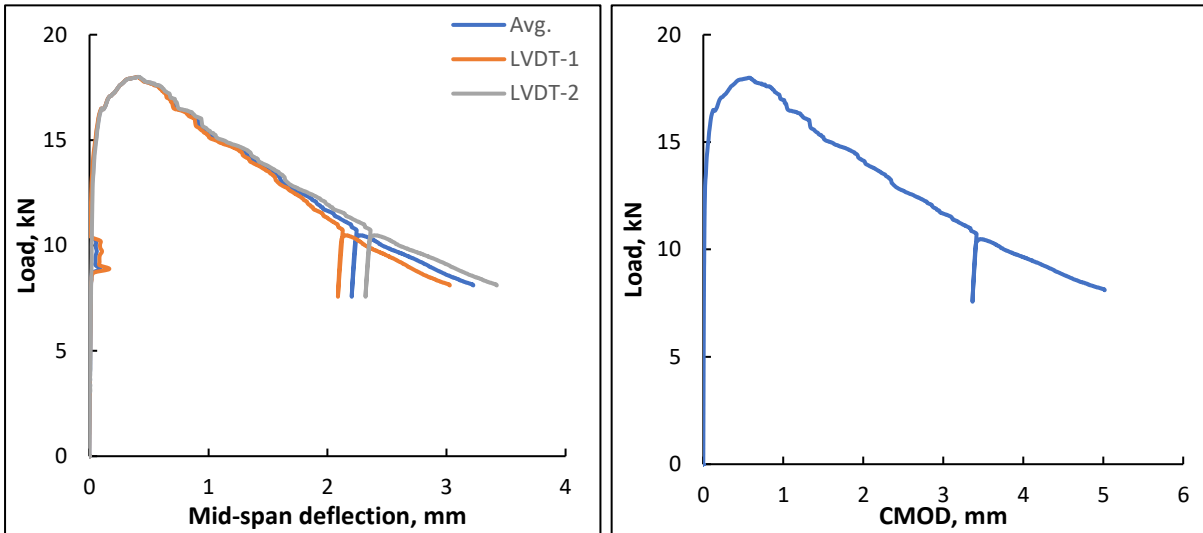
Specimen Name	**WP3-OSE**
Depth (mm)	149.67
Width (mm)	149.67
Notch depth (mm)	126.5
Flexural Strength, $f_{fct,L}$ (MPa)	4.94
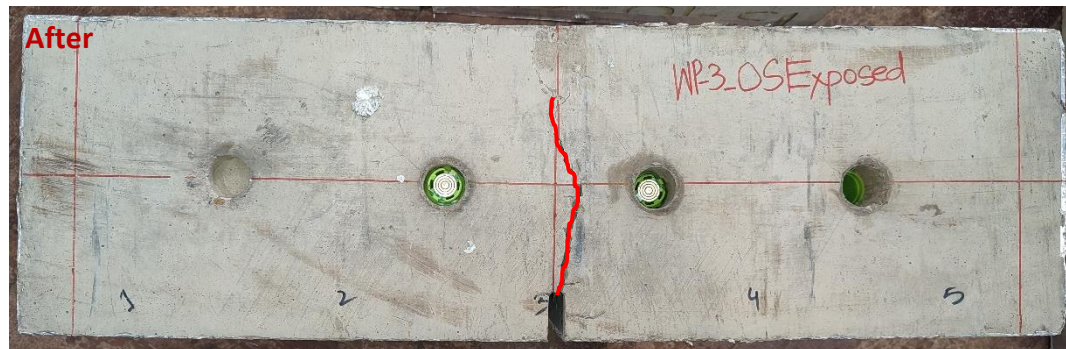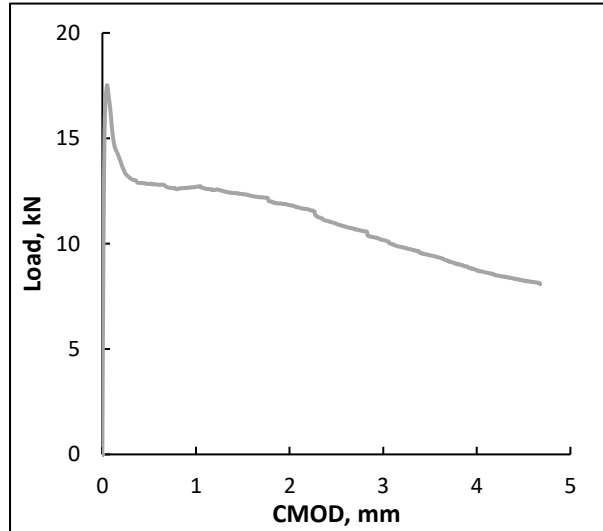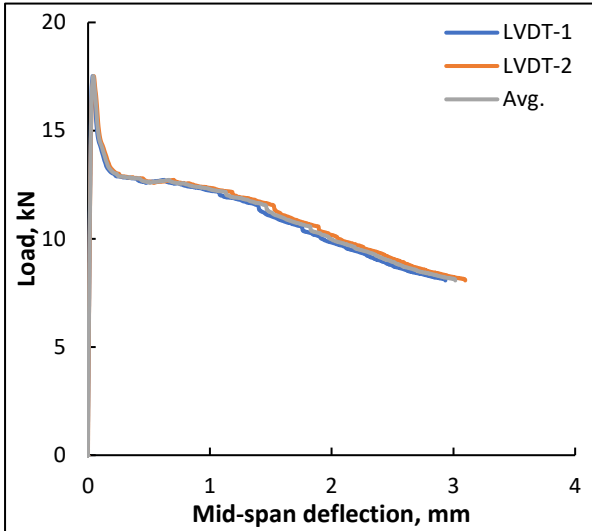
Specimen Name	**WP3-CS**
Depth (mm)	151
Width (mm)	151.33
Notch depth (mm)	125.5
Flexural Strength, $f_{fct,L}$ (MPa)	5.02
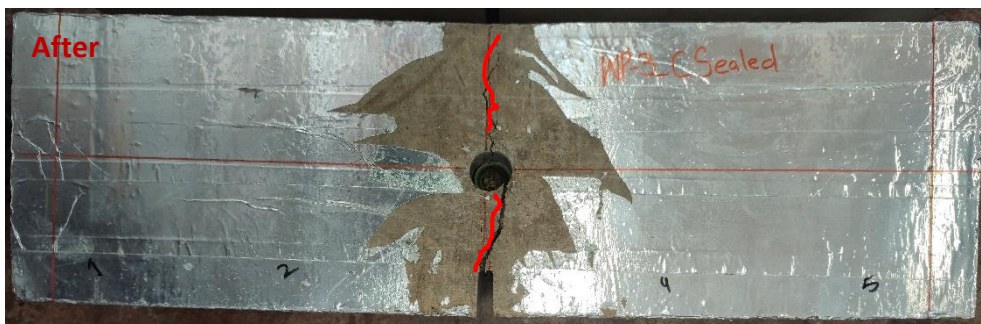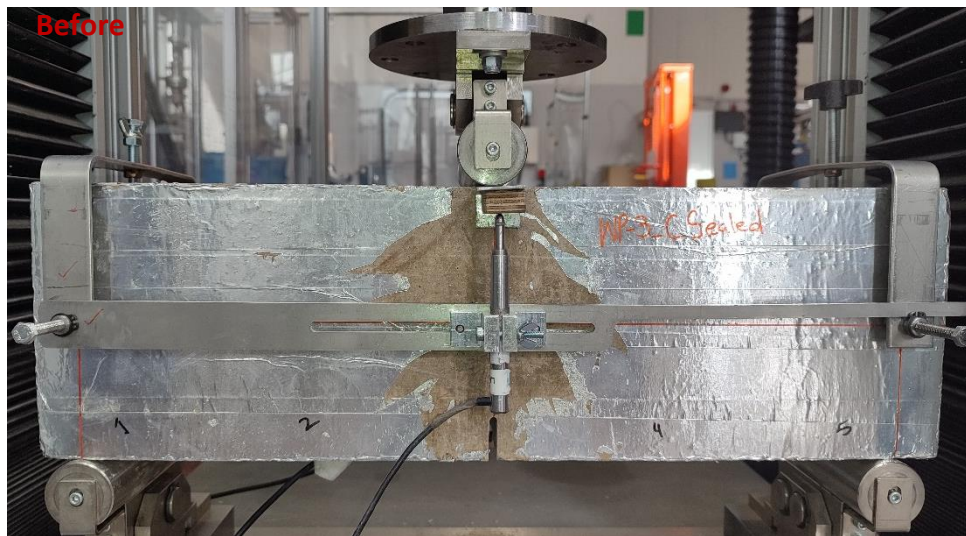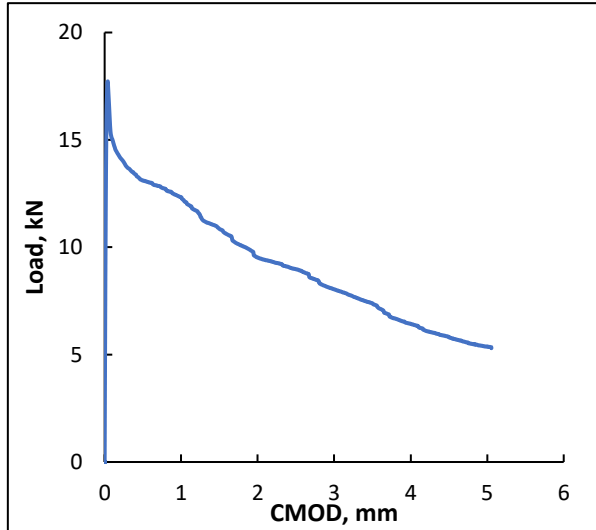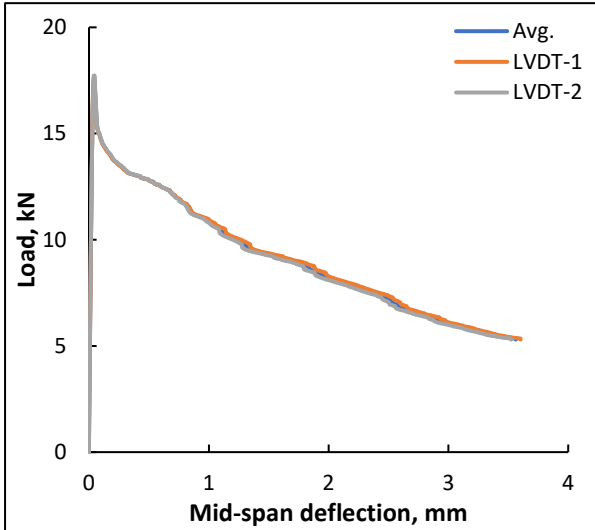
Appendix F: Calibrated Load-deflection Curves

This appendix presents numerically calibrated load-deflection curves of the three-point bending tests. The concrete damage plasticity material model (CDP) input parameters are calibrated through inverse analysis to get the curve close to the experimental. The numerical load-deflection curves are also compared with the curves based on Model Code 2010 and RILEM-suggested stress-strain parameters.

Section F.1 has an FEA two-dimensional (2D) deformable planar shell element having 4-noded bilinear plane stress quadrilateral element (CPS4R) geometry of the prism. Whilst sections F.2, F.3 and F4 summarize all the curves of the F30 and F40 specimens and inverse analysis of multilinear stress strains for the CDP material model, respectively.

F.1   FEA Geometry

F.2   F30 Concrete

F30: OSE

F30: ASE

F30: ASE_W

F.3 F40 Concrete

F40: OSE

F40: ASE

F40: ASE_W
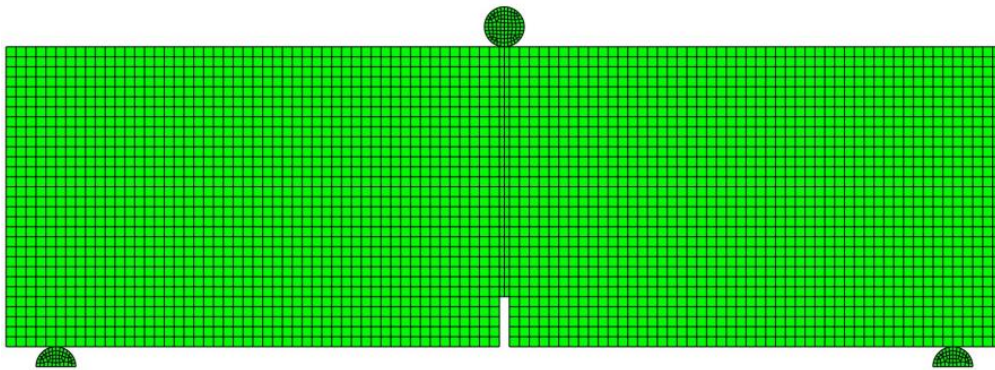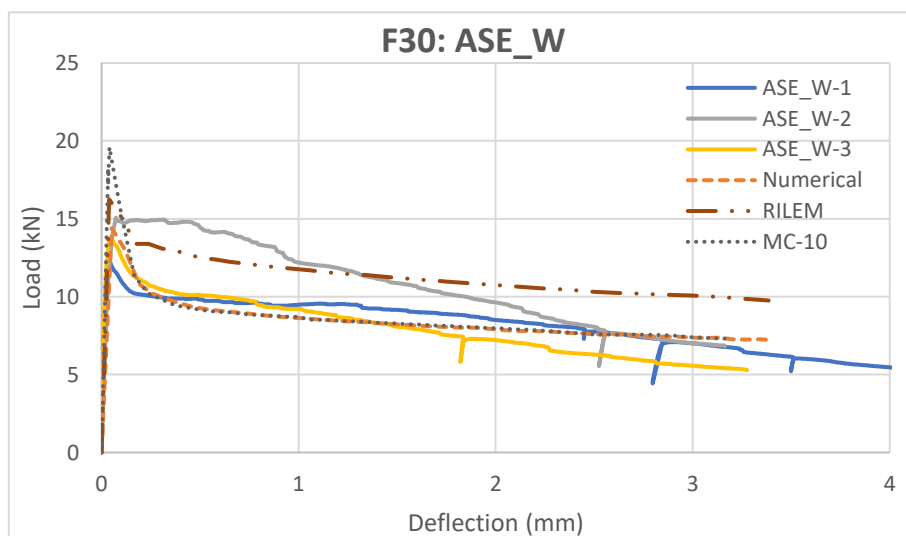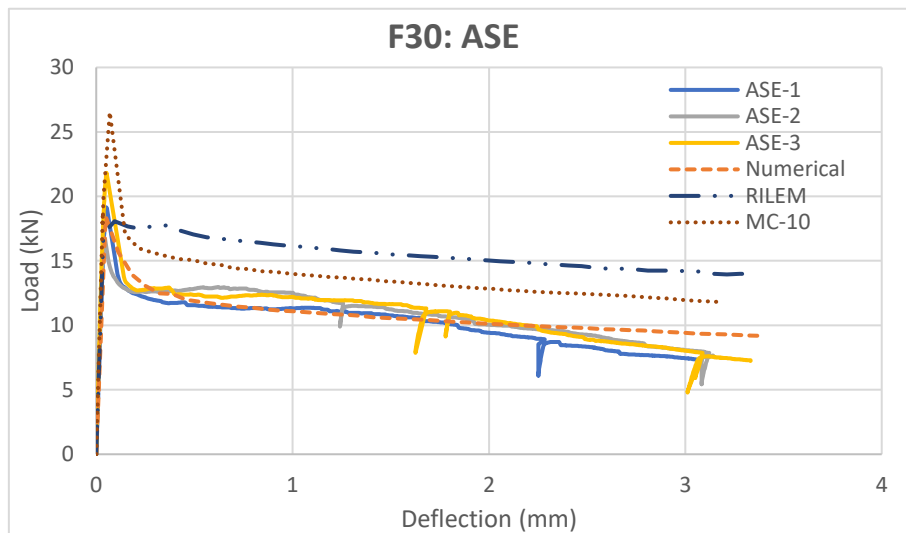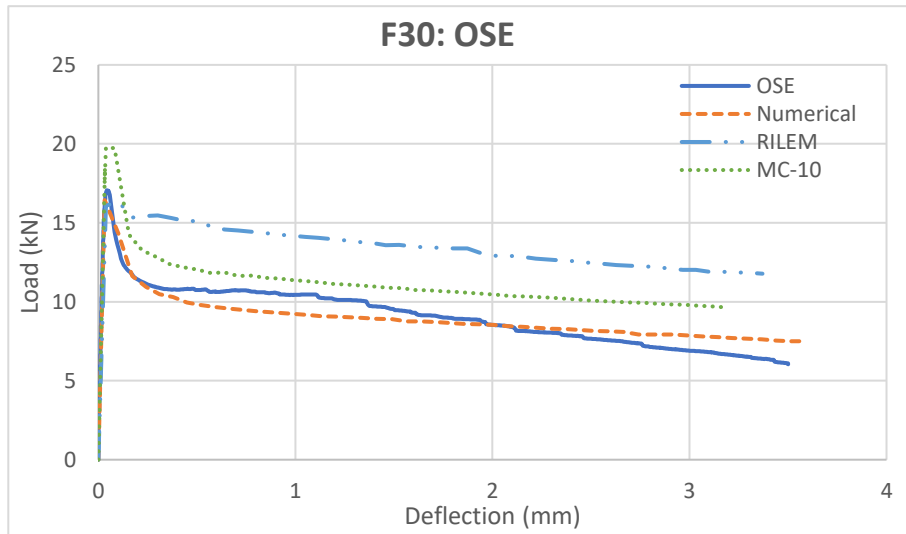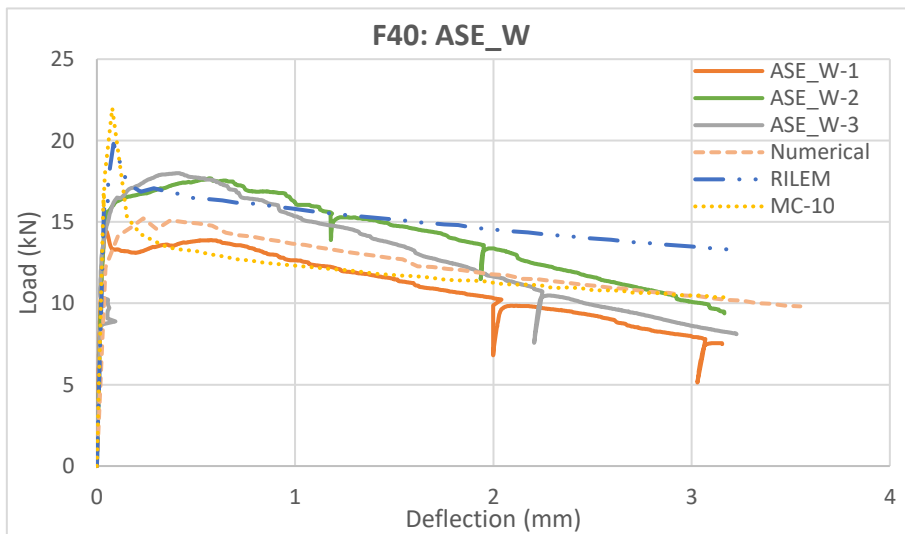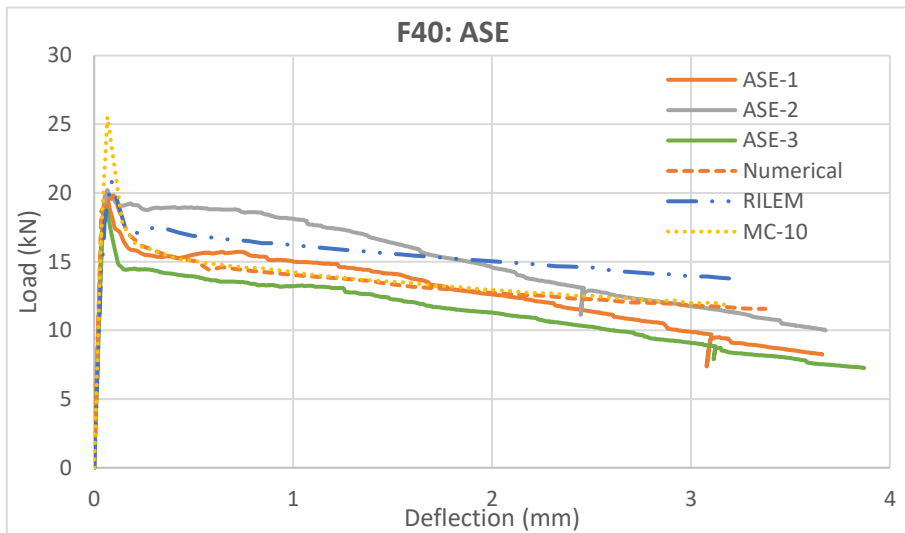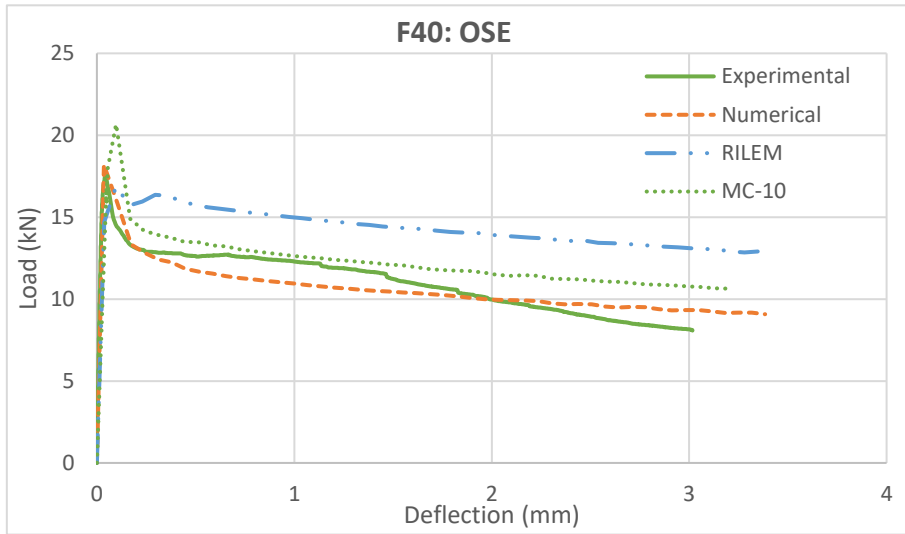
F.4   Back Calculated Tensile Stress-Strain Multilinear Relationship

F30: Stress vs Strain

F40: Stress vs Strain
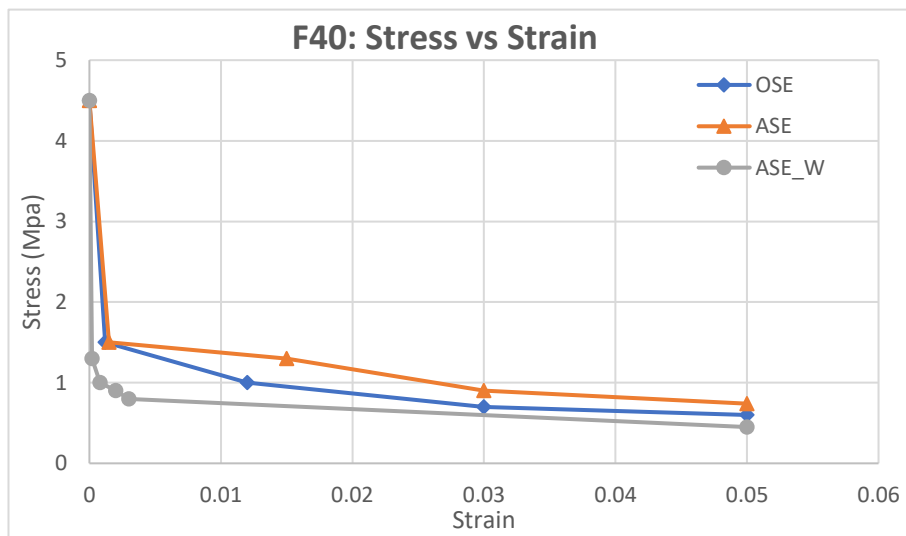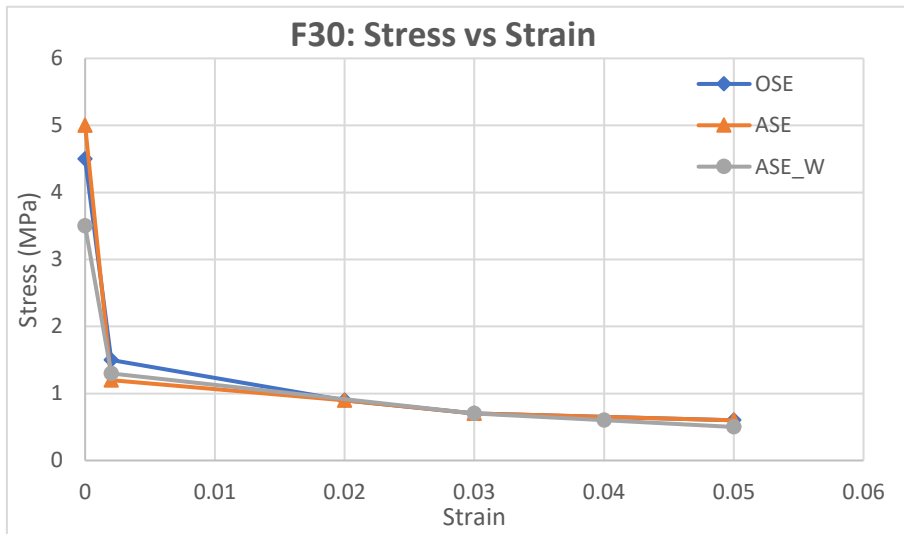
Appendix G: Strength and Shrinkage Prediction Models

This appendix provides a summary of prediction models. Section G.1 provides details of compressive strength models. Section G.2 summarises autogenous and drying shrinkage prediction models. Finally, section G.3 has tensile stress-strain models for fibre-reinforced concrete.

G. 1   Compressive Strength Prediction Models

G.1.1   Model Code 2010

$$f_{cm}(t) = \beta_{cc}(t) \cdot f_{cm}$$

$$\beta_{cc}(t) = exp\left\{s \cdot \left[1 - \left(\frac{28}{t}\right)^{0.5}\right]\right\}$$

Where:

$f_{cm}(t)$ = mean compressive strength in MPa at an age t in days;

f_{cm} = mean compressive strength in MPa at an age of 28 days in days;

$\beta_{cc}(t)$ = function of strength development with time t;

t = age of concrete in days;

s = coefficient depends on the strength class of cement as given in Table G.1

Table G. 1 Coefficient s for different types of cement.

f_{cm} (MPa)	Strength class of cement	s	α_{bs}
≤60	32.5N	0.38	800
	32.5R, 42.5N	0.25	700
	42.5R, 52.5N, 52.5R	0.20	600
>60	All classes	0.20	

G.1.2   ACI 209

$$f_{cmt} = f_{cm28}\left(\frac{t}{a + bt}\right)$$

Where:

f_{cmt} = mean compressive strength at any time t;

f_{cm28} = concrete mean compressive strength at 28 days

a and b = constants a and b are functions of both the type of cement used and the type of curing employed as given in Table G.2

Table G. 2 Values of constants a and b.

Type of cement	Moist-cured concrete		Steam-cured concrete	
	a	b	a	b
I	4.0	0.85	1.0	0.95
II	2.3	0.92	0.70	0.98

G. 2 Shrinkage Prediction Models

G.2.1 Eurocode 2

$$\varepsilon_{cs} = \varepsilon_{cd} + \varepsilon_{ca}$$

$$\varepsilon_{cd}(t) = \beta_{ds}(t, t_s) \cdot k_h \cdot \varepsilon_{cd,0}$$

$$\beta_{ds}(t, t_s) = \frac{(t - t_s)}{(t - t_s) + 0.04 \sqrt{h_0{}^3}}$$

$$\varepsilon_{cd,0} = 0.85 \left[(220 + 110 \cdot \alpha_{ds1}) \cdot exp\left(-\alpha_{ds2} \cdot \frac{f_{cm}}{f_{cm0}} \right) \right] \cdot 10^{-6} \cdot \beta_{RH}$$

$$\beta_{RH} = 1.55 \left[1 - \left(\frac{RH}{RH_0} \right)^3 \right]$$

$$\varepsilon_{ca}(t) = \beta_{as}(t) \cdot \varepsilon_{ca}(\infty)$$

$$\varepsilon_{ca}(\infty) = 2.5(f_{ck} - 10) \cdot 10^{-6}$$

$$\beta_{as}(t) = 1 - exp(-0.2t^{0.5})$$

Where:

ε_{cs} = total shrinkage strain;

ε_{cd} = drying shrinkage strain;

ε_{ca} = autogenous shrinkage strain;

k_h = coefficient depending on the notional size $h_0 = \dfrac{2A_c}{u}$ as given in Table G.3;

A_c = concrete cross-sectional area;

u = perimeter of the part of the cross-section which is exposed to drying;

$\varepsilon_{cd,0}$ = basic drying shrinkage strain;

t = age of concrete at the moment considered, in days;

t_s = age of concrete (in days) at the beginning of drying shrinkage;

f_{cm} = mean compressive strength (in MPa);

f_{cm0} = 10 MPa;

α_{ds1} and α_{ds2} = coefficients which depend on the type of cement as given in Table G.4;

RH = ambient relative humidity (in %);

RH_0 = 100%;

Table G.3 Values of k_h.

h_0	k_h
100	1.0
200	0.85
300	0.75
$\geq$500	0.70

Table G.4 Values of coefficients α_{ds1} and α_{ds2}.

Type of cement	Strength class of cement	α_{ds1}	α_{ds2}
Class S	32.5N	3	0.13
Class N	32.5R, 42.5N	4	0.12
Class R	42.5R, 52.5N, 52.5R	6	0.11

G.2.2 Model Code 2010

$$\varepsilon_{cs}(t, t_s) = \varepsilon_{cbs}(t) + \varepsilon_{cds}(t, t_s)$$

$$\varepsilon_{cbs}(t) = \varepsilon_{cbs0}(f_{cm}) \cdot \beta_{bs}(t)$$

$$\varepsilon_{cds}(t, t_s) = \varepsilon_{cds0}(f_{cm}) \cdot \beta_{RH}(RH) \cdot \beta_{ds}(t - t_s)$$

$$\varepsilon_{cbs0}(f_{cm}) = -\alpha_{bs} \left\{ \frac{0.1 f_{cm}}{6 + 0.1 f_{cm}} \right\}^{2.5} \cdot 10^{-6}$$

$$\beta_{bs}(t) = 1 - \exp(-0.2 \cdot \sqrt{t})$$

$$\varepsilon_{cds0}(f_{cm}) = [(220 + 110 \cdot \alpha_{ds1}) \cdot exp(-\alpha_{ds2} \cdot f_{cm})] \cdot 10^{-6}$$

$$\beta_{RH}(RH) = -1.55 \cdot \left[1 - \left(\frac{RH}{100} \right)^3 \right] \, for \, 40 \leq RH < 99\% \cdot \beta_{s1}$$
$$\beta_{RH}(RH) = 0.25 \, for \, RH \geq 99\% \cdot \beta_{s1}$$

$$\beta_{ds}(t - t_s) = \left[\frac{(t - t_s)}{0.035 \cdot h^2 + (t - t_s)} \right]^{0.5}$$

$$\beta_{s1} = \left[\frac{35}{f_{cm}} \right]^{0.1} \leq 1.0$$

Where:

$\varepsilon_{cs}(t, t_s)$ = the total shrinkage;

$\varepsilon_{cbs}(t)$ = basic/autogenous shrinkage;

$\varepsilon_{cds}(t, t_s)$ = drying shrinkage

t = age of the concrete, in days;

t_s = age of concrete (in days) at the beginning of drying shrinkage;

$t - t_s$ = duration of drying in days;

f_{cm} = mean compressive strength of concrete at 28 days in MPa;

α_{bs} = coefficient depends upon the type of cement as given in Table G.1;

α_{ds1} and α_{ds2} = coefficients which depend on the type of cement as given in Table G.4;

RH = relative humidity of the ambient environment in %;

$h = {2A_c}/{u}$, notional size of the member in mm

A_c = concrete cross-sectional area in mm^2;

u = perimeter of the part of the cross-section, in mm, which is exposed to drying;

G.2.3 ACI 209 (all formulae are SI unit based)

$$\varepsilon_{sh}(t, t_c) = \frac{(t - t_c)^\alpha}{f + (t - t_c)^\alpha} \cdot \varepsilon_{shu}$$

$$\varepsilon_{shu} = 780 \times 10^{-6} \cdot \gamma_{sh} \, {}^{mm}/_{mm} \, OR \, {}^{in.}/_{in.}$$

$$f = 26.0e^{\{1.42 \times 10^{-2}(V/_S)\}}$$

$$\gamma_{sh} = \gamma_{sh,tc} \cdot \gamma_{sh,RH} \cdot \gamma_{sh,vs} \cdot \gamma_{sh,s} \cdot \gamma_{sh,\psi} \cdot \gamma_{sh,c} \cdot \gamma_{sh,\alpha}$$

$$\gamma_{sh,tc} = 1.202 - 0.2337\log(t_c)$$

$$\gamma_{sh,RH} = 1.40 - 1.02h \qquad for \; 0.40 \leq h \leq 0.80$$
$$\gamma_{sh,RH} = 3.00 - 3.00h \qquad for \; 0.80 \leq h \leq 1$$

$$\gamma_{sh,vs} = 1.2e^{\{-0.00472(V/_S)\}}$$

$$\gamma_{sh,s} = 0.89 + 0.00161s$$

$$\gamma_{sh,\psi} = 0.30 + 0.014\psi \qquad for \; \psi \leq 50\%$$
$$\gamma_{sh,\psi} = 0.90 + 0.002\psi \qquad for \; \psi > 50\%$$

$$\gamma_{sh,c} = 0.75 + 0.00061c$$

$$\gamma_{sh,\alpha} = 0.95 + 0.008\alpha \geq 1$$

Where:

$\varepsilon_{sh}(t, t_c)$ = shrinkage strain at the age of concrete t, in days, measured from the start of drying at t_c in days;

$f \; and \; \alpha$ = shape and size factors that define the time-ration part;

208

ε_{shu} = ultimate shrinkage strain;

$t - t_c$ = time from the end of initial curing;

V/S = volume to surface ratio;

γ_{sh} = cumulative product of the applicable correction factors;

$\gamma_{sh,tc}$ = initial moist curing coefficient;

$\gamma_{sh,RH}$ = ambient relative humidity coefficient;

$\gamma_{sh,vs}$ = volume to surface ratio coefficient;

$\gamma_{sh,s}$ = slump coefficient;

$\gamma_{sh,\psi}$ = fine aggregates coefficient;

$\gamma_{sh,c}$ = cement content coefficient;

$\gamma_{sh,\alpha}$ = air content coefficient;

RH = ambient relative humidity;

h = relative humidity in decimals;

s = slump of fresh concrete;

ψ = ratio of fine aggregates to total aggregates by weight expressed as a percentage;

c = cement content;

α = air content in per cent

G.2.4 B3 Model (all formulae are SI unit based)

$$\varepsilon_{sh}(t, t_c) = -\varepsilon_{sh\infty} \cdot k_h \cdot S(t - t_c)$$

$$\varepsilon_{sh\infty} = -\varepsilon_{s\infty} \frac{E_{cm607}}{E_{cm(t_c+\tau_{sh})}}$$

$$\varepsilon_{s\infty} = -\alpha_1 \cdot \alpha_2 \cdot [0.019w^{2.1}f_{cm28}^{-0.28} + 270] \times 10^{-6}$$

$$E_{cmt} = E_{cm28} \left(\frac{t}{4+0.85t}\right)^{0.5}$$

$$S(t - t_c) = tanh \sqrt{\frac{t - t_c}{\tau_{sh}}}$$

$$\tau_{sh} = 0.085t_c^{-0.08}f_{cm28}^{-0.25}\left[2k_s(V/_S)\right]^2$$

$$E_{cm28} = 4734\sqrt{f_{cm28}}$$

Where:

$\varepsilon_{sh}(t, t_c)$ = mean shrinkage strain

$\varepsilon_{sh\infty}$ = ultimate shrinkage strain;

k_h = humidity dependence factor, as given in Table G.5;

$S(t - t_c)$ = time curve;

$t - t_c$ = time from the end of initial curing;

$\varepsilon_{s\infty}$ = constant;

$\frac{E_{cm607}}{E_{cm(t_c + \tau_{sh})}}$ = factor to account for the time dependence of ultimate shrinkage;

w = water content;

$\alpha_1 and \ \alpha_2$ = constant related to cement type and curing conditions, as given in Table G.6;

t = age of concrete, in days;

t_c = age when drying commenced or end of moist curing, in days;

τ_{sh} = shrinkage half time, in days;

k_s = cross-section shape correction factor, as given in Table G.7;

$V/_S$ = volume over surface ratio;

f_{cm28} = concrete mean compressive strength at 28 days, in MPa;

Table G.5 Humidity dependence k_h.

Relative humidity	k_h
$h \le 0.98$	$1 - h^3$
$h = 1.00$	-0.2
$0.98 < h < 1.00$	$linear\ interpolation: 12.75$ $- 12.94h$

Table G.6 α_1 as function cement type; and α_2 as function of curing condition.

Type of cement	α_1	Curing method	α_2
Type I	1.00	Steam cured	0.75
Type II	0.85	Cured in water OR 100% relative humidity	1.00
Type III	1.10	Sealed during curing OR normal curing in the air with initial protection against drying	1.20

Table G.7 k_s as function cross section shape.

Cross section shape	k_s
Infinite slab	1.00
Infinite cylinder	1.15
Infinite square prism	1.25
Sphere	1.30
Cube	1.55

G.2.5   B4 Model (all formulae are SI unit based)

$$\varepsilon_{sh}(total) = \varepsilon_{au}(\tilde{t} - \tilde{t_0}) + \varepsilon_{sh}(\tilde{t} - \tilde{t_0})$$

$$\varepsilon_{au}(\tilde{t} - \tilde{t_0}) = \varepsilon_{au\infty}\left[1 + \left(\frac{\tau_{au}}{\tilde{t} + \tilde{t_0}}\right)^{\alpha}\right]^{r_t}$$

$$\alpha = r_a\left(\frac{w/c}{0.38}\right)$$

$$\varepsilon_{au\infty} = -\varepsilon_{au,cem}\left(\frac{a/c}{6}\right)^{r_{\epsilon a}}\left(\frac{w/c}{0.38}\right)^{r_{\epsilon w}}$$

$$\tau_{au} = \tau_{au,cem}\left(\frac{w/c}{0.38}\right)^{r_{\tau w}}$$

$$\varepsilon_{sh}(\tilde{t} - \tilde{t_0}) = \varepsilon_{sh\infty}(\tilde{t_0})k_h S(\tilde{t})$$

$$S(\tilde{t}) = tanh\sqrt{\frac{\tilde{t}}{\tau_{sh}}}$$

$$\varepsilon_{sh\infty}(\widetilde{t_0}) = -\epsilon_0 k_{\epsilon a} \frac{E(7\beta_{Th} + 600\beta_{Ts})}{E(\widetilde{t_0} + \tau_{sh}\beta_{Ts})}$$

$$\epsilon_0 = \epsilon_{cem} \left(\frac{a/c}{6}\right)^{p_{\epsilon a}} \left(\frac{w/c}{0.38}\right)^{p_{\epsilon w}} \left(\frac{6.5c}{\rho}\right)^{p_{\epsilon c}}$$

$$\tau_{sh} = \tau_0 k_{\tau a} \left(k_s \frac{D}{1\ mm}\right)^2$$

$$\tau_0 = \tau_{cem} \left(\frac{a/c}{6}\right)^{p_{\tau a}} \left(\frac{w/c}{0.38}\right)^{p_{\tau w}} \left(\frac{6.5c}{\rho}\right)^{p_{\tau c}}$$

Where:

Table G.8 Humidity dependence k_h factor.

Relative humidity	k_h
$h \leq 0.98$	$1 - h^3$
$0.98 \leq h \leq 1.00$	$12.94(1 - h) - 0.2$

Table G.9 k_s as function cross section shape.

Cross section shape	k_s
Infinite slab	1.00
Infinite cylinder	1.15
Infinite square prism	1.25
Sphere	1.30
Cube	1.55

Table G.10 Autogenous shrinkage parameters depending on cement type.

Parameter	R	RS	SL
$\tau_{au,cem}$ (in Days)	1.00	41.0	1.00
$r_{\tau w}$	3.00	3.00	3.00
r_t	-4.50	-4.50	-4.50
r_a	1.00	1.40	1.00
$\varepsilon_{au,cem}$	210×10^{-6}	-84×10^{-6}	-0.00×10^{-6}
$r_{\epsilon a}$	-0.75	-0.75	-0.75
$r_{\epsilon w}$	-3.50	-3.50	-3.5

Table G.11 Drying shrinkage parameters depending on cement type.

Parameter	R	RS	SL
τ_{cem} (in Days)	0.016	0.080	0.010
$p_{\tau a}$	-0.33	-0.33	-0.33
$p_{\tau w}$	-0.06	-2.40	3.55
$p_{\tau c}$	-0.10	-2.70	3.80
ε_{cem}	360×10^{-6}	860×10^{-6}	410×10^{-6}
$p_{\epsilon a}$	-0.80	-0.80	-0.80
$p_{\epsilon w}$	1.10	-0.27	1.00
$p_{\epsilon c}$	0.11	0.11	0.11

G.2.6   Japanese Society of Civil Engineers (JSCE) Model

$$\varepsilon'_{cs}(t, t_0) = \varepsilon'_{ds}(t, t_0) + \varepsilon'_{as}(t, t_0)$$

$$\varepsilon_{as}(t) = \gamma \varepsilon_{as\infty} \beta(t)$$

$$\varepsilon_{as\infty} = 3070 \, e^{[-7.2(W/B)]} \qquad for \; 0.2 \leq W/B \leq 0.5$$

$$\varepsilon_{as\infty} = 80 \qquad for \; 0.5 < W/B$$

$$\beta(t) = 1 - e^{[-a(t-t_s)^b]}$$

$$\varepsilon'_{ds}(t, t_0) = \frac{\varepsilon'_{ds\infty} \cdot (t - t_0)}{\beta + (t - t_0)}$$

$$\beta = \frac{4W \sqrt{V/S}}{100 + 0.7t_0}$$

$$\varepsilon'_{ds\infty} = \frac{\varepsilon_{ds\rho}}{1 + \eta \cdot t_0}$$

$$\varepsilon_{ds\rho} = \frac{\alpha(1 - RH/100)W}{1 + 150 \, e^{\left\{-\frac{500}{f'_c(28)}\right\}}}$$

$$\eta = 10^{-4}\{15\,e^{(0.007f_c'(28))} + 0.25W\}$$

Where:

W = unit water content (kg/m^3);

V/S = volume to the surface ratio (mm);

RH = relative humidity (%);

$f_c'(28)$ = compressive strength of concrete at 28 days in MPa;

α = coefficient representing the influence of cement type;

t_0 = effective age (in days) of the concrete at the beginning of drying;

t = effective age (in days) of the concrete during drying;

$a\ and\ b$ = coefficient depends on water to cement ratio as given in Table G.12.

Table G.12 Values of $a\ and\ b$ as a function of water-to-cement ratio.

W/C ratio	a	b
0.20	1.20	0.40
0.23	1.50	0.40
0.30	0.60	0.50
0.40	0.10	0.70
0.50	0.03	0.80
1.00	0.03	0.80

G. 3 Stress-strain Models
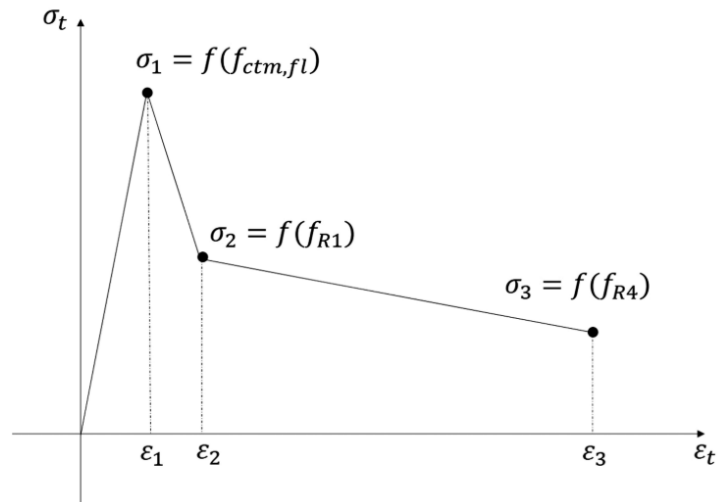
G.3.1 RILEM TC 162-TDF

Figure G.1 Trilinear $\sigma - \varepsilon$ diagram for steel fibres reinforced concrete (SFRC), according to RILEM TC 162-TDF.

$$\sigma_1 = 0.7 f_{ctm,fl}(1.6 - d)$$

$$\varepsilon_1 = \frac{\sigma_1}{E}$$

$$\sigma_2 = 0.45 f_{R1} k_h$$

$$\varepsilon_2 = \varepsilon_1 + 0.1\%_0$$

$$\sigma_3 = 0.37 f_{R4} k_h$$
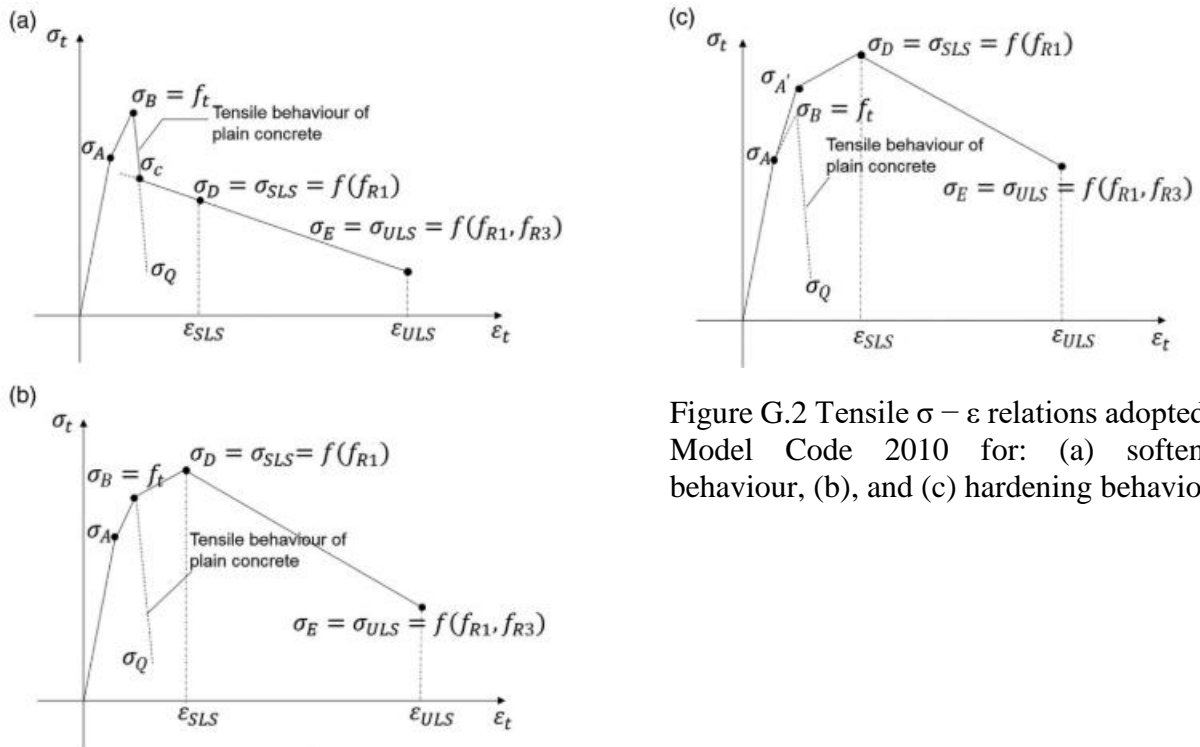
$$\varepsilon_3 = 25\%_0$$

G.3.2 Model Code 2010

Figure G.2 Tensile σ − ε relations adopted by Model Code 2010 for: (a) softening behaviour, (b), and (c) hardening behaviour.

$$\sigma_A = 0.9 f_t$$

$$\varepsilon_A = \frac{\sigma_A}{E}$$

$$\sigma_B = f_t$$

$$\varepsilon_B = 0.00015$$

$$\sigma_D = \sigma_{SLS} = 0.45 f_{R1}$$

$$\varepsilon_{SLS} = \frac{CMOD_1}{l_{cs}}$$

$$\sigma_A' = 0.9 \sigma_{SLS}$$

$$\varepsilon_A' = \frac{\sigma_A'}{E_c}$$

$$\sigma_E = \sigma_{ULS} = \sigma_{SLS} - \frac{W_u}{CMOD_3}(\sigma_{SLS} - 0.5 f_{R3} + 0.2 f_{R1})$$

216

$$\varepsilon_{ULS} = \frac{W_u}{l_{cs}} = \min\left(\varepsilon_{Fu}, \frac{2.5}{l_{cs}}\right) l_{cs} = min(s_m, y)$$

$$CMOD_1 = 0.5 \; mm$$

$$\varepsilon_{ULS} = \frac{W_u}{l_{cs}} = \min\left(\varepsilon_{Fu}, \frac{2.5}{l_{cs}}\right) l_{cs} = min(s_m, y)$$

$$CMOD_1 = 0.5 \; mm$$